ISSN 1349-113X
JAXA-SP-05-021E

JAXA Special Publication

The Second Open Competition for the Hayabusa Asteroidal Sample Preliminary Examination Team (HASPET)

Tetsuo YAMAMOTO, Ikuo KUSHIRO,
Akira FUJIWARA and Hajime YANO

March 2006

Japan Aerospace Exploration Agency

JAXA-SP-05-021E

JAXA Special Publication

The Second Open Competition for the Hayabusa Asteroidal Sample Preliminary Examination Team (HASPET)

Edited by

Tetsuo YAMAMOTO
The Institute of Low Temperature Research, Hokkaido University

Ikuo KUSHIRO
The University of Tokyo (Emeritus)

Akira FUJIWARA and Hajime YANO
The Institute of Space and Astronautical Science,
Japan Aerospace Exploration Agency

March 2006

Japan Aerospace Exploration Agency

JAXA-SP-05-021E

The Second Open Competition for the Hayabusa Asteroidal Sample
Preliminary Examination Team (HASPET)

CONTENTS

Preface:
The Second HASPET Open Competition and Its Test Analog Samples

By

Tetsuo YAMAMOTO[1], Ikuo KUSHIRO[2] ,

Akira FUJIWARA[3] , and Hajime YANO[3]

1. HAYABUSA MISSION UPDATES

Hayabusa has landed and flown again. On the smooth terrain Muses-C Regio of the near Earth asteroid (25143) Itokawa, the Japanese engineering demonstration spacecraft attempted the touch-and-go sampling twice in November 2005 (Yano, *et al*., 2006). It was the first sample return mission from another celestial body surface other than the Moon in human history. Due to multiple malfunctions of the attitude control devices, the fate of its successful sampling will not be revealed until the Hayabusa spacecraft can eventually return to the earth.

Since its recovery from temporal communication loss in January 2006, the Hayabusa operation team successfully managed to restore most of the spacecraft capabilities for attitude control by alternatives, to recharge surviving battery cells and to transfer the sample cacther to the Earth return capsule. From the spring of 2007, Hayabusa will reignite its ion engines and manage three-axis stability with one remaining reaction wheel with solar radiation pressure and IES gimbal control. The spacecraft will be then on its way back home in June 2010, three years later than the original plan of the landing on the desert of Australia.

Hayabusa employed an impact sampling system consisted of projectors, a deployable “horn”, cylindrical/conical concentrator to receive and deflect ejected fragments, and a sample catcher, with separate rooms for each sampling, and a transfer mechanism to the capsule (Yano, *et al*., 2002). During the sampling sequence, as soon as its touchdown is autonomously detected, a Ta metal projectile of 5-g mass is shot at velocity of 300 m/s. Impact of the projectile produces fragment ejecta, which are concentrated through the horn toward the catcher. Expected amount of the samples from results of 1G and microgravity impact tests for monolithic targets, mm-sized pebble/gravel targets and regolith simulants are all around several hundred mg to several g per shot of fine grained particles, rather than large pieces of rocks. Even without firing the projectile, recent microgravity simulations suggested that small amount of slowly uplifted samples might have reached inside the catcher during an unexpected landing of the spacecraft at the MUSES-C Regio about a half hour in the first touchdown.

2. HASPET OPEN COMPETITIONS

JAXA has pledged that, as long as amount of returned samples are enough for such purposes, Itokawa samples will be distributed to qualified researchers all over the world for maximizing its scientific output. However, such detailed analysis proposals must rely on general characteristics of the samples during the initial analysis phase. The Hayabusa Asteroidal Sample Preliminary Examination Team (HASPET) is therefore formed under the Hayabusa Joint Science Team and, should consist of JAXA scientists, NASA and Australian Co-Is based on each bilateral agreement, and Japanese researchers from outsourcing institutions, who are selected in respective disciplines through this open competition scheme.

The HASPET is, in principle, responsible for characterizing general features of the bulk and some of major samples. They

1 Hokkaido University, Sapporo, Hokkaido, Japan

2 University of Tokyo (Emeritus), Bunkyo-ku, Tokyo, Japan

3 Institute of Space and Astronautical Science, Japan Aerospace Exploration Agency, Sagamihara, Kanagawa, Japan

also must make acquired data available to the public after the first results published; then international scientists can request samples for detailed analyses accordingly. The similar but internationally enhanced initial analysis team was formed and functioned well for NASA's cometary coma dust sample return mission STARDUST, which successfully brought cometary dust to ground laboratories in 2006 (Brownlee, *et al*., 2006).

The first HAPSET competition was conducted in 2000-2001 and the MUSES-C Sample Advisory Committee endorsed the final recommendation in 2002. Among eleven applicants, six teams were recognized as qualified to join the preliminary examination team as of 2002 (Kushiro, *et al*, 2003). After the spacecraft launch, the second open competition was repeated in 2004-2005 and two teams out of five applicants were recommended for the final HASPET membership by the now-called Hayabusa Sample Advisory Committee in early 2006.

This document is a compilation of some of analysis reports in the second HASPET open competition, permitted to publish by respective applicants. Therefore, each report focuses on specific suitability for general characterization of the returned samples; yet neither new discoveries nor scientific achievements of the report are objectives of their writing. Instead, the authors demonstrate how much their technical capabilities, analytical precision, and usefulness of the derived results for subsequent detailed analyses are worth being included in the Hayabusa initial analysis. This document may also serve as a source book for JAXA to construct an astromaterial curation and initial analysis facility, which will be completed in 2008.

3. TEST ANALOG SAMPLES

In this round of the competition, each applied team received two kinds of "asteroid sample analogs", meteoritic samples that no applicant knew what they were in advance, to conduct proposed analysis with self-claimed amount of samples (the maximum of 100 mg each) in self-claimed duration (the maximum of 6 months). This is the same rule as the first competition. One major distinction between the first and the second competitions is that, at the time of their applications, the second round applicants should know that Itokawa is an S-type asteroid (e.g., Fujiwara, *et al*., 2006) as well as major results of the NEAR-Shoemaker mission to the S-type asteroid Eros (Veverka, *et al*., 2001). Therefore, the Selection Committee chose a unique H-"ordinary" chondrite Burnwell as the analog samples at this time.

The simulant samples are kindly provided to JAXA by Dr. E. Jarosewich of the Smithsonian National Museum of Natural History, U.S.A. via Dr. M.E. Zolensky of NASA/JSC, one of the two NASA-selected HASPET members. At first, the samples were separated to two size fractions (ID-A and B) as shown in Table 1 by sieving at the Smithsonian. Then both samples were divided to 100 mg each by only using the Al foils approved by the NASA/JSC Lunar Sample Laboratory, wrapped with them and sealed in a borosilicate glass vial (thus the samples only touched the Al foil but not the interior of vials) by HY at an ISAS clean room for distribution.

Table 1: Test Analog Samples Conditions

Catalog Number	Sample ID	Sieve Mesh Size (μm)	Mass Fraction
USNM7073	**A	<100 (Small)	78.49 wt%
USNM7073	**B	>100 (Large)	21.51 wt%

The Burnwell meteorite fell as a single stone of 1.504 kg mass in Burnwell, Pike County, Kentucky, U.S.A. (37°37'19"N 82°14'14"W) at 15:45 EDT (19:45 UT) on September 4, 1990. Classification and mineralogy were determined by T. McCoy, R. Ash, G. Jarosewich and S. Russell at the Smithsonian Institute. According to Russell *et al*. (1998), this meteorite has lower Fa in olivine (15.8 mol%), Fs in orthopyroxene (13.4 mol%), Co in kamacite (0.36 wt%), FeO from bulk chemical analysis (9.43 wt%), and $\triangle^{17}O$(0.51 ±0.02 %), and higher Fe, Ni, Co metal (19.75 wt% from bulk wet chemical analysis) than observed in H chondrites. This meteorite plots on extensions of H-L-LL chondrite trends for each of these properties towards more reducing

compositions than in H chondrites. Russell, *et al*. (1998) also quoted: "...extensions of this trend has been previously suggested in the case of other low-FeO chondrites or silicate inclusions in the IIE iron Netschaevo, but interpretation of the evidence in these meteorites is complicated by terrestrial weathering, chemical deisequilibrium or reduction. In contrast, the Burnwell meteorite is an equilibrated fall that exhibits no evidence for reduction".

For these reasons, keys of analyzing these samples are to notice that (1) this is not a typical ordinary chondrite although its spectral information may suggest some similarities to Itokawa (i.e., bright albedo for S-type asteroid) and (2) samples A and B actually came from the same meteorite but sorted by size such that metal percentages may vary between the two samples.

REFERENCES

Brownlee, D., Tsou, P., Aléon, J., Alexander, C.M.O'D., Araki, T., Bajt, S., Baratta, G.A., Bastien, R., Bland, P., Bleuet, P., Borg, J., Bradley, J.P., Brearley, A., Brenker, F., Brennan, S., Bridges, J.C., Browning, N.D., Brucato, J.R., Bullock, E., Burchell, M.J., Busemann, H., Butterworth, A., Chaussidon, M., Cheuvront, A., Chi, M., Cintala, M.J., Clark, B.C., Clemett, S.J., Cody, G., Colangeli, L., Cooper, G., Cordier, P., Daghlian, C., Dai, Z., D'Hendecourt, L., Djouadi, Z., Dominguez, G., Duxbury, T., Dworkin, J.P., Ebel, D.S., Economou, T.E., Fakra, S., Fairey, S.A.J., Fallon, S., Ferrini, G., Ferroir, T., Fleckenstein, H., Floss, C., Flynn, G., Franchi, I.A., Fries, M., Gainsforth, Z., Gallien, J.-P., Genge, M., Gilles, M.K., Gillet, P., Gilmour, J., Glavin, D.P., Gounelle, M., Grady, M.M., Graham, G.A., Grant, P.G., Green, S.F., Grossemy, F., Grossman, L., Grossman, J.N., Guan, Y., Hagiya, K., Harvey, R., Heck, P., Herzog, G.F., Hoppe, P., Hörz, F., Huth, J., Hutcheon, I.D., Ignatyev, K., Ishii, H., Ito, M., Jacob, D., Jacobsen, C., Jacobsen, S., Jones, S., Joswiak, D., Jurewicz, A., Kearsley, A.T., Keller, L.P., Khodja, H., Kilcoyne, A.L.D., Kissel, J., Krot, A., Langenhorst, F., Lanzirotti, A., Le, L., Leshin, L.A., Leitner, J., Lemelle, L., Leroux, H., Liu, M-C., Luening, K., Lyon, I., MacPherson, G., Marcus, M.A., Marhas, K., Marty, B., Matrajt, G., McKeegan, K., Meibom, A., Mennella, V., Messenger, K., Messenger, S., Mikouchi, T., Mostefaoui, S., Nakamura, T., Nakano, T., Newville, M., Nittler, L.R., Ohnishi, I., Ohsumi, K., Okudaira, K., Papanastassiou, D.A., Palma, R., Palumbo, M.E., Pepin, R.O., Perkins, D., Perronnet, M., Pianetta, P., Rao, W., Rietmeijer, F.J.M., Robert, F., Rost, D., Rotundi, A., Ryan, R., Sandford, S.A., Schwandt, C.S., See, T.H., Schlutter, D., Sheffield-Parker, J., Simionovici, A., Simon, S., Sitnitsky, I., Snead, C.J., Spencer, M.K., Stadermann, F.J., Steele, A., Stephan, T., Stroud, R., Susini, J., Sutton, S. R., Suzuki, Y., Taheri, M., Taylor, S., Teslich, N., Tomeoka, K., Tomioka, N., Toppani, A., Trigo-Rodríguez, J.M., Troadec, D., Tsuchiyama, A., Tuzzolino, A.J., Tyliszczak, T., Uesugi, K., Velbel, M., Vellenga, J., Vicenzi, E., Vincze, L., Warren, J., Weber, I., Weisberg, M., Westphal, A.J., Wirick, S., Wooden, D., Wopenka, B., Wozniakiewicz, P., Wright, I., Yabuta, H., Yano, H., Young, E.D., Zare, R.N., Zega, T., Ziegler, K., Zimmerman, L., Zinner, E. and Zolensky, M., 2006, Comet 81P/Wild 2 Under a Microscope, *Science*, **314**, 1711-1716.

Fujiwara, A., Kawaguchi, J., Yeomans, D.K., Abe, M., Mukai, T., Okada, T., Saito, J., Yano, H., Yoshikawa, M., Scheeres, D.J., Barnouin-Jha, O., Cheng, A.F., Demura, H., Gaskell, R.W., Hirata, N., Ikeda, H., Kominato, T., Miyamoto, H., Nakamura, A.M., Nakamura, R., Sasaki, S. and Uesugi, K., 2006, The rubble-pile asteroid Itokawa as observed by Hayabusa, *Science*, **312**, 1330-1334.

Kushiro, I., Fujiwara, A. and Yano, H (eds.), 2003, The First Open Competition for the MUSES-C Asteroidal Sample Preliminary Examination Team, **ISAS Report SP-16**.

Russell, S.S., McCoy, T.J., Jarosewich, E. and Ash, R.D., 1998, The Burnwell, Kentucky, low-FeO chondrite fall: Description, classification and origin, *Meteoritics and Planetary Science*, **33**, 853-856.

Veverka, J., Thomas, P.C., Robinson, M., Murchie, S., Chapman, C., Bell, M., Harch, A., Merline, W.J., Bell III, J.F., Bussey, B.,

Carcich, B., Cheng, A., Clark, B., Domingue, D., Dunham, D., Farquhar, R., Gaffey, M.J., Hawkins, E., Izenberg, N., Joseph, J., Kirk, R., Li, H., Lucey, P., Malin, M., McFadden, L., Miller, J.K., Owen Jr, W.M., Peterson, C., Prockter, L., Warren, J., Wellnitz, D., Williams, B.G. and Yeomans, D.K., 2001, Imaging of Small-Scale Features on 433 Eros from NEAR: Evidence for a Complex Regolith, *Science*, **292**, 484-487.

Yano, H., Hasegawa, S., Abe, M. and Fujiwara, A., 2002, Asteroidal surface sampling by the MUSES-C spacecraft, *Proc. Asteroids, Comets and Meteors 2002*, **ESA SP-500**, 103-106.

Yano, H., Kubota, T., Miyamoto, H., Okada, T., Scheeres, D., Takagi, Y., Yoshida, K., Abe, M., Abe, S., Barnouin-Jha, O.S., Fujiwara, A., Hasegawa, S., Hashimoto, T., Ishiguro, M., Kato, M., Kawaguchi, J., Mukai, T., Saito, J., Sasaki, S. and Yoshikawa, M., 2006, Touch-down sites of the Hayabusa spacecraft at the Muses Sea area on asteroid 25143 Itokawa, *Science*, **312**, 1350-1355.

Mineralogy of 100-μg Powder Test Samples II: Evolved Procedures for the Initial Analysis of Regolith Materials of the Asteroid Itokawa

By

Tomoki NAKAMURA[1], Takaaki NOGUCHI[2], and Masahiko TANAKA[3]

Abstract: Applying a combined analytical method specialized for cosmic-dust research, we have characterized mineralogy of individual mineral particles in 2A and 2B powder test samples that were prepared for the second analysis competition of the Hayabusa mission. Thirty-eight mineral particles mostly less than 300 μm in diameter and ten fine-grained mineral aggregates less than 200 μm in diameter were picked out from the test samples. Individual samples were X-rayed using synchrotron radiation to have powder X-ray diffraction patterns for identification of constituent minerals. The relative abundances of major constituent minerals in individual samples were determined by applying the Rietveld refinement to diffraction patterns. The X-rayed samples were polished and analyzed by a scanning electron microscope (SEM) for imaging and an electron-probe microanalyzer (EPMA) for quantitative concentrations of thirteen elements. Finally, ten selected samples were thinned by ultramicrotomy, argon ion bombardment, or focused ion beam (FIB) method for detailed mineralogical characterization by transmission electron microscopy (TEM). Small plagioclase compositions are determined by analytical electron microscopy (AEM) using a cold sample stage. The bulk mineralogy, chemical composition, and nano-scale textures were all obtained from a single small particles less than 300 μm and the total mass of each test sample we used for the present study was only 100 μg. Therefore, we can accomplish complete mineral characterization using very small quantity of regolith materials of the asteroid Itokawa, when the initial analysis of the returned samples is undertaken.

The results showed that 2A powder sample consists mainly of olivine ($Fa_{15.1\pm0.6}$ on an average), low-Ca pyroxene ($Fs_{13.9\pm0.7}$ on an average), plagioclase, troilite, and kamacite with minor amounts of high-Ca pyroxene, taenite, chromite, Ca-phosphate, and alkali feldspar. The compositions and compositional variations of silicates and the minor element abundances in FeNi metals indicate that the 2A sample bears a close resemblance to H chondrites with petrologic type 4 to 5. Fe/Mg ratios of both olivine and low-Ca pyroxene in the 2A sample correspond to the lowest-end of Fe/Mg variation for H chondrites, suggesting that it is a sample of most reduced type of H chondrites. In addition, the 2A samples contain small amounts of artificial contamination such as quartz-calcite composites, Ni-free Mn-bearing iron metals, and carbonaceous particles like epoxy resin. These particles probably got mixed during preparation of the 2A sample powder from a meteorite. The 2B sample is coarse particles that are composed mainly of metallic phases such as kamacite. Olivine and low-Ca pyroxene are also contained, but metal/silicate ratio of the 2B test sample is apparently higher than that of the 2A test sample. However, Mg/Fe ratios of silicate ($Fa_{15.8\pm0.5}$ and $Fs_{14.4\pm0.7}$ on an average) and the presence of well-defined chondrules suggest that the 2B sample is also similar to H chondrites with petrologic type 4 to 5. All mineralogical characteristics, except for the mode of occurrence of FeNi metals, are very similar between 2A and 2B test samples. This may indicate that the two test samples were prepared from the same meteorite. The high metal/silicate ratio of the 2B test sample is therefore artifact, most probably the

1 Department of Earth and Planetary Sciences, Faculty of Sciences, Kyushu University, Hakozaki, Fukuoka 812-8581, Japan

2 Department of Materials and Biological Sciences, Ibaraki University, Bunkyo 2-1-1, Mito, Ibaraki 310-8512, Japan

3 WEBRAM, National Institute for Materials Science, SPring-8, Kouto Mikazuki-cho 1-1-1, Sayo-gun, Hyogo 679-5198, Japan

results of mechanical separation of magnetic components from a powder of an H chondrite.

1. INTRODUCTION

Surface materials of the asteroid Itokawa will be collected in 2005 and recovered to the Earth in the summer of 2007, only two years ahead from the present. The recovered samples will be powders consisting of particles ranging in size from submicron to submillimeter, analogous to cosmic dust and fine-grained constituents of brecciated regolith meteorites. Characterization of fine particles is extremely difficult and differs completely from that of coarse-grained crystalline meteorites. In addition, individual particles on the asteroidal regolith are not always fragments of the host asteroid, because many particles from other asteroids and comets are deposited there, as is commonly observed in many meteorites from the asteroidal regolith. Ultimately, individual particles in the powder regolith samples are different in origin. Therefore, the powder regolith samples need to be characterized on particle-basis, like characterization of cosmic dust such as micrometeorites and interplanetary dust particles. According to above principles of characterization, we set goals of the mineralogical investigation of the powder regolith samples: (1) evaluation of basic mineralogy of the host asteroid, and (2) identification of foreign particles coming from other planetary bodies. In the present paper, we have characterized powder test samples 2A and 2B to uncover these two essential properties.

As we claimed in the previous report (Nakamura and Noguchi, 2003), the amounts of the test samples allocated to us were very large, which is never expected for the initial characterization of the true sample recovered from the asteroid Itokawa. The most important point we think for the initial characterization is to characterize mineralogy using minimum quantity of the samples. From this viewpoint, only small amounts of test samples, less than 100 μg of each test sample, were used for our characterization and most parts of the samples were left unprocessed. Thus, the remaining samples can be provided for other scientific purposes. Our mineralogical techniques applied in the present investigation are those developed mainly for characterization of Antarctic micrometeorites (Nakamura et al., 1999; 2001a; 2001b; 2003; Noguchi and Nakamura, 2000; Noguchi et al., 2002; Nakashima et al., 2003). A main protocol of the analysis for a single particle consists of synchrotron X-ray diffraction technique for bulk mineralogy and transmission electron microscopy for detailed mineralogy.

2. SAMPLES AND EXPERIMENTAL PROCEDURES

2.1. Sample selection and preparation

2A test sample is a powder, consisting of a variety of minerals and mineral composites ranging in size from submicron to 300 μm. We have picked out twenty eight single particles from 50 to 300 μm in diameter showing different optical characteristics under a high-resolution stereomicroscope. These coarse particles are referred hereafter as 2AC1 to 2AC28. For very fine particles, we gathered them using a small amount of acetone-soluble resin on the top of a thin glass fiber to make a fine-grained mineral aggregate. Ten aggregates were prepared from the 2A test sample and referred hereafter as 2AF1 to 2AF10.

2B test sample is also a powder but consists of relatively coarse particles ranging from 100 to 800 μm in diameter. We selected 10 particles showing different optical characteristics and hereafter refer them as 2BC1 to 2BC10. Analyses of multiple disciplines were performed on these 48 particles, 38 from the 2A sample and 10 from the 2B sample, and the experimental procedures for each sample particle are summarized in Table 1.

2.2. Synchrotron X-ray diffraction analysis

Synchrotron radiation was applied for X-ray diffraction analysis of individual sample particles, because strong synchrotron X-rays, whose intensity is higher at least three orders of magnitudes than that of a normal X-ray generator, induce strong diffractions from small minerals in a sample particle. The experiment was performed at the beam line 3A of the Photon Factory, High energy accelerator research organization, Tsukuba, Japan. A gandolfi X-ray camera, which can obtain a powder X-ray pattern from a single mineral particle with diameters from 5 to 500 μm, was used for the analysis. The synchrotron X-ray was monochromated to

Table 1: Experimental procedures for each sample particle

	SR-XRD*	Rietveld analysis	OP#	SEM	EPMA	TEM	TEM sample preparation
2AC1 ~ 2AC26	○		○	○	○		
2AC26	○		○	○	○		
2AC27 ~ 2AC28	○		○				
2AF1 ~ 2AF5	○	○	○			○	ultramicrotomy
2AF5 ~ 2AF10	○	○	○	○	○		
2BC1 ~ 2BC5	○		○	○	○		
2BC6 ~ 2BC7	○		○	○	○	○	Ar bombardment
2BC8 ~ 2BC9			○	○	○	○	Ar bombardment
2BC10			○			○	FIB

* synchrotron X-ray diffraction
# optical microscope

2.161 +/- 0.002 Å using a monochromator and focused at the sample particle in the gandolfi camera using a focusing mirror. The wavelength of X-ray was precisely determined from a diffraction pattern of a standard Si particle. The monochromated X-ray gives sharp X-ray reflection peaks with very low background level. Each sample particle was mounted on a thin glass fiber with 5 μm in diameter with a very small amount of glue and exposed to synchrotron X-ray for 10 to 40 minutes, depending on the size of the particle.

The diffracted X-rays from samples are recorded on a high-resolution imaging plate (IP) set in the gandolfi camera. IP has a wide dynamic range of recordable X-ray intensity compared with films and shows a better linearity between X-ray intensity and blackness on the IP. We had used films in the previous report (Nakamura and Noguchi, 2003), but in the present report we successfully utilizes IP. After exposure to X-ray, IP was scanned by an IP reader BAS 2500 with angle resolution of 0.05°. The read data were converted to diffraction patterns and analyzed for integrated intensities and peak center positions of diffractions using an original software GanCon2 that we have developed.

2.3 Rietveld analysis

The relative abundances of the major four crystalline minerals, olivine, low-Ca pyroxene, plagioclase and troilite, in 2AF1 to 2AF10 samples were obtained through the Rietveld quantitative phase analysis of the powder X-ray diffraction data. In the multi-phase Rietveld refinement, the scale factors are in proportion to the amount of included crystalline phases. And the mass weight ratio is calculated from a following formula,

$$x_n = (s_n Z_n M_n V_n) / (\Sigma_i s_i Z_i M_i V_i)$$

Where x is the mass weight ratio, s is the scale factor, Z is the chemical number, M is the molecular weight and V is the unit cell volume. The mass weight ratio is determined by evaluation of s values with Rietveld method. The Rietveld structure refinement program, PFLS (Toraya, 1998), was used for Rietveld analysis and this program carries out the quantitative phase analysis, above-mentioned method, as structure refinements. In principle, when quantitative phase analysis by Rietveld method is carried out, all of the component minerals in the sample should be included in calculation. But in this analysis the minor minerals, such as kamacite or taenite, were neglected. Because the amounts of these minerals are little and if these minerals were included in refinement calculation, the refinement cycles had not been convergence and solutions could not be obtained. Starting crystal structure models for each mineral were obtained from references (Morimoto and Guven, 1970, Prewitt et al., 1976, Tokonami et al., 1972, Birle et al., 1968). Isotropic temperature factors, which were also adopted from the same references, were used and the values were fixed through out the refinements. The chemical compositions determined by EPMA analysis were used and these values also fixed through out refinements. The chemical compositions of each crystalline phase were assumed to be homogeneous. As concerns olivine, pyroxene and plagioclase, the scale factors, the lattice constants, the atomic positions and the peak profile parameters were refined. But in troilite case, the scale factor was only refined. The Rietveld least square cycles were also hard to

converge, when atomic or peak profile parameters of troilite were included in calculation because of the insufficiency of observed diffraction peaks. Absorption correction was carried out using the estimated absorption coefficient from that of olivine, which is the major component of these samples. The magnitude of errors is considered to be several percents because of the many assumptions such as neglect of minor minerals, neglect of variation of chemical composition of each mineral phase, use of estimated absorption coefficient and neglect of difference of crystal quality of each mineral phase and so on.

2.4. EPMA analysis

The X-rayed sample particles were embedded in a small amount of epoxy resin and polished using the micro-diamond paste, and analyzed by an EPMA (JEOL JXA-733 superprobe) equipped with a wave-length-dispersive X-ray spectrometer (WDS). WDS quantitative analyses were performed at 15 kV accelerating voltage and 10 nA beam current with a focused beam 2 μm in diameter. Quantitative chemical compositions of oxides SiO_2, TiO_2, Al_2O_3, FeO, MnO, MgO, CaO, NaO, K_2O, Cr_2O_3, NiO, P_2O_5, and SO_3 for silicates and elements Ni, Fe, Mn, Co, Cr, S, and P for sulfides and metals were obtained via the ZAF correction method. Special care was taken for the analysis of FeNi metals. In the analysis of FeNi metals, Co concentrations were obtained through correction of Fe-Kß contribution on Co-K*α*. The X-ray energy of Fe-Kß is very close to that of Co-K*α*, therefore the contribution from Fe-Kß need to be corrected especially for the minerals rich in Fe such as FeNi metals. We analyzed pure Fe metal and found that the contribution of Fe-Kß from 100% Fe on Co abundance is 0.15 wt%. We corrected Co concentrations of FeNi metals in both 2A and 2B test samples according to the Fe content in the metals.

2.5. TEM observation

2.5.1. Sample preparation

Subsequent to X-ray diffraction analysis, selected samples were processed to have thin plates for TEM observation. Three methods for thinning were applied, ultramicrotomy, Ar ion bombardment, and focused Ga ion beam sputtering (Table 1). The former was applied for fine-grained samples of 2AF1 to 2AF5. The latter two methods were applied for metal-rich coarse 2B samples, 2BC6, 2BC7, 2BC8, 2BC9, and 2BC10.

Ultramicrotomy: A sample made of fine-grained mineral fragments bounded of acetone soluble resin were disaggregated on one sharp end of a rod made of consolidated EMbed 812 epoxy resin by a small drop of acetone. After disaggregation of the fine-grained fragments, the fragments were covered by a small drop of epoxy resin. The sample was cured at 70 ^{o}C for 48 hrs. Embedding was performed in a clean bench (class 100) set in a clean room (class 1000) at Ibaraki University to prevent contaminant mixing with the sample. The cured samples were microtomed by Leitz-Reihert Super Nova ultramicrotome. The thickness of each section was ~ 70 nm. Only one ultra-thin section among serial sections on a Cu grid was used to prevent multiple analyses of the same mineral grains. TEM observation of the ultramicrotomed sample revealed that one section contains more than 150 individual grains.

Ar ion bombardment: Conventional Ar bombardment method was used for coarse 2B test samples (Table 1). Four samples were prepared by using this method. Polished thin sections of the samples were demounted from glass slides after EPMA analysis. The demounted samples were attached to single-hole Mo grids by epoxy resin. Argon bombardment was performed by using GATAN model 600 ion milling machine. Accelerating voltage and current were 2.5 kV and 1.0 mA.

Focused Ga ion beam sputtering: FIB thining system (Hitachi FB 2000) was applied for the TEM sample preparation of 2BC10 that consists mainly of FeNi metal. The FIB is an appropriate method for thinning a sample with a variety of mineralogy. Gallium ion beam with accelerating voltage 30 KeV and beam current 9.5 μA has exposed on a thin sample slice that was placed on a single-hole Mo grid. The thickness of the sample slice before FIB sputtering was 20 μm and that of the sputtered sample was approximately 100 nm with an area of 10 x 10 μm. The thinning takes 5 hours to complete.

2.5.2. Transmission electron microscopy

TEM observation was performed by using JEOL JEM-2000FX II with accelerating voltage 200 KeV. Along with high-resolution imaging and electron diffraction analysis, quantitative elemental analysis was performed by EDAX DX4 energy-dispersive X-ray spectrometer. Although the analysis was based on Cliff-Lorimer approximation, the effects by absorption were considered by regarding k factors. K factors have been already determined by one of the authors (T. Noguchi) using many mineral standards. For K factors of silicate analysis, we determined 12 factors. K factors for Na, Mg, Al, Cl, K, Ca, and Fe were determined by using ultramicrotomed mineral standards. K factors for S, Ti, Cr, Mn, and Ni were determined by using ion thinned mineral standards. K factors for Fe-Ni metals and sulfides were determined by using ultramicrotomed mineral standard.

For the analysis of feldspar minerals in the fine-grained 2AF series samples, we used liquid nitrogen cooled analytical stage, Gatan model 633. The sample was cooled to -173 ^{o}C during observation and analysis of feldspars. As shown later, the cooling greatly lessens the compositional change of feldspars during analysis and the decomposition rates of crystal structures during observation under high magnifications.

3. RESULTS OF ANALYSIS

The results of SEM observation, EPMA analysis, and X-ray diffraction analysis of all sample particles except for 2BC10, which was examined only by TEM, are summarized in Appendix so as to show textural, mineralogical, and compositional characteristics of individual samples.

3.1. 2A test sample - host mineralogy

Coarse particles, 2AC1 to 2AC28, show a variety of mineralogical properties. Only 8 particles are dominated by a single phase (see Appendix): olivine (2AC10, 2AC24, and 2AC25), troilite (2AC7 and 2AC8), kamcite (2AC1 and 2AC15), and taenite (2AC18). The presence of the single-phase particles indicates that the largest crystal size of these minerals exceeds 100 μm. The other 20 particles are composites of several kinds of minerals. Among 28 sample particles, most abundant mineral is olivine and next is low-Ca pyroxene. Olivine has a homogeneous Fe/Mg ratio with Fa 15.1 ± 0.6 (Fig. 1a). CaO and MnO concentrations in olivine are less than 0.1 wt% and from 0.4 to 0.6 wt%, respectively (Fig. 2a). Low-Ca pyroxene also has a homogeneous Fe/Mg ratio with Fs 13.9 ± 0.7 (Fig. 1b). But Ca/(Mg+Fe) ratio is not homogenized between grains (Fig. 3a). Both MnO and Cr_2O_3 concentrations in low-Ca pyroxene varies from < 0.1 to 0.8 wt% (Fig. 4a). TiO_2 and Al_2O_3 concentrations are both less than 0.4 wt% (Fig. 5a).

High-Ca pyroxene and plagiocalse are also contained in the 2A samples. Wo content varies from 12 to 48, while Mg/Fe ratio is relatively constant (Fig. 3a). MnO concentration is similar to that of low-Ca pyroxene, but Cr_2O_3 is higher than that of low-Ca pyroxene (Fig. 6a). TiO_2, Al_2O_3, and Na_2O concentrations are from 0.3 to 1.4, from 1.3 to 5.5, and < 1.1, respectively. Plagioclase is contained in many 2A test particles based on the X-ray diffraction patterns, but only a few samples have regions more than 10 μm rich in plagiocalse. In such a region, tiny grains of olivine, pyroxene, and FeNi metal are present together with plagioclase. Therefore, chemical composition of plagioclase is difficult to obtain by EPMA analysis and thus it is determined by AEM method using a cold sample stage, as shown later.

Troilite and FeNi metals occur in abundance in the 2A test samples. They are commonly present with silicates. Troilite is the only sulfide contained in the 2A sample. FeNi metals are kamacite with Ni content up to 6 wt% and taenite with Ni from 33 to 50 wt% (Fig. 7a). Chromite, typically less than 10 μm but occasionally up to 30 μm, occurs together with troilite and FeNi metals in samples such as 2AC8, and 2AC20. Calium phosphate from 10 to 20 μm in size also occurs in samples 2AC14 and 2AC19. 2AC4 shows signatures of melting (Appendix 2AC4). The sample contains many small gas bubbles indicative melting of silicates. X-ray diffraction petterns of this sample indicates the presence of magnetite (Appendix 2AC4). This suggests that the sample was melted at elevated oxygen fugacity and thus it may be a fragment of the fusion crust that was formed during atmosoheric entry of the test-sample meteorite.

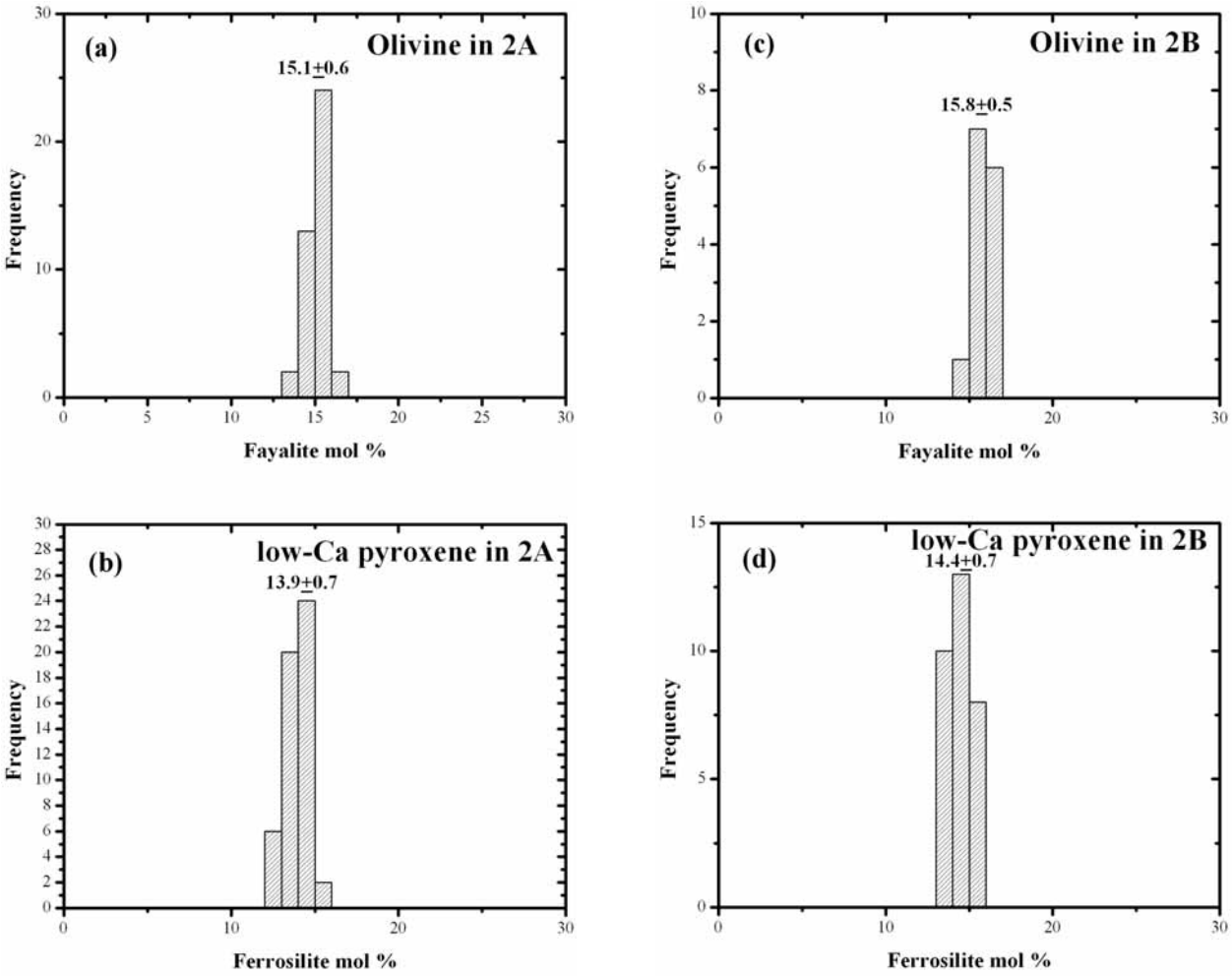

Figure 1. Histograms showing distributions of Fs and Fa contents. (a) Fa of olivine in the 2A sample. (b) Fs of low-Ca pyroxene in the 2A sample. (c) Fa of olivine in the 2B sample. (d) Fs of low-Ca pyroxene in the 2B sample.

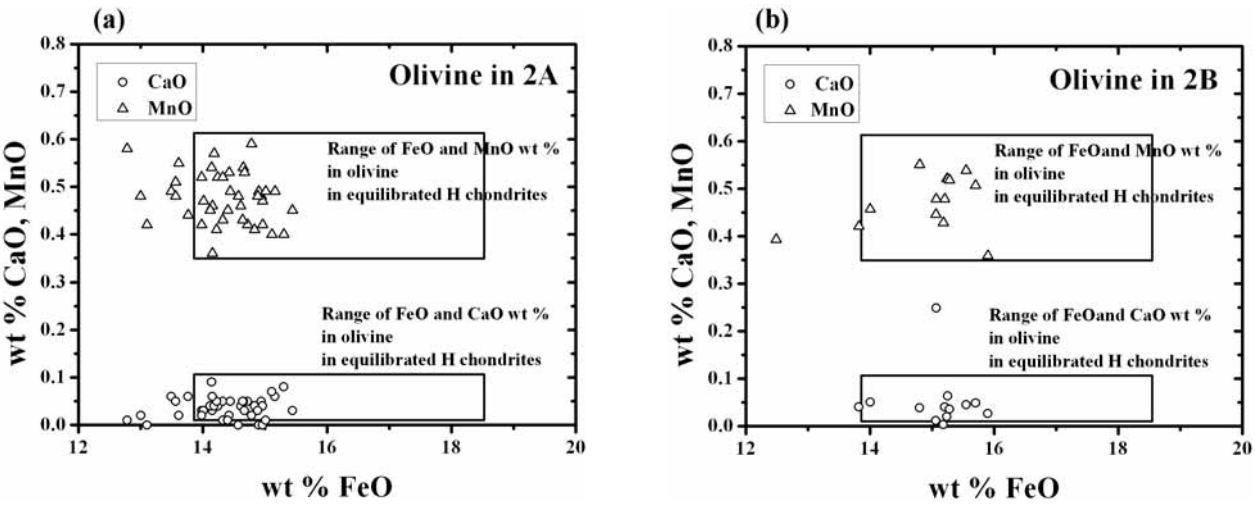

Figure 2. CaO and MnO concentrations in olivine in the 2A sample (a) and that in the 2B sample (b).

Samples being composed of fine particles, 2AF1 to 2AF10, show X-ray diffraction patterns similar to each other (see Appendices 2AF1 to 2AF10). Major phases are olivine, low-Ca pyroxene, plagioclase, and troilite. Based on the intensity ratio of some strong diffractions of low-Ca pyroxene between 38 and 45 diffraction angle (see Appendix section in Nakamura et al.,

2001b), low-Ca clinopyroxene are overabundant compared with orthopyroxene. FeNi metals are rare in fine-grained 2AF samples, compared with coarse 2AC samples. This is probably because metals are ductile and hard to be grinded during preparation of test samples. In order to obtain the relative abundance of major constituent minerals, olivine, low-Ca clinopyroxene, plagiocalse, and troilite, Rietveld analysis was performed on the X-ray diffraction data of 2AF1 to 2AF10. Figure 8 shows the results of the Rietveld refinement of the 2AF6 sample and Table 2 shows the results of quantitative phase analysis of 2AF1 to 2AF10. The magnitude of errors is considered to be several percents. Samples, 2AF1 to 2AF10, show X-ray diffraction patterns similar to each other, and accordingly the relative mineral abundance is basically similar to each other (Table 2). All sample particles contain major minerals in the order of olivine > low-Ca clinopyroxene > plagioclase >> troilite. The results demonstrate that the Rietveld analysis is an appropriate method to obtain the relative mineral abundance and, in our knowledge, this is the first report of application of the Rietveld refinement to the fine-grained extraterrestrial material.

Table 2. The results of quantitative phase analysis of olivine, low-Ca pyroxene, plagioclase and troilite, by Rietveld analysis

Sample No.	Olivine	Low-Ca Pyroxene	Plagioclase	Troilite	(wt%)
2AF1	60.8	24.0	13.1	2.1	
2AF2	46.3	31.6	18.1	4.0	
2AF3	61.6	23.2	14.9	0.3	
2AF4	58.8	26.4	12.6	2.3	
2AF5	52.2	32.6	13.8	1.5	
2AF6	70.5	17.1	11.5	0.9	
2AF7	50.5	30.5	16.5	2.6	
2AF8	54.3	29.2	14.6	1.8	
2AF9	56.5	27.2	14.0	2.3	
2AF10	52.0	32.8	12.3	2.9	

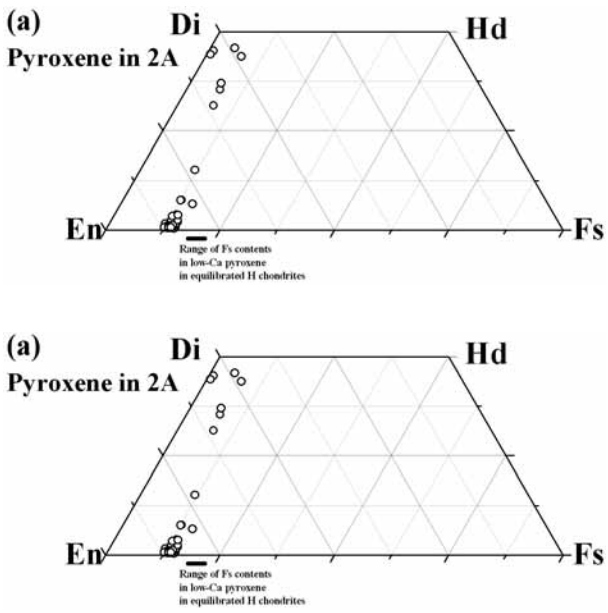

Figure 3. Pyroxene compositions of the 2A sample (a) and the 2B sample (b).

TEM observation was performed on 5 samples, 2AF1 to 2AF5. Detailed TEM observation was performed on one sample 2AF2, because bulk mineralogy of these five samples was basically the same, as was revealed by X-ray diffraction analysis, and because more than 150 mineral grains could be investigated using only one sample. Low-Ca pyroxene is composed of areas of both ortho- and clinopyroxene (Fig. 9a). Weak intensities of diffraction spots from orthopyroxene suggest that clinopyroxene is

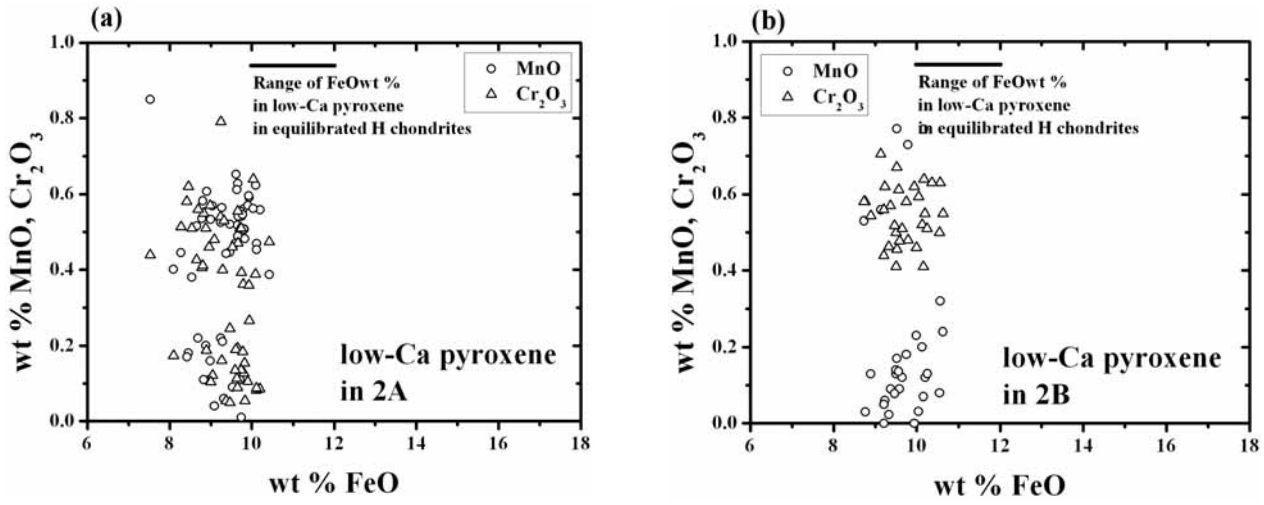

Figure 4. MnO and Cr_2O_3 concentrations in low-Ca pyroxene in the 2A sample (a) and the 2B sample (b).

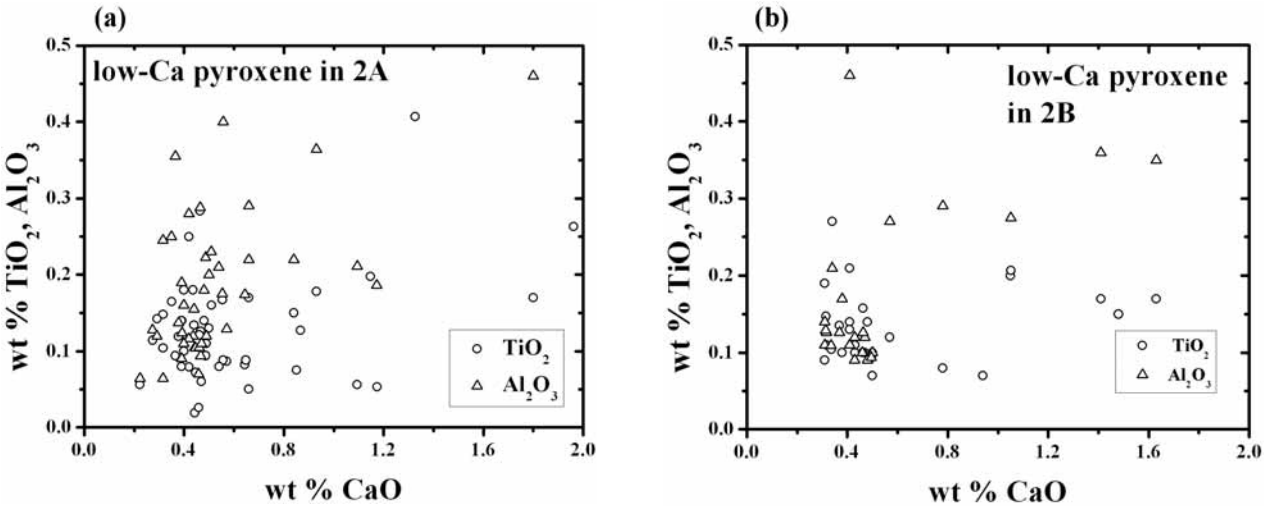

Figure 5. TiO_2 and Al_2O_3 concentrations in low-Ca pyroxene in the 2A sample (a) and the 2B sample (b).

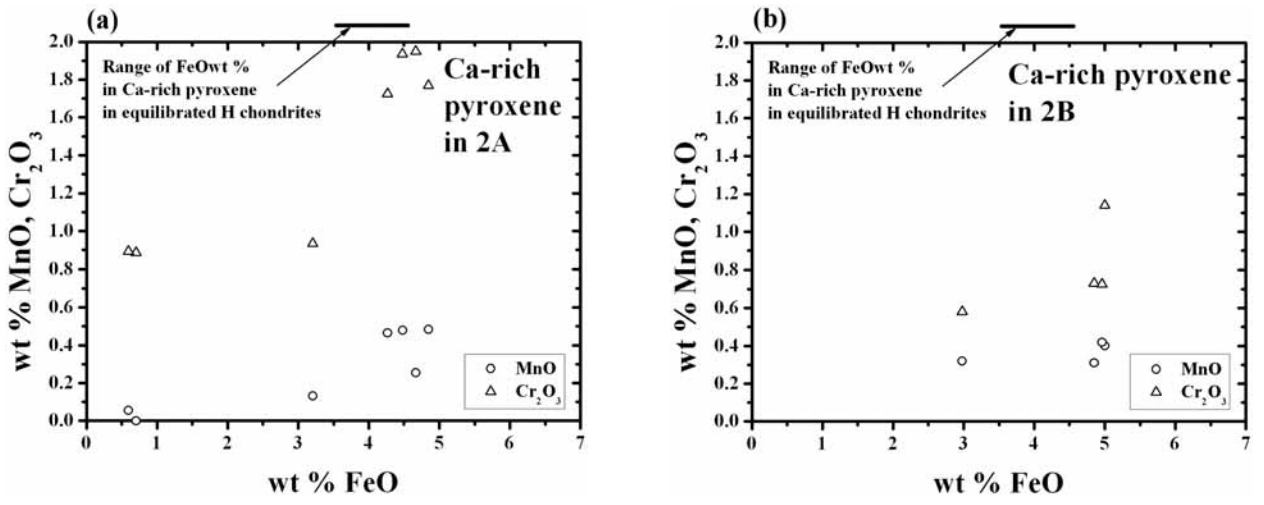

Figure 6. MnO and Cr_2O_3 concentrations in high-Ca pyroxene in the 2A sample (a) and the 2B sample (b).

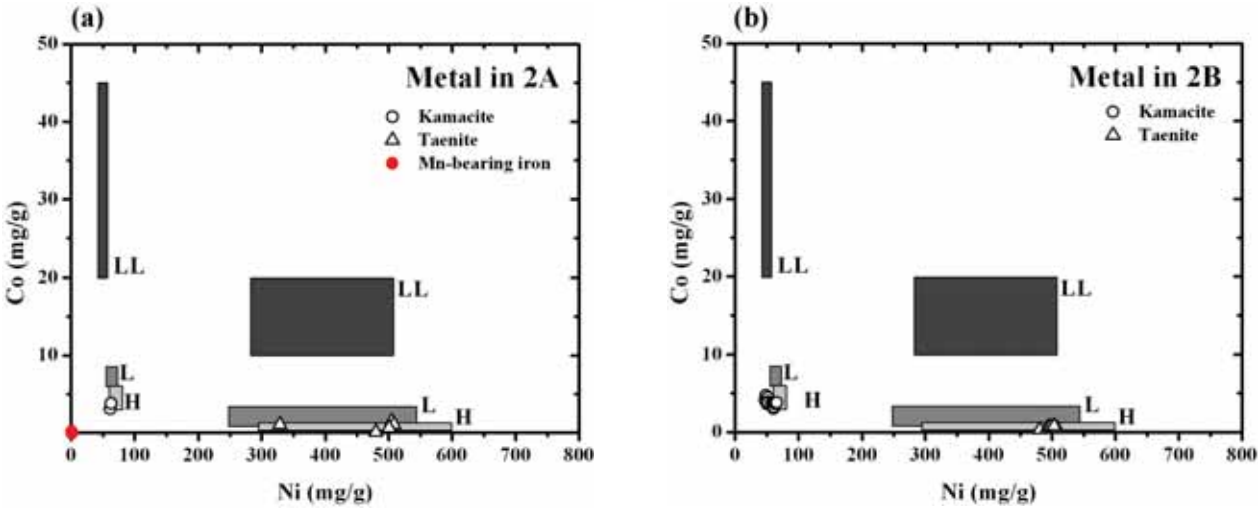

Figure 7. Co and Ni concentrations in FeNi metals in the 2A sample (a) and the 2B sample(b).

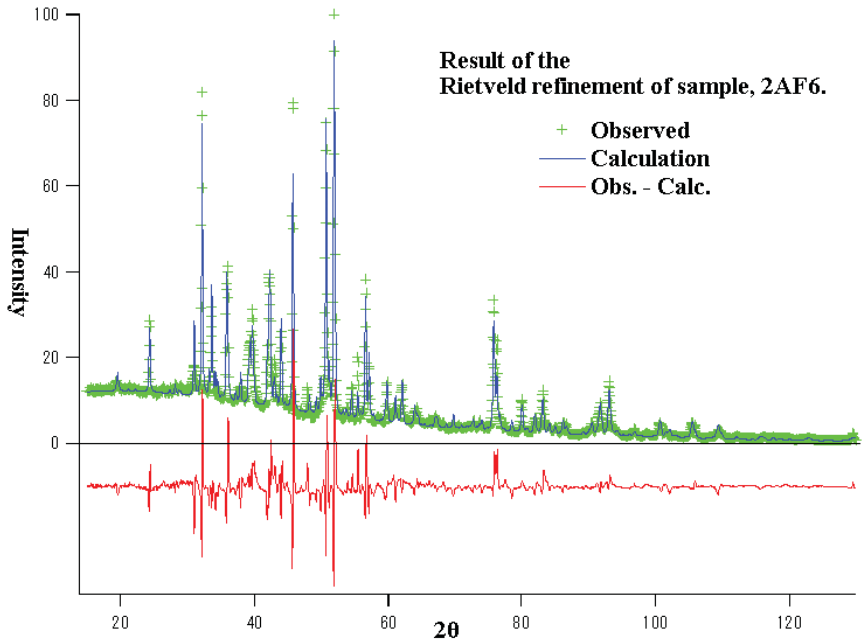

Figure 8. The result of Rietveld analysis of sample of 2AF6. The green cross is observed intensity, the blue line is calculated intensity and the red line is error. Some errors are still remained around strong diffraction peaks but the observed and calculated diffraction patterns are basically corresponded.

more abundant than orthopyroxene. Plagioclase is less than several microns diameter. AEM analysis showed that most plagioclase has compositions between An9Ab86Or5 and An13Ab83Or4, but there are also some alkali feldspar enriched in potasium with compositions from $An_1Ab_{33}Or_{66}$ to $An_0Ab_{47}Or_{53}$ (Fig. 10). Alkali feldspar (Fig. 9b) coexists with albitic plagioclase. Troilite is often observed, but kamacite is rare (Fig. 9c). Chromite occurs in both olivine and low-Ca pyroxene (Fig. 9d). Iron hydroxides lepidocrosite was found in a vein where 6-line ferrihydrite occurs together with lepidocrosite (Figs. 9e and f). The presence of iron hydroxides suggests that the 2A test sample is a "find" meteorite.

Optical microscope observation showed that olivine and low-Ca pyroxene crystals in both 2AC and 2AF samples such as 2AC18 (major phases are olivine and low-Ca pyroxene), 2AC22 (olivine and low-Ca pyroxene), 2AC23 (olivine and low-Ca pyroxene), 2AC24 (olivine), 2AF8, 2AF9, and 2AF10 exhibit wavy extinction, indicative of shock effects.

3.2. 2A test sample -mineralogy of contaminants

2A test sample contains very small amounts of strange materials that are never expected to occur in primitive chondritic meteorites. It is important to describe the mineralogy of these strange materials, because in the analysis of a real asteroidal sample they are "xenolith" materials coming from other planetary bodies.

Quartz-calcite composite: this strange material is detected in the four samples 2AC26, 2AC27, 2AC28, and 2AF2. The former three samples are dominated by quartz-calcite composite as is indicated by X-ray diffraction analysis (see Appendices 2AC26, 2AC27, and 2AC28), while the latter sample contain several tiny quartz particles that are detected only by TEM observation. SEM observation of 2AC26 indicates that the quartz-calcite composite also contains small amounts of dolomite $CaMgCO_3$, sillimanite Al_2SiO_5, corundum Al_2O_3, and carbonaceous materials (Appendix 2AC26). Sillimanite crystals occur in the form of lath-like acicular morphology. X-ray diffraction patterns of 2AC27 and 2AC28 are very similar to that of 2AC26, suggesting the same mineralogy. The quartz-calcite composite is probably a constituent of terrestrial metamorphic rocks. TEM observation of 2AF2 showed that the sample contains a single quartz crystal (Fig. 9g). It may be a fragment of larger quartz-calcite composites such as 2AC26.

Ni-free Mn-bearing Fe metal: the sample of 2AC15 is a particle of Fe metal (Appendix 2AC15). The features set this Fe metal apart from metals in other sample particles are the complete absence of both Ni and Co and the presence of approximately 1 wt% of Mn. These compositional features have never observed in FeNi metals in primitive chondritic meteorites. A nickel-cobalt diagram of FeNi metals in the 2A test sample (Fig. 7a) indicates that only Fe metal of 2AC15 is plotted on the origin (free of Ni and Co), out of the compositional trend of other FeNi metals. In addition, small amounts of magnetite are also present together with Fe metal based on the X-ray diffraction pattern (Appendix 2AC15). The presence of Mn and the coexistence of magnetite suggest that 2AC15 is a piece of factory-produced Fe metal, probably a fragment of some metallic tools.

Carbonaceous materials: the samples of 2AC2 and 2AC6 consist mostly of carbonaceous material. Interesting feature of the samples is that small grains of silicates and sulfides stick to surface of the carbonaceous materials (Appendices 2AC2 and 2AC6). X-ray diffraction analysis uncovers that the carbonaceous materials are amorphous and small silicates are olivine, low-Ca pyroxene, and plagioclase. Individual mineral particles are too small to be analyzed by EPMA. But the silicate mineralogy is similar to that of the other sample particles based on the X-ray diffraction patterns. Under an optical microscope, the carbonaceous materials are pale yellow similar to the color of epoxy resin. Therefore, the two samples 2AC2 and 2AC6 are probably pieces of epoxy resin that has cemented the test-sample meteorite.

3.3. 2B test sample

2B test sample consists of relatively coarse particles and all particles shows magnetism. X-ray diffraction analysis showed that 2BC1, 2BC2, and 2BC3 samples are dominated by FeNi metals, but rest of the samples contain silicates and sulfides as well as FeNi metals (see appendices 2BC1, 2BC2, and 2BC3). Both kamacite and taenite occur and the former contains Ni up to 7 wt%, while the latter contains Ni approximately 50 wt% (Fig. 7b). Cobalt concentrations in kamacite (~ 0.5 wt %) is higher than those in taenite (~ 0.2 wt %) (Fig. 7b). The anti-correlation of Ni and Co in metals is consistent with the properties of metallic grains in ordinary chondrites, especially equilibrated H chondrites (Fig. 7b). Troilite is also abundant. Chromite up to 20 μm in diameter occurs in 2BC4 and 2BC5. Compositional features of both major and minor elements in chromite again match those of chondrites, especially equilibrated H chondrites (Figs. 11a, b, and c). Calcium phosphate up to 20 μm is present in 2BC7 and 2BC8 samples. Most of them are whitlockite. Varieties and occurrence of metals, sulfide, and accessory minerals are similar to those of the 2A test sample.

X-ray diffraction analysis indicates that major silicates in the 2B sample are olivine, low-Ca pyroxene, and plagioclase (see Appendix). High-Ca pyroxenes such as augite and pigionite also occur, but less abundant. Many silicate crystals are included in FeNi metals. Important textural evidence was found in a sample of 2BC9, where a well-defined radial pyroxene chondrule is present in contact to a large FeNi metal (Appendix 2BC9 and Fig. 12). Blebs of troilite occur in the periphery of the chondrule. The presence of the chondrule suggests that the 2B sample is a chondrite, in spite of metal-rich mineralogy.

Olivine in the 2B sample has a homogeneous Fe/Mg ratio with an average Fa content of 15.8 ± 0.5 (Fig. 1c). CaO and MnO concentrations in olivine are less than 0.1 wt% and from 0.4 to 0.6 wt%, respectively (Fig. 2b). Low-Ca pyroxene also has a homogeneous Fe/Mg ratio with Fs 14.4 ± 0.7 (Fig. 1d). The average Fe/Mg ratios of both olivine and low-Ca pyroxene of the 2B sample are in agreement with those of 2A sample within 1-sigma variation. Ca/(Mg+Fe) ratio of low-Ca pyroxene is not homogenized between grains (Fig. 3b). Both MnO and Cr_2O_3 concentrations varies from < 0.1 to 0.8 wt% (Fig. 4b). TiO_2 and Al_2O_3 concentrations are both less than 0.5 wt% (Fig. 5b). Minor element concentrations in olivine and low-Capyroxene in the 2B sample are also similar to those of the 2A sample. High-Ca pyroxene and plagiocalse occur in minor amounts in the 2B samples. Wo content varies up to 47 with constant Mg/Fe ratios (Fig. 3b). Both MnO and Cr_2O_3 concentrations are similar to those of low-Ca pyroxene (Fig. 6b). TiO_2, Al_2O_3, and Na_2O concentrations range from 0.3 to 1.0, from 0.5 to 3.0, and < 1.0, respectively. Based on the X-ray diffraction patterns, plagioclase occurs in many 2B samples such as 2BC7. Grain size of plagioclase is less than 5 μm, similar to the plagioclase in the 2A samples.

TEM analysis was carried out on samples of 2BC6, 2BC7, 2BC8, 2BC9, and 2BC10. Intensive observation was done on 2BC7, 2BC8, and 2BC9 thin sections prepared by Ar ion bombardment and a 2BC10 thin section prepared by FIB method. Olivine in 2BC7 contains abundant dislocations with the density is 3.8 x 10^9 cm^{-2} (Fig. 13a). Their straight and parallel occurrences are typical for olivine grains in shocked meteorites. Low-Ca pyroxene is a mixture of ortho- and clinopyroxene (Fig. 13b). Some low-Ca pyroxenes contain numerous stacking faults and unit dislocations, suggesting that they are impacted (Fig. 13c). Like 2A samples, both sodic plagioclase (Fig. 13d) and alkali feldspar (Fig. 13e) occur. Both feldspars are very small ranging in size from 0.5 to 3 μm. The sodic plagioclase shows albite twin (Fig. 13d), while the alkali feldspar and coexisting plagioclase shows albite-Carlsbad twin (Fig. 13e). High-Ca pyroxene pigionite in both 2BC8 and 2BC9 samples contain exsolution lamellae of augite (Figs. 13f and g). High-resolution imaging shows that an augite lamella has coherent boundaries to the host pigionite (Figs. 13h and i). In contrast to the 2BC7, 2BC8, and 2BC9 samples, 2BC10 sample consists predominantly of elongated domains of FeNi metals (Fig. 13j).

4. DISCUSSION

A combination of multidiscipline analyses revealed that whole- and local-scale mineralogy of individual test sample particles. The procedures used in the present study are basically similar to those used in the previous technical report for the Hayabusa mission (Nakamura and Noguchi, 2003), but the procedures have evolved in the last four years through the study of cosmic dust. The main achievements are (1) application of Rietveld refinements to determination of the relative mineral abundance from synchrotron X-ray diffraction data, and (2) sample preparation techniques for TEM including ultramicrotomy for fine-grained aggregates and FIB method for single particles.

2A sample particles have mineralogy quite similar to H chondrites with petrologic type late 4 to early 5. Evidence for H chondrite classification is (1) Fe/Mg ratios of olivine and low-Ca pyroxene (Fig. 14), (2) CaO and MnO concentrations in olivine (Fig. 2a), and (3) Co and Ni distributions in FeNi metals (Fig. 7a). The Fe/Mg ratios of both olivine and low-Ca pyroxene in the 2A sample correspond to the lowest-end of the Fe/Mg variations for H chondrites (Fig. 14), suggesting that it is a sample of most reduced type of H chondrites. Evidence for the petrologic type 4-5 classification is (1) well equilibration of Fe/Mg ratios of both olivine and low- and high-Ca pyroxene, (2) the presence of crystalline plagioclase with several microns in size, (3) the presence of taenite with Ni concentration higher than 20 wt%, and (4) the variation of Wo contents in high-Ca pyroxenes. The former three criteria are well-known classification scheme defined by Van Schmus and Wood, but the last one is derived from TEM observation (Noguchi et al., 1992; Noguchi, 2005, unpublished data). One sigma variations of Wo contents in high-Ca pyroxene decrease with an increase of petrologic type (Fig. 15). The variation of the pyroxenes in the 2A test samples is plotted in a region where many type 4 and 5 ordinary chondrites are plotted (Fig. 15, also see 3a), which verifies the classification of the 2A sample to petrologic type 4-5. However, high abundance of low-Ca clinopyroxene is inconsistent with the petrologic 4-5 classification. This can be explained due to mechanical conversion from orthopyroxene to clinopyroxene under high pressures during shock metamorphism.

The presence of shock-induced wavy extinction of olivine and low-Ca pyroxene is consistent with the interpretation.

2A test sample contains a variety of contaminants: quartz-calcite composites (Appendix 2AC26), Ni-free Mn-bearing Fe metal (Appendix 2AC15), and carbonaceous materials (Appendix 2AC6). The quartz-calcite composites are unstable during thermal metamorphism on the H4-5 parent body and moreover such composites have never been reported even in chondritic regolith breccias. The Ni-free Mn-bearing Fe metal is also a strange component, as is clearly shown in a Co-Ni diagram (Fig. 7a). The Co and Ni contents of this metallic particle are out of regions for typical equilibrated H chondrites (e. g., Brearley and Jones, 1998). The carbonaceous materials show yellow in color and ductile properties, which differs black and brittle carbonaceous materials occasionally present in chondrites with low petrologic types. All these considerations suggest that the three kinds of materials are probably artificial contaminants.

2B test sample completely differs from the 2A test sample in appearance: the former is larger, magnetic, and dull in color. However, the mineralogy is very similar between the two test samples, including minor and major element concentrations of olivine, low- and high-Ca pyroxene, FeNi metals, sulfide, and chromite. The only difference is that 2B sample is richer in metals than 2A sample. Therefore, we suggest that 2A and 2B test samples may be prepared from the same meteorite and that 2B sample may be a concentrate of metallic particles. The similarity in mineralogy between the two test samples suggests that 2B test sample is also H chondrite with petrologic type 4-5. The Wo variation of low- and high-Ca pyroxene in 2B sample is similar to that in 2A sample (Figs. 3b and 15). In addition, pigeonite in 2B sample exsolved augite lamellae with thickness of < 50 nm (Figs. 13f and g). The augite lamellae were formed during thermal metamorphism of the meteorite parent body and thus the occurrence and thickness of the lamellae reflect thermal regime of the host pigionite. TEM observation of pigeonites in ALH77208 H4 and Jilin H5 chondrite (Noguchi et al., 1992; Noguchi, 2005, unpublished data) indicates that the pigeonites contain augite exsolution lamellae with thickness of < 50 and < 200 nm, respectively (Figs. 16a and b). The occurrence and thickness of the augite lamellae in the 2B test samples are similar to those in the two H chondrites, confirming the classification of the 2B sample to H chondrites with petrologic type 4-5.

Primitive achondrites such as acaplucoites and lodoranites are next candidate for source materials of both 2A and 2B samples, although the possibility is quite low considering some mineralogical features of primitive achondrites as discussed below. Primitive achondrites, acaplucoites and lodoranites, consist of olivine, low- and high-Ca pyroxene, plagioclase, FeNi metals, like 2A and 2B test samples. Their textures are basically granular except for rare relict chondrules in acaplucoites. It is difficult to reconstruct original textures before crushing of 2A and 2B test samples, but, at least the 2B test sample seems to have contained some chondrules based on SEM observation of textures of some 2B sample particles.

Averages Fe/Mg ratios of olivine and low-Ca pyroxene are $Fa_{15.1}$ and $Fs_{13.9}$, respectively, for the 2A test sample and $Fa_{15.8}$ and $Fs_{14.4}$, respectively, for the 2B test sample. On the other hand, in acaplucoites, compositional ranges of olivine and low-Ca pyroxene are $Fa_{4.2\text{-}13.3}$ and $Fs_{6.5\text{-}12.6}$, respectively (McCoy et al., 1996; 1997a, b). Their compositions are more magnesian than both 2A and 2B test samples. In lodoranites, these minerals are more magnesian than acaplucoites and show reverse zoning due to reduction during thermal metamorphism. No ferromagnesian mineral with such reduction was not found in both 2A and 2B samples. In addition, grain size of plagioclase correlates with intensity of thermal metamorphism. Plagioclase crystals in both 2A and 2B samples are very small less than 5 μm in diameter, which is far smaller than plagioclase in acapulcoites (more than 100 μm in diameter: McCoy et al. 1996). This indicates that thermal effects on plagioclase in both 2A and 2B test samples much weaker than those in acaplucoites. These data strongly suggest that both 2A and 2B samples are not fragments of primitive achondrites. Another supporting evidence of this interpretation is relative mineral abundances between olivine and low-Ca pyroxene in the 2A sample obtained by the Rietveld method. As shown in Table 2, olivine is always more abundant than low-Ca pyroxene in the 2A test sample, which is contrary to the case of acaplucoites (McCoy et al. 1996).

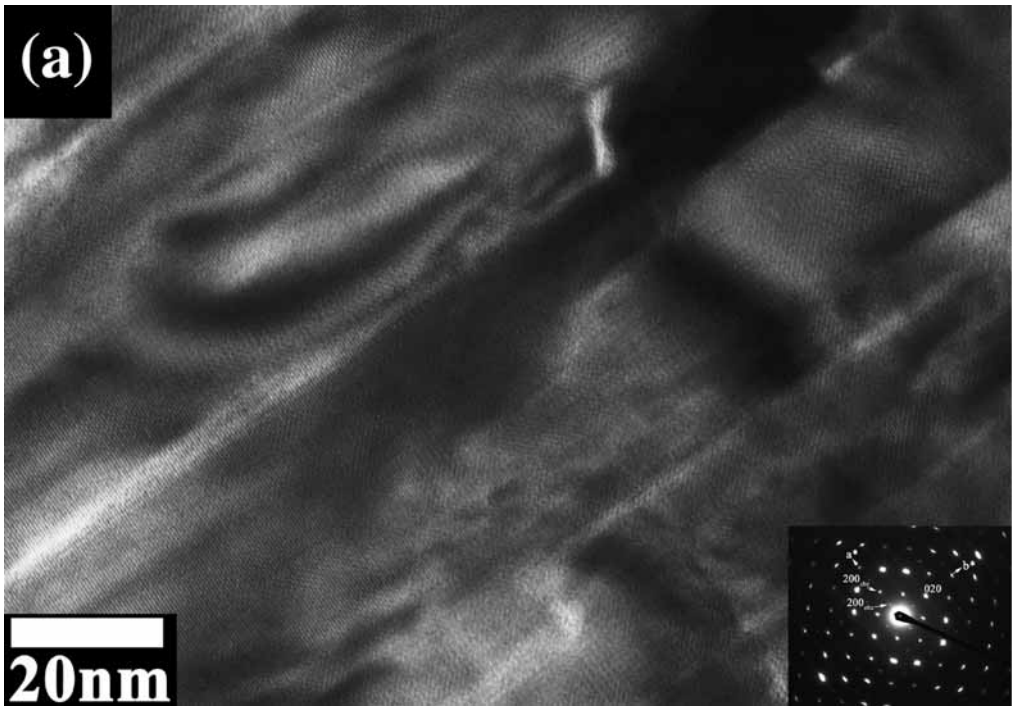

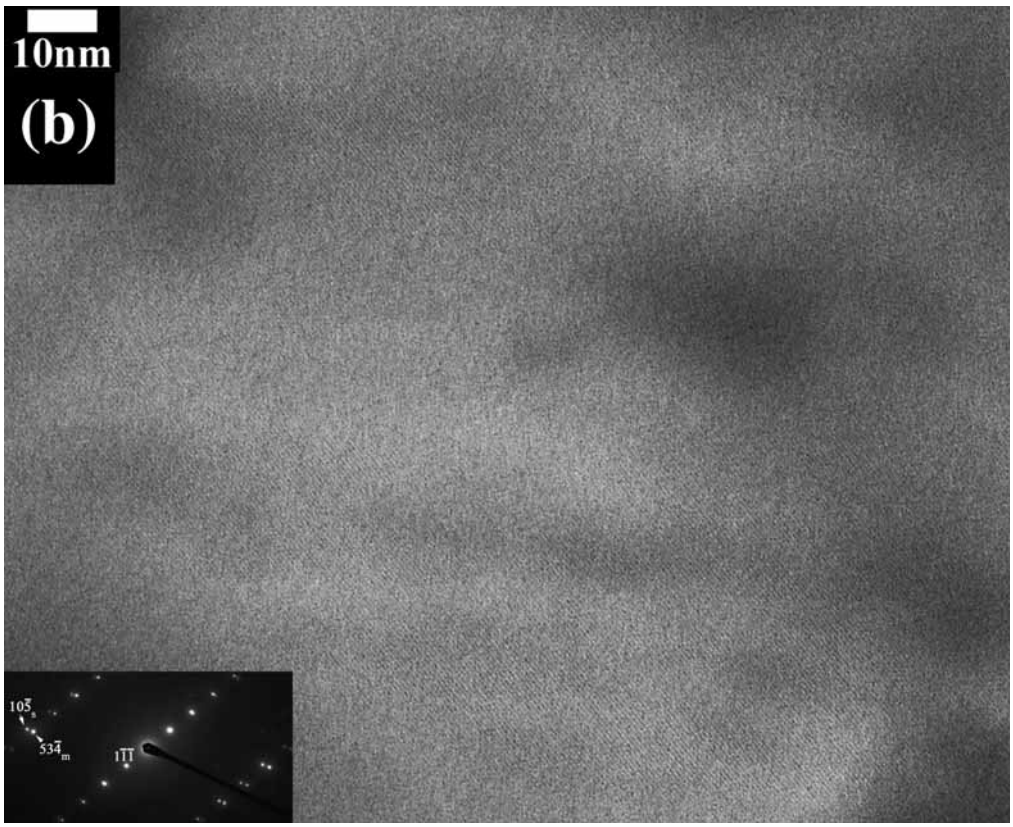

Figures 9(a) and (b)

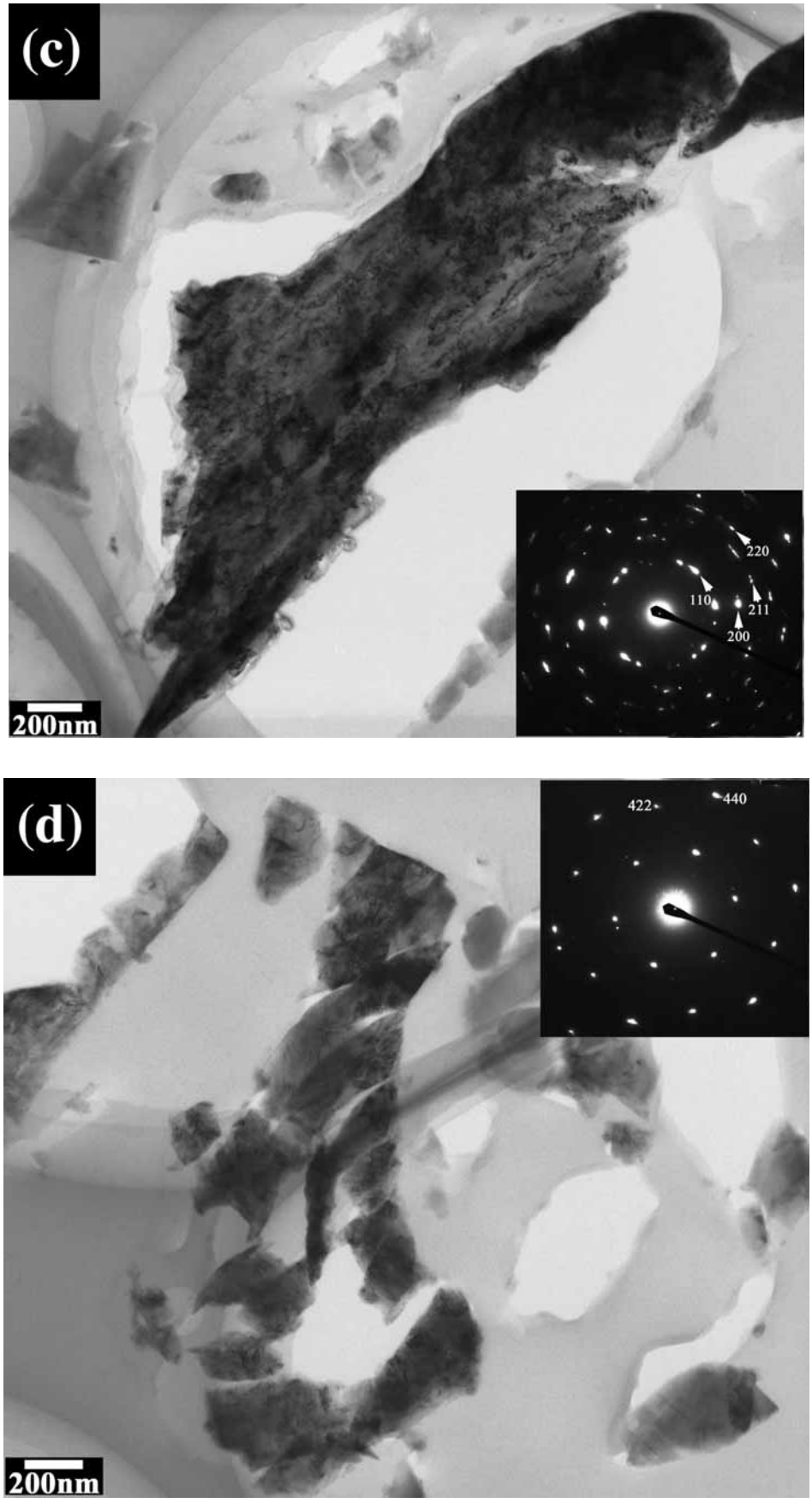

Figures 9(c) and (d)

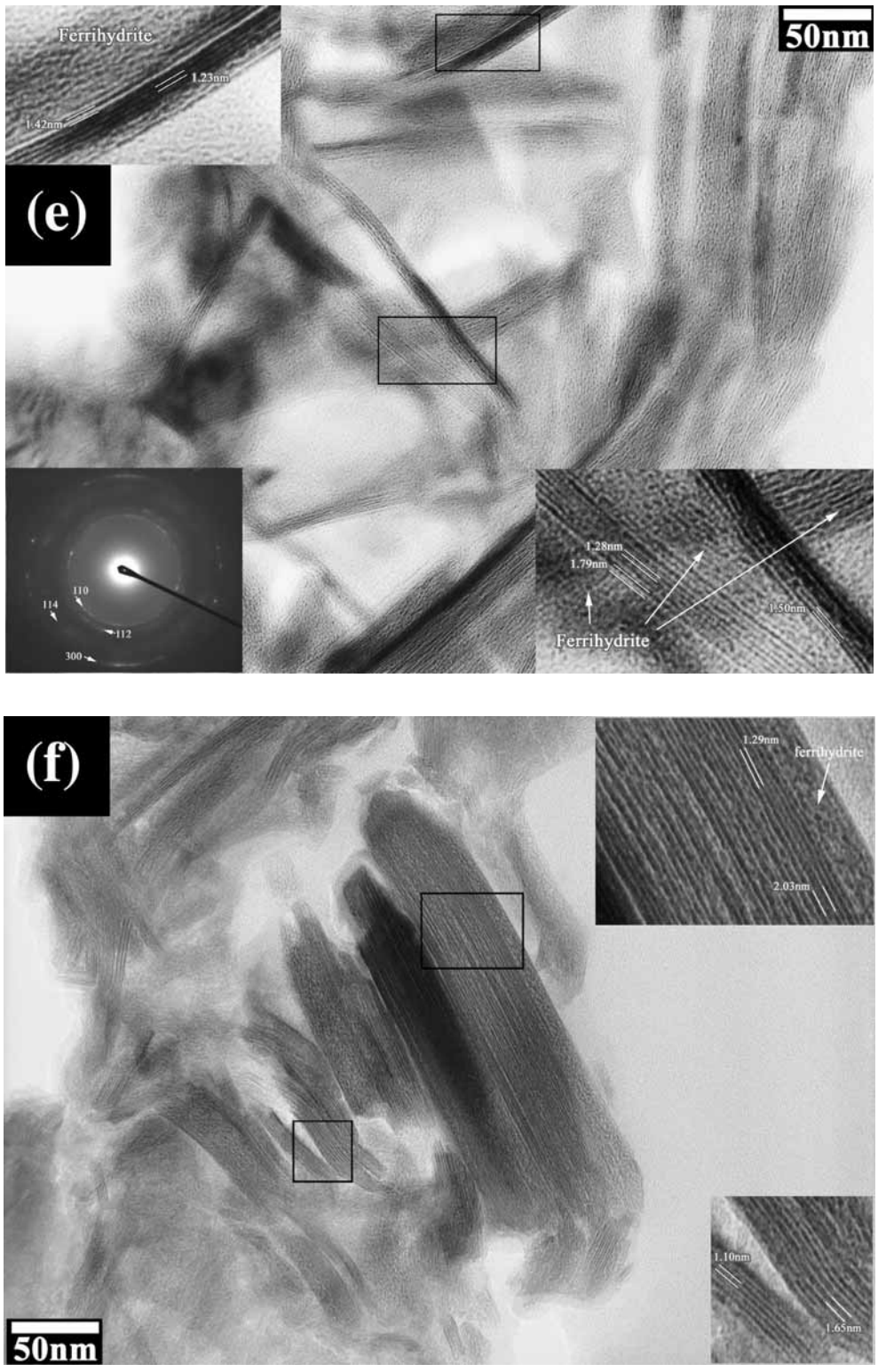

Figures 9(e) and (f)

Figure 9(g)

Figure 9. TEM images of 2AF2 sample particle. (a) High-resolution image of a low-Ca pyroxene fragment in 2AF2 sample down to the c* direction. Selected area electron diffraction (SAED) pattern of this area shows that this low-Ca pyroxene is composed of areas of both ortho- and clino- low-Ca pyroxene (ortho- and clinobronzite based on AEM data). Weak intensities of diffraction spots from orthobronzite suggest that clinobronzite is more abundant than orthobronzite. (b) High-resolution image of an alkali feldspar fragment in 2AF2 sample. We encountered several such feldspar grains. In this case, EDS analysis shows that it has compositional variation from $An_{0.8}Ab_{32.9}Or_{66.2}$ to $An_{0.0}Ab_{47.0}Or_{53.0}$. SAED pattern shows that there are diffraction spots from both triclinic and monoclinic forms. However, there are no remarkable exsolution lamellae shown in perthite. Photomicrograph shows that there are modulations in this feldspar. They were probably caused by incomplete transformation from orthoclase to microcline. (c) Bright-field image of a kamacite fragment in 2AF2 sample. Kamacite is quite rare in 2AF2 sample. Only this fragment was discovered among the observation of 150 individual grains. SAED pattern of this fragment clearly shows that this kamacite grain was deformed during ultramicrotomy. (d) Bright-field image of a chromite fragment in 2AF2 sample. The occurrence of chromite as a single mineral fragment is rare. Most of them occur as inclusions in ferromagnesian silicates. (e) One fragment contains 0.5-micrometer vein. SAED pattern of this vein has four discontinuous diffraction rings. All of them coincide with diffraction peaks of 6-line ferrihydrite. However, high-resolution images of the vein (insets) revealed that the vein contains thin (< 20 nm) fibrous minerals. Their fringes are various from 1.23 to 1.79 nm. It is clear that these fibrous minerals are not ferrihydrite. They may be mixtures of lepidocrosite and clay minerals. And the interstices of these fibrous minerals are filled by ferrihydrite. (f) Another high-resolution image of the same vein shown in Fig. 9e. In this photomicrograph, Fe-predominant mineral grains partially keep tabular shapes. High-resolution images (insets) show that ferrihydrite replaces the tabular mineral. (g) We found one silica mineral grain in 2AF2 sample. SAED pattern of the grain shows that it is alpha-quartz.

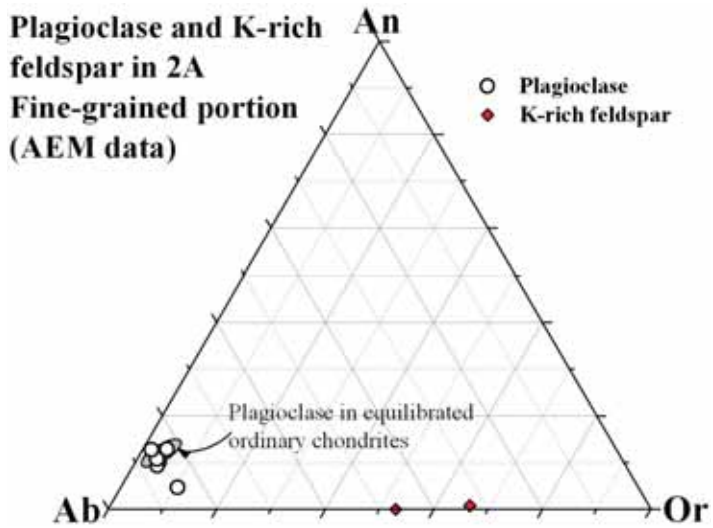

Figure 10. Plagioclase compositions of the 2AF2 sample, showing the presence of both sodic plagioclase and alkali feldspar.

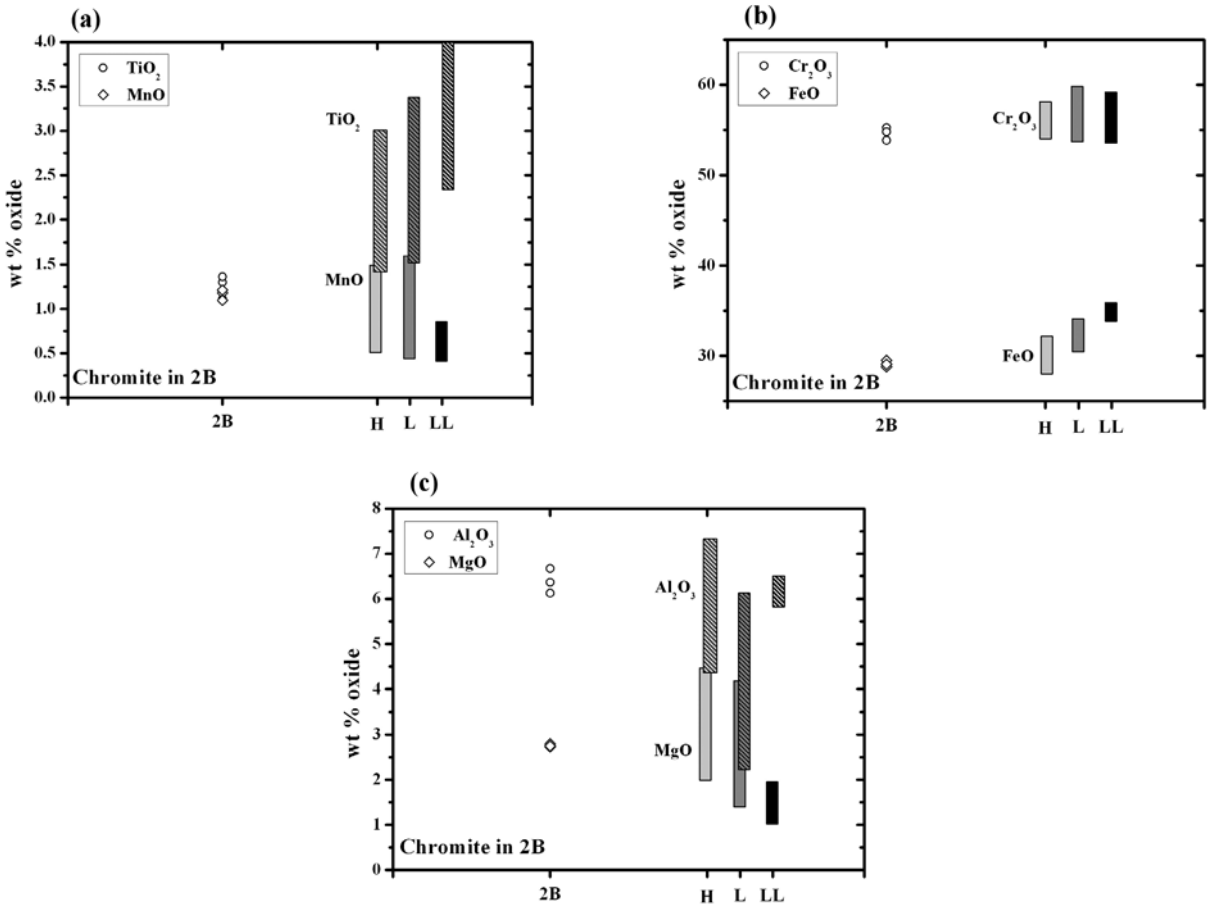

Figure 11. Major and minor element concentrations in chromite in the 2B sample. TiO_2 and MnO contents (a), Cr_2O_3 and FeO contents (b), and Al_2O_3 and MgO contents (c).

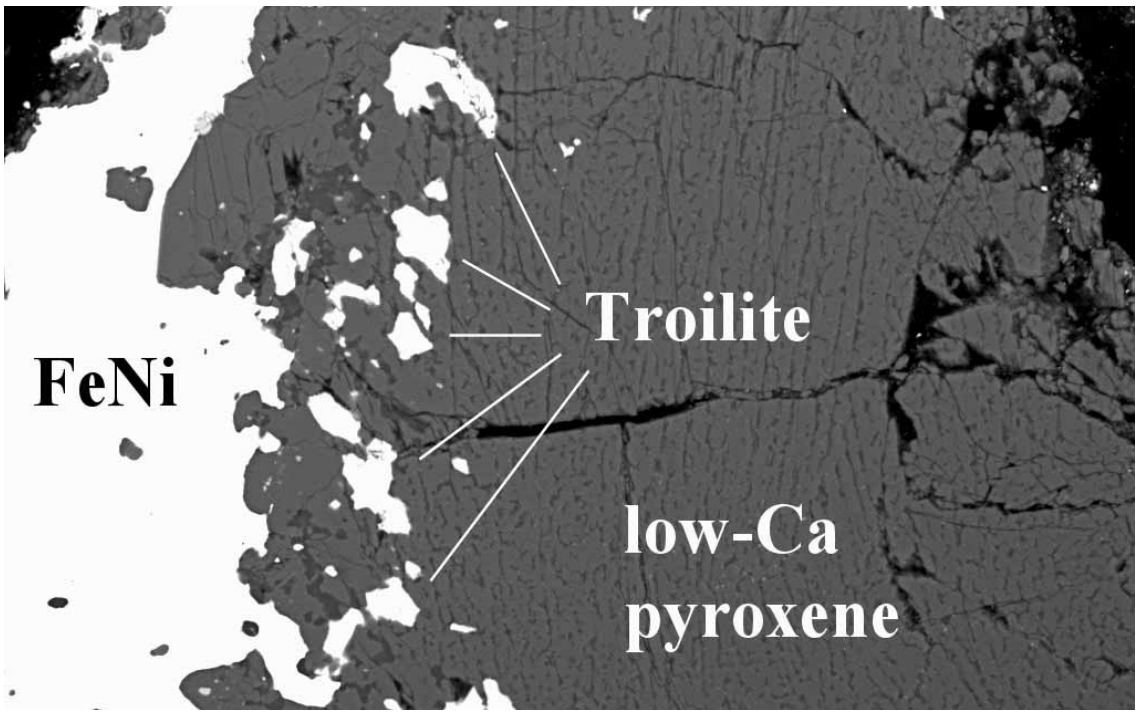

Figure 12. An enlarged view of a radial pyroxene chondrule in the 2B sample. Many troilite inclusions occur at the outer portions of the chondrule. A whole view of this chondrule is shown in Appendix 2BC9.

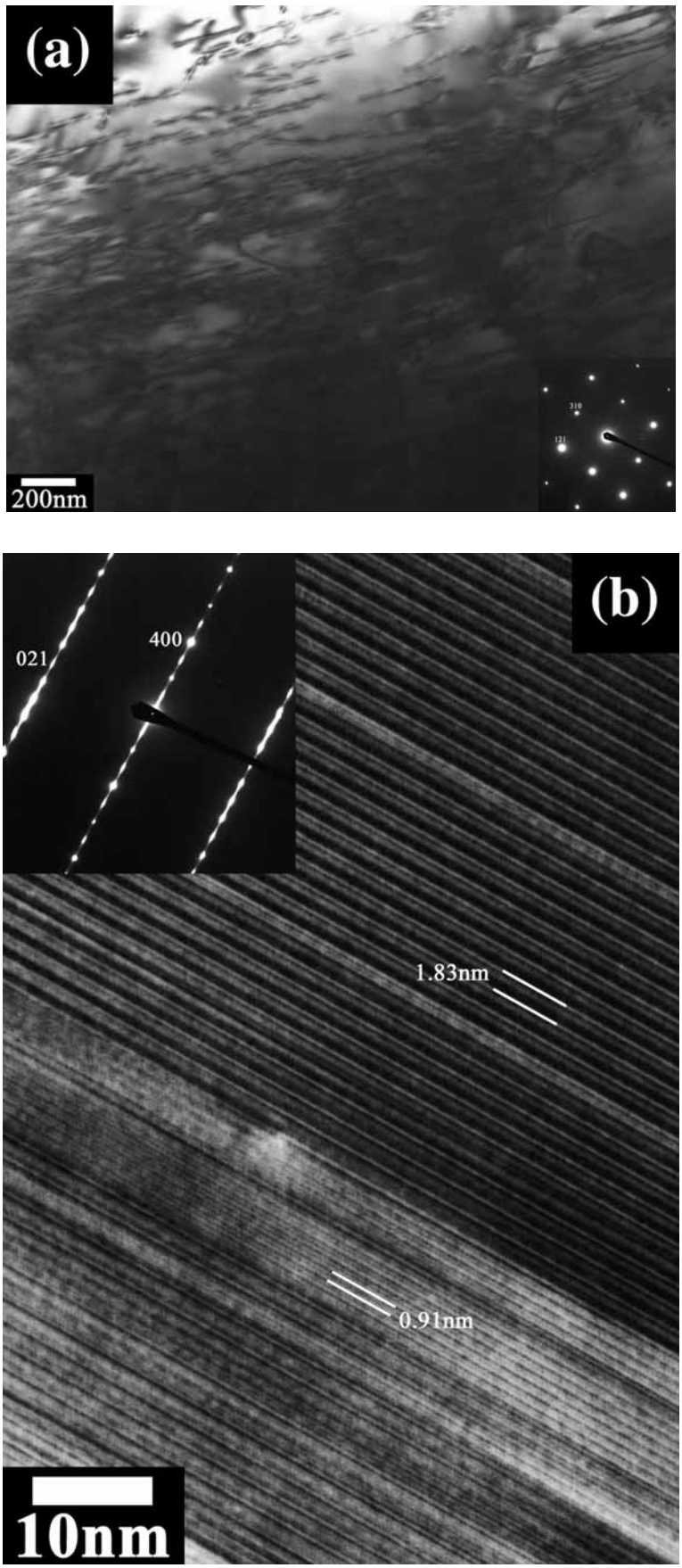

Figures 13(a) and (b)

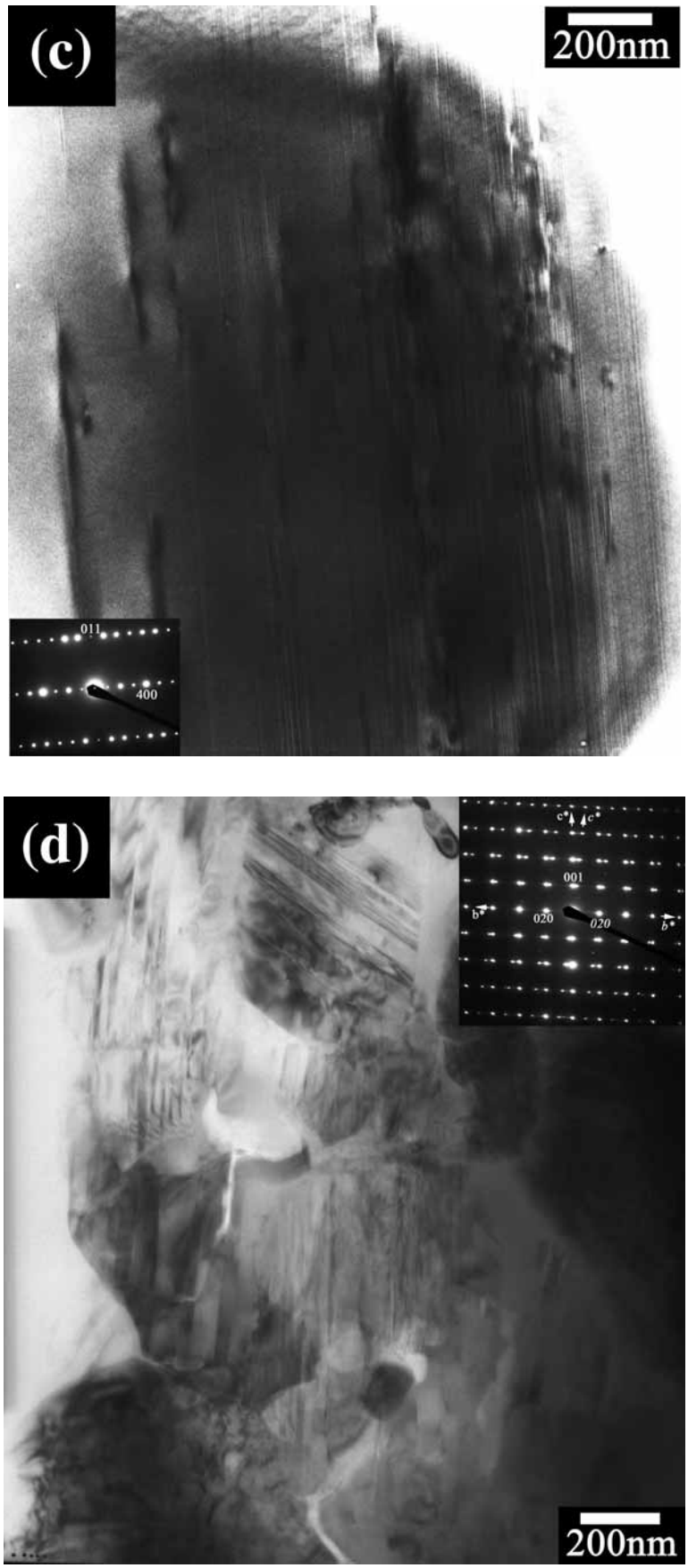

Figures 13(c) and (d)

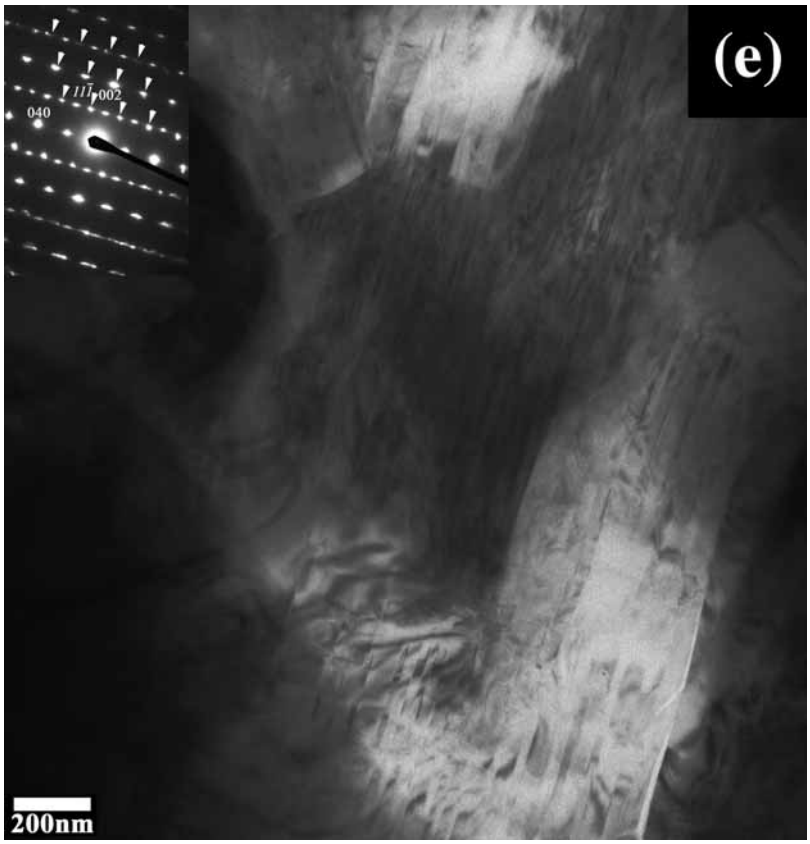

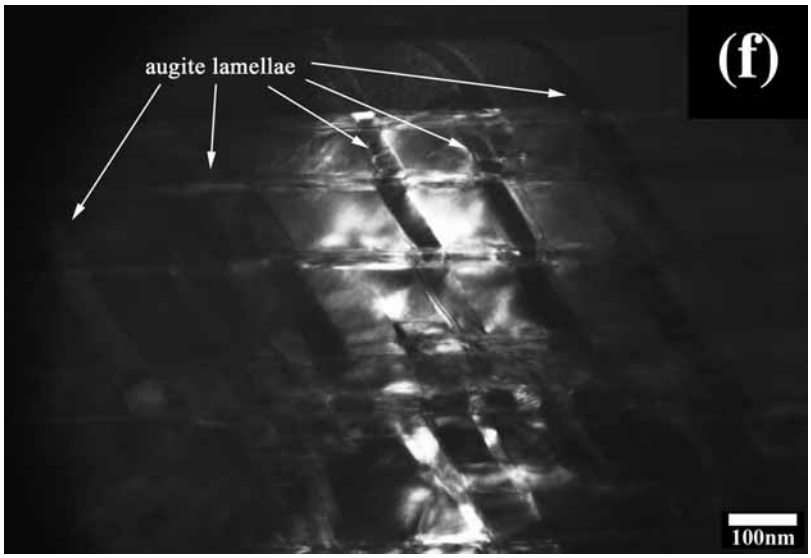

Figures 13(e) and (f)

Figures 13(g) and (h)

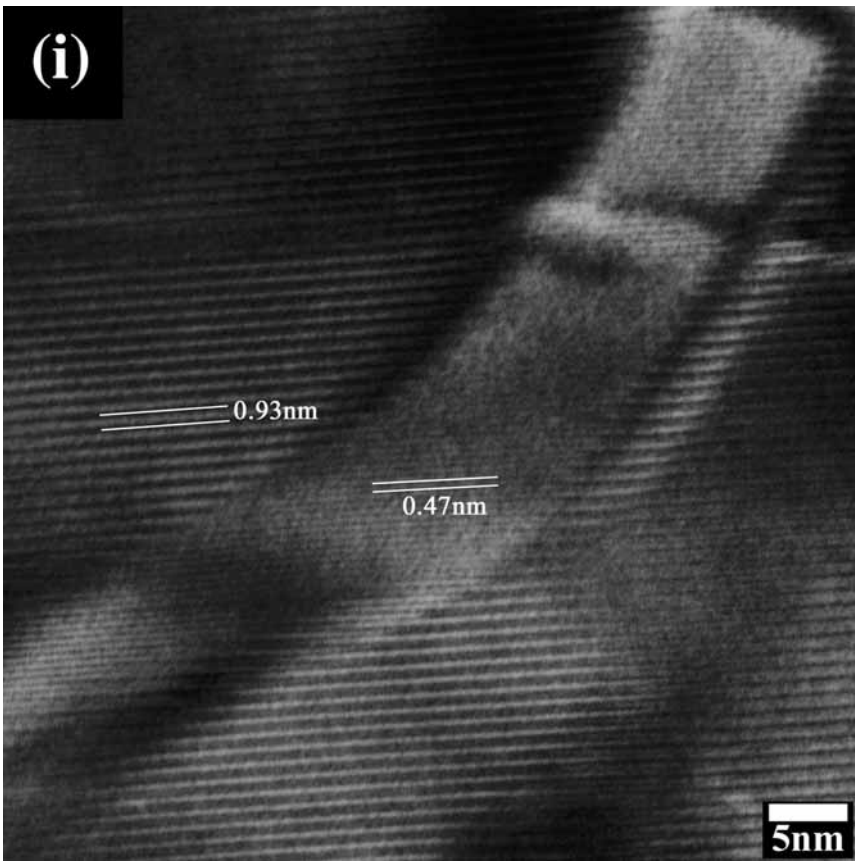

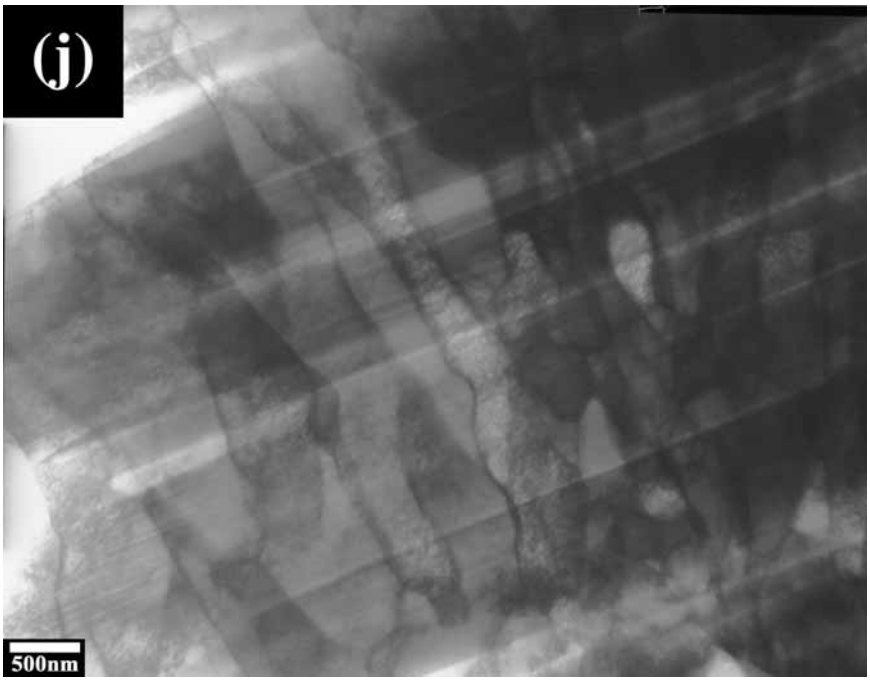

Figures 13(i) and (j)

Figure 13. (a) Olivine in this sample contains abundant dislocations. Their straight and parallel occurrences are typical for olivine grains in shocked meteorites. Dislocation density of this grain is 3.8 x 10^9 cm^{-2}. (b) High-resolution image of low-Ca pyroxene in 2BC7 sample. Low-Ca pyroxene of this sample is composed of abundant areas with orthorhombic structure and less abundant monoclinic structure. There is also some stacking disorder between the boundaries between ortho- and monoclinic- areas. (c) TEM image of a low-Ca pyroxene grain in 2BC9 sample. SAED pattern of this grain clearly shows that the majority of the grain is composed of orthopyroxene although TEM image shows that it contains abundant stacking disorder between ortho- and clino-areas. Some unit dislocations are also observed. (d) Bright-field image of sodic plagioclase grains in the interstices of low-Ca pyroxene and olivine large grains in 2BC7 sample. Sodic

plagioclase is 0.5 to 3 micrometer across. SAED pattern of a sodic plagioclase at the center of this photomicrograph shows albite twin. (e) There are alkali feldspar grains as well as sodic plagioclase among the interstices of coarse low-Ca pyroxene and olivine in 2BC7 sample. Their sizes are also from 0.5 to 3 micrometer across. SAED pattern of the alkali feldspar shows that it is microcline. The SAED pattern is composed of superimposed diffractions along [100] and [101] having the albite-Carlsbad twin relationship. (f) Dark-field image of augite lamellae-bearing pigeonite ($g=102_P$) in BC9 sample. Thin (< 50 nm) augite lamellae were also observed in pigeonite. It is remarkable that augite lamellae continue although the host pigeonite is twinned. It means that augite lamellae exsolved before twining of pigeonite. The twining of pigeonite is probably related transformation from pigeonite to orthopyroxene during thermal metamorphism. (g) Dark field-image of augite lamellae-bearing pigeonite in 2BC8 sample ($g=402_A$). Many bright augite lamellae with thickness < 20 nm can be seen. They are continuous although there are some stacking disorder and twins in the host pigeonite. (h) High-resolution image of lamellae-bearing pigeonite and low-Ca pyroxene in BC9 sample. Upper SAED pattern shows that low-Ca pyroxene is composed of a mixture of orthorhombic and monoclinic structures. In pigeonite, an augite lamella has coherent boundaries between host pigeonite. The lamella has a sigmoidal shape. The augite lamella is intermitted by stacking disorders in pigeonite. (i) High-resolution image of an augite lamella and the host pigeonite in 2BC8 sample. The boundaries between the lamella and the host are coherent although the direction of elongation of the lamella gradually changes. (j) Low magnification TEM image of a metallic grain in a fragment of 2BC10. This sample was prepared by FIB method. This metallic region is composed of elongated kamacite grains. Their high aspect ratios suggest that these grains experienced deformation probably due to shock. Grain boundaries of each kamacite grain are not thinned preferentially as often encountered when using conventional ion bombardment method.

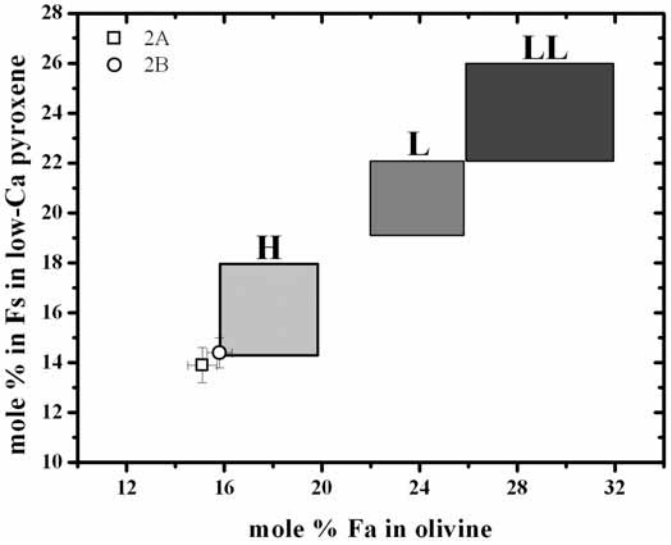

Figure 14. A correlation of Fs content in low-Ca pyroxene and Fa contents in olivine in ordinary chondrites. Fs and Fa contents of both 2A and 2B samples are located at the lowest-end of H chondrite compositional region.

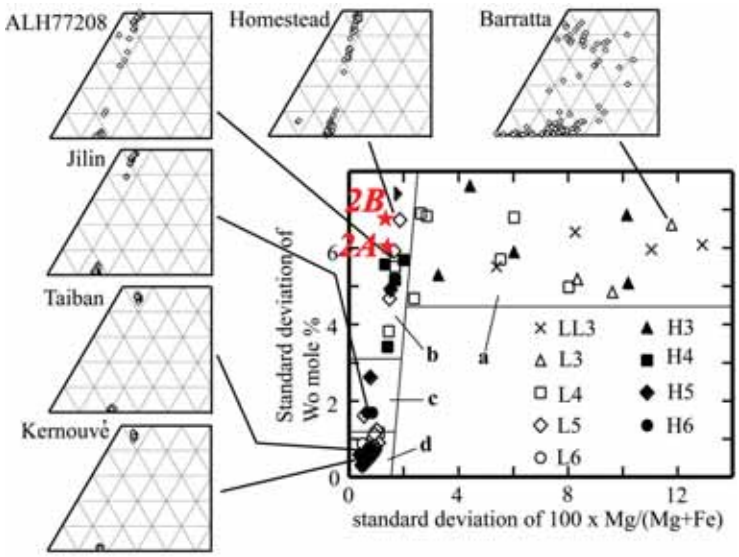

Figure 15. A correlation between variations of Wo contents and variations of Fs contents in high-Ca pyroxene in H and L chondrites with various petrologic types. Regions a, b, c, and d correspond to petrologic type 3-4, 4-5, 5-6, and 6, respectively. High-Ca pyroxenes in both 2A and 2B samples are plotted in the region of petrologic type 4-5.

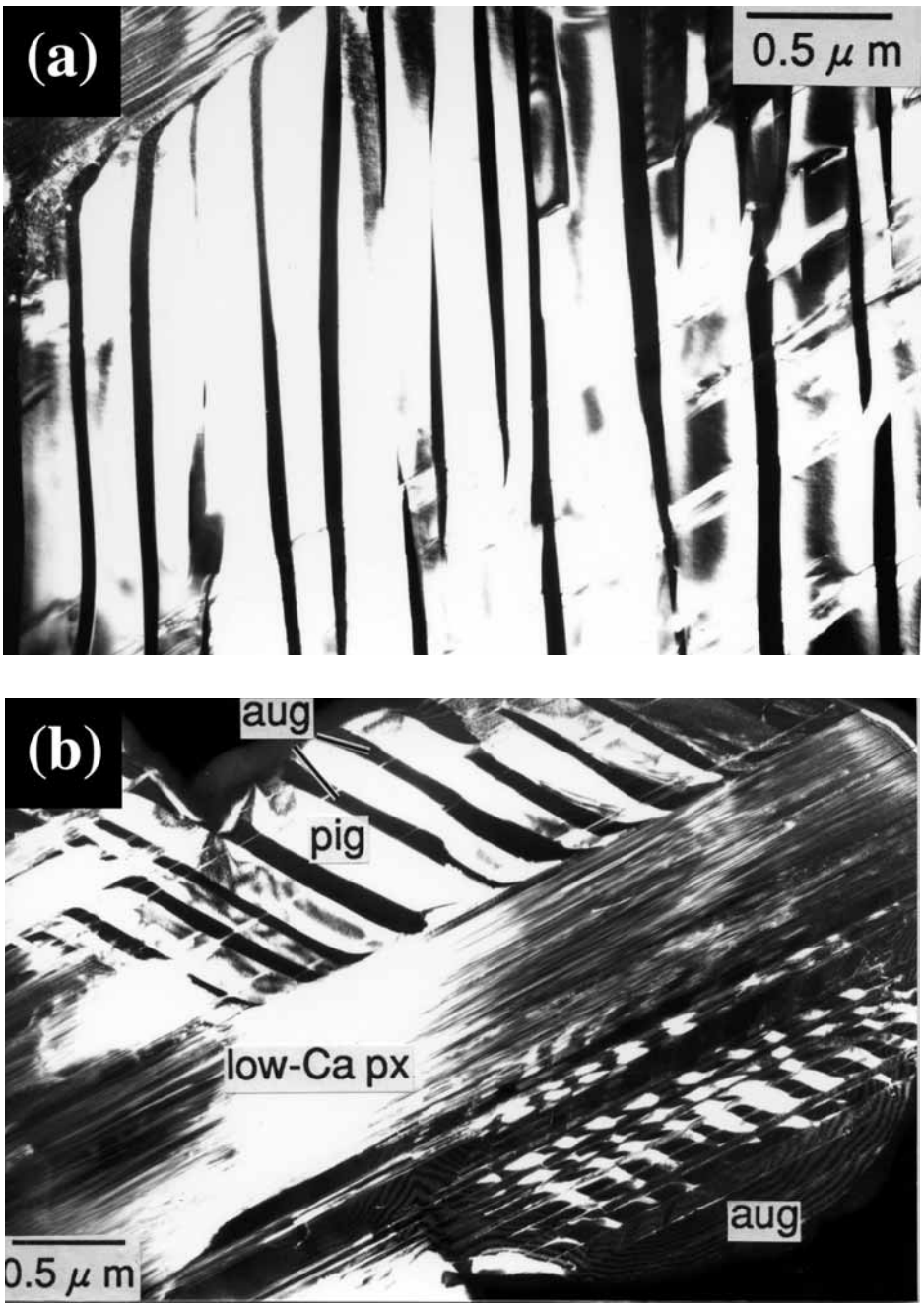

Figure 16. (a) Dark-field image of augite lamellae-bearing pigeonite in ALH 77208 H4 chondrite. The thickness of the lamellae is < 50 nm. The lamellae are continuous although there are some stacking disorder and twins in the host pigeonite. (b) Dark-field image of low-Ca pyroxene core and augite lamellae-bearing rims in Jilin H5 chondrite. Low-Ca pyroxene core is composed of orthorhombic areas with a lesser amount of monoclinic areas. Pigeonite is twinned and augite lamellae are affected by the twining of the host pigeonite. The thickness of the lamellae is < 200 nm.

REFERENCES

Birle, J.D., Gibbs, G.V., Moore, P.B. and Smith, J.V., 1968, Crystal structures of natural olivines. *Am. Mineral.,* **53**, 807-824.

Brearley, A.J. and Jones, R.H., 1998, Chondritic meteorites. In *Reviews in Mineralgy Vol. 36 Planetary Materials,* (ed. J. J. Papike), pp. Chapter 3 1-398. Mineralogical Society of America, Washington.

McCoy, T.J., Keil, K., Clayton, R.N., Mayeda, T.K., Bogard, D.D., Garrison, D.H., Huss, G.R., Hutcheon, I.D. and Wieler, R., 1996, A petrologic, chemical and isotopic study of Monument Draw and comparison with other acaplucoites: evidence for formation by incipient partial melting. *Geochim. Cosmochim. Acta,* **60**, 2681-708.

McCoy, T., Keil, K., Muenow, D.W., and Wilson, L., 1997a, Partial melting and melt migration in the acaplucoite-lodranite parent body. *Geochim. Cosmochim. Acta,* **61**, 639-50.

McCoy, T.J., Keil, K., Clayton, R.N., Mayeda, T.K., Bogard, D.D., Garrison, D.H., Hutcheon, I.D. and Wieler, R., 1997b, A petrologic and isotopic study of lodranites: evidence for early formation as partial melt residues from heterogeneous precursors. *Geochim. Cosmochim. Acta,* **61**, 623-37.

Morimoto, N. and Guven, N., 1970, Refinement of the crystal structure of pigionite. *Am. Mineral.,* **55**, 1195-1209.

Nakamura, T., Yada, T., Noguchi, T., Nakamura, Y., Takaoka, N., Terada, Y., Nakai, I., and Tanaka, M., 1999, X-ray diffraction analysis of individual interplanetary dust particles and Antarctic micrometeorites using synchrotron radiation. *Meteoritics,* **34**, A86.

Nakamura, T., Nakamuta, Y. and Tanaka, M., 2001a, Identification of anhydrous and hydrous interplanetary dust particles by X-ray diffraction analysis. in Photon Factory Activity Report 2000, Part A (Highlights and Facility Report #18), *Section 6 Crystallography* (ed. by Ohsumi K), *KEK Progress Report* 2001-2, 30-31.

Nakamura, T., Noguchi, T., Yada, T., Nakamuta, Y., and Takaoka, N., 2001b, Bulk mineralogy of individual micrometeorites determined by X-ray diffraction analysis and transmission electron microscopy. *Geochim. Cosmochim. Acta,* **65**, 4385-4397.

Nakamura, T. and Noguchi, T., 2003, Mineralogy of 100-mg test samples for Muses C mission. in The First Open Competition for the MUSES-C Asteroidal Sample Preliminary Examination Team (eds. by Kushiro, I., Fujiwara, A., and Yano, H.) *ISAS report SP No. 16,* 103-120.

Nakamura, T., Noguchi, T., Zolensky, M.E., and Tanaka, M., 2003, Noble-gas signatures and mineralogy of the carbonate-rich lithology of the Tagish Lake carbonaceous chondrite: Evidence for an accretionary breccia, *Earth and Planetary Science Letters* **207**, 83-101.

Nakashima, D., Nakamura, T., and Noguchi, T., 2003, Formation history of CI-like phyllosilicate-rich clasts in the Tsukuba meteorite inferred from mineralogy and noble gas signatures. *Earth and Planetary Science Letters,* **212**, 321-336.

Noguchi, T., Fujino, K., and Momoi, H., 1992, A transmission electron microscope study of exsolution lamellae of pyroxenes in ordinary chondrites. Papers presented to the 17th Symposium on Antarctic Meteorites. 89-91. National Institute of Polar Research, Tokyo.

Noguchi, T. and Nakamura, T., 2000, Mineralogy of Antarctic micrometeorites recovered from the Dome Fuji Station. *Antarctic Meteorite Research,* **13**, 285-301.

Noguchi, T., Nakamura, T., and Nozaki, W., 2002, Mineralogy of phyllosilicate-rich micrometeorites and comparison with Tagish

Lake and Sayama meteorites. *Earth and Planetary Science Letters*, **202**, 229-246.

Prewitt, C.T., Sueno, S. and Papike, J.J., 1976, The crystal structures of high albite and monalbite at high temperatures. *Am. Mineral.,* **61**, 1213-1225.

Tokonami, M., Nishiguchi, K. and Morimoto, N., 1972, Crystal structure of a monoclinic pyrrhotite (Fe7S8). *Am. Mineral.,* **57**, 1066-1080.

Toraya, H., 1998, Weighting Scheme for the Minimization Function in Rietveld Refinement. *J. Appl. Cryst.,* **31**, 333-343.

Appendix:
back-scattered electron images, chemical compositions, diagrams for olivine and low- and high-Capyroxene, and synchrotron X-ray diffraction patterns

Abbreviations

tr: troilite
kam: kamacite
ol: olivine
low-Ca px: low-Ca pyroxene
high-Ca px: high-Ca pyroxene

2AC1

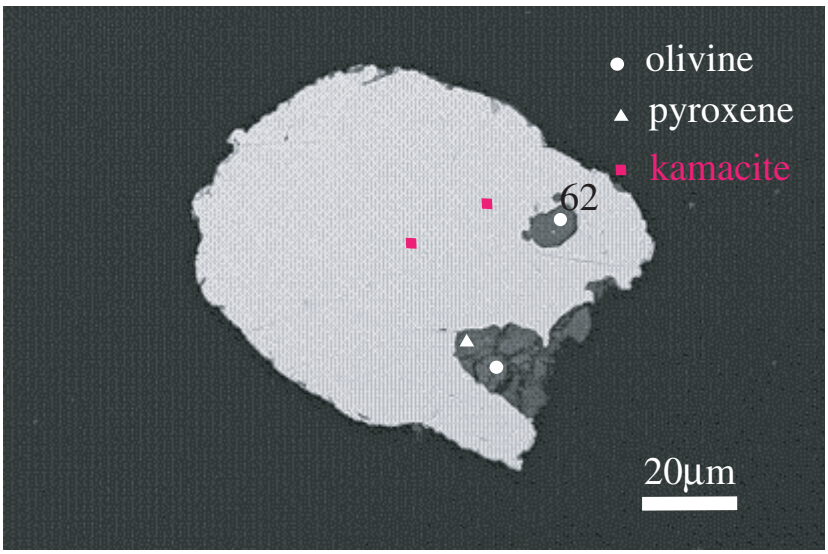

wt %	tr	kam
Ni		6.2
Fe		93.5
Mn		0.1
Co		0.3
Cr		0.0
S		0.0
P		0.0
Total		100.1

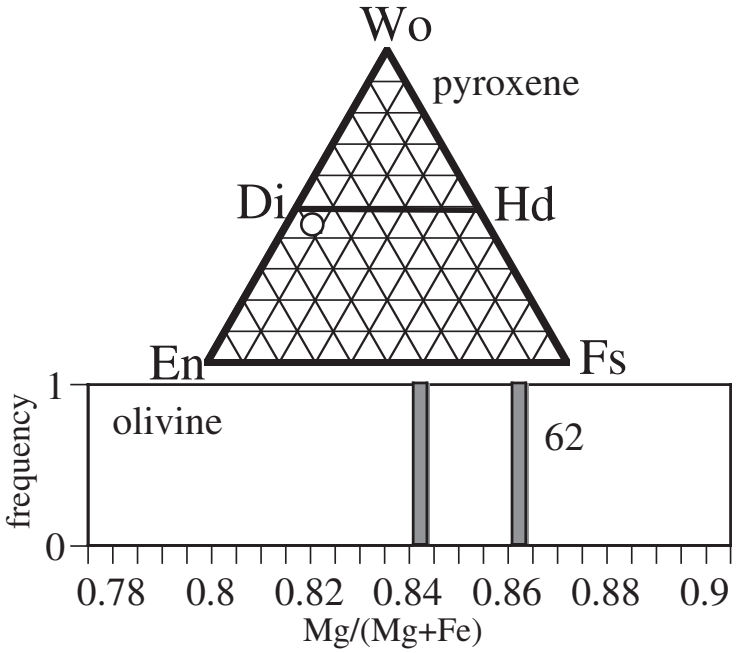

wt%	ol	low-Ca px	high-Ca px
SiO_2	39.5		51.1
TiO2	0.0		1.0
Al_2O_3	0.0		4.6
FeO	13.0		4.7
MnO	0.5		0.3
MgO	46.5		16.0
CaO	0.0		20.1
Na_2O	0.0		1.1
K_2O	0.0		0.0
Cr_2O_3	0.0		1.9
NiO	0.0		0.1
P_2O_5	0.0		0.0
SO_3	0.0		0.0
total	99.5		101.0

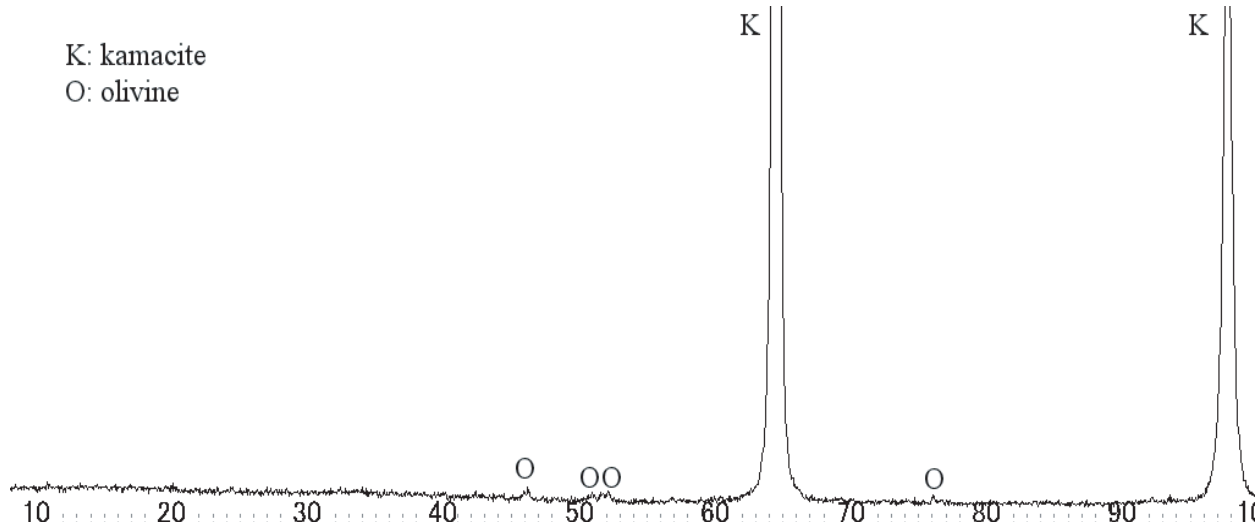

2AC2

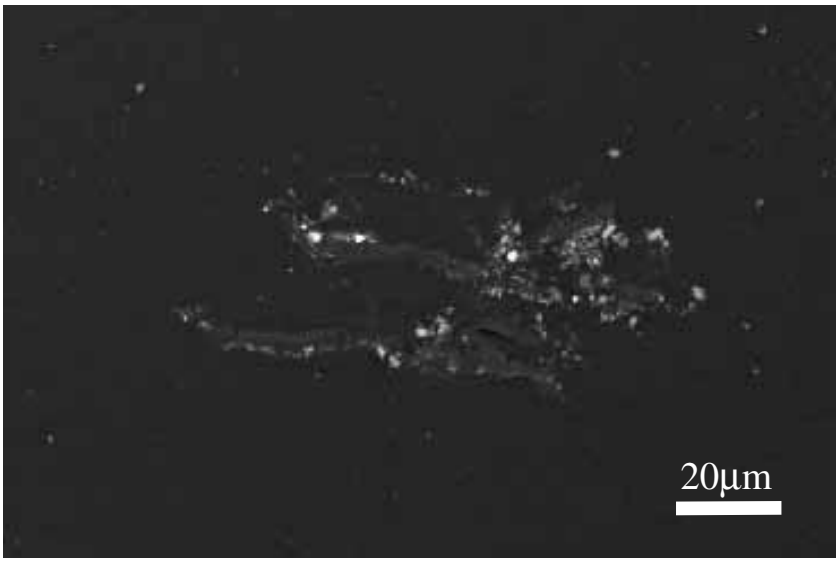

wt %	tr	kam
Ni		
Fe		
Mn		
Co		
Cr		
S		
P		
Total		

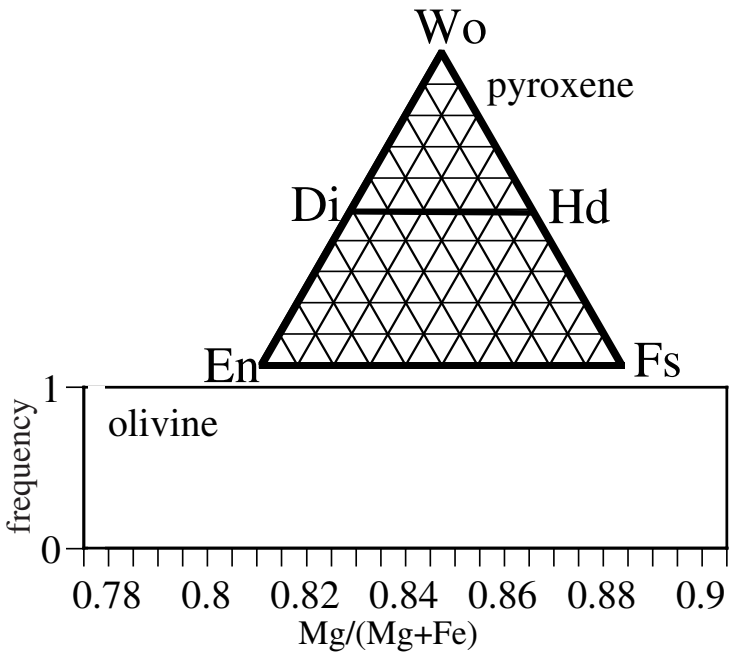

wt%	ol	low-Ca px	high-Ca px
SiO_2			
TiO2			
Al_2O_3			
FeO			
MnO			
MgO			
CaO			
Na_2O			
K_2O			
Cr_2O_3			
NiO			
P_2O_5			
SO_3			
total			

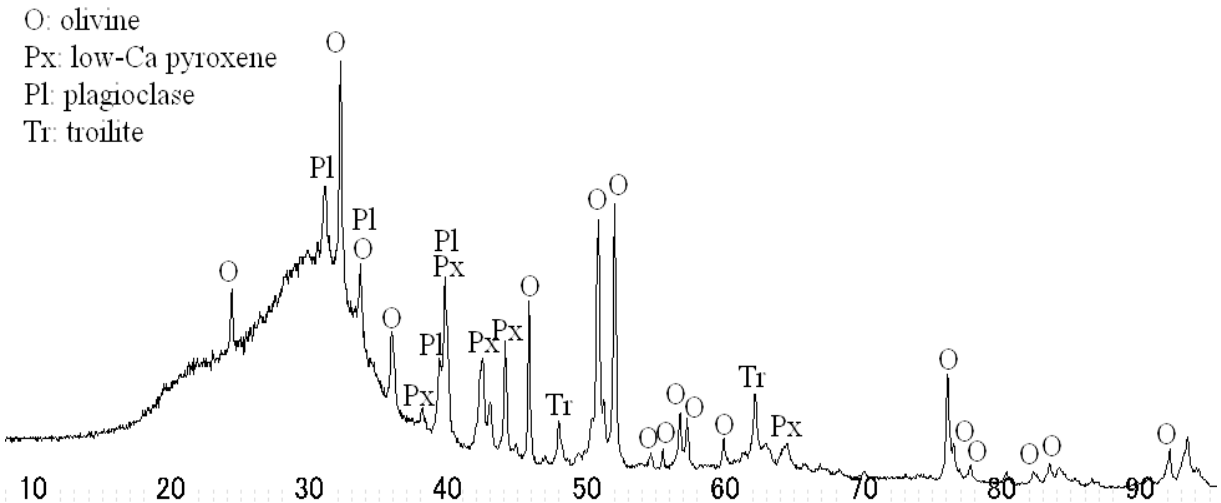

2AC3

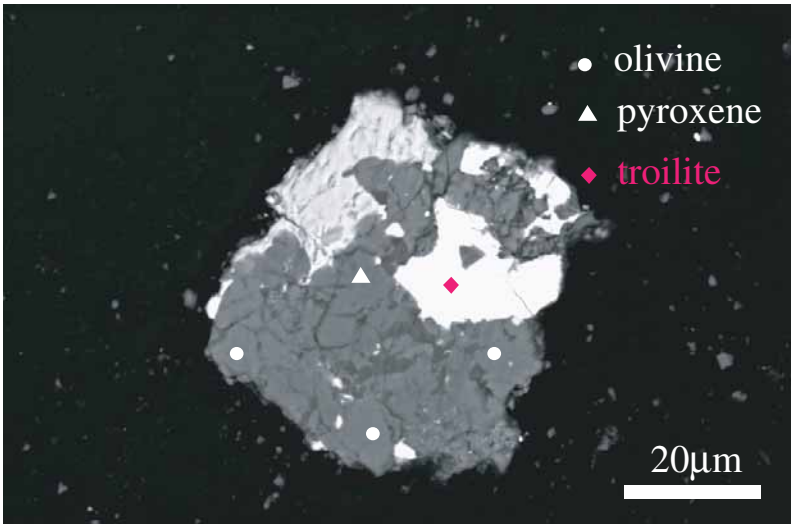

wt %	tr	kam
Ni	0.0	
Fe	62.8	
Mn	0.0	
Co	0.0	
Cr	0.7	
S	36.3	
P	0.0	
Total	99.9	

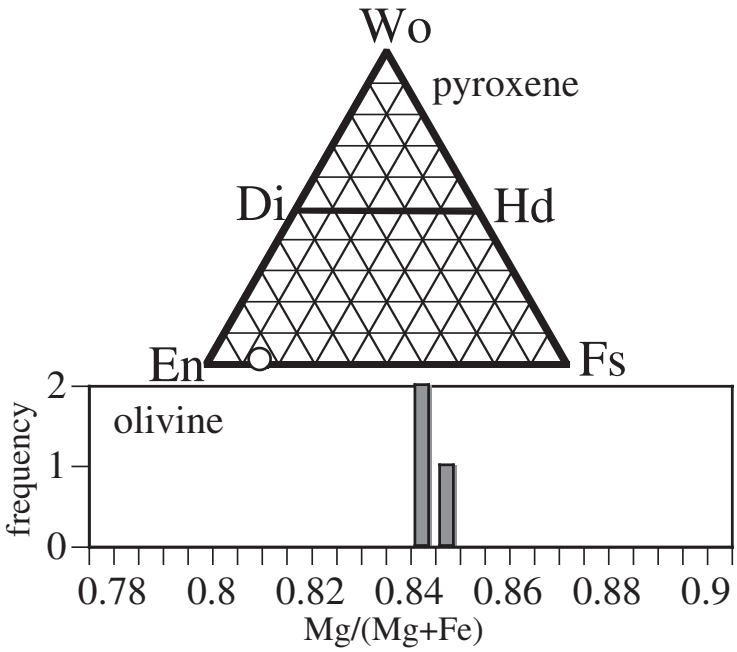

wt%	ol	low-Ca px	high-Ca px
SiO_2	39.7	55.1	
TiO2	0.0	0.1	
Al_2O_3	0.0	0.4	
FeO	14.9	9.7	
MnO	0.5	0.5	
MgO	45.7	31.2	
CaO	0.1	0.6	
Na_2O	0.0	0.2	
K_2O	0.0	0.0	
Cr_2O_3	0.0	0.5	
NiO	0.0	0.0	
P_2O_5	0.0	0.0	
SO_3	0.0	0.0	
total	100.9	98.2	

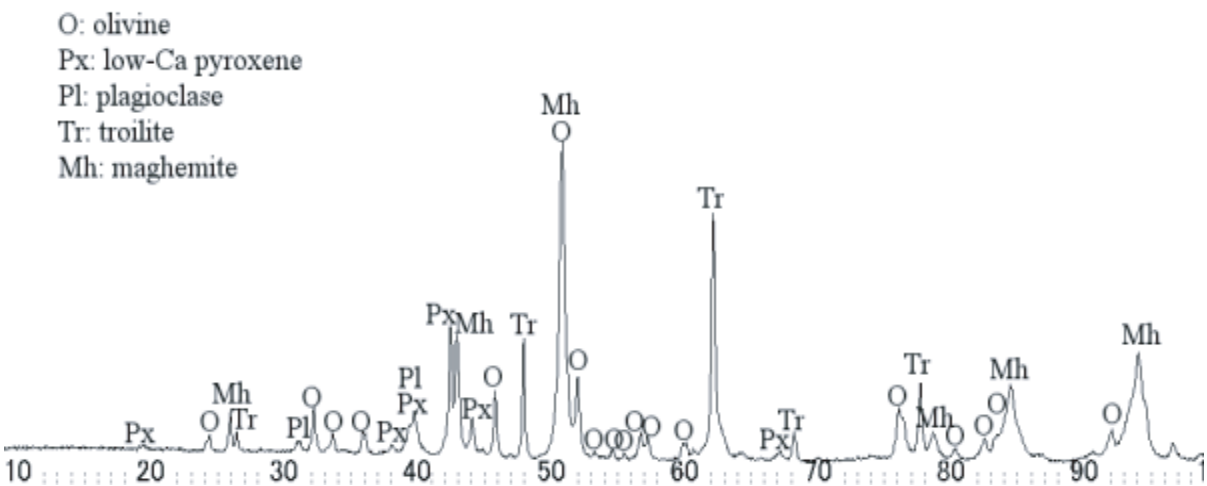

2AC4

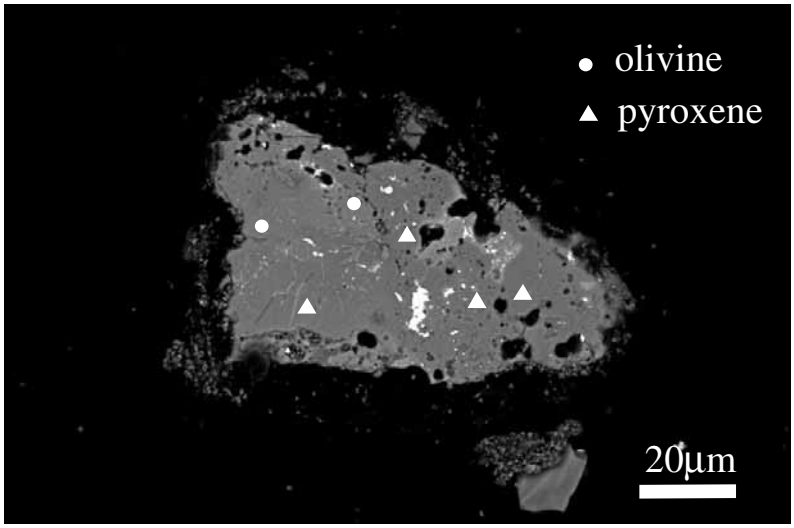

wt %	tr	kam
Ni		
Fe		
Mn		
Co		
Cr		
S		
P		
Total		

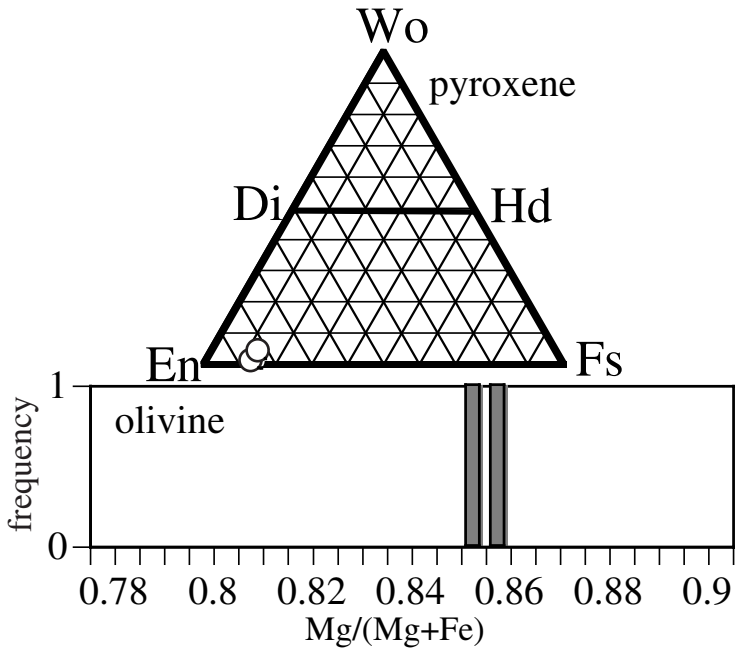

wt%	ol	low-Ca px	high-Ca px
SiO_2	39.6	56.3	
TiO2	0.0	0.1	
Al_2O_3	0.1	0.2	
FeO	14.0	8.9	
MnO	0.5	0.6	
MgO	45.6	32.5	
CaO	0.1	0.4	
Na_2O	0.4	0.1	
K_2O	0.0	0.0	
Cr_2O_3	0.1	0.2	
NiO	0.0	0.0	
P_2O_5	0.1	0.0	
SO_3	0.1	0.1	
total	100.5	99.5	

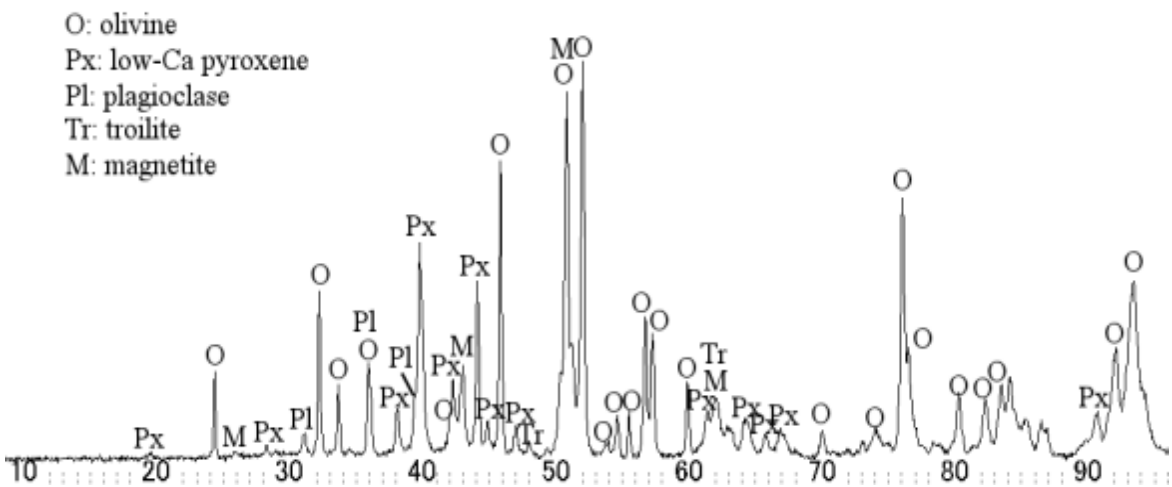

2AC5

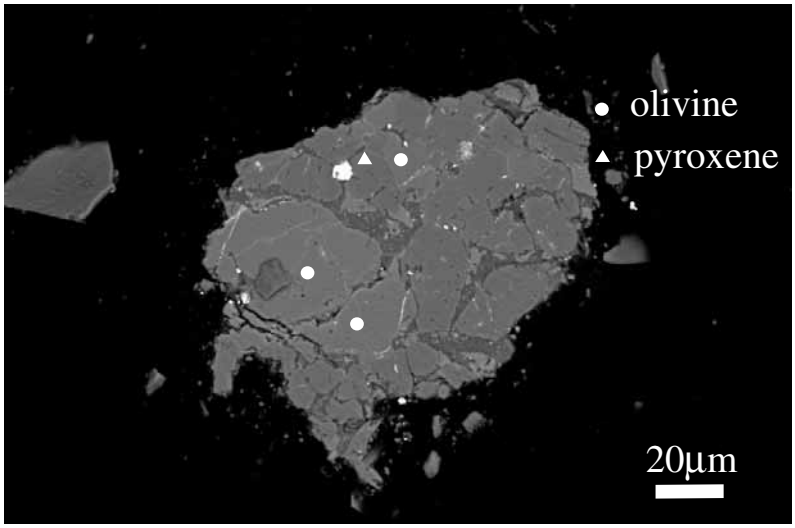

wt %	tr	kam
Ni		
Fe		
Mn		
Co		
Cr		
S		
P		
Total		

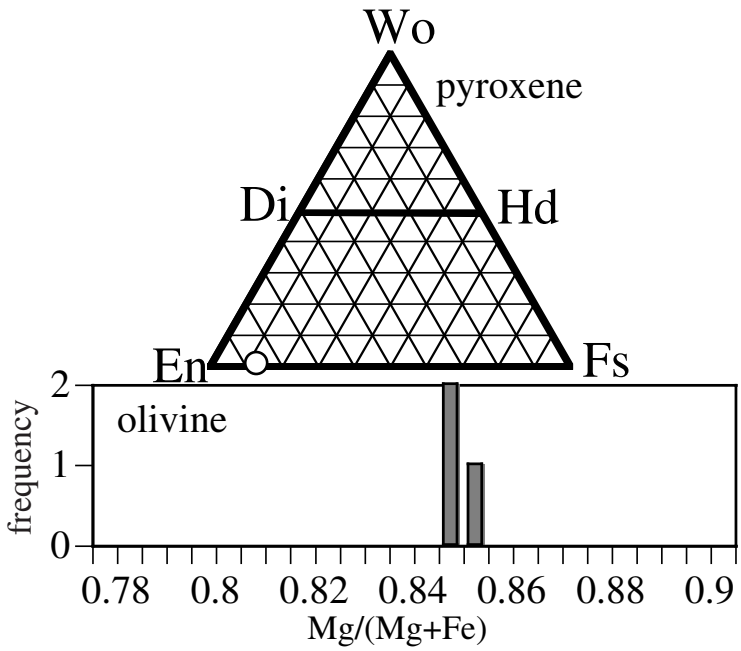

wt%	ol	low-Ca px	high-Ca px
SiO_2	39.6	57.3	
TiO2	0.0	0.2	
Al_2O_3	0.0	0.3	
FeO	14.9	9.0	
MnO	0.5	0.5	
MgO	46.0	33.2	
CaO	0.0	0.4	
Na_2O	0.0	0.0	
K_2O	0.0	0.0	
Cr_2O_3	0.0	0.1	
NiO	0.0	0.0	
P_2O_5	0.1	0.0	
SO_3	0.0	0.0	
total	101.0	100.9	

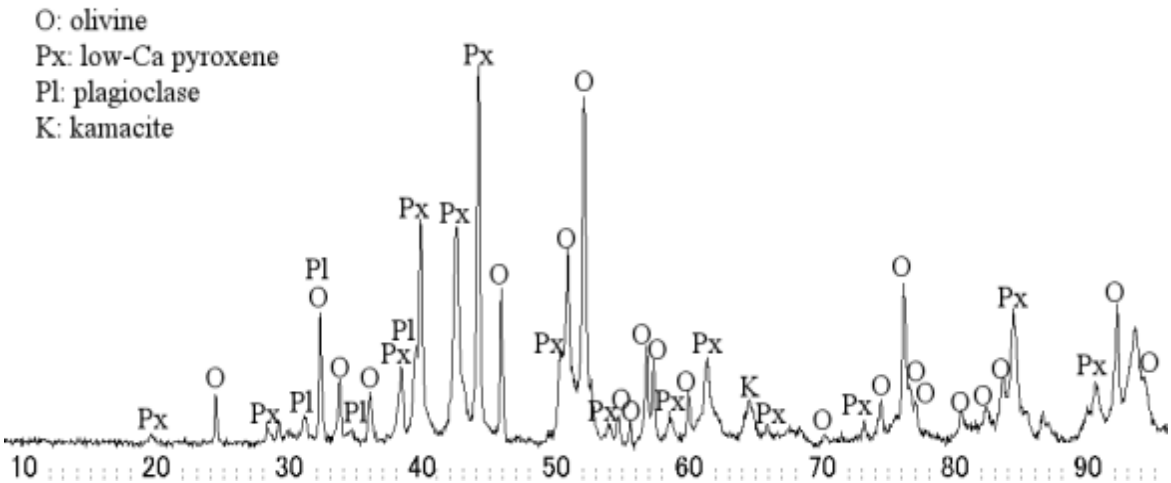

2AC6

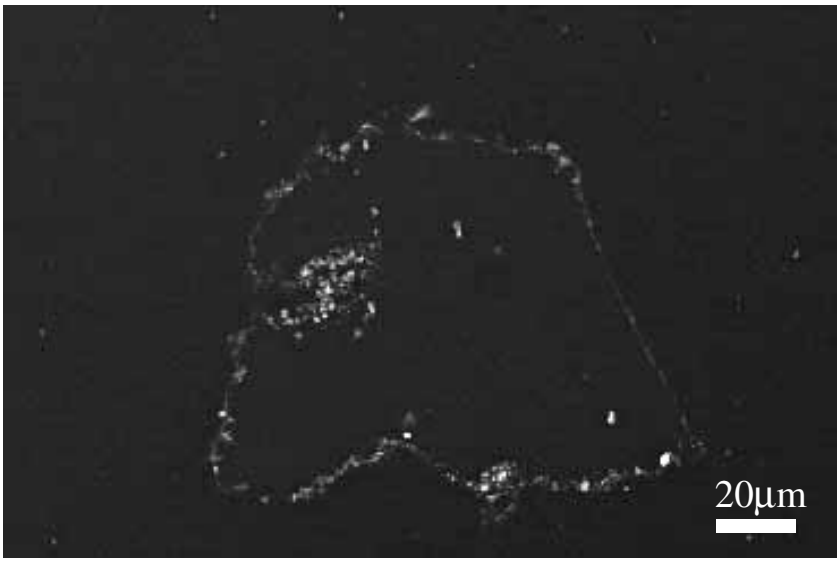

wt %	tr	kam
Ni		
Fe		
Mn		
Co		
Cr		
S		
P		
Total		

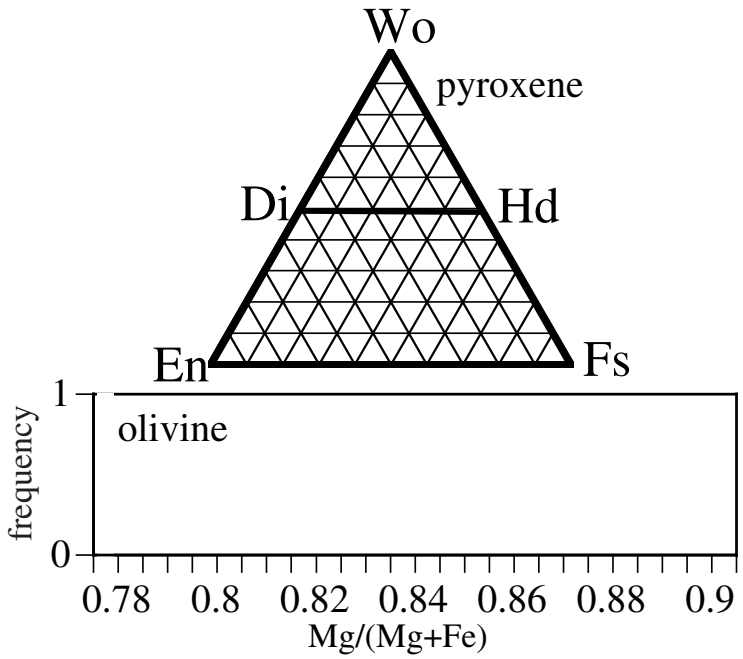

wt%	ol	low-Ca px	high-Ca px
SiO_2			
TiO2			
Al_2O_3			
FeO			
MnO			
MgO			
CaO			
Na_2O			
K_2O			
Cr_2O_3			
NiO			
P_2O_5			
SO_3			
total			

O: olivine
Px: low-Ca pyroxene
Pl: plagioclase
Tr: troilite

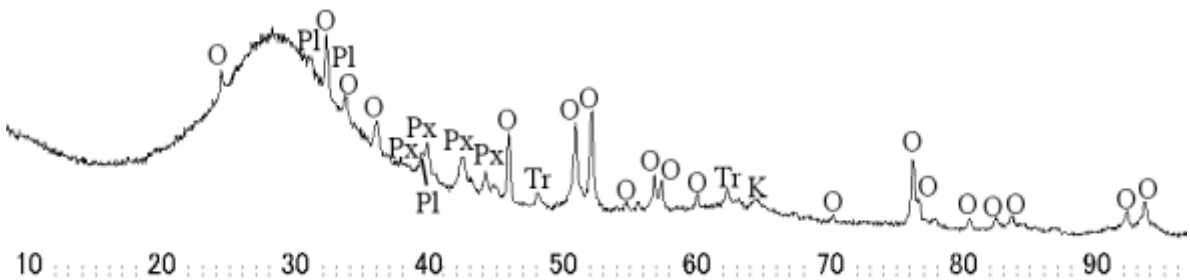

2AC7

wt %	tr	kam
Ni	0.0	
Fe	63.5	
Mn	0.1	
Co	0.0	
Cr	0.0	
S	36.8	
P	0.0	
Total	100.5	

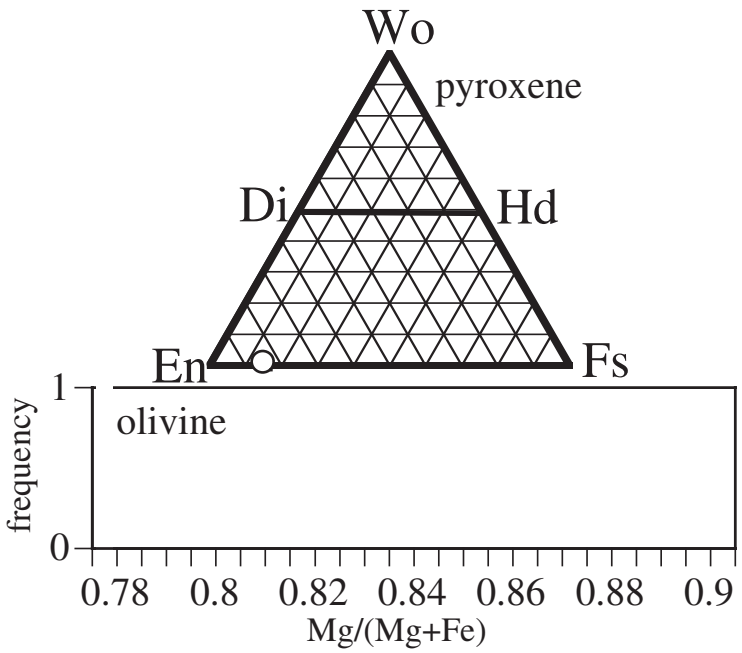

wt%	ol	low-Ca px	high-Ca px
SiO_2		55.9	
TiO2		0.1	
Al_2O_3		0.1	
FeO		10.2	
MnO		0.6	
MgO		32.3	
CaO		0.4	
Na_2O		0.1	
K_2O		0.0	
Cr_2O_3		0.1	
NiO		0.0	
P_2O_5		0.0	
SO_3		0.1	
total		99.9	

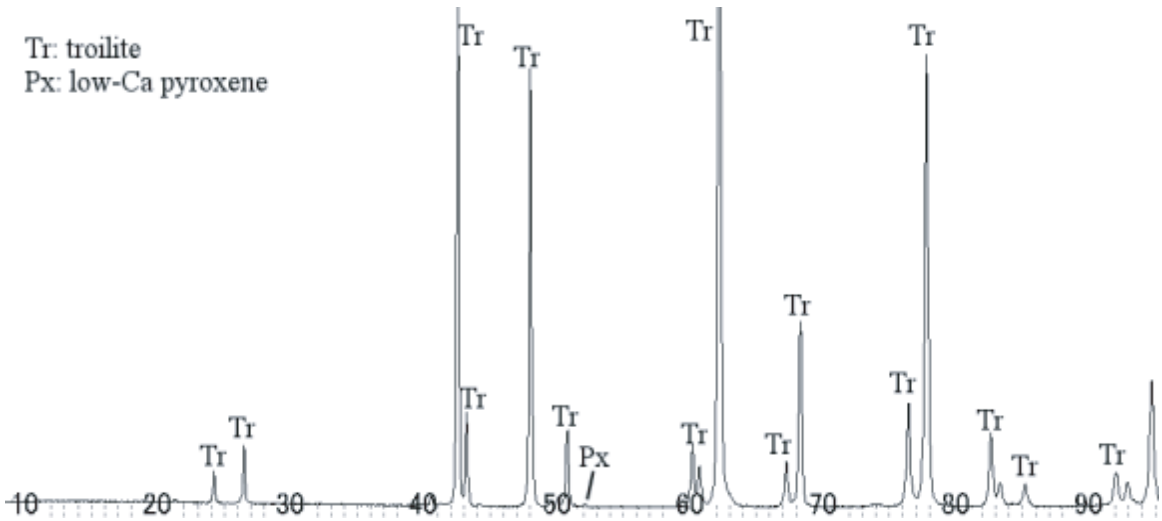

2AC8

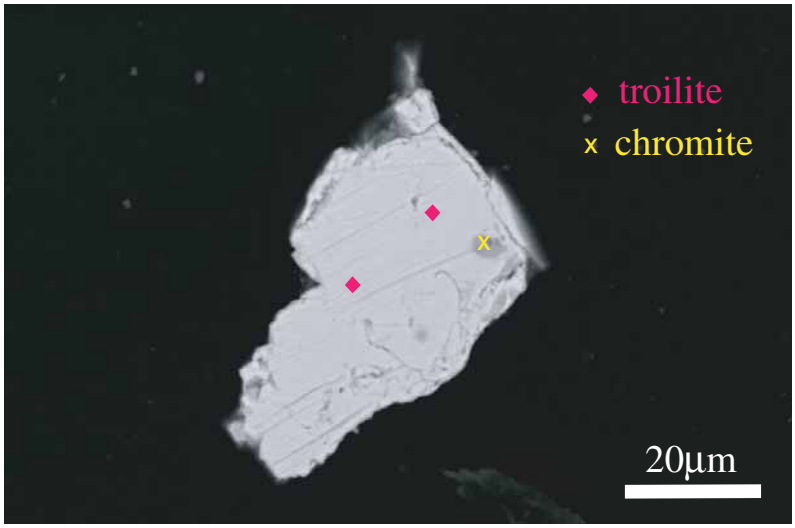

wt %	tr	kam
Ni	0.0	
Fe	62.6	
Mn	0.0	
Co	0.0	
Cr	0.0	
S	36.8	
P	0.0	
Total	99.4	

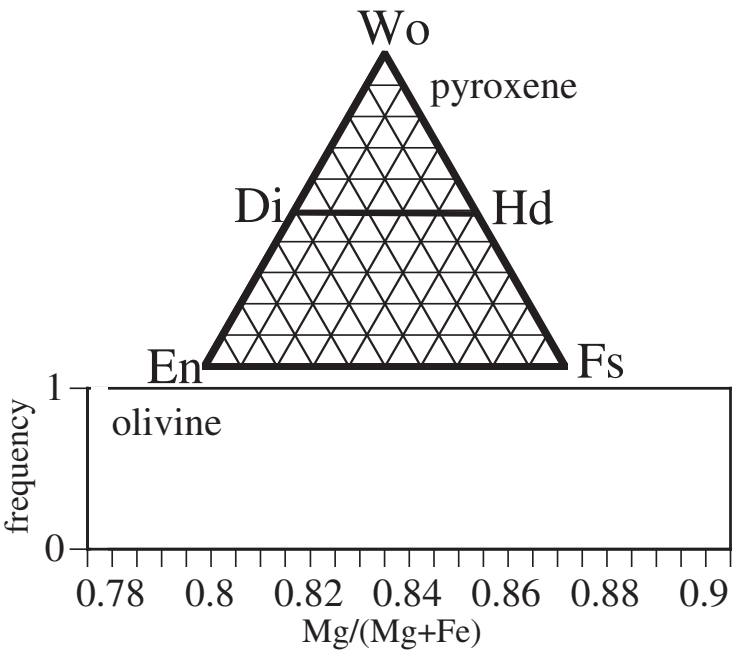

wt%	ol	low-Ca px	high-Ca px
SiO_2			
TiO2			
Al_2O_3			
FeO			
MnO			
MgO			
CaO			
Na_2O			
K_2O			
Cr_2O_3			
NiO			
P_2O_5			
SO_3			
total			

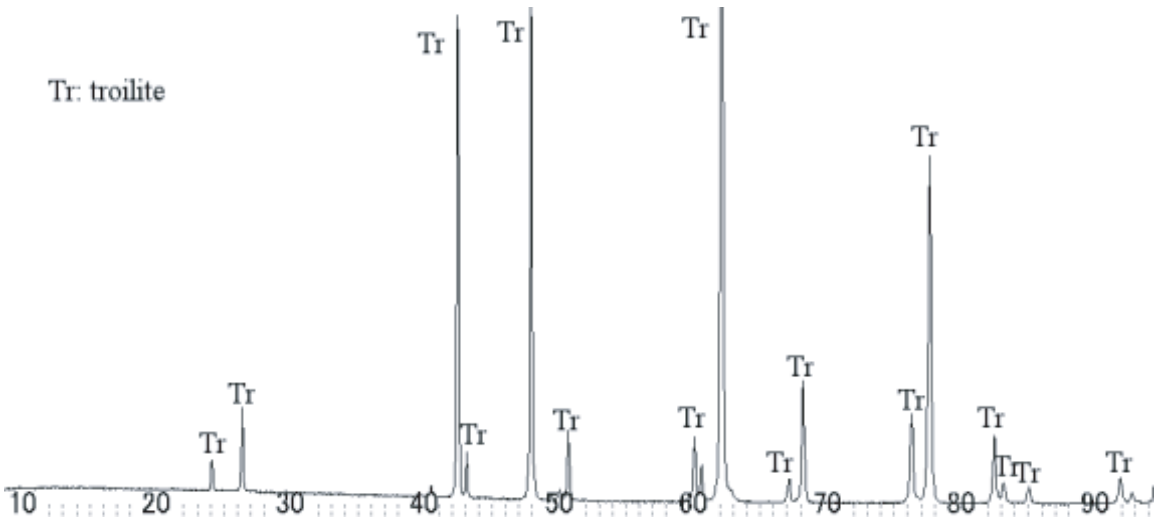

2AC9

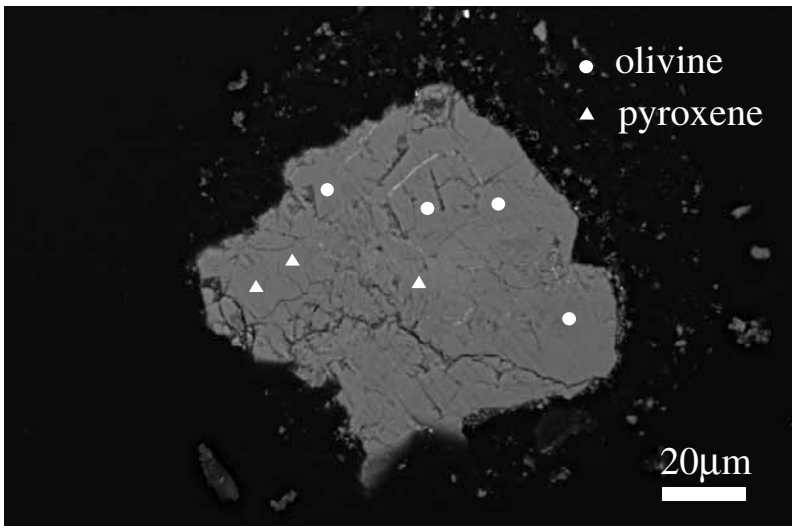

wt %	tr	kam
Ni		
Fe		
Mn		
Co		
Cr		
S		
P		
Total		

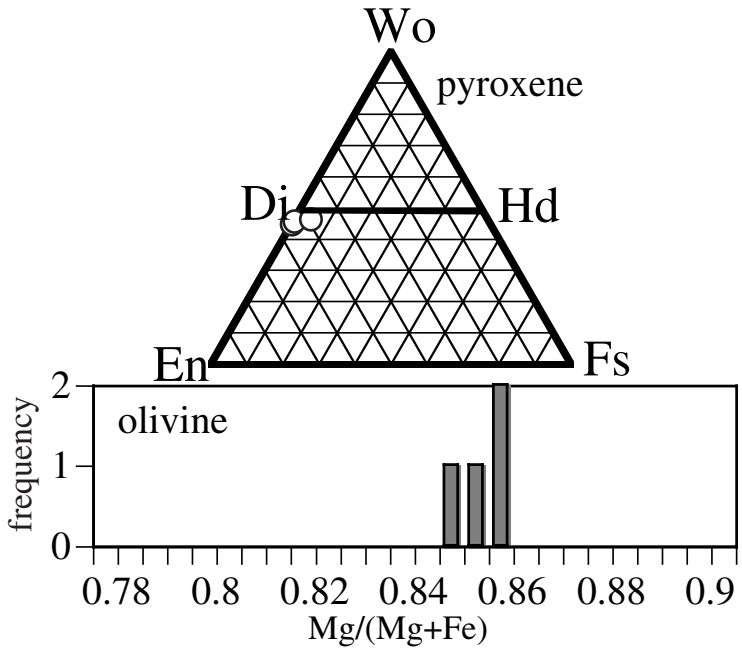

wt%	ol	low-Ca px	high-Ca px
SiO_2	39.6		50.8
TiO2	0.0		1.4
Al_2O_3	0.0		5.2
FeO	14.0		0.7
MnO	0.4		0.0
MgO	45.6		18.7
CaO	0.0		21.8
Na_2O	0.0		0.2
K_2O	0.0		0.0
Cr_2O_3	0.0		0.9
NiO	0.1		0.0
P_2O_5	0.0		0.0
SO_3	0.0		0.0
total	99.8		99.6

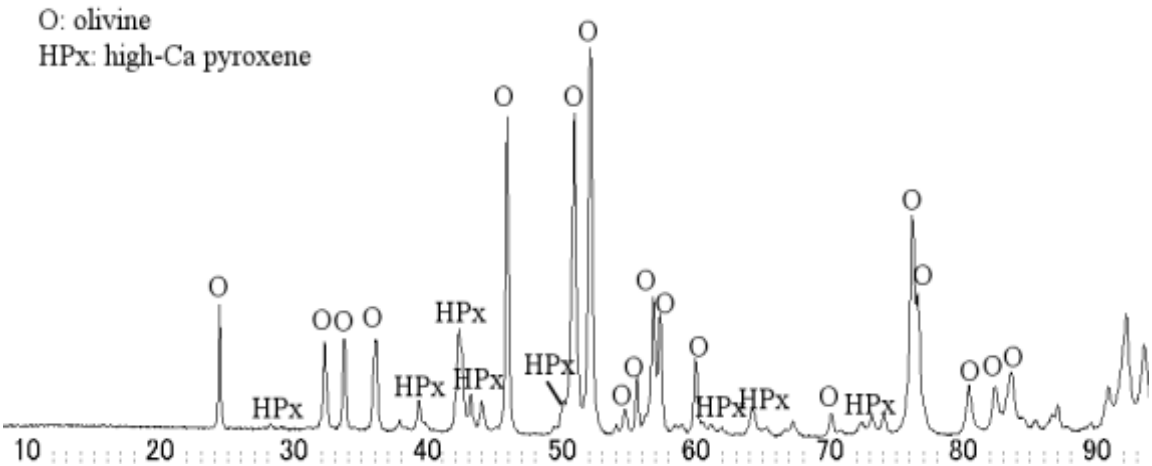

2AC10

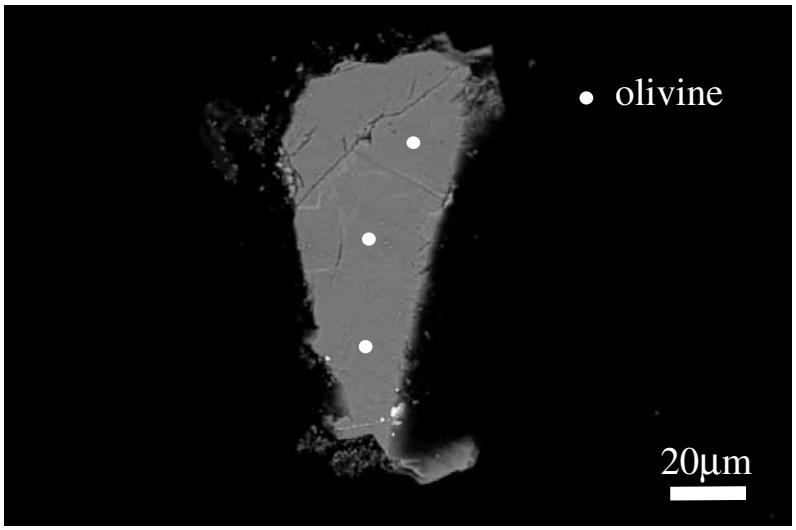

wt %	tr	kam
Ni		
Fe		
Mn		
Co		
Cr		
S		
P		
Total		

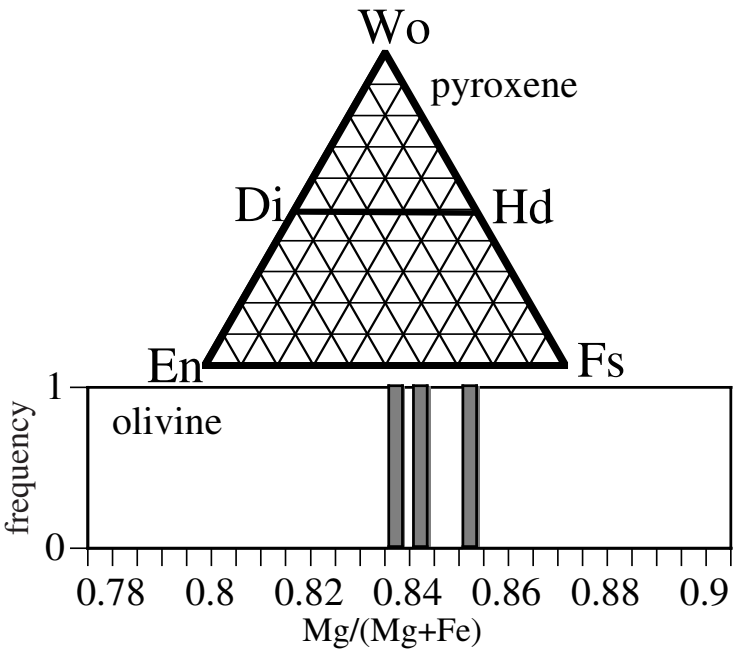

wt%	ol	low-Ca px	high-Ca px
SiO_2	39.1		
TiO2	0.0		
Al_2O_3	0.0		
FeO	14.8		
MnO	0.4		
MgO	44.8		
CaO	0.0		
Na_2O	0.0		
K_2O	0.0		
Cr_2O_3	0.0		
NiO	0.0		
P_2O_5	0.1		
SO_3	0.0		
total	99.3		

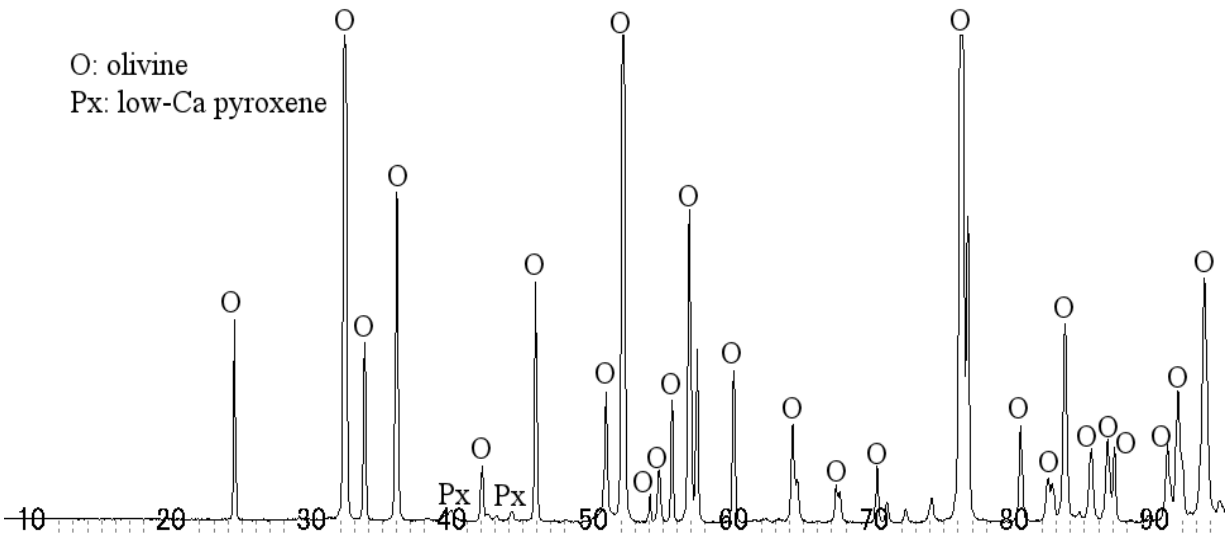

2AC11

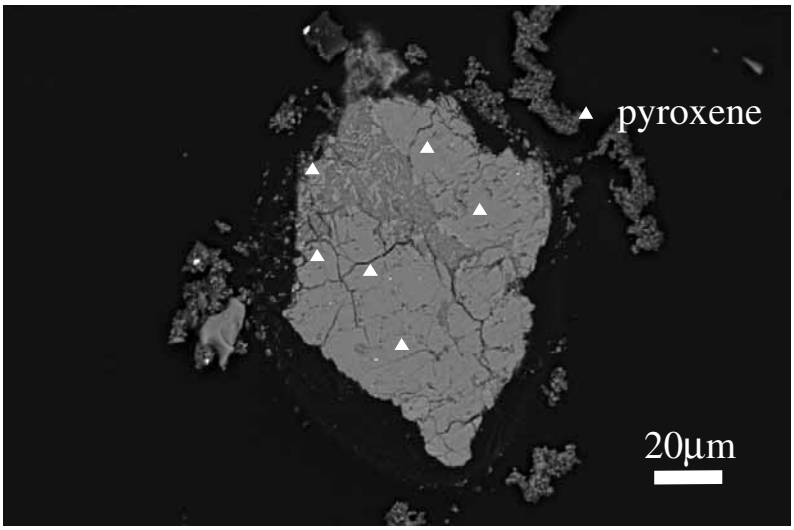

wt %	tr	kam
Ni		
Fe		
Mn		
Co		
Cr		
S		
P		
Total		

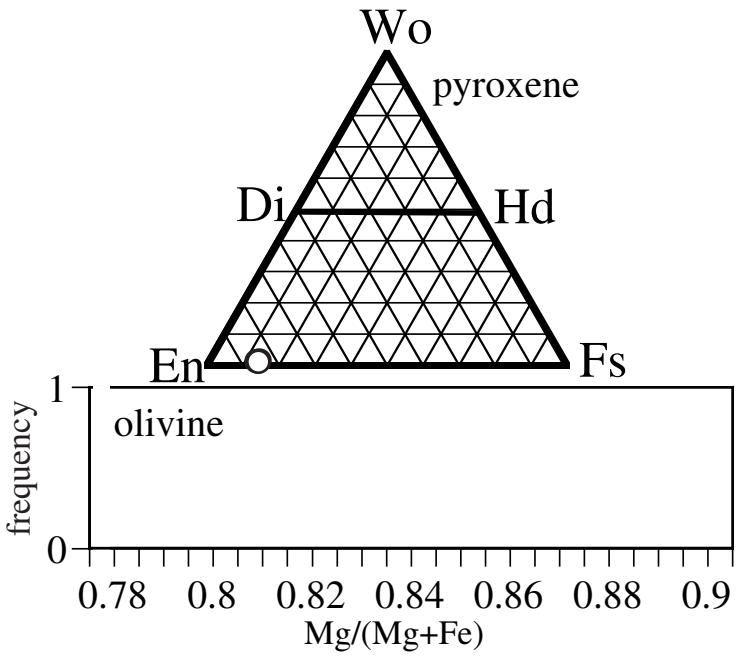

wt%	ol	low-Ca px	high-Ca px
SiO_2		56.3	
TiO2		0.2	
Al_2O_3		0.1	
FeO		9.8	
MnO		0.5	
MgO		32.4	
CaO		0.4	
Na_2O		0.0	
K_2O		0.0	
Cr_2O_3		0.2	
NiO		0.0	
P_2O_5		0.1	
SO_3		0.0	
total		100.0	

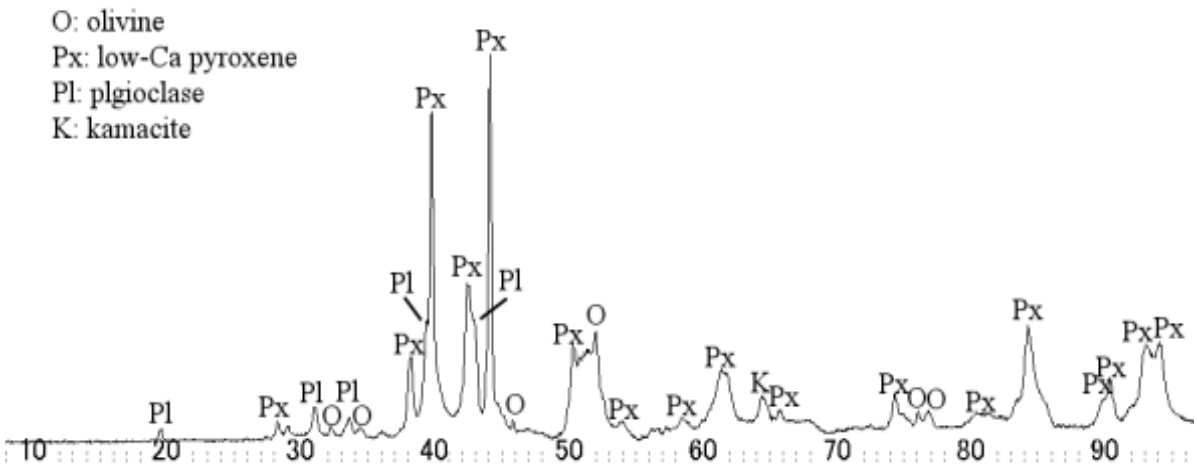

2AC12

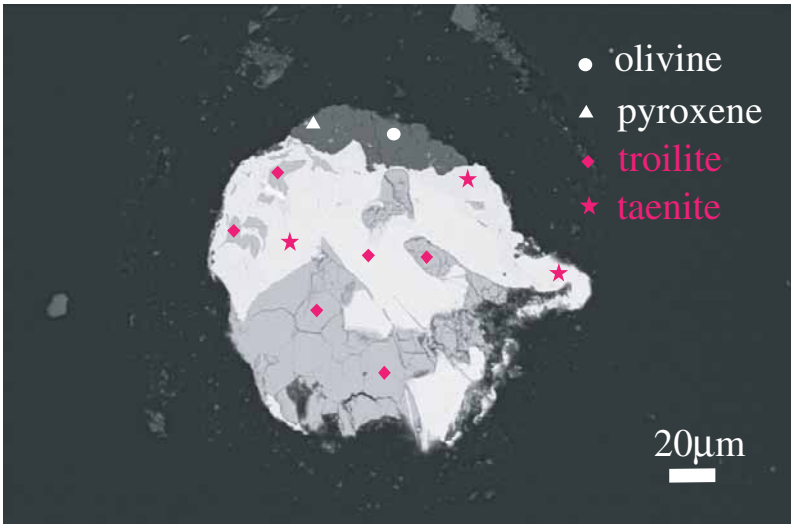

wt %	tr	tae
Ni	0.9	50.6
Fe	62.9	49.4
Mn	0.0	0.0
Co	0.0	0.1
Cr	0.0	0.0
S	36.0	0.0
P	0.0	0.0
Total	99.9	100.2

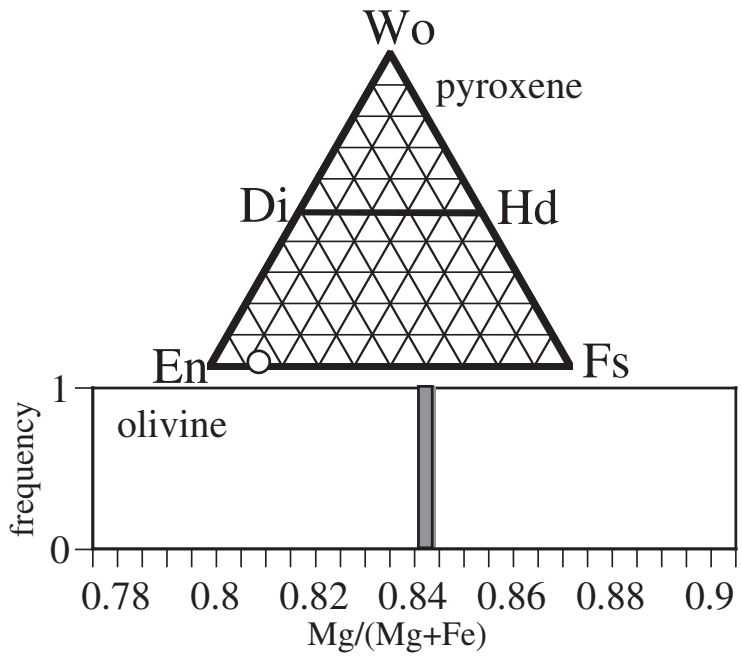

wt%	ol	low-Ca px	high-Ca px
SiO_2	39.1	57.0	
TiO2	0.0	0.2	
Al_2O_3	0.0	0.2	
FeO	15.4	9.5	
MnO	0.5	0.5	
MgO	45.2	32.9	
CaO	0.0	0.4	
Na_2O	0.0	0.1	
K_2O	0.0	0.0	
Cr_2O_3	0.1	0.1	
NiO	0.1	0.0	
P_2O_5	0.0	0.0	
SO_3	0.1	0.1	
total	100.6	100.8	

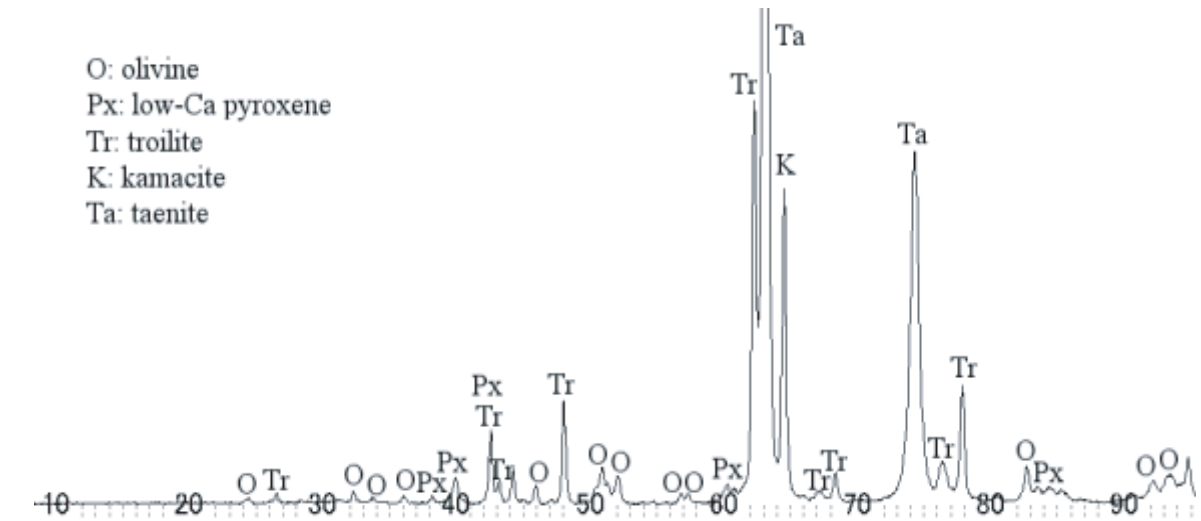

2AC13

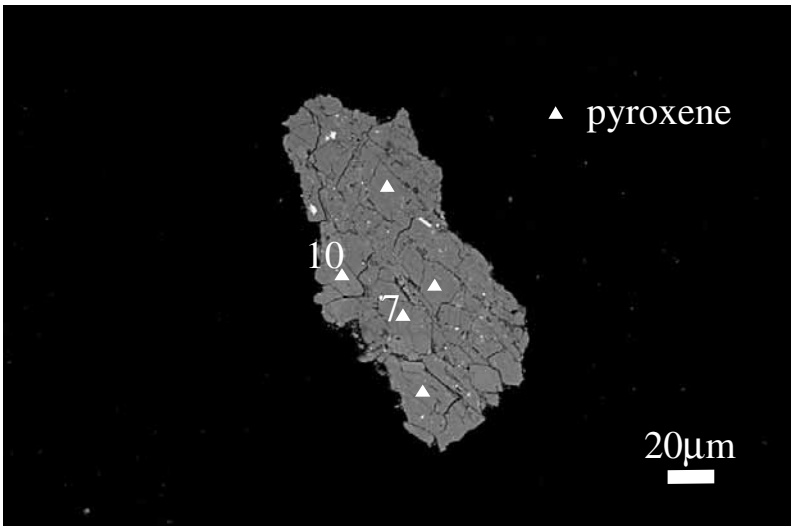

wt %	tr	kam
Ni		
Fe		
Mn		
Co		
Cr		
S		
P		
Total		

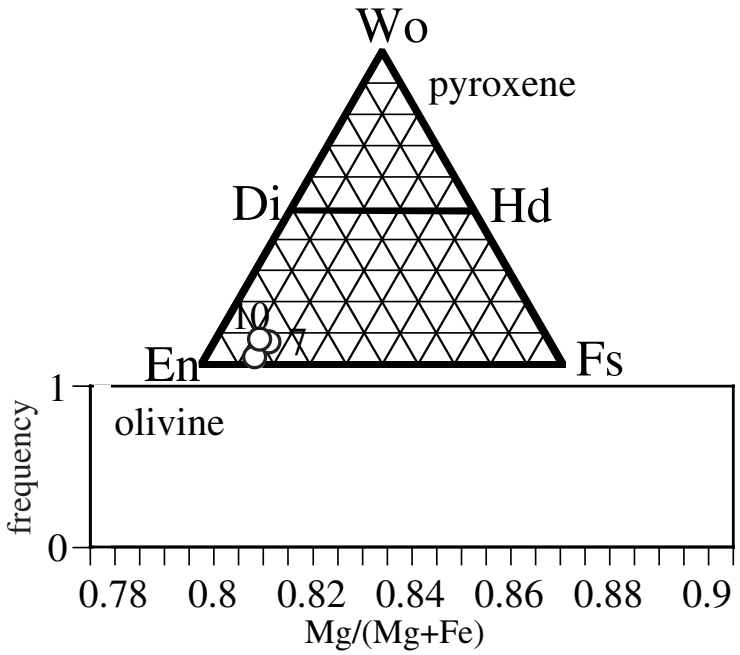

wt%	ol	low-Ca px	high-Ca px
SiO_2		55.8	54.2
TiO2		0.2	0.1
Al_2O_3		0.4	1.2
FeO		9.6	10.4
MnO		0.7	0.4
MgO		31.7	28.7
CaO		0.9	3.4
Na_2O		0.1	0.1
K_2O		0.0	0.0
Cr_2O_3		0.2	0.5
NiO		0.0	0.0
P_2O_5		0.1	0.1
SO_3		0.0	0.0
total		99.5	99.1

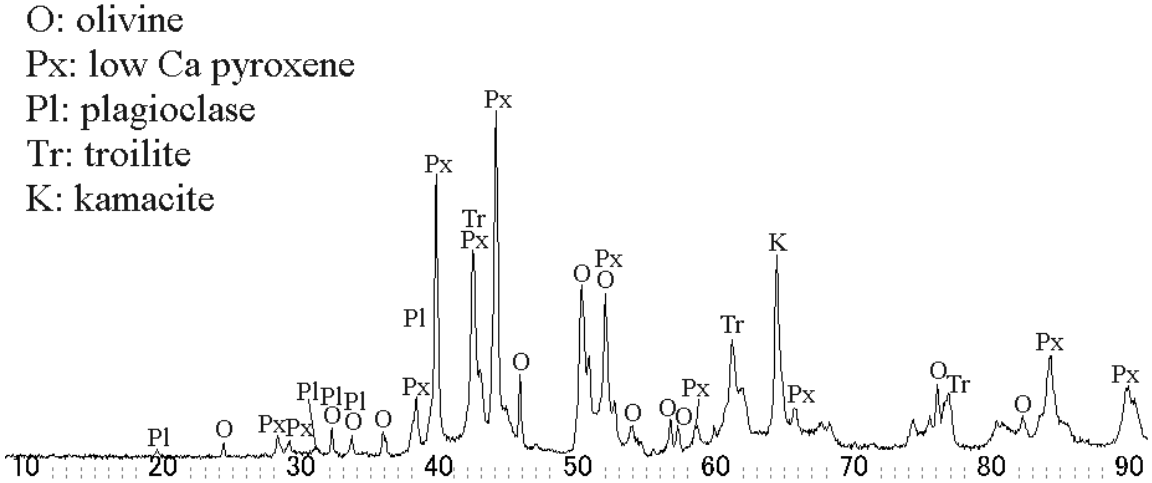

2AC14

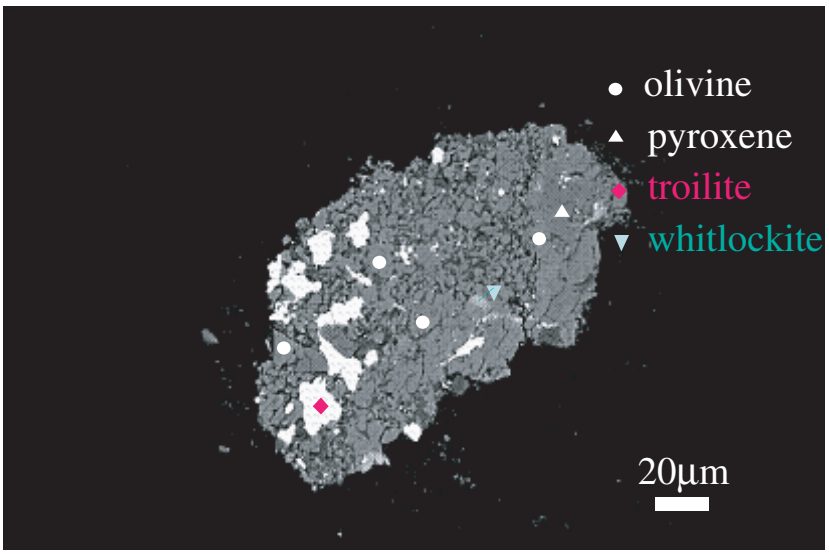

wt %	tr	kam
Ni	0.0	
Fe	63.1	
Mn	0.0	
Co	0.0	
Cr	0.0	
S	37.7	
P	0.0	
Total	100.8	

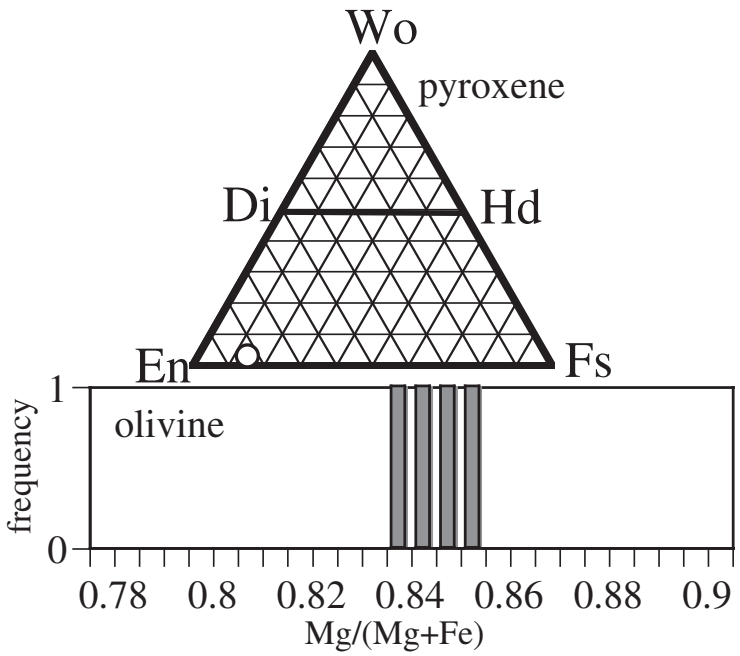

wt%	ol	low-Ca px	high-Ca px
SiO_2	39.3	55.8	
TiO2	0.0	0.4	
Al_2O_3	0.1	0.7	
FeO	14.0	9.9	
MnO	0.6	0.6	
MgO	45.2	32.0	
CaO	0.1	1.3	
Na_2O	0.2	0.1	
K_2O	0.0	0.0	
Cr_2O_3	0.1	0.4	
NiO	0.0	0.0	
P_2O_5	0.3	0.0	
SO_3	0.0	0.0	
total	99.8	101.2	

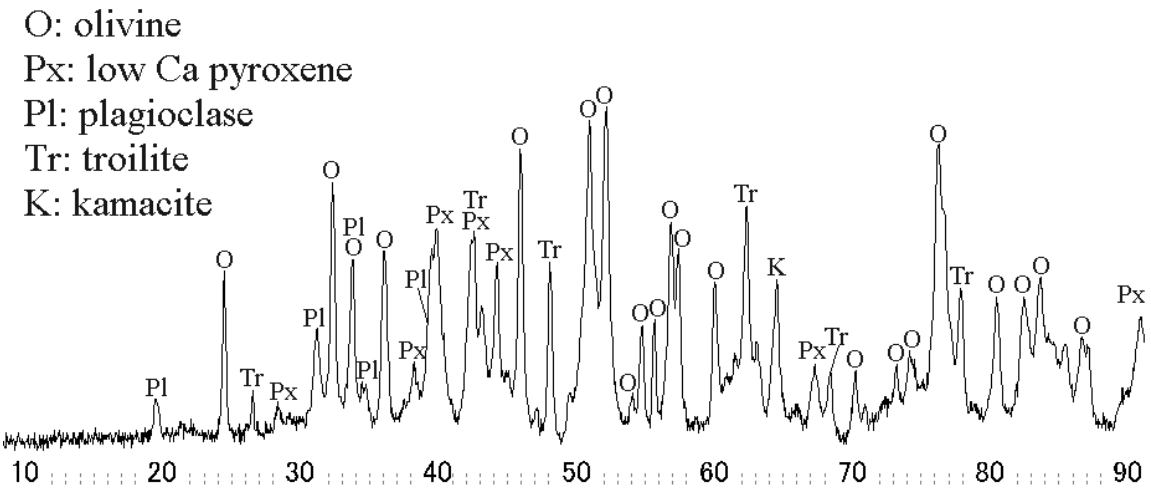

2AC15

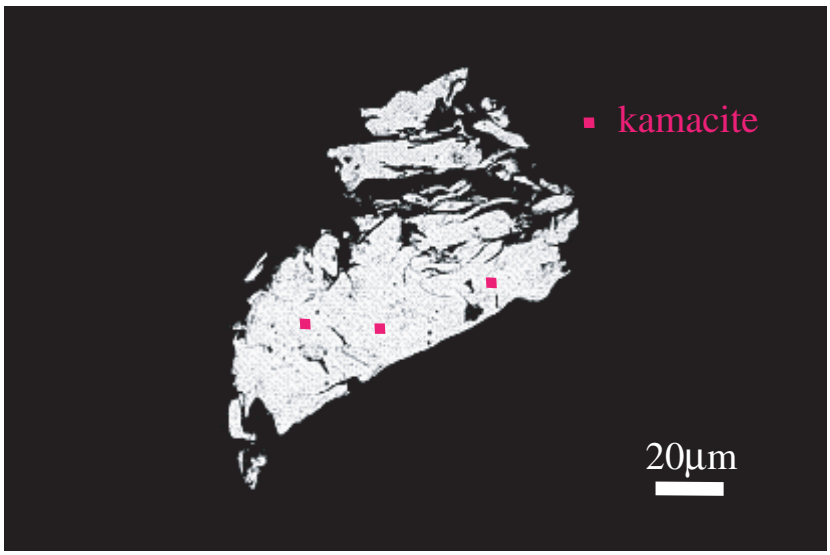

wt %	tr	kam
Ni		0.1
Fe		99.1
Mn		0.9
Co		0.0
Cr		0.1
S		0.0
P		0.0
Total		100.2

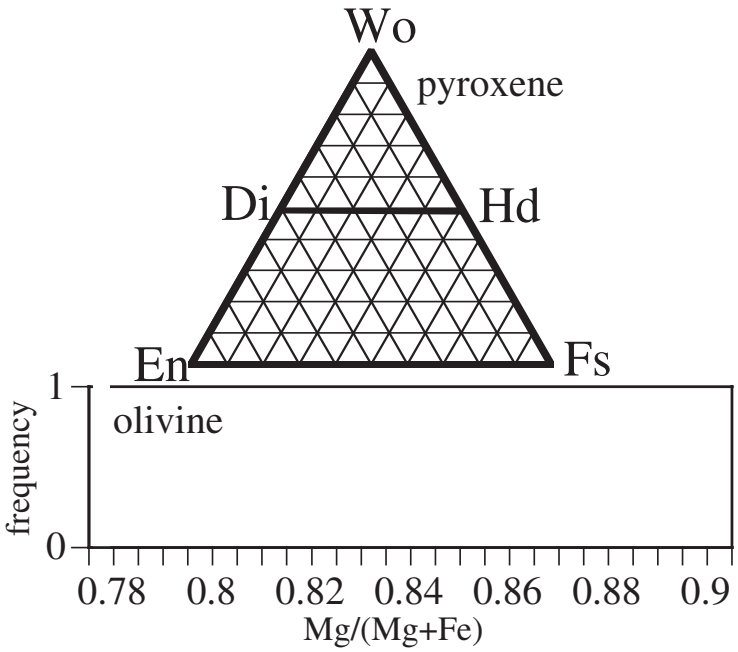

wt%	ol	low-Ca px	high-Ca px
SiO_2			
TiO2			
Al_2O_3			
FeO			
MnO			
MgO			
CaO			
Na_2O			
K_2O			
Cr_2O_3			
NiO			
P_2O_5			
SO_3			
total			

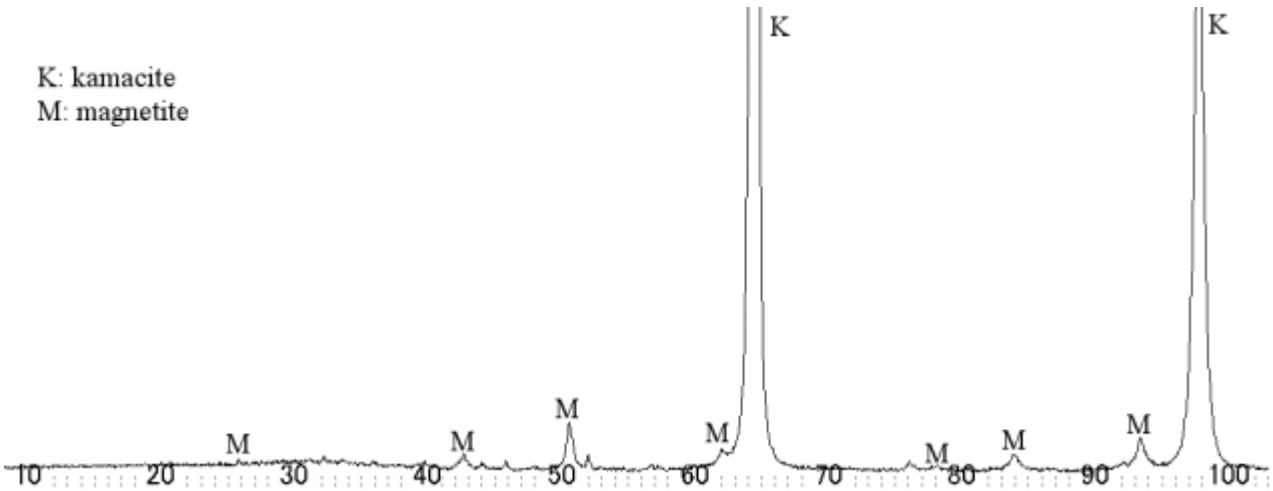

2AC16

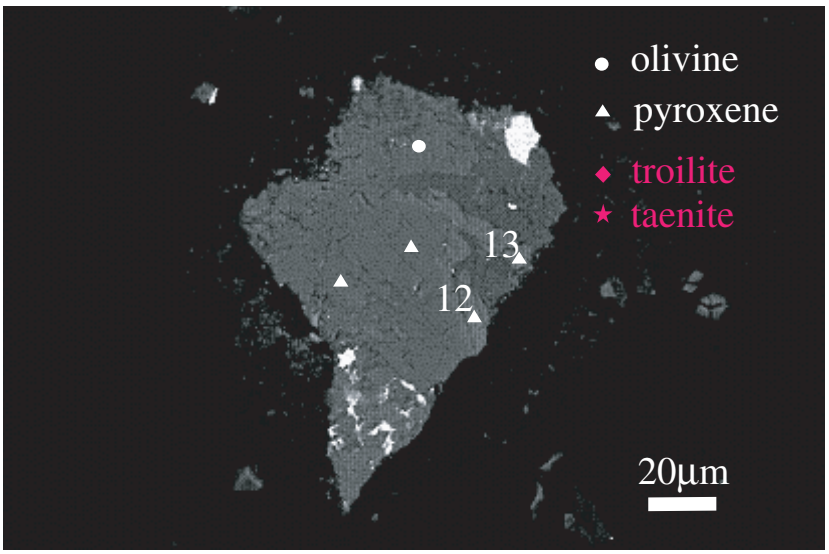

wt %	tr	kam
Ni		
Fe		
Mn		
Co		
Cr		
S		
P		
Total		

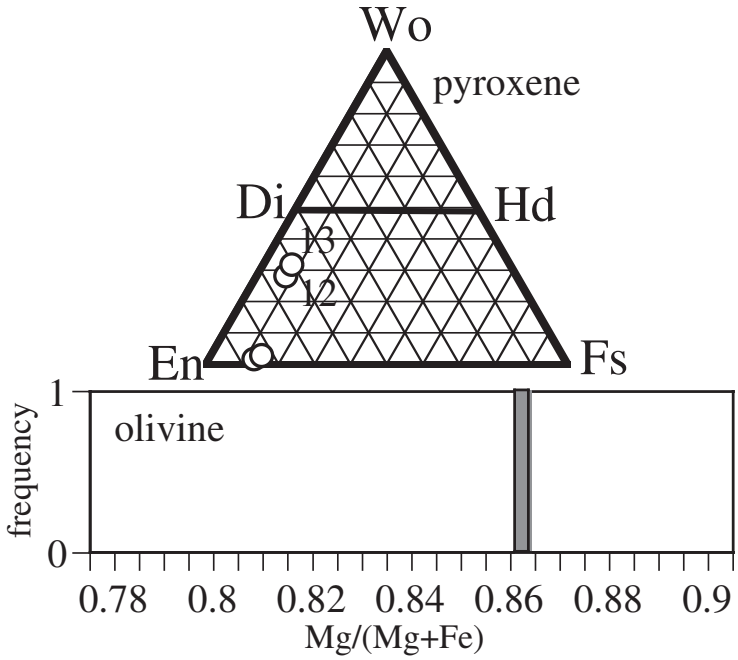

wt%	ol	low-Ca px	high-Ca px
SiO_2	40.5	56.4	54.0
TiO2	0.0	0.1	0.2
Al_2O_3	0.0	0.2	1.1
FeO	13.3	9.7	5.4
MnO	0.5	0.5	0.3
MgO	45.6	30.8	22.2
CaO	0.1	1.2	13.5
Na_2O	0.0	0.1	0.6
K_2O	0.0	0.0	0.0
Cr_2O_3	0.1	0.4	1.8
NiO	0.0	0.1	0.0
P_2O_5	0.0	0.0	0.1
SO_3	0.0	0.1	0.0
total	100.2	99.6	99.1

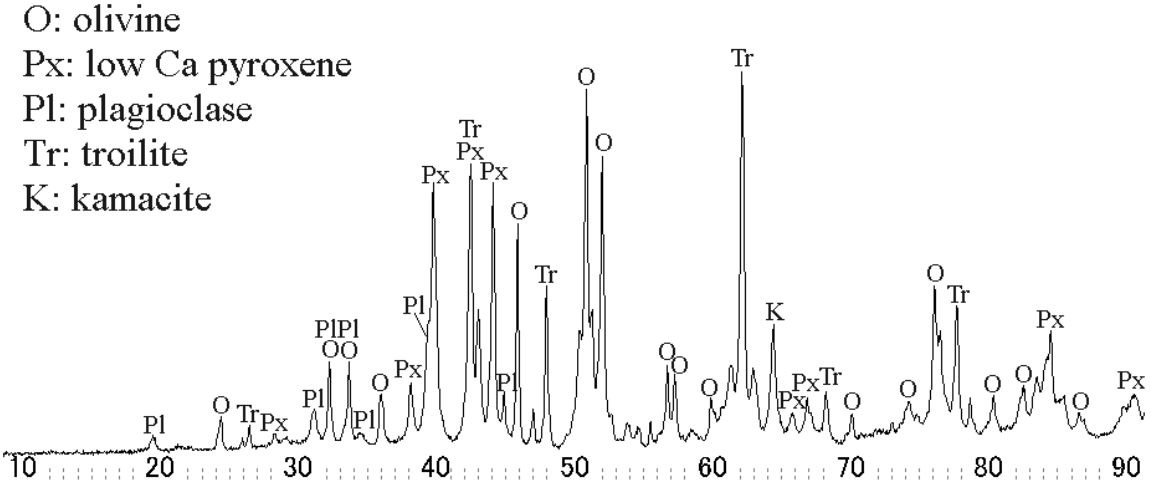

2AC17

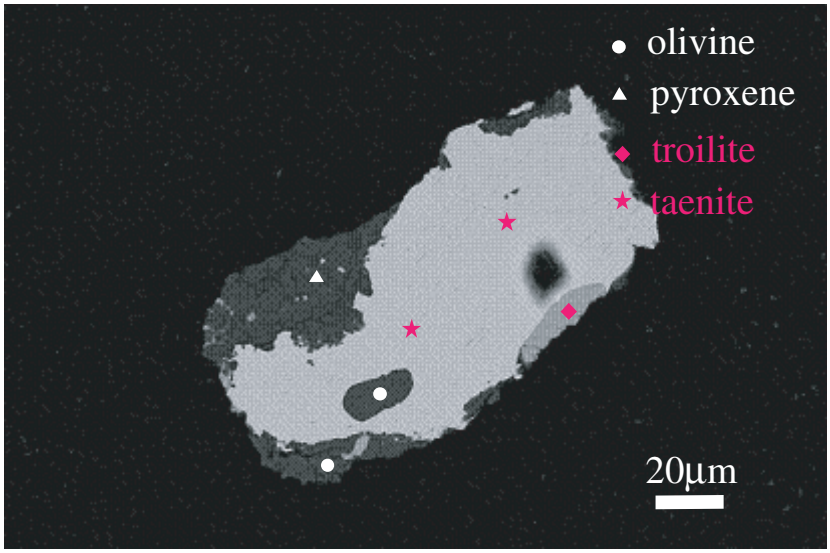

wt %	tr	tae
Ni	0.9	50.2
Fe	62.2	50.0
Mn	0.0	0.0
Co	0.0	0.1
Cr	0.0	0.0
S	37.1	0.0
P	0.0	0.0
Total	100.3	100.2

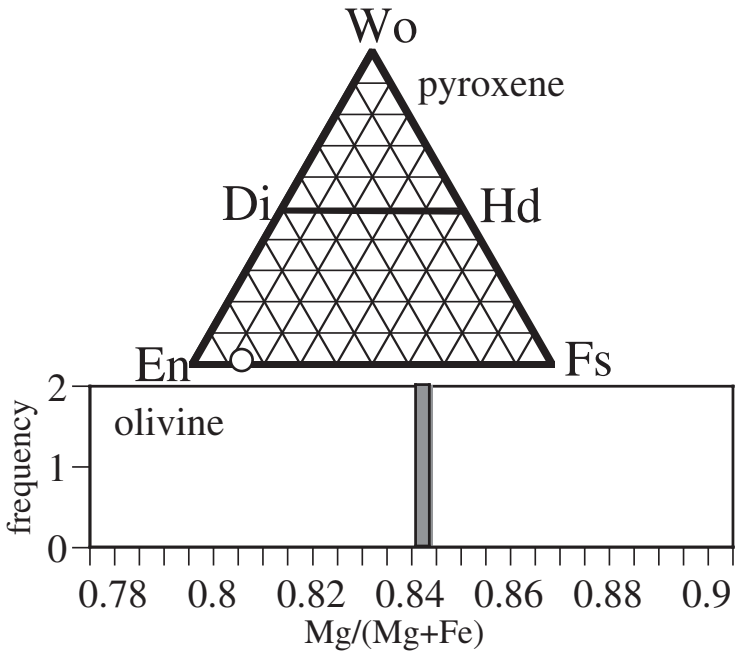

wt%	ol	low-Ca px	high-Ca px
SiO_2	39.6	56.2	
TiO2	0.0	0.3	
Al_2O_3	0.0	0.2	
FeO	15.4	9.2	
MnO	0.5	0.7	
MgO	45.3	32.2	
CaO	0.0	0.4	
Na_2O	0.0	0.1	
K_2O	0.0	0.0	
Cr_2O_3	0.0	0.2	
NiO	0.2	0.0	
P_2O_5	0.1	0.0	
SO_3	0.0	0.0	
total	101.2	99.4	

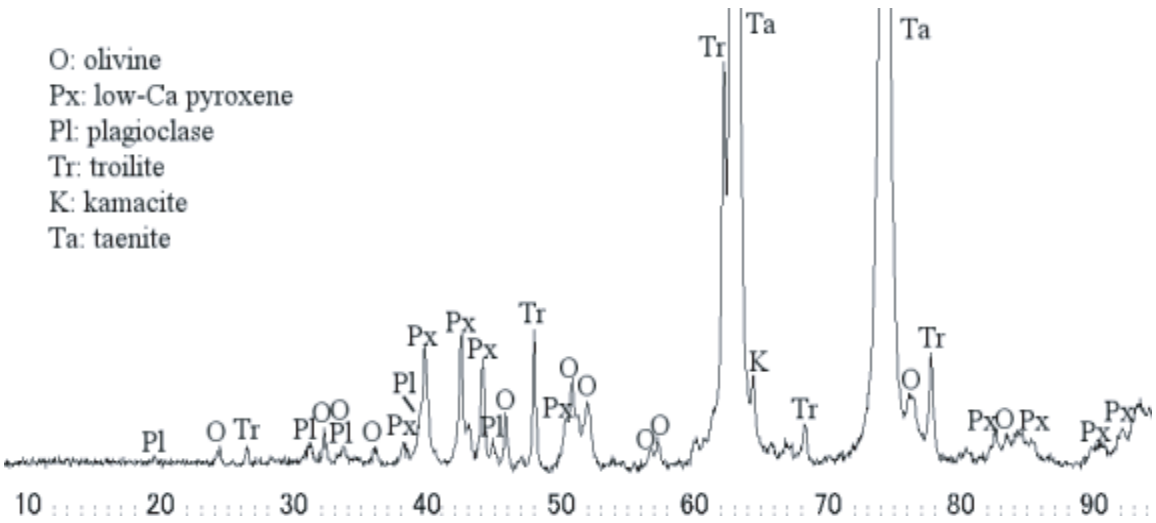

2AC18

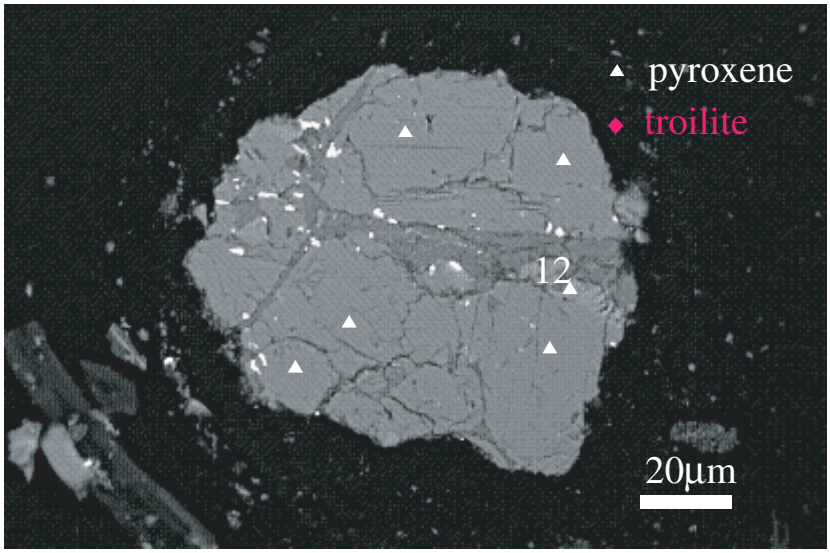

wt %	tr	kam
Ni		
Fe		
Mn		
Co		
Cr		
S		
P		
Total		

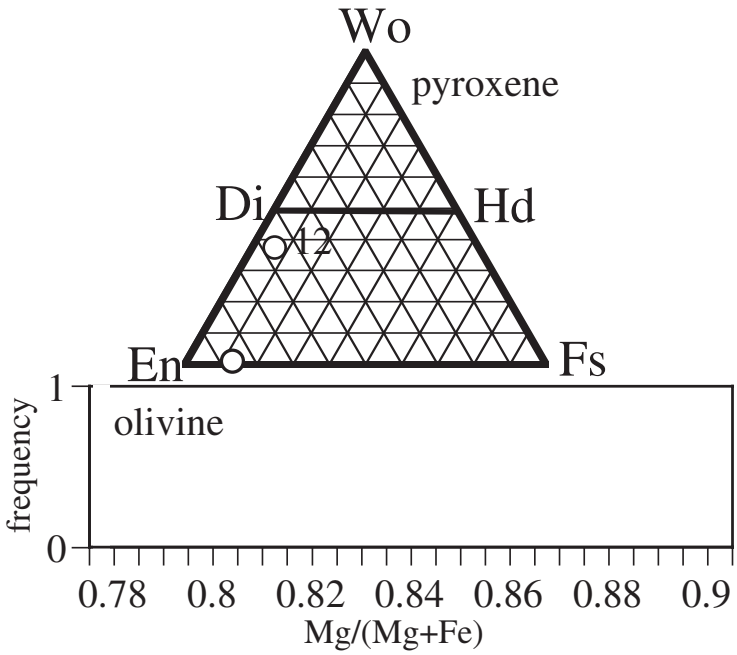

wt%	ol	low-Ca px	high-Ca px
SiO_2		56.4	53.0
TiO2		0.1	0.5
Al_2O_3		0.1	3.4
FeO		9.1	4.3
MnO		0.4	0.5
MgO		32.7	19.4
CaO		0.2	17.7
Na_2O		0.0	0.6
K_2O		0.0	0.0
Cr_2O_3		0.1	1.7
NiO		0.0	0.0
P_2O_5		0.0	0.0
SO_3		0.0	0.0
total		99.3	101.2

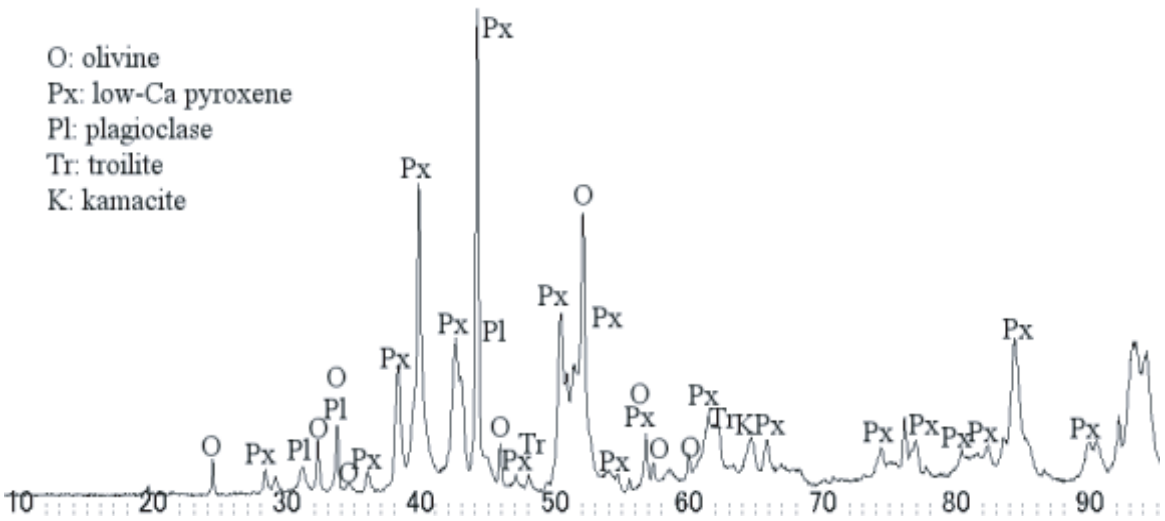

2AC19

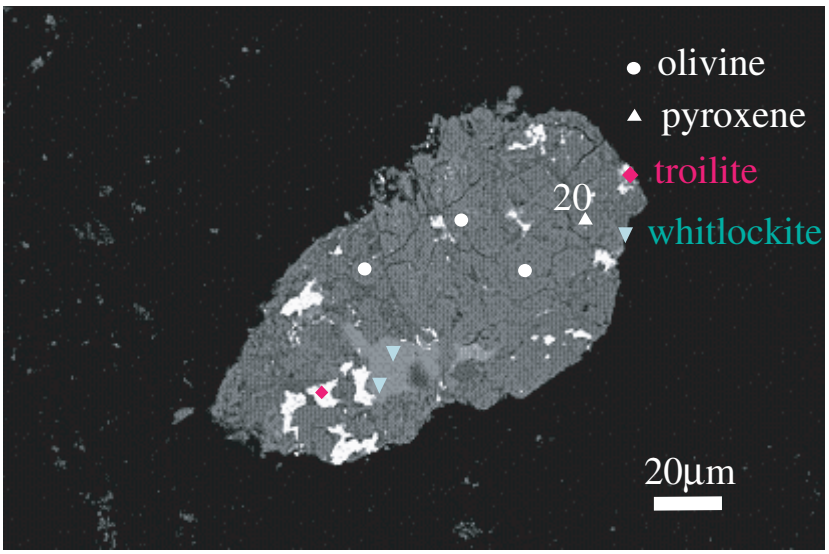

wt %	tr	kam
Ni	0.0	
Fe	63.6	
Mn	0.0	
Co	0.0	
Cr	0.1	
S	37.0	
P	0.0	
Total	100.6	

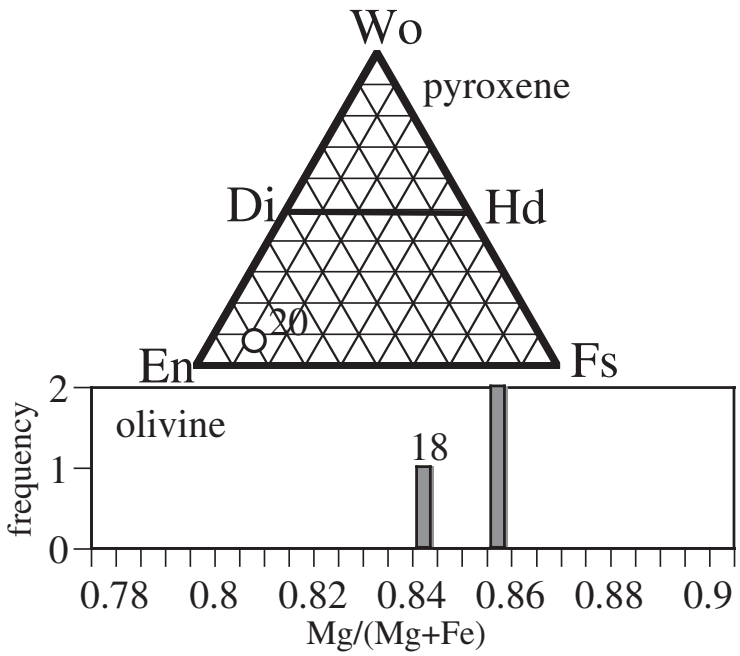

wt%	ol	low-Ca px	high-Ca px
SiO_2	39.8		57.0
TiO2	0.0		0.2
Al_2O_3	0.0		1.8
FeO	13.6		8.1
MnO	0.5		0.4
MgO	45.6		28.4
CaO	0.1		3.7
Na_2O	0.0		0.6
K_2O	0.0		0.0
Cr_2O_3	0.0		0.2
NiO	0.0		0.0
P_2O_5	0.1		0.0
SO_3	0.0		0.4
total	99.6		100.8

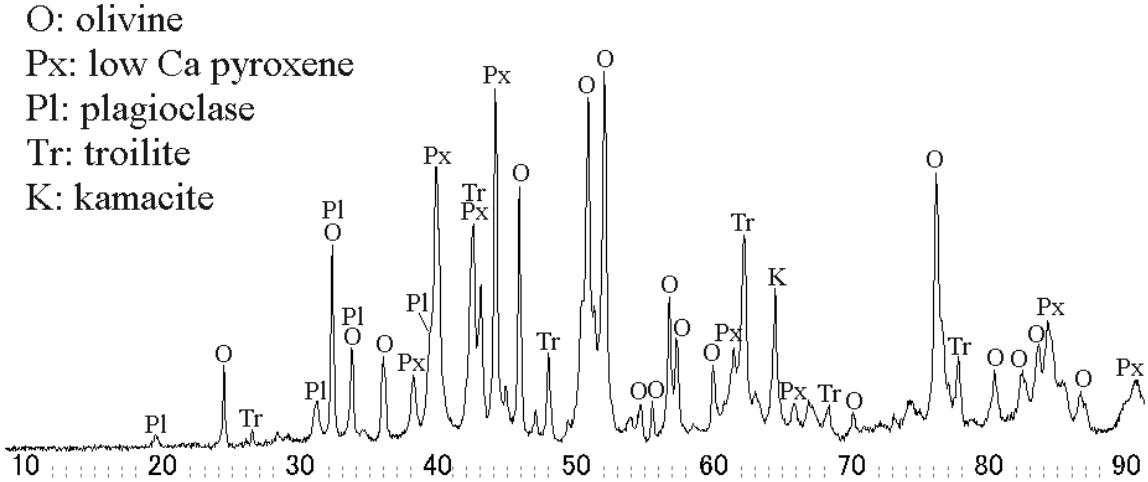

2AC20

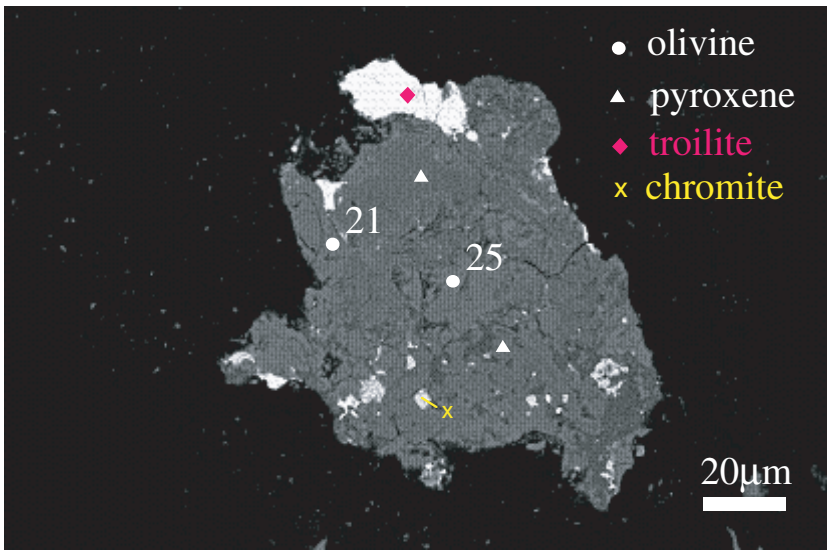

wt %	tr	kam
Ni	0.0	
Fe	63.1	
Mn	0.0	
Co	0.0	
Cr	0.0	
S	37.4	
P	0.0	
Total	100.6	

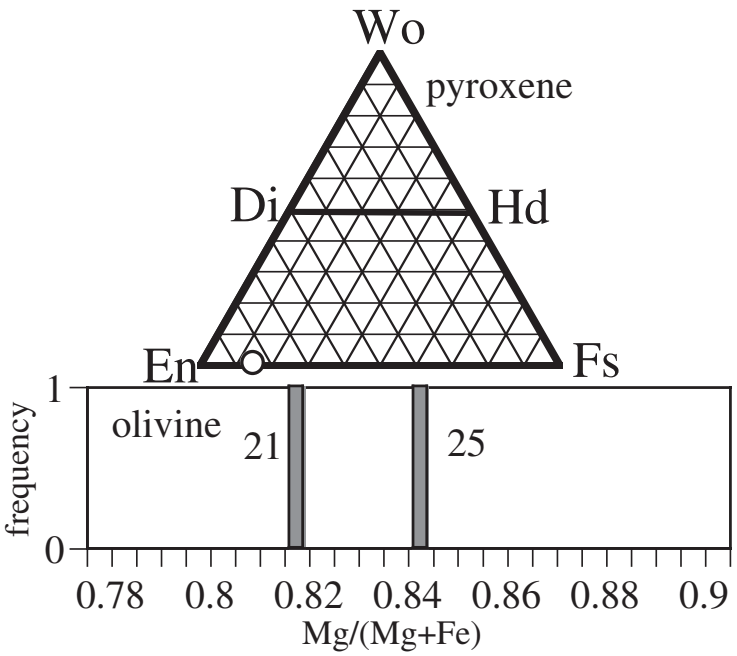

wt%	ol	low-Ca px	high-Ca px
SiO_2	39.4	56.2	
TiO2	0.0	0.1	
Al_2O_3	0.0	0.1	
FeO	15.0	9.8	
MnO	0.5	0.5	
MgO	45.4	32.6	
CaO	0.0	0.5	
Na_2O	0.1	0.0	
K_2O	0.0	0.0	
Cr_2O_3	0.0	0.2	
NiO	0.0	0.0	
P_2O_5	0.0	0.0	
SO_3	0.0	0.0	
total	100.4	100.0	

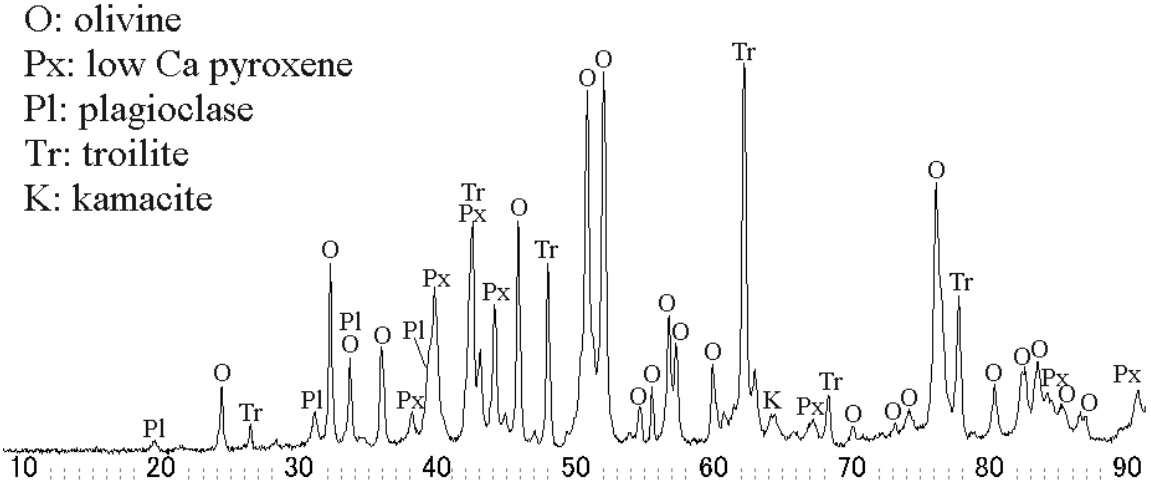

2AC21

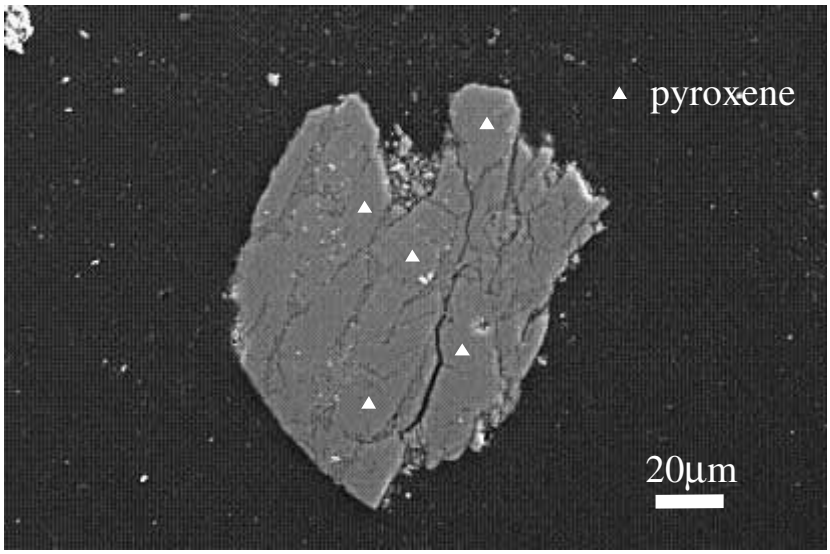

wt %	tr	kam
Ni		
Fe		
Mn		
Co		
Cr		
S		
P		
Total		

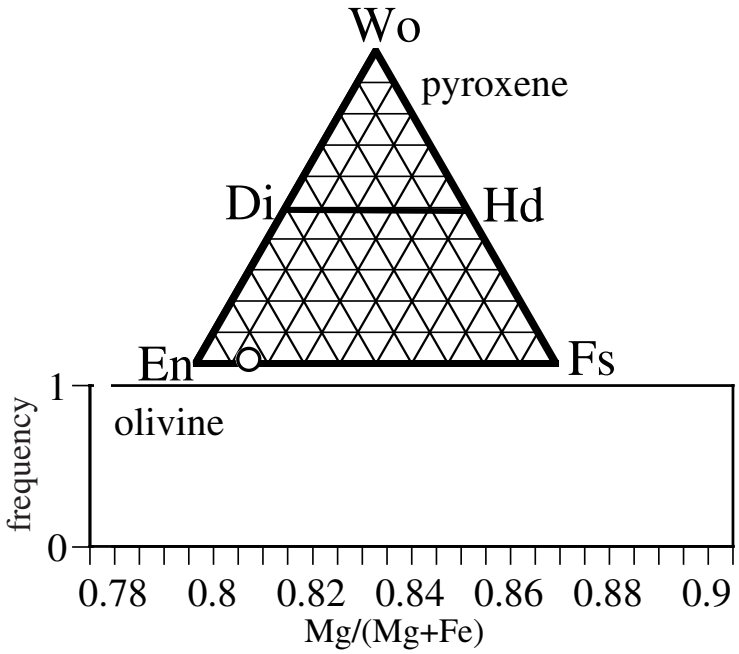

wt%	ol	low-Ca px	high-Ca px
SiO_2		56.4	
TiO2		0.1	
Al_2O_3		0.2	
FeO		9.6	
MnO		0.5	
MgO		32.1	
CaO		0.5	
Na_2O		0.0	
K_2O		0.0	
Cr_2O_3		0.1	
NiO		0.0	
P_2O_5		0.1	
SO_3		0.0	
total		99.6	

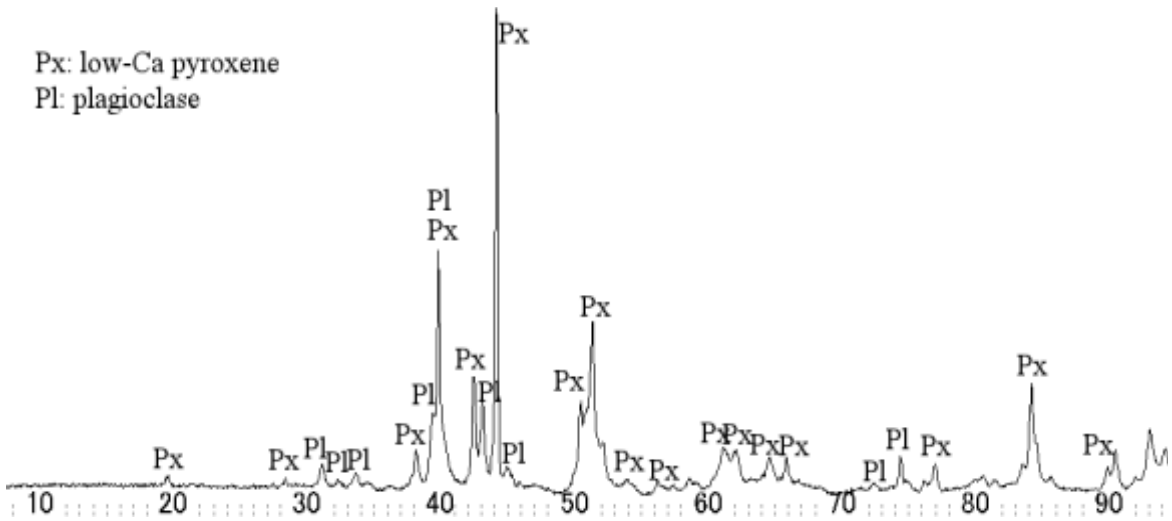

2AC22

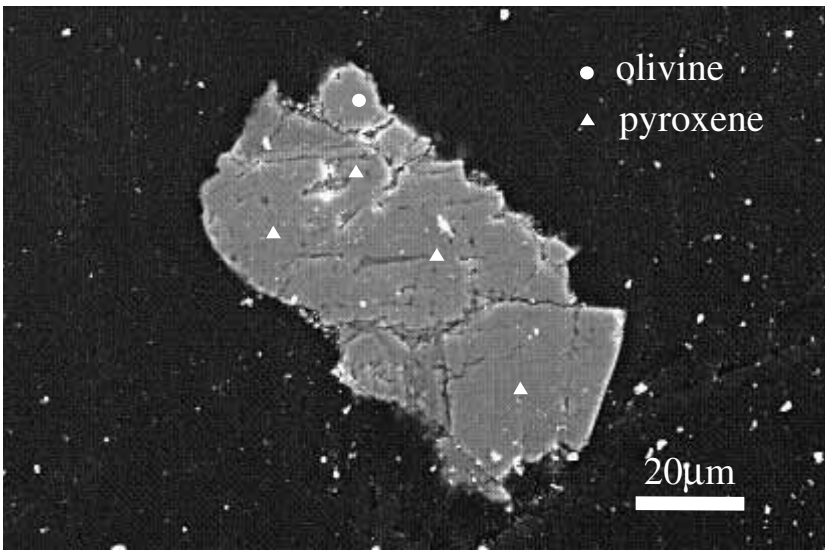

wt %	tr	kam
Ni		
Fe		
Mn		
Co		
Cr		
S		
P		
Total		

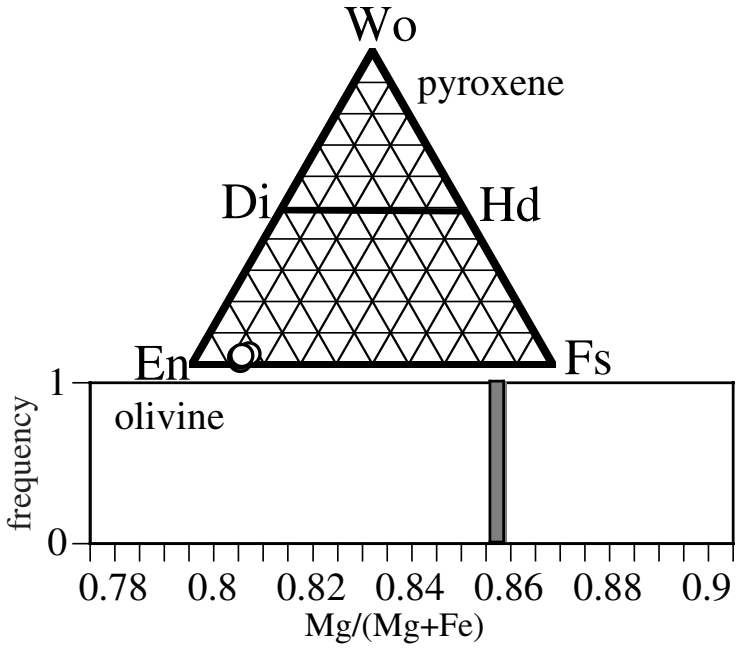

wt%	ol	low-Ca px	high-Ca px
SiO_2	39.5	56.4	
TiO2	0.0	0.1	
Al_2O_3	0.0	0.6	
FeO	13.6	8.7	
MnO	0.5	0.5	
MgO	45.2	32.2	
CaO	0.0	0.9	
Na_2O	0.0	0.0	
K_2O	0.0	0.0	
Cr_2O_3	0.0	0.4	
NiO	0.0	0.0	
P_2O_5	0.0	0.0	
SO_3	0.0	0.0	
total	99.0	99.8	

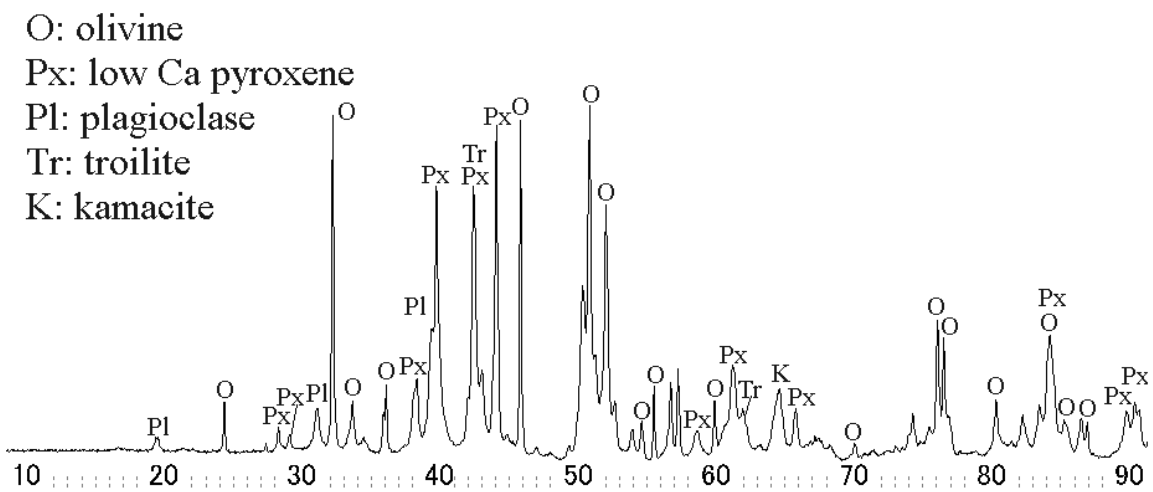

2AC23

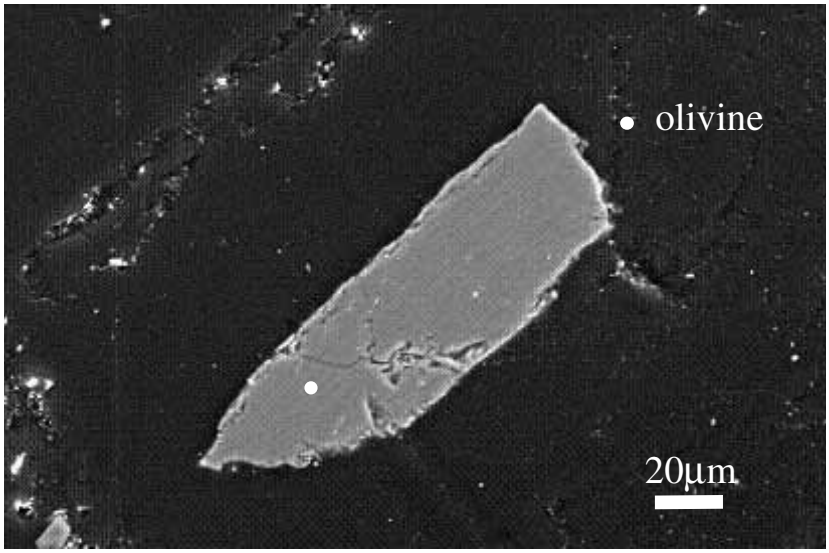

wt %	tr	kam
Ni		
Fe		
Mn		
Co		
Cr		
S		
P		
Total		

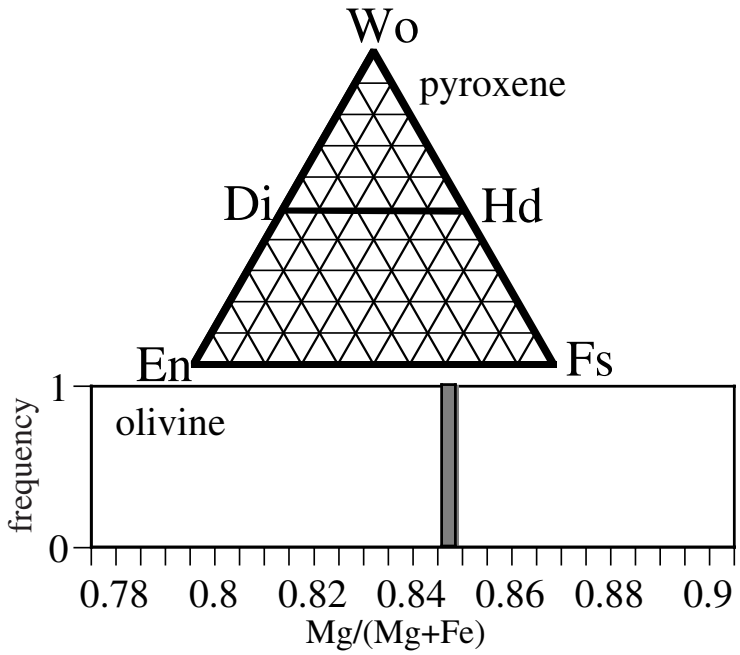

wt%	ol	low-Ca px	high-Ca px
SiO_2	41.3		
TiO2	0.0		
Al_2O_3	0.0		
FeO	14.2		
MnO	0.6		
MgO	44.4		
CaO	0.1		
Na_2O	0.0		
K_2O	0.0		
Cr_2O_3	0.0		
NiO	0.0		
P_2O_5	0.0		
SO_3	0.0		
total	100.6		

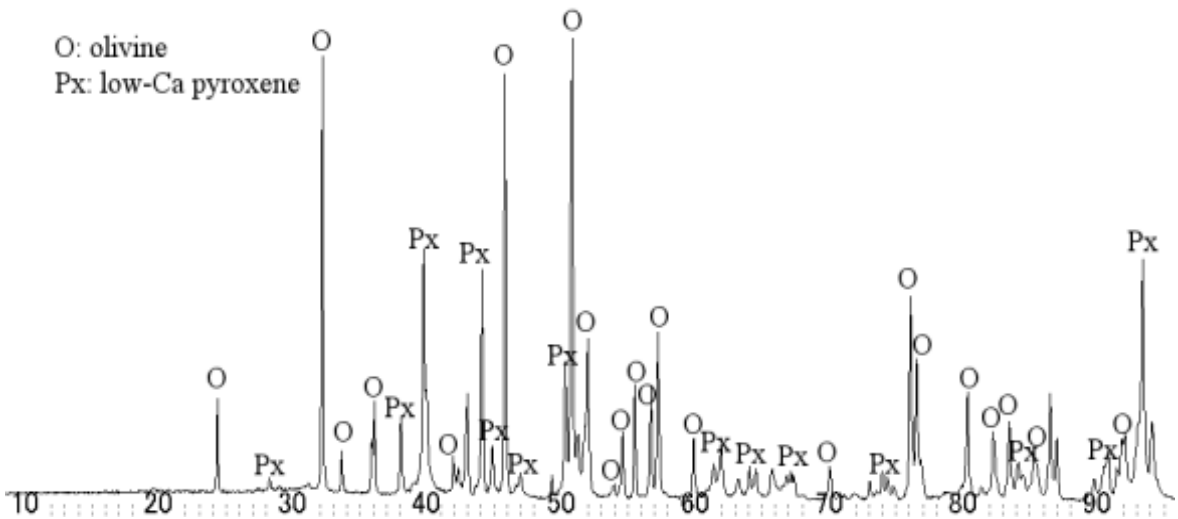

2AC24

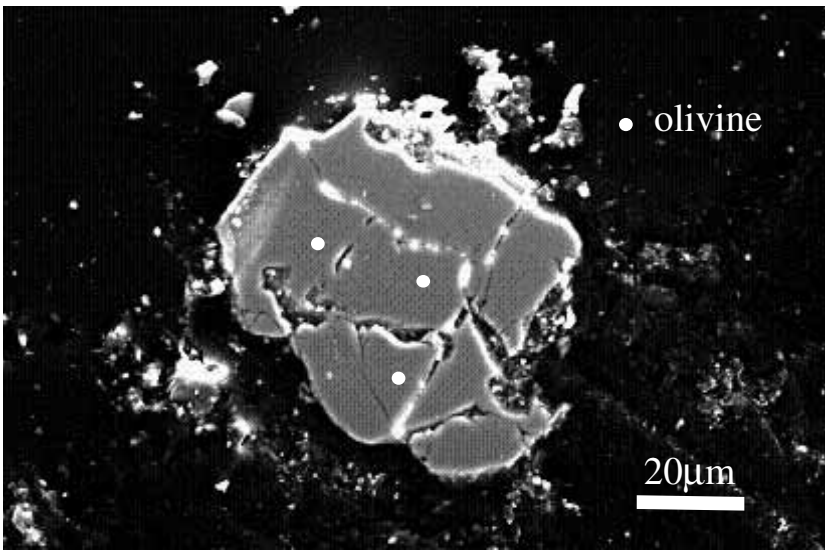

wt %	tr	kam
Ni		
Fe		
Mn		
Co		
Cr		
S		
P		
Total		

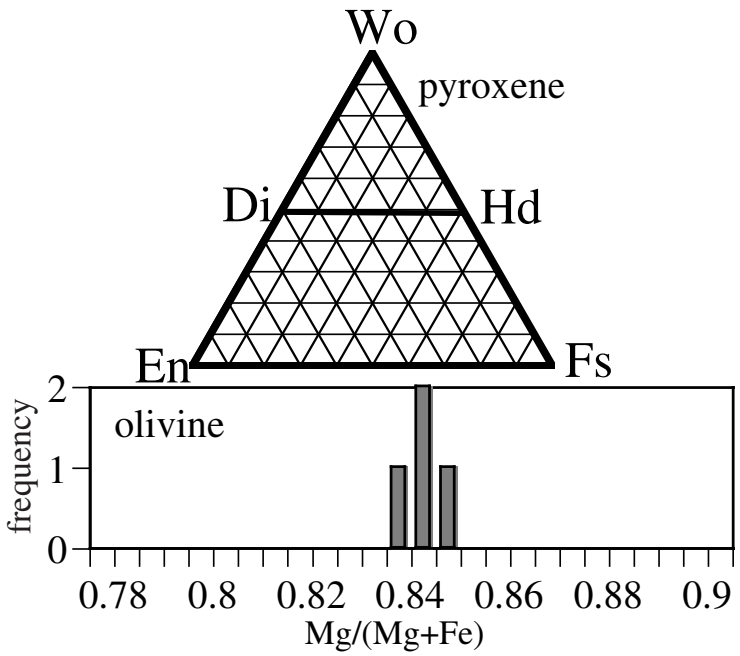

wt%	ol	low-Ca px	high-Ca px
SiO_2	39.7		
TiO2	0.0		
Al_2O_3	0.0		
FeO	14.9		
MnO	0.5		
MgO	45.2		
CaO	0.0		
Na_2O	0.0		
K_2O	0.0		
Cr_2O_3	0.0		
NiO	0.0		
P_2O_5	0.0		
SO_3	0.0		
total	100.4		

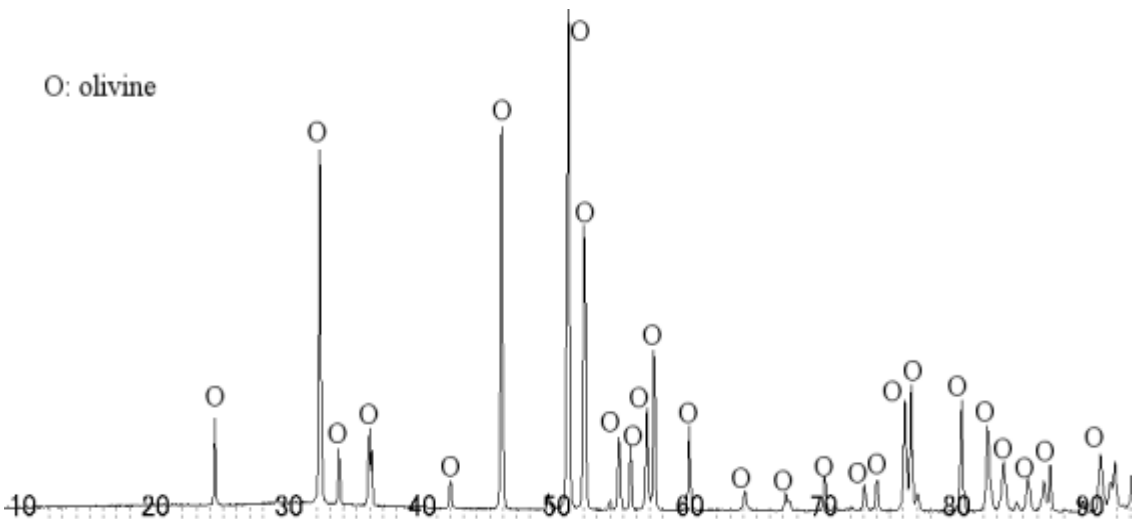

2AC25

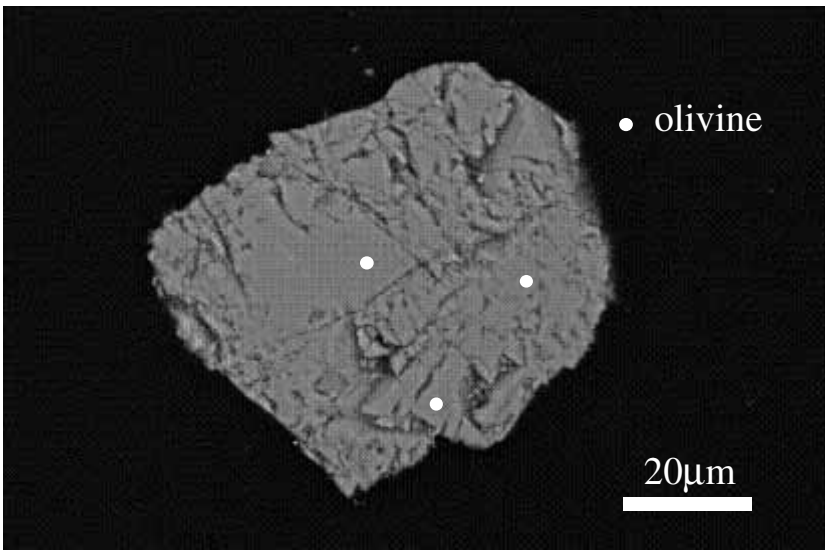

wt %	tr	kam
Ni		
Fe		
Mn		
Co		
Cr		
S		
P		
Total		

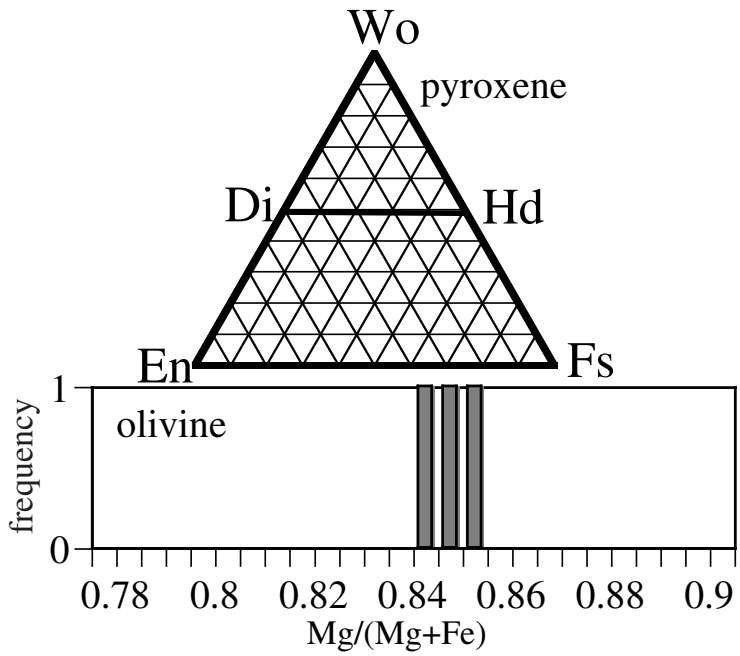

wt%	ol	low-Ca px	high-Ca px
SiO_2	39.5		
TiO2	0.0		
Al_2O_3	0.0		
FeO	14.7		
MnO	0.4		
MgO	44.9		
CaO	0.1		
Na_2O	0.0		
K_2O	0.0		
Cr_2O_3	0.0		
NiO	0.0		
P_2O_5	0.1		
SO_3	0.0		
total	99.7		

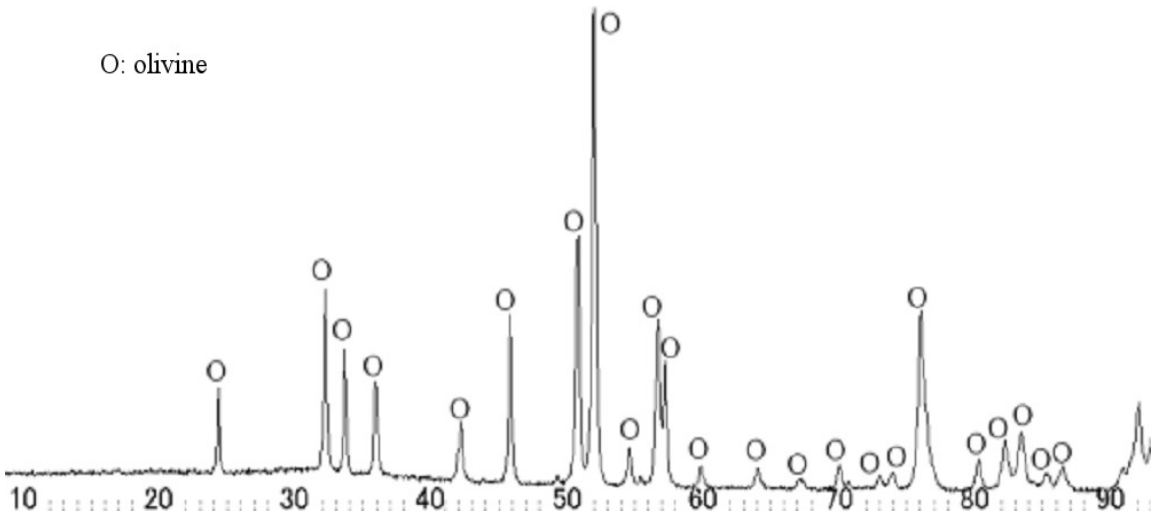

2AC26

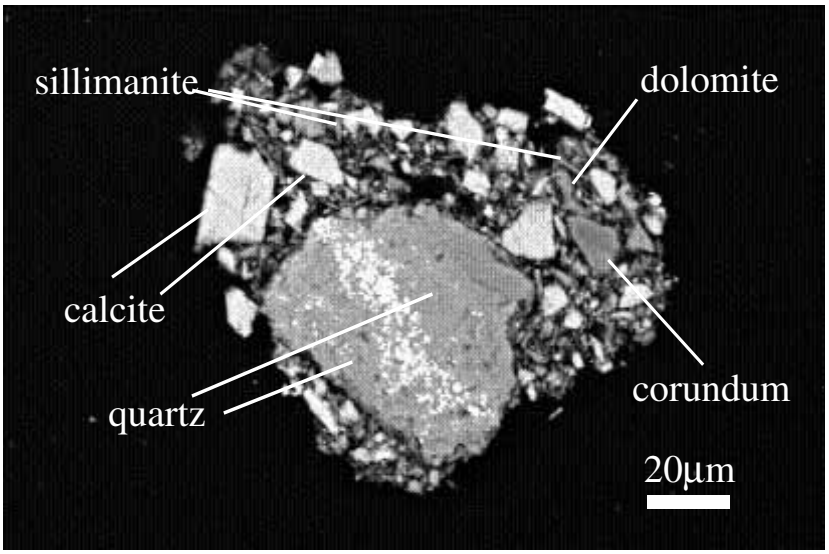

wt %	tr	kam
Ni		
Fe		
Mn		
Co		
Cr		
S		
P		
Total		

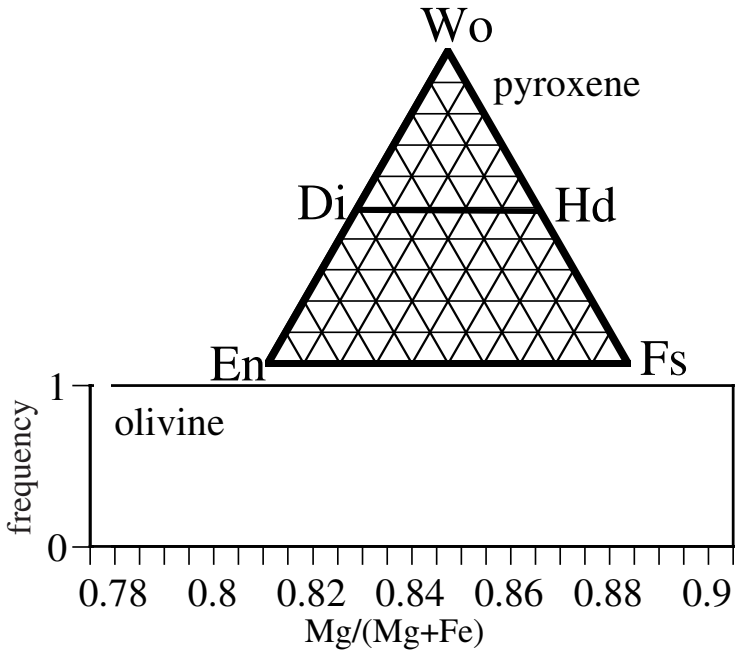

wt%	ol	low-Ca px	high-Ca px
SiO_2			
TiO2			
Al_2O_3			
FeO			
MnO			
MgO			
CaO			
Na_2O			
K_2O			
Cr_2O_3			
NiO			
P_2O_5			
SO_3			
total			

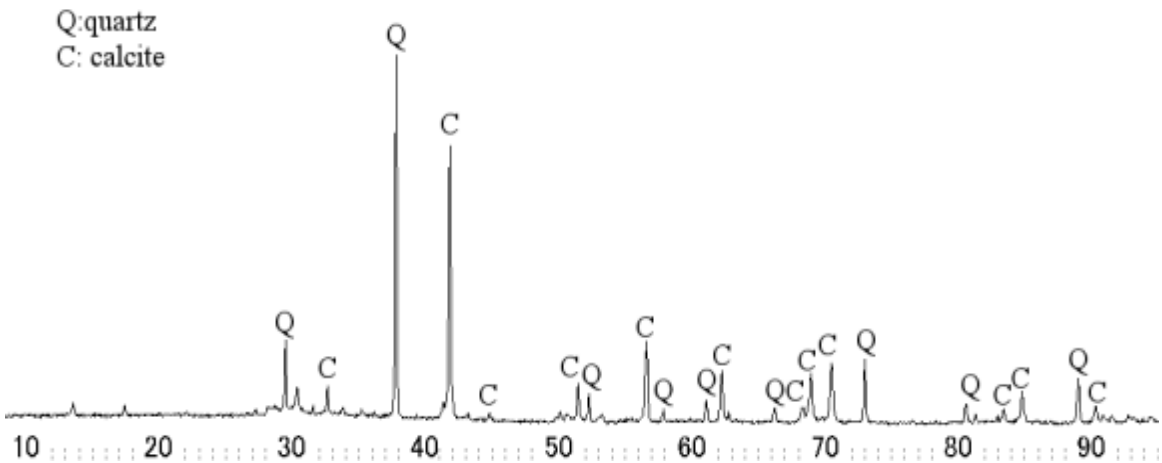

2AC27

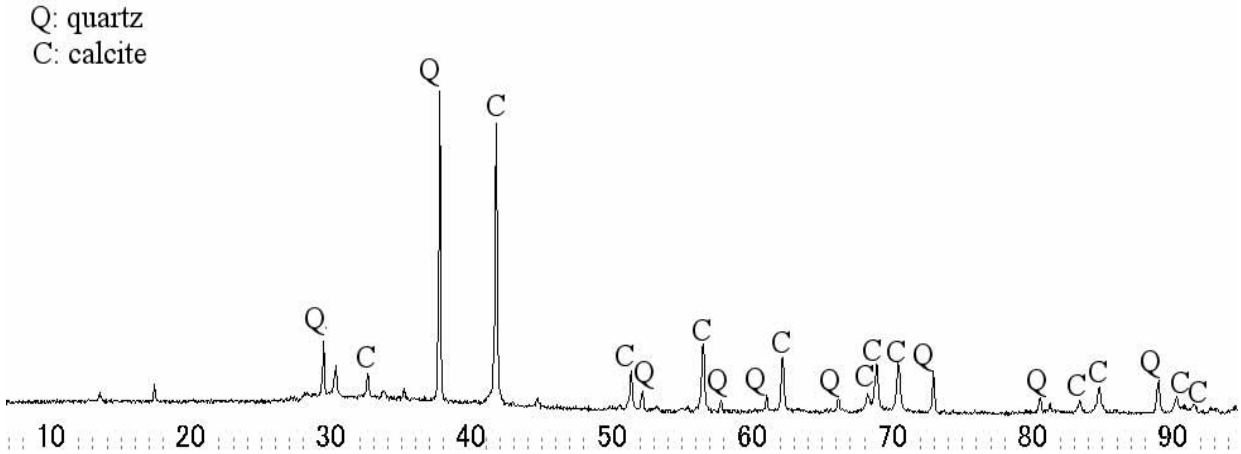

2AC28

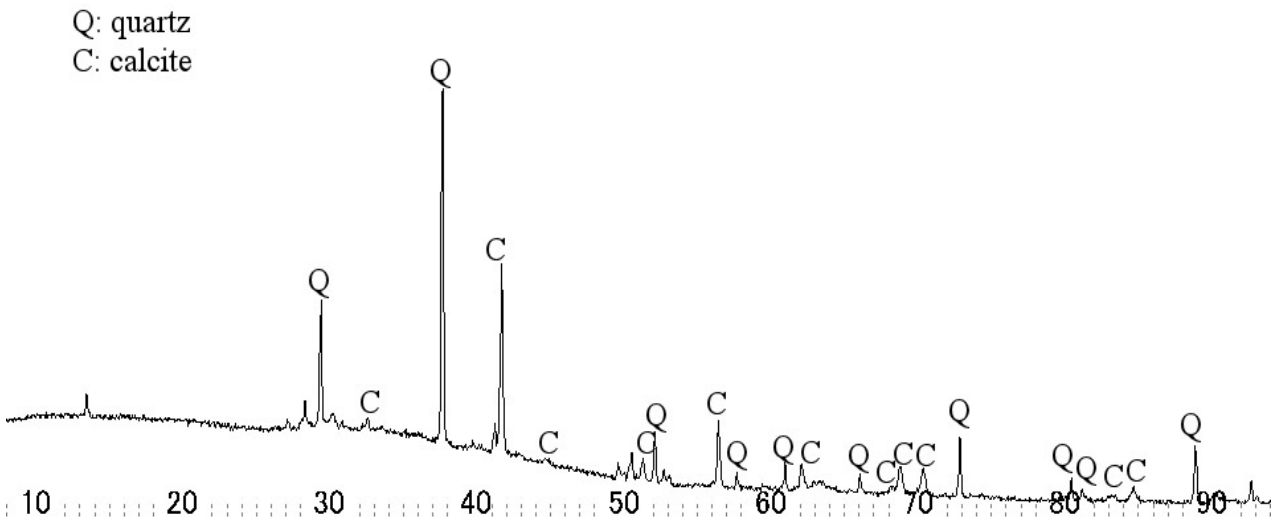

2AF1

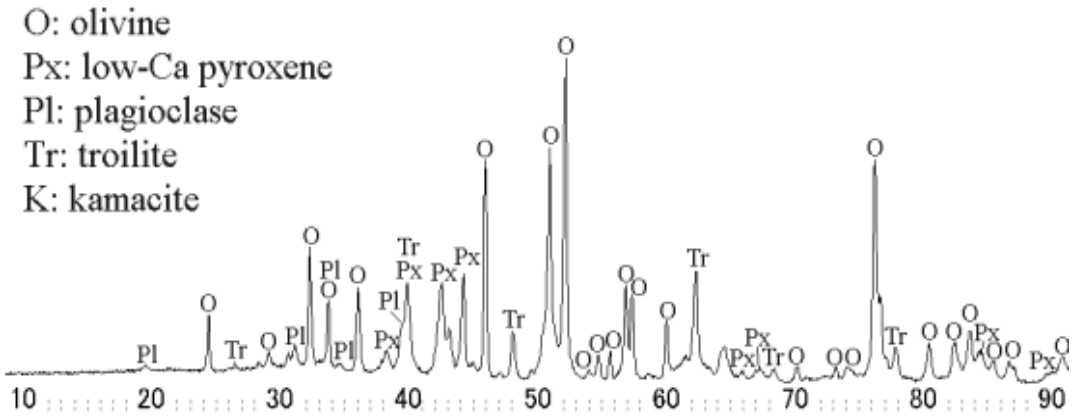

2AF2

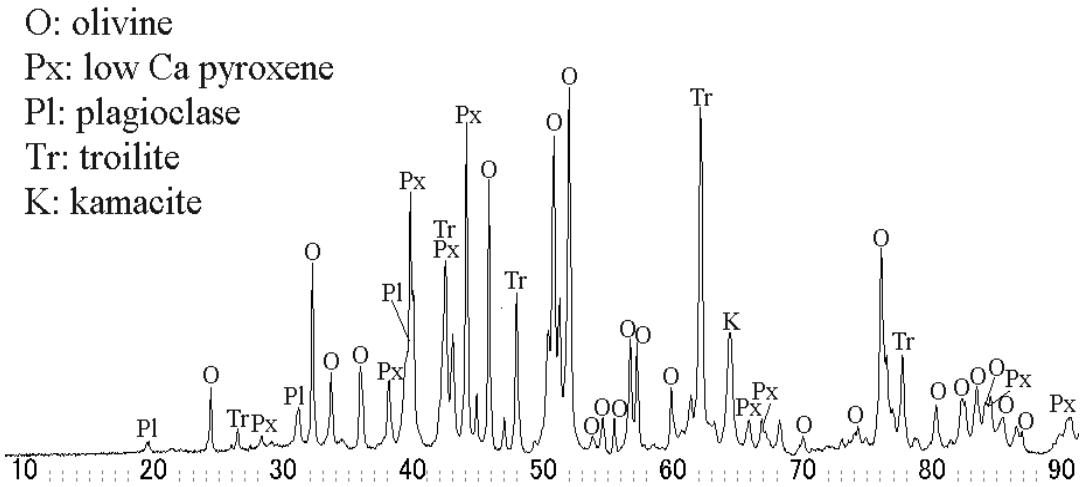

2AF3

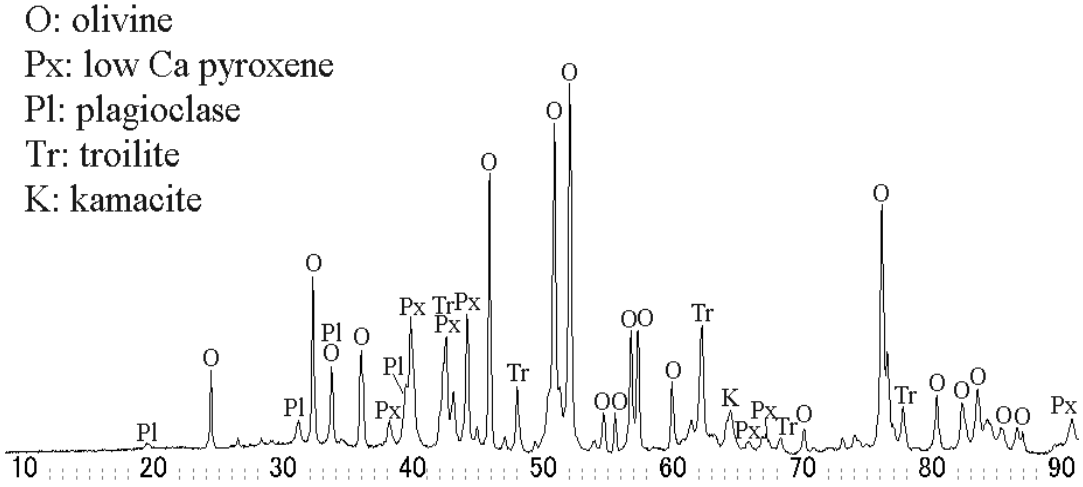

SEM and EPMA analyses did not performed on these samples.

2AF4

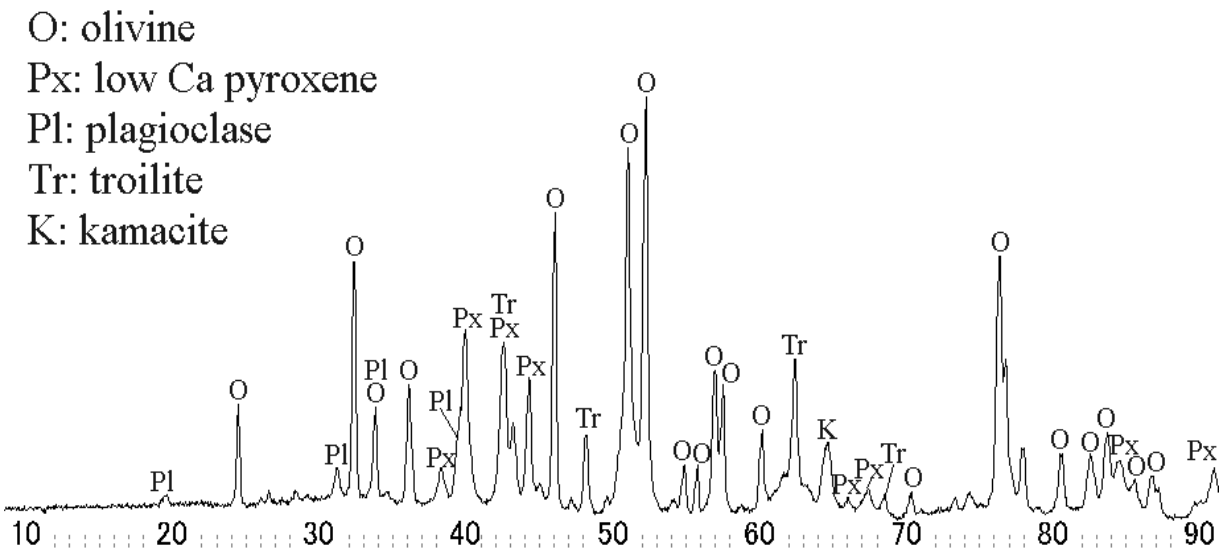

2AF5

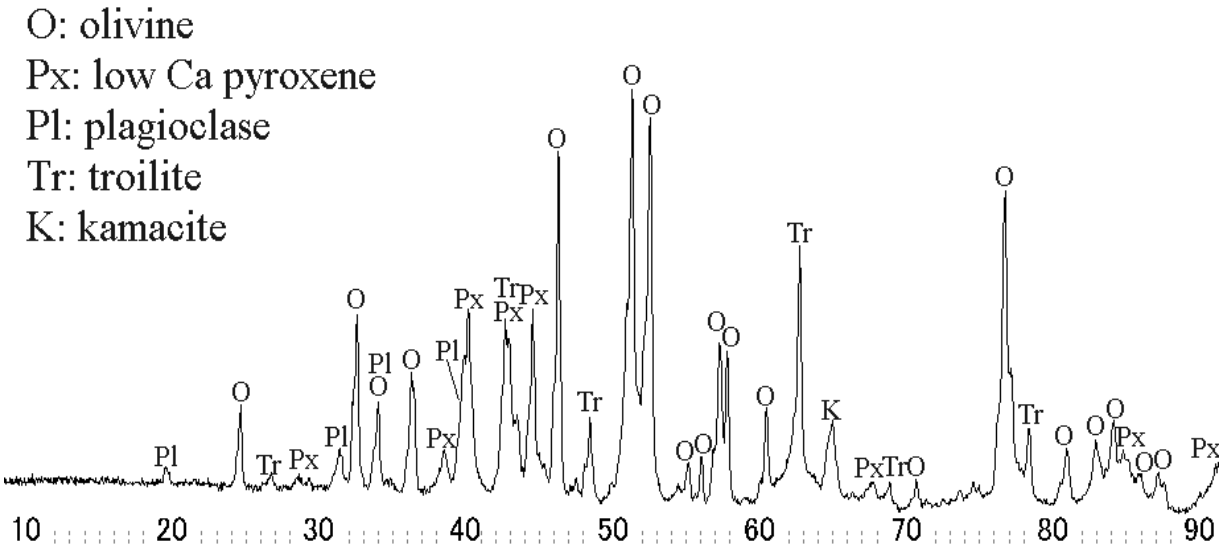

SEM and EPMA analyses did not performed on these samples.

2AF6

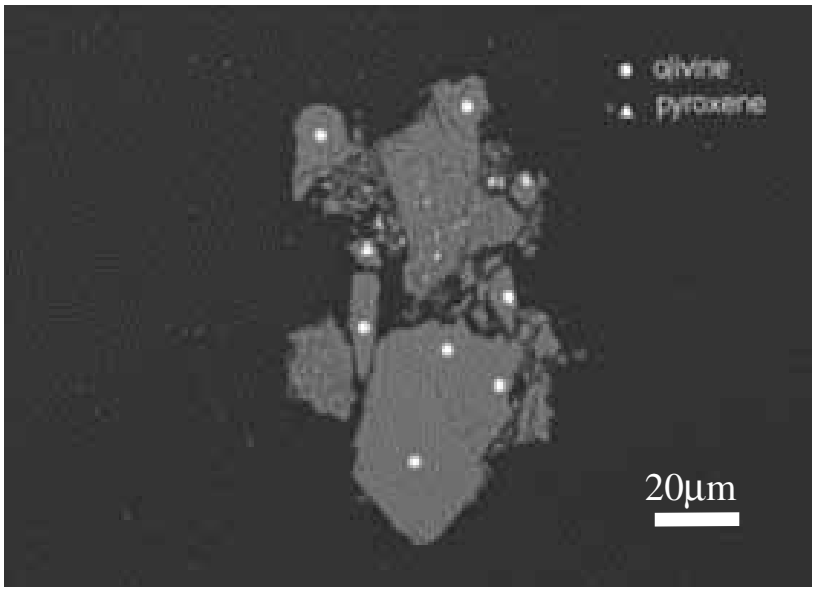

wt %	tr	kam
Ni		
Fe		
Mn		
Co		
Cr		
S		
P		
Total		

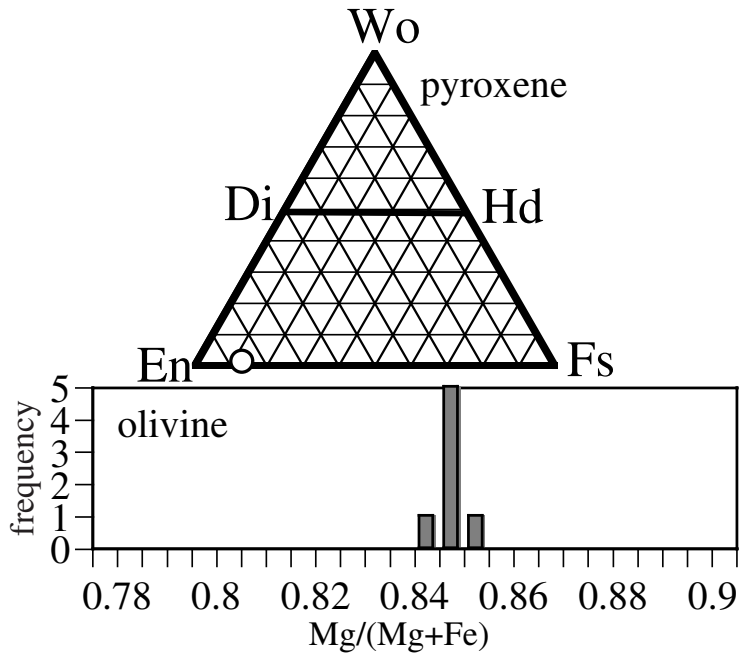

wt%	ol	low-Ca px	high-Ca px
SiO_2	39.4	56.2	
TiO_2	0.0	0.1	
Al_2O_3	0.0	0.2	
FeO	15.1	8.7	
MnO	0.4	0.6	
MgO	45.3	32.2	
CaO	0.1	0.5	
Na_2O	0.0	0.2	
K_2O	0.0	0.0	
Cr_2O_3	0.1	0.2	
NiO	0.1	0.0	
P_2O_5	0.1	0.0	
SO_3	0.0	0.1	
total	100.5	99.0	

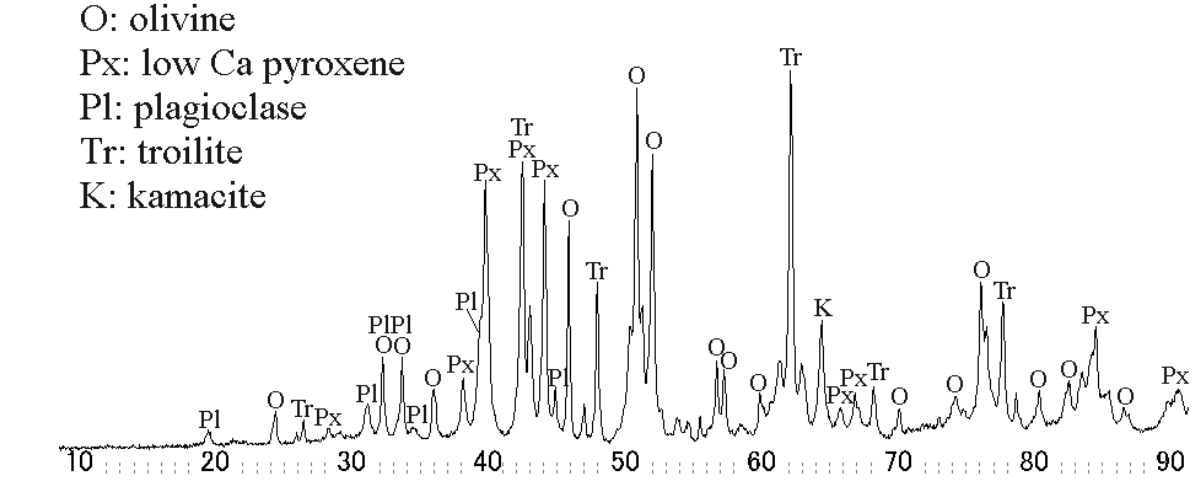

2AF7

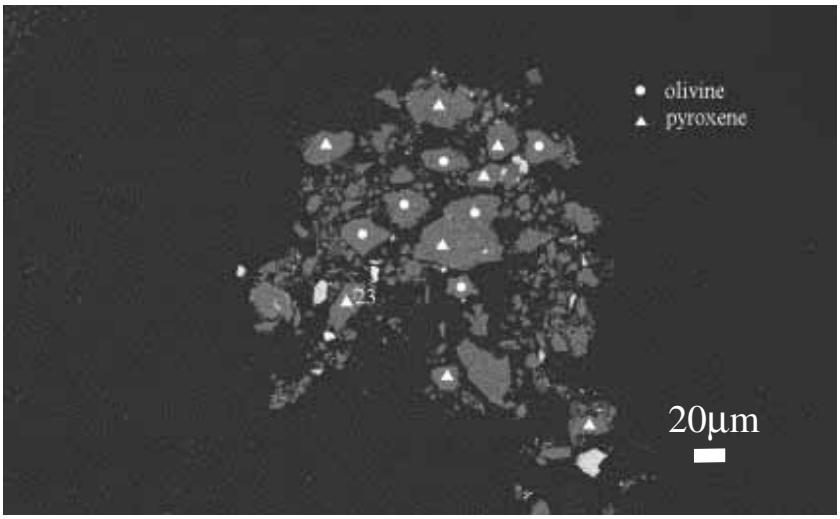

wt %	tr	kam
Ni		
Fe		
Mn		
Co		
Cr		
S		
P		
Total		

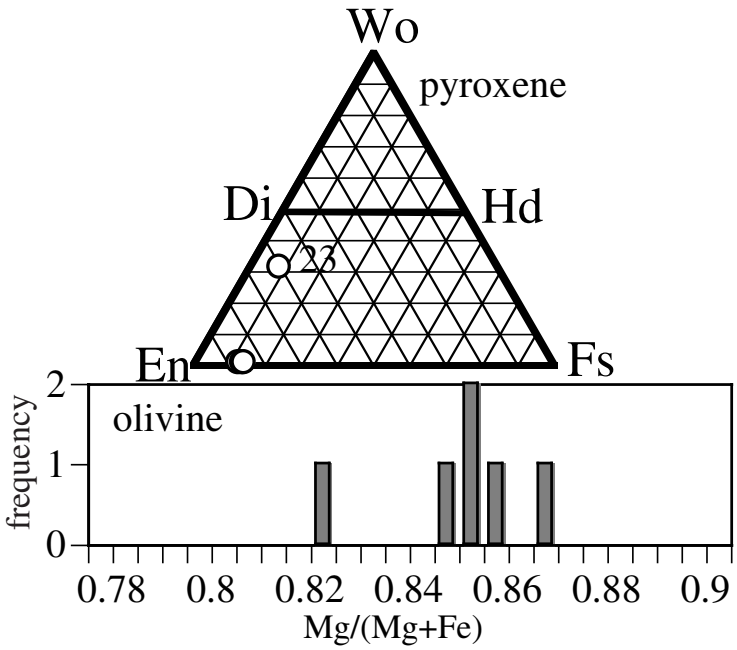

wt%	ol	low-Ca px	high-Ca px
SiO_2	39.6	56.3	53.6
TiO_2	0.0	0.1	0.2
Al_2O_3	0.0	0.3	1.2
FeO	14.1	9.7	5.3
MnO	0.4	0.5	0.3
MgO	45.7	32.5	20.9
CaO	0.1	0.7	15.2
Na_2O	0.1	0.0	0.6
K_2O	0.0	0.0	0.0
Cr_2O_3	0.0	0.1	0.6
NiO	0.0	0.0	0.0
P_2O_5	0.1	0.0	0.0
SO_3	0.0	0.0	1.3
total	100.0	100.3	99.2

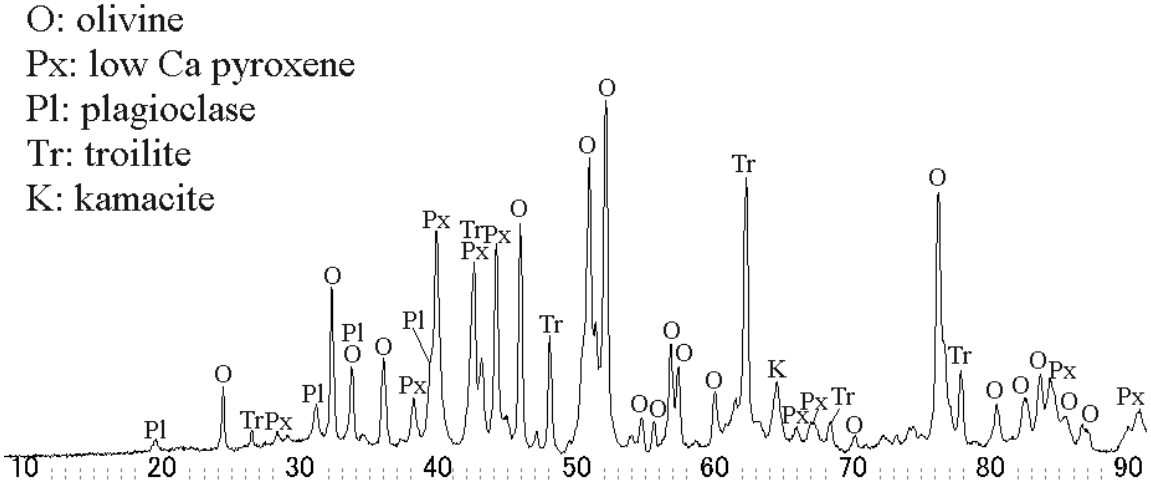

2AF8

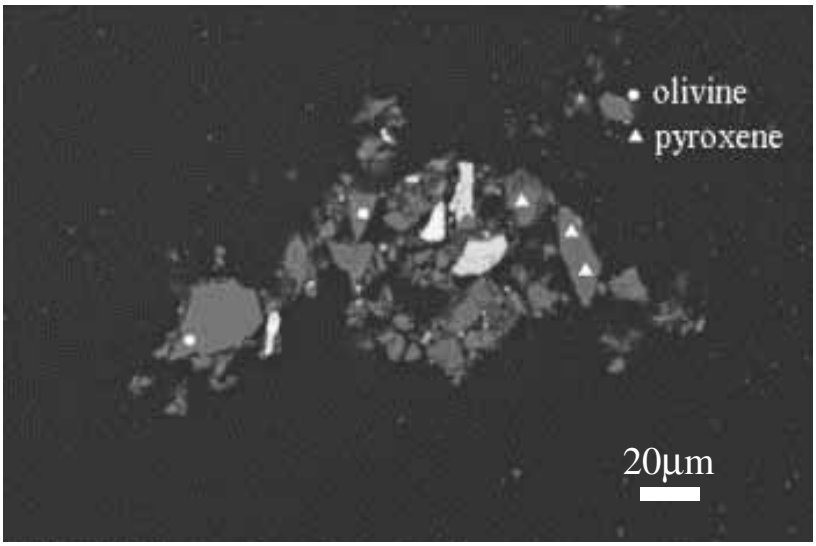

wt %	tr	kam
Ni		
Fe		
Mn		
Co		
Cr		
S		
P		
Total		

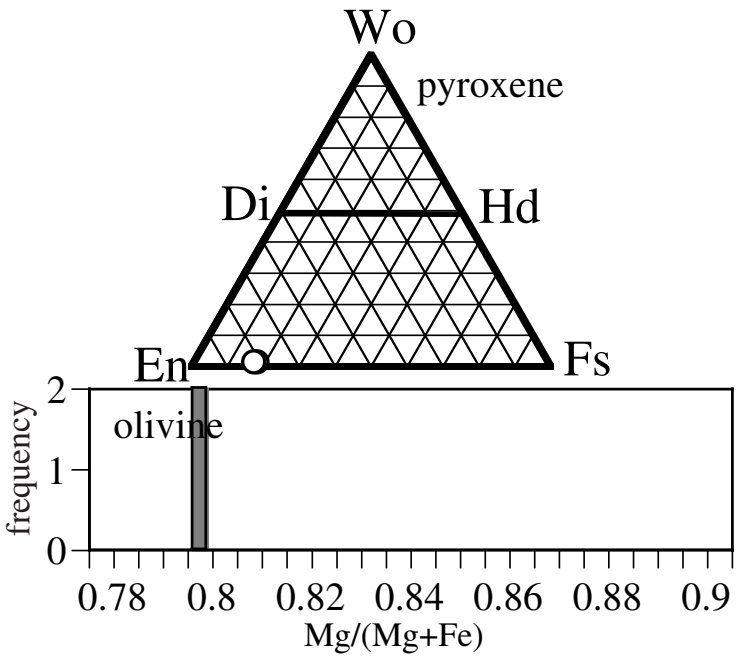

wt%	ol	low-Ca px	high-Ca px
SiO_2	40.7	57.2	
TiO_2	0.0	0.2	
Al_2O_3	0.0	0.3	
FeO	18.0	11.5	
MnO	0.6	0.8	
MgO	40.2	28.4	
CaO	0.0	0.5	
Na_2O	0.1	0.0	
K_2O	0.0	0.0	
Cr_2O_3	0.1	0.2	
NiO	0.0	0.0	
P_2O_5	0.0	0.0	
SO_3	0.0	0.0	
total	99.7	99.0	

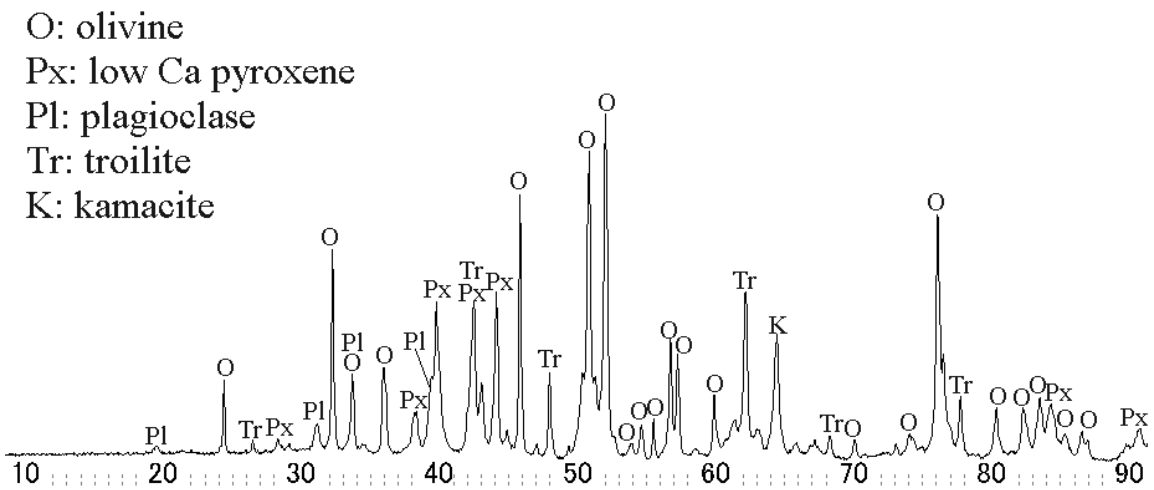

2AF9

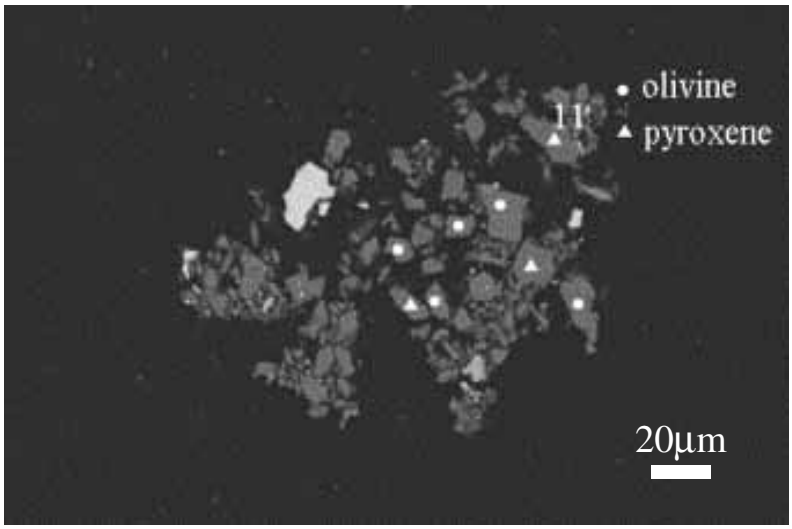

wt %	tr	kam
Ni		
Fe		
Mn		
Co		
Cr		
S		
P		
Total		

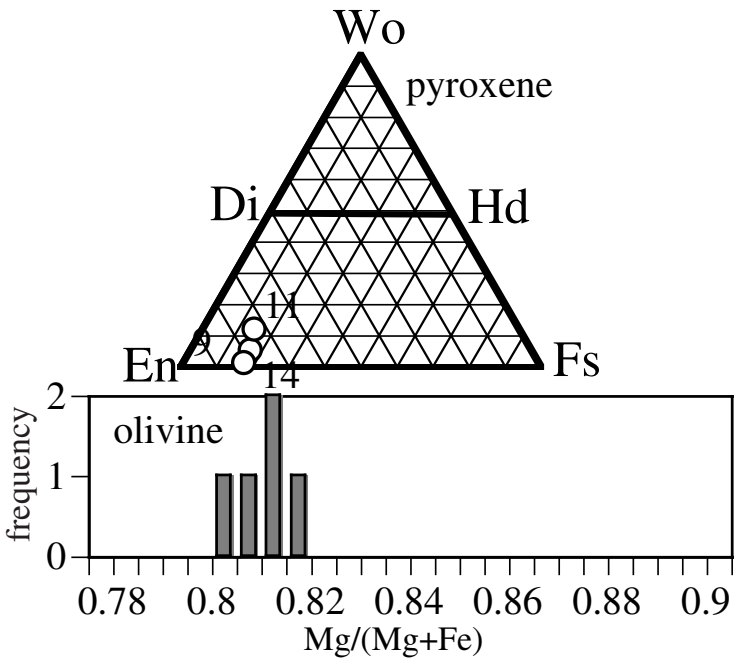

wt%	ol	low-Ca px	high-Ca px
SiO_2	41.5	57.0	59.3
TiO_2	0.0	0.1	0.1
Al_2O_3	0.0	0.5	1.1
FeO	16.7	10.8	9.1
MnO	0.6	0.5	0.5
MgO	41.4	27.4	24.5
CaO	0.1	2.4	5.5
Na_2O	0.2	0.1	0.5
K_2O	0.0	0.0	0.0
Cr_2O_3	0.0	0.2	0.3
NiO	0.0	0.0	0.0
P_2O_5	0.0	0.1	0.1
SO_3	0.0	0.0	0.1
total	100.6	99.1	101.1

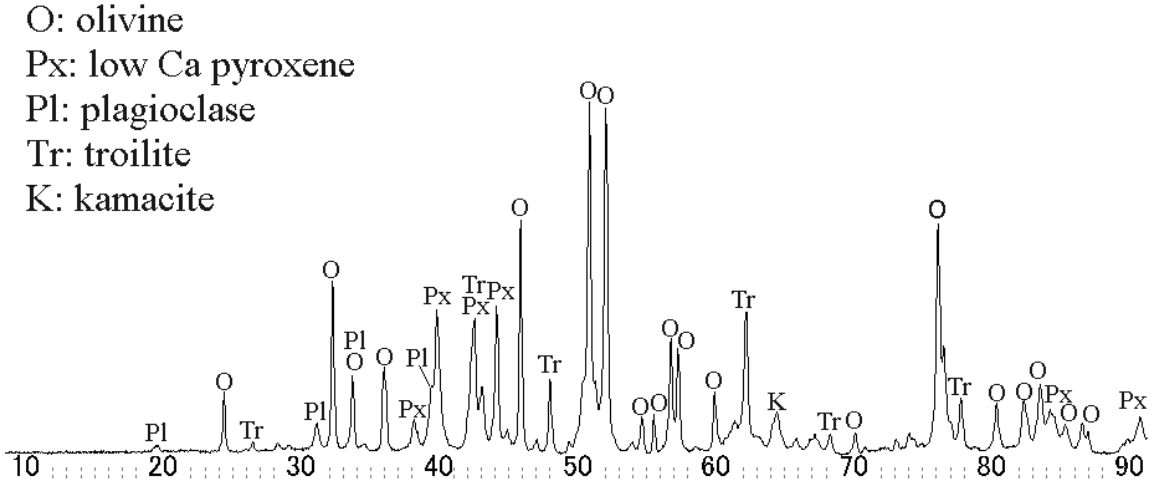

2AF10

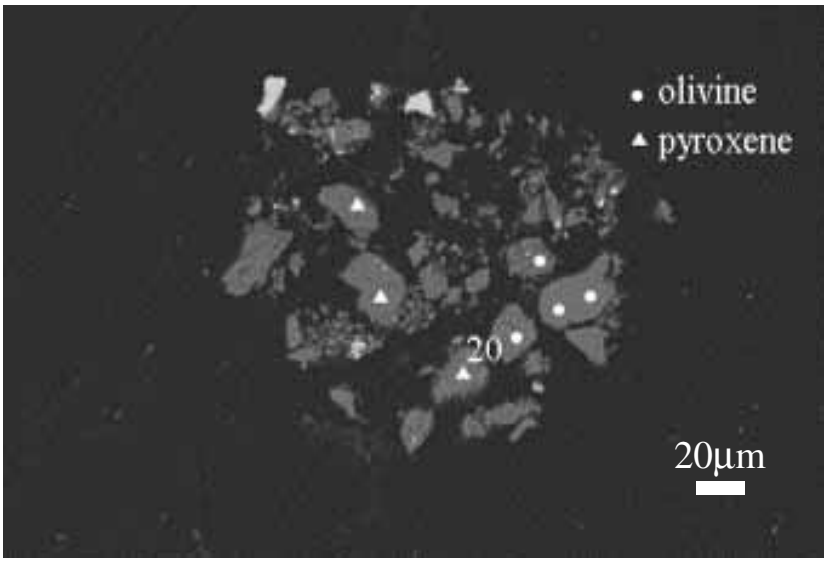

wt %	tr	kam
Ni		
Fe		
Mn		
Co		
Cr		
S		
P		
Total		

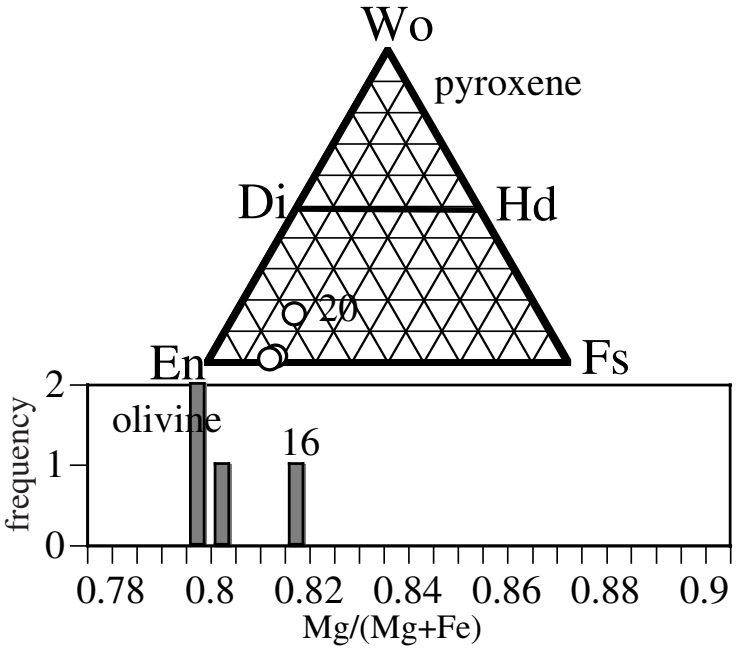

wt%	ol	low-Ca px	high-Ca px
SiO_2	41.6	56.9	56.4
TiO_2	0.0	0.1	0.2
Al_2O_3	0.0	0.2	0.9
FeO	16.5	11.5	10.6
MnO	0.5	0.6	0.6
MgO	41.0	28.7	23.7
CaO	0.0	0.8	7.3
Na_2O	0.0	0.2	0.3
K_2O	0.0	0.0	0.0
Cr_2O_3	0.0	0.2	1.0
NiO	0.0	0.0	0.0
P_2O_5	0.0	0.0	0.0
SO_3	0.0	0.0	0.0
total	99.7	99.3	100.8

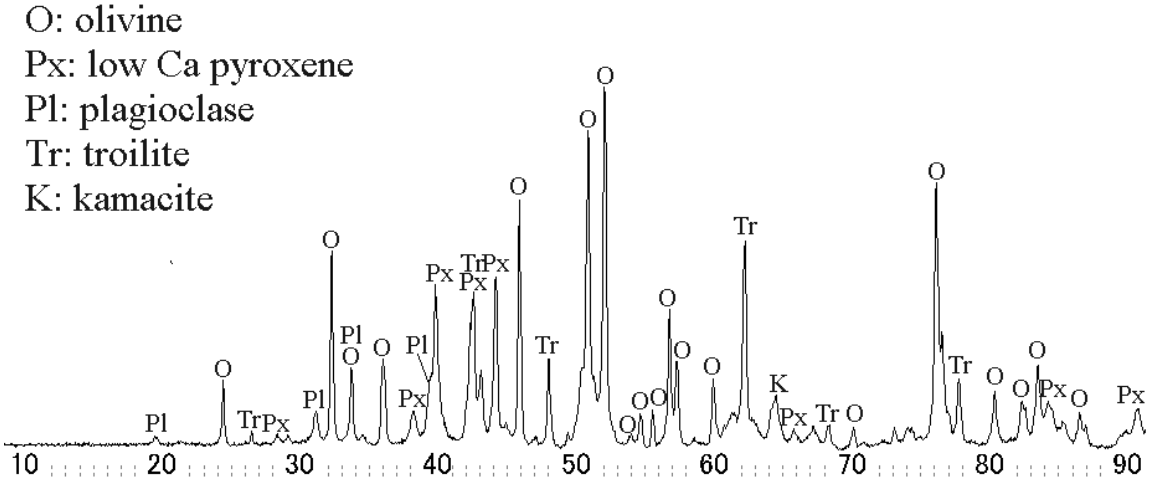

2BC1

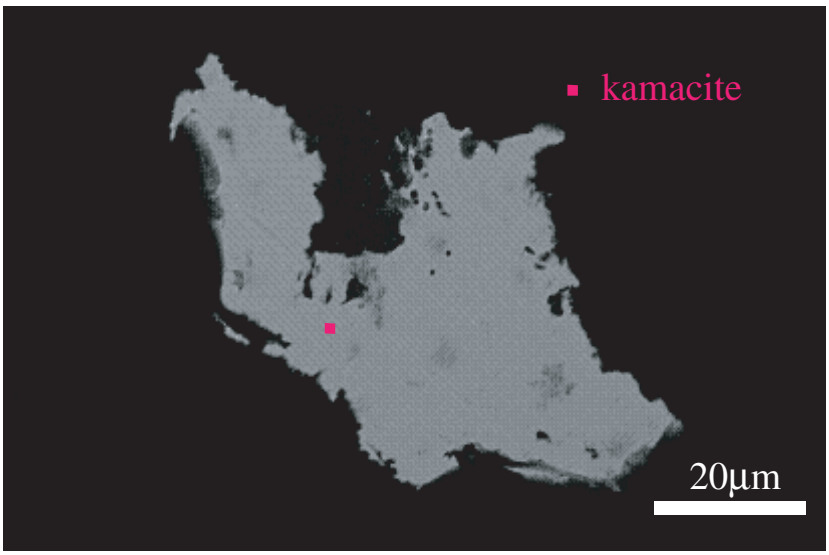

wt %	tr	kam
Ni		5.2
Fe		94.4
Mn		0.0
Co		0.4
Cr		0.0
S		0.0
P		0.0
Total		100.1

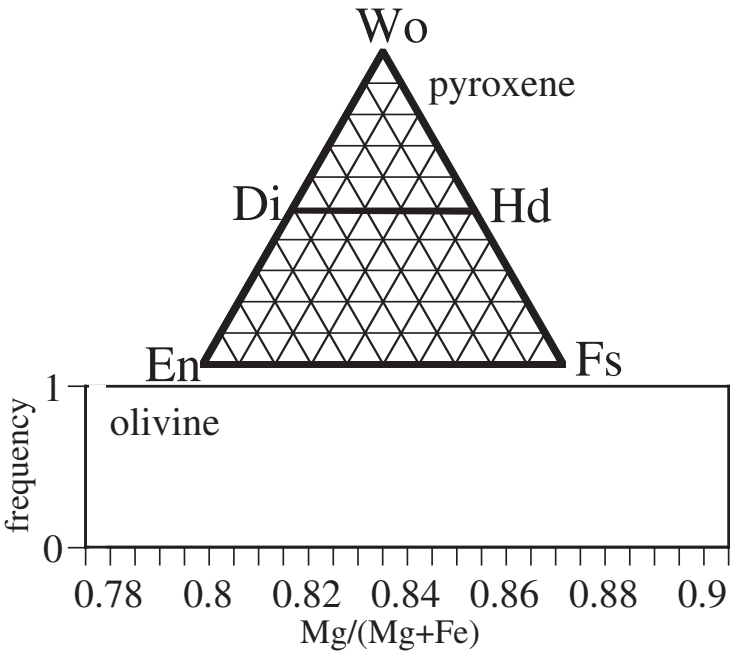

wt%	ol	low-Ca px	high-Ca px
SiO_2			
TiO2			
Al_2O_3			
FeO			
MnO			
MgO			
CaO			
Na_2O			
K_2O			
Cr_2O_3			
NiO			
P_2O_5			
SO_3			
total			

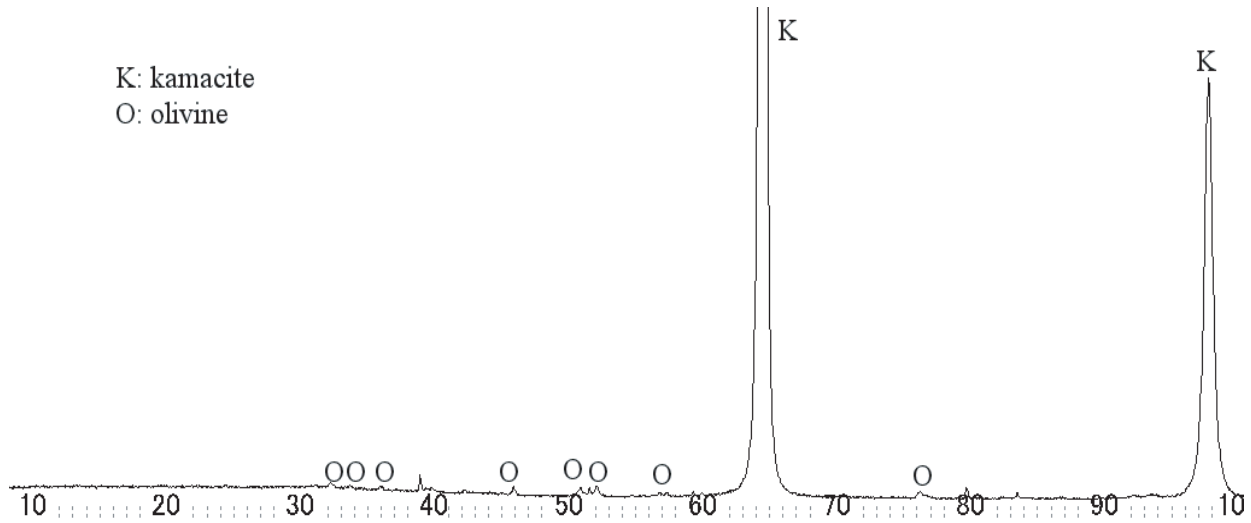

2BC2

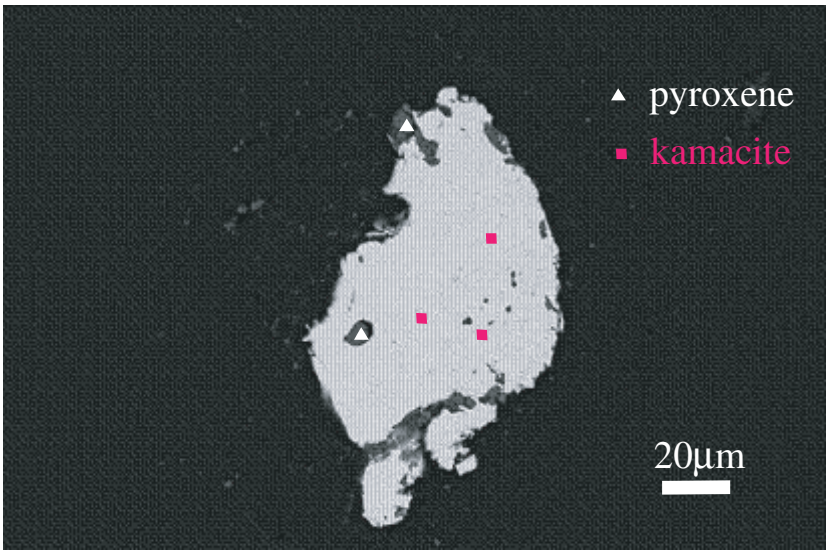

2BC2

wt %	tr	kam
Ni		5.2
Fe		94.2
Mn		0.0
Co		0.4
Cr		0.0
S		0.0
P		0.0
Total		100.0

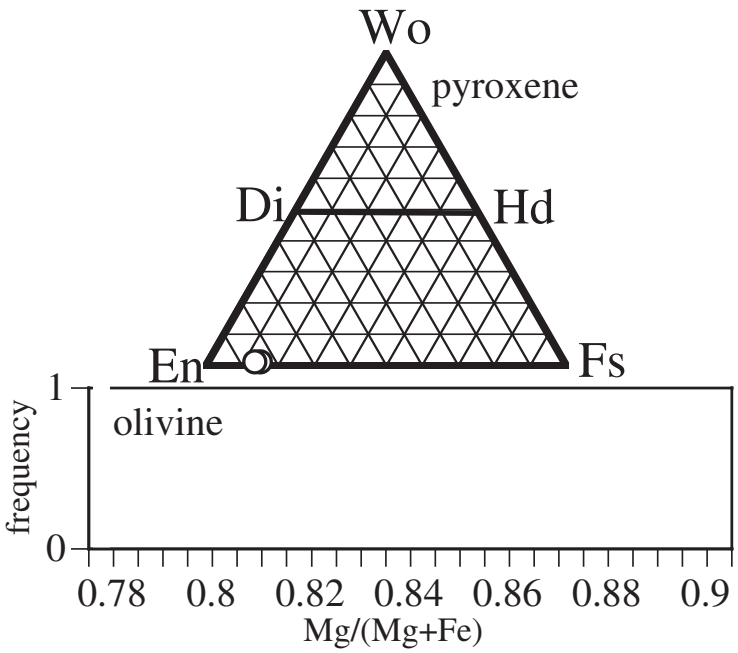

wt%	ol	low-Ca px	high-Ca px
SiO_2		56.8	
TiO2		0.1	
Al_2O_3		0.1	
FeO		9.5	
MnO		0.5	
MgO		33.3	
CaO		0.4	
Na_2O		0.0	
K_2O		0.0	
Cr_2O_3		0.1	
NiO		0.0	
P_2O_5		0.0	
SO_3		0.0	
total		100.8	

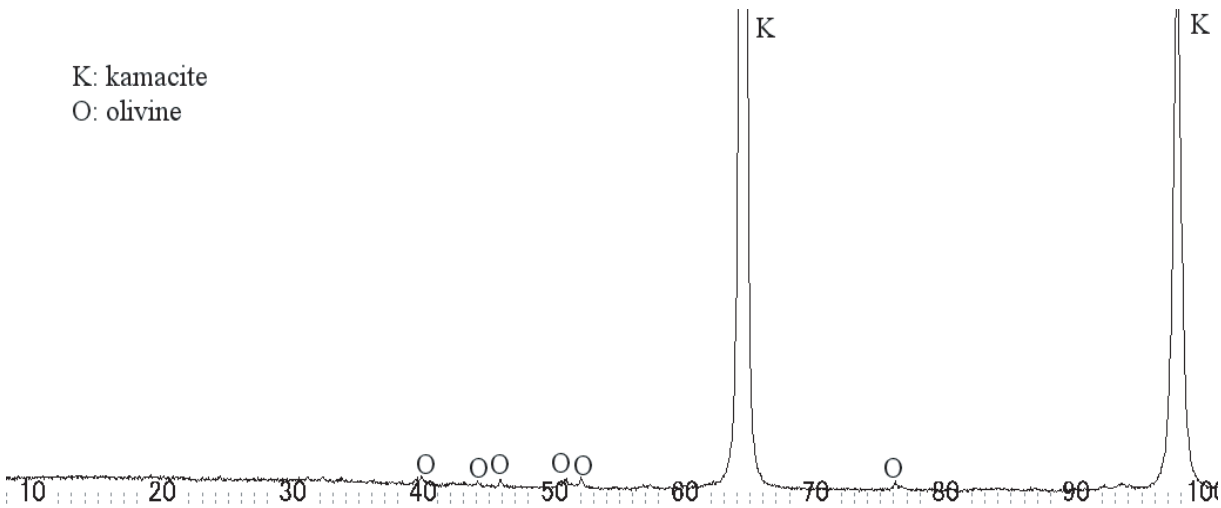

2BC3

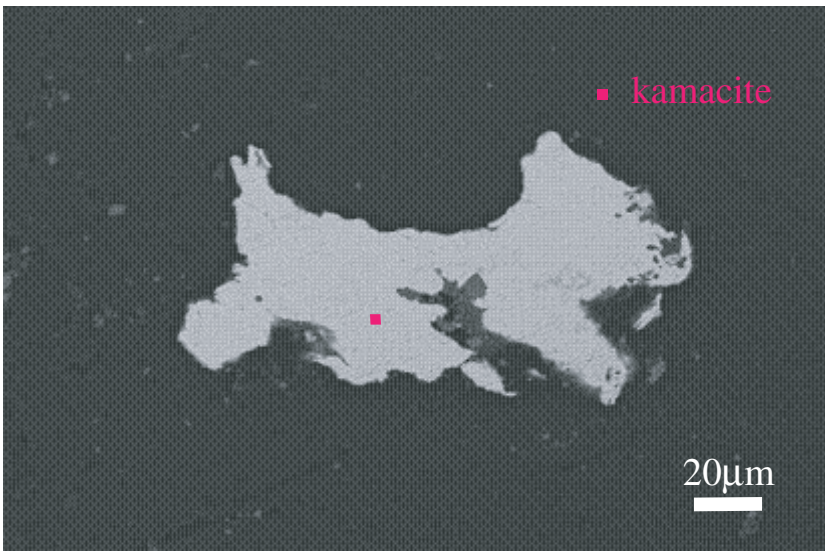

2BC3		
wt %	tr	kam
Ni		5.8
Fe		94.2
Mn		0.0
Co		0.4
Cr		0.0
S		0.0
P		0.0
Total		100.4

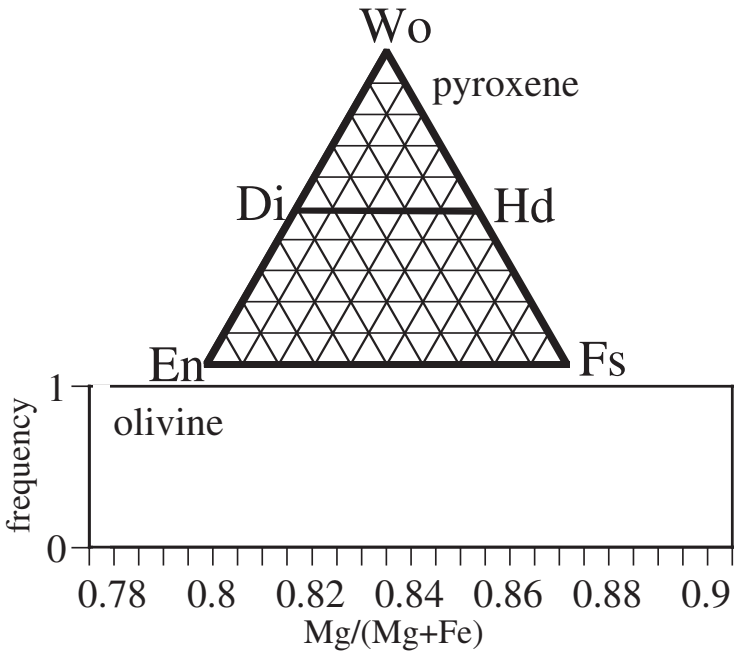

wt%	ol	low-Ca px	high-Ca px
SiO_2			
TiO2			
Al_2O_3			
FeO			
MnO			
MgO			
CaO			
Na_2O			
K_2O			
Cr_2O_3			
NiO			
P_2O_5			
SO_3			
total			

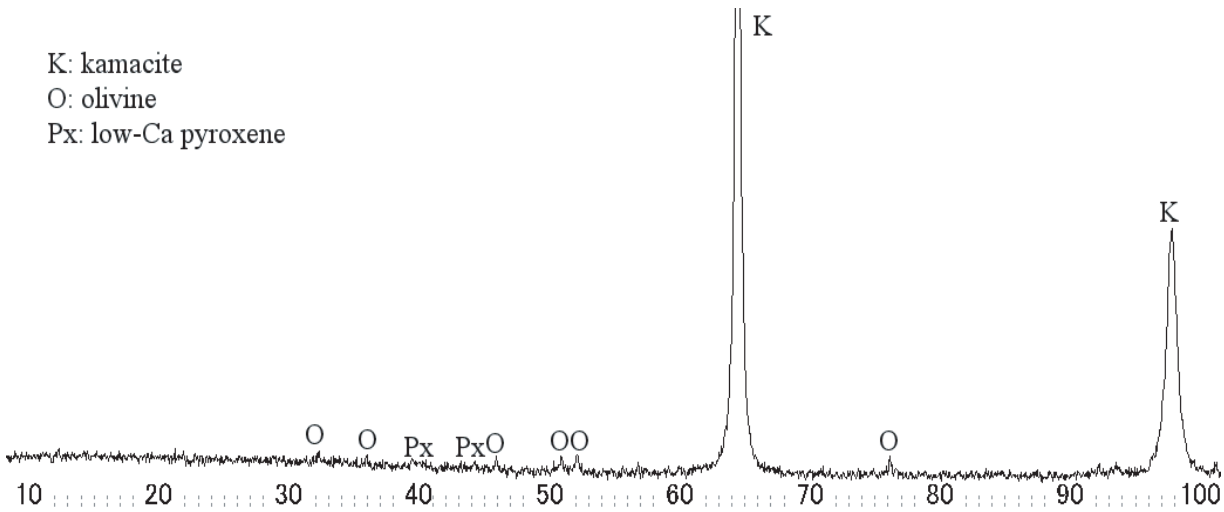

2BC4

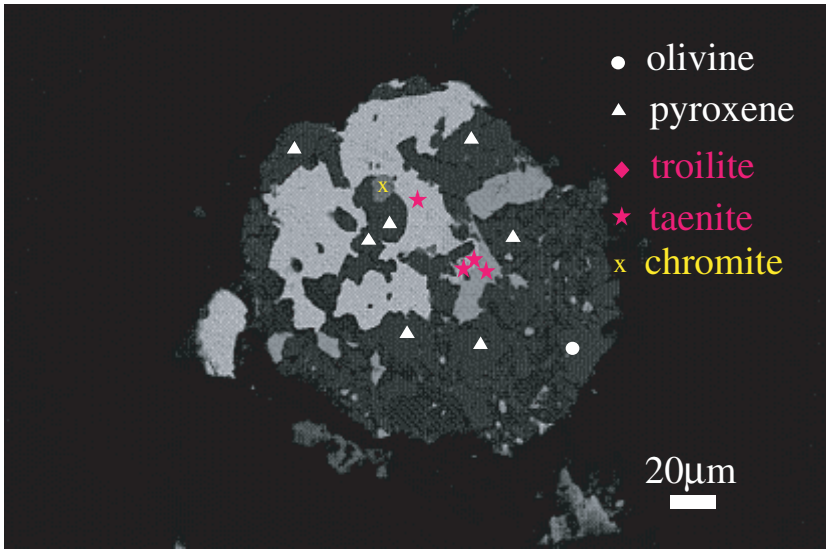

wt %	tr	tae
Ni		49.9
Fe		50.1
Mn		0.0
Co		0.1
Cr		0.1
S		0.0
P		0.0
Total		100.2

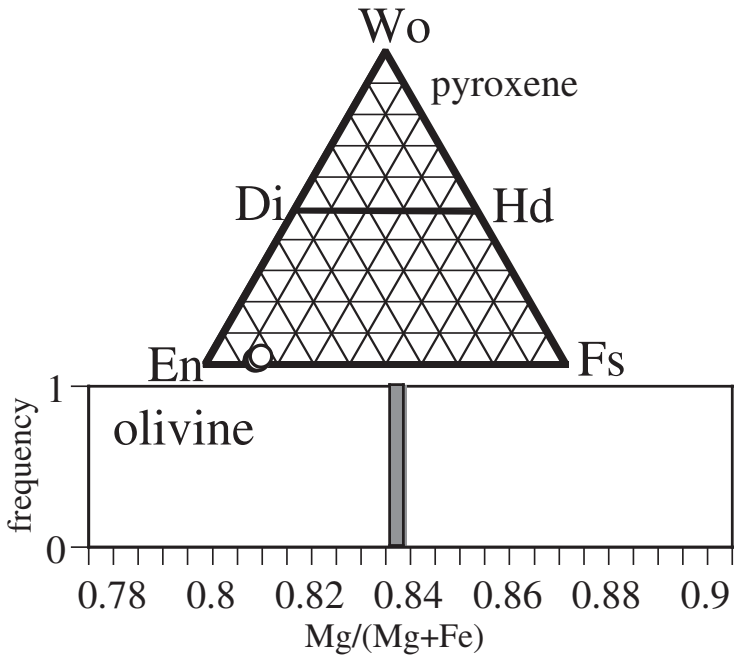

wt%	ol	low-Ca px	high-Ca px
SiO_2	38.8	55.6	
TiO2	0.0	0.1	
Al_2O_3	0.0	0.7	
FeO	15.2	9.9	
MnO	0.5	0.6	
MgO	44.3	31.1	
CaO	0.0	0.9	
Na_2O	0.0	0.4	
K_2O	0.0	0.0	
Cr_2O_3	0.1	0.0	
NiO	0.1	0.4	
P_2O_5	0.0	0.3	
SO_3	0.0	0.0	
total	99.0	100.0	

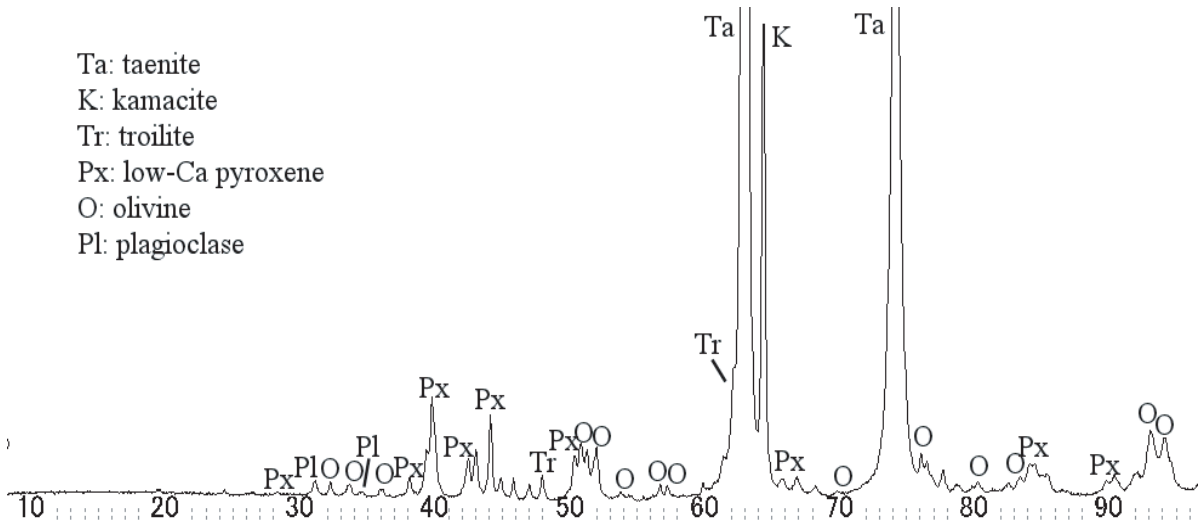

2BC5

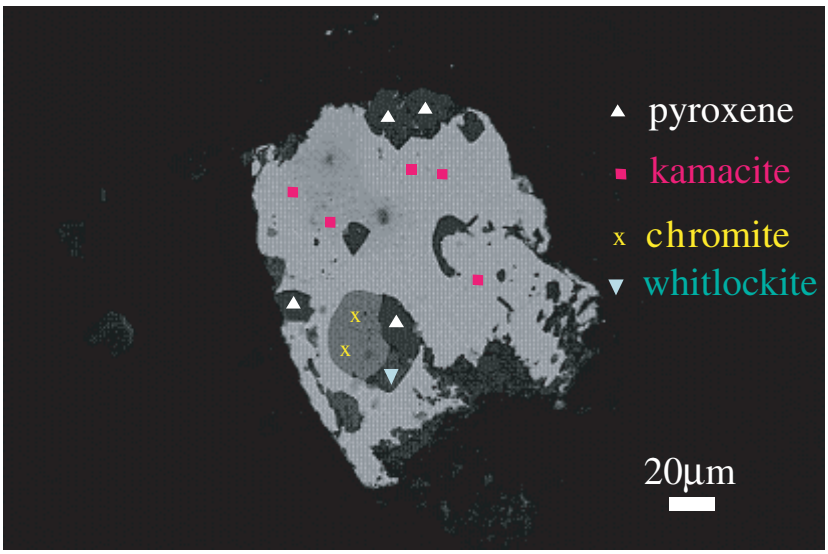

wt %	tr	kam
Ni		4.8
Fe		94.0
Mn		0.0
Co		0.5
Cr		0.0
S		0.0
P		0.0
Total		99.4

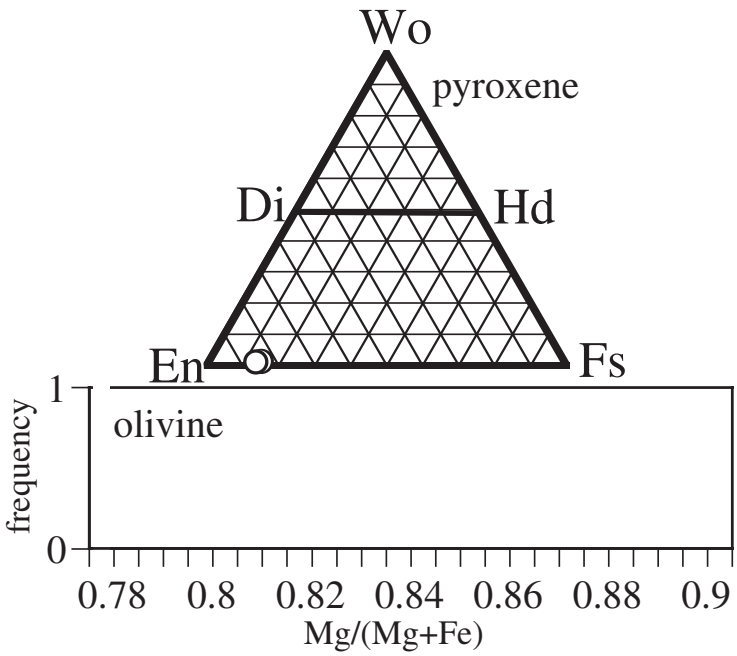

wt%	ol	low-Ca px	high-Ca px
SiO_2		56.8	
TiO2		0.1	
Al_2O_3		0.2	
FeO		10.1	
MnO		0.5	
MgO		32.3	
CaO		0.4	
Na_2O		0.1	
K_2O		0.0	
Cr_2O_3		0.2	
NiO		0.0	
P_2O_5		0.0	
SO_3		0.1	
total		100.8	

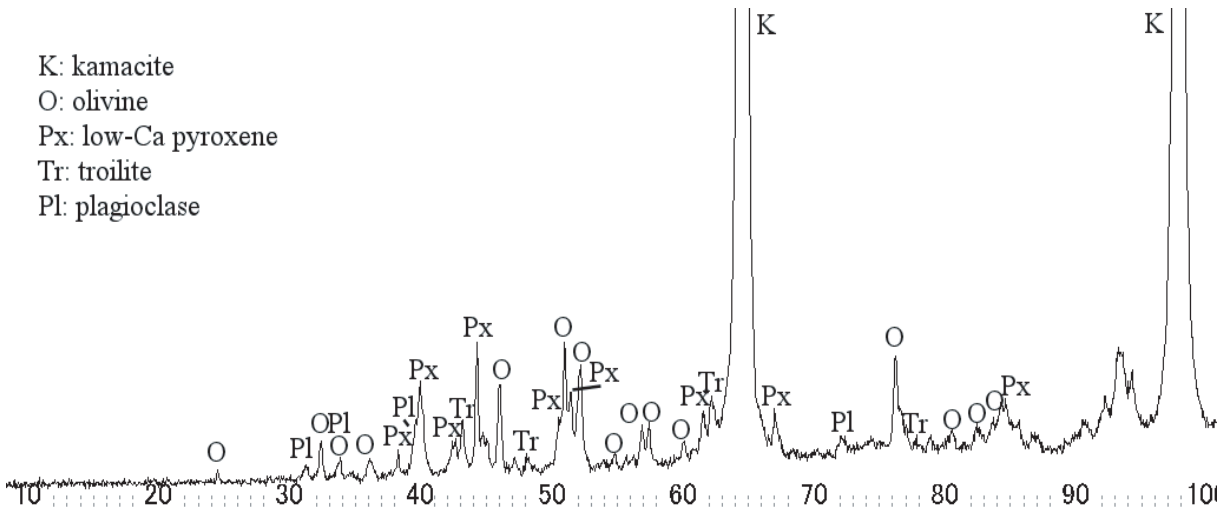

2BC6

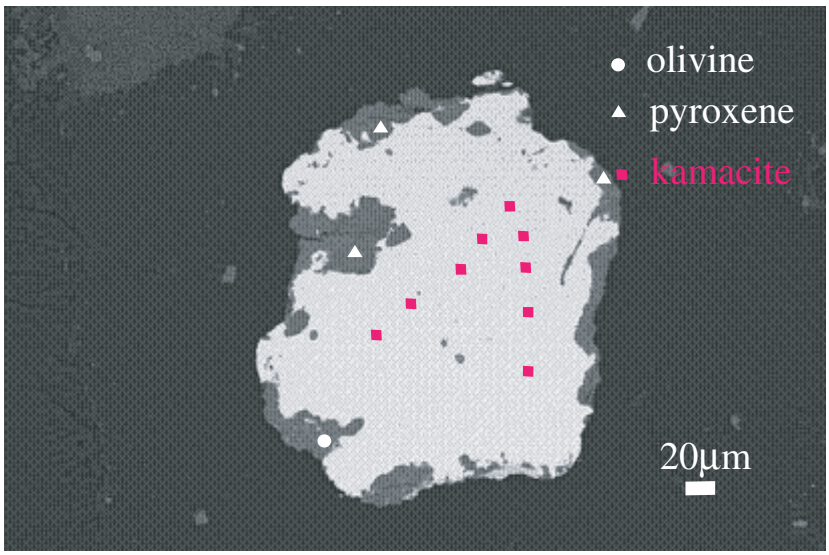

wt %	tr	kam
Ni		6.2
Fe		94.1
Mn		0.0
Co		0.3
Cr		0.0
S		0.0
P		0.0
Total		100.6

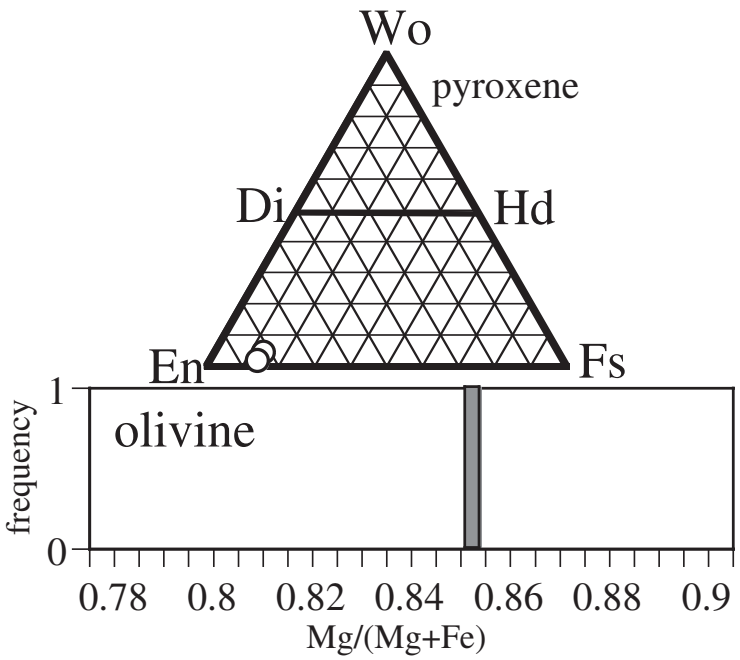

wt%	ol	low-Ca px	high-Ca px
SiO_2	39.6	55.4	
TiO2	0.0	0.1	
Al_2O_3	0.0	0.2	
FeO	13.8	9.8	
MnO	0.4	0.5	
MgO	45.4	31.2	
CaO	0.0	2.2	
Na_2O	0.0	0.0	
K_2O	0.0	0.0	
Cr_2O_3	0.1	0.7	
NiO	0.0	0.0	
P_2O_5	0.0	0.1	
SO_3	0.0	0.0	
total	99.5	100.3	

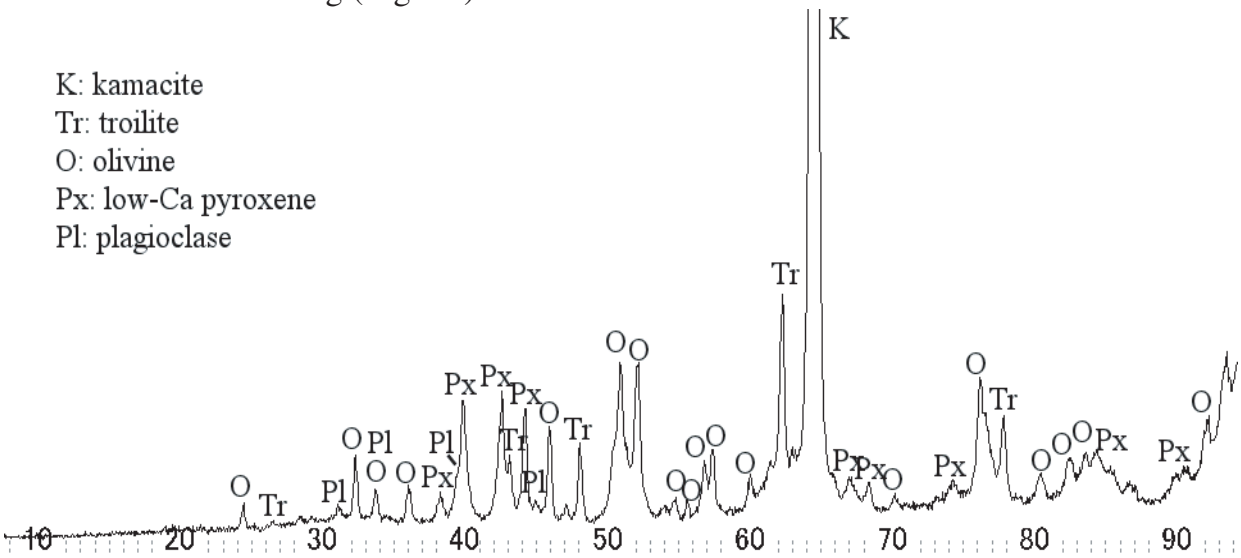

2BC7

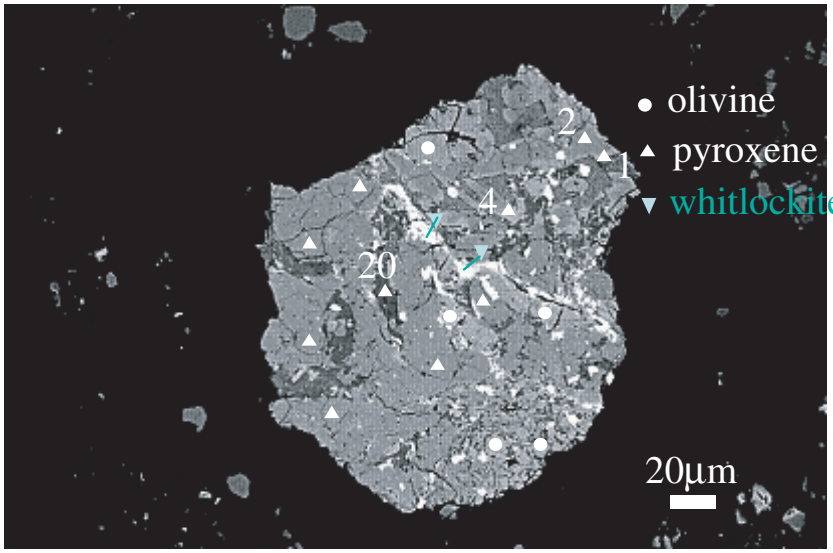

wt %	tr	kam
Ni		
Fe		
Mn		
Co		
Cr		
S		
P		
Total		

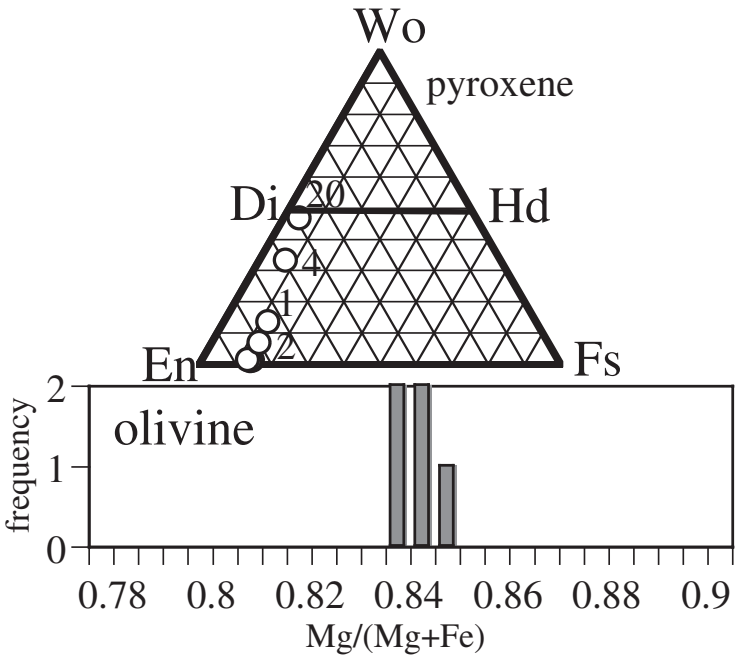

wt%	ol	low-Ca px	high-Ca px
SiO_2	39.3	56.2	54.9
TiO2	0.0	0.1	0.2
Al_2O_3	0.0	0.3	0.4
FeO	15.1	9.1	5.0
MnO	0.5	0.7	0.4
MgO	44.6	29.7	21.1
CaO	0.2	3.3	16.3
Na_2O	0.0	0.2	0.5
K_2O	0.0	0.0	0.0
Cr_2O_3	0.0	0.6	0.7
NiO	0.0	0.0	0.0
P_2O_5	0.2	0.0	0.1
SO_3	0.0	0.0	0.0
total	100.0	100.1	99.6

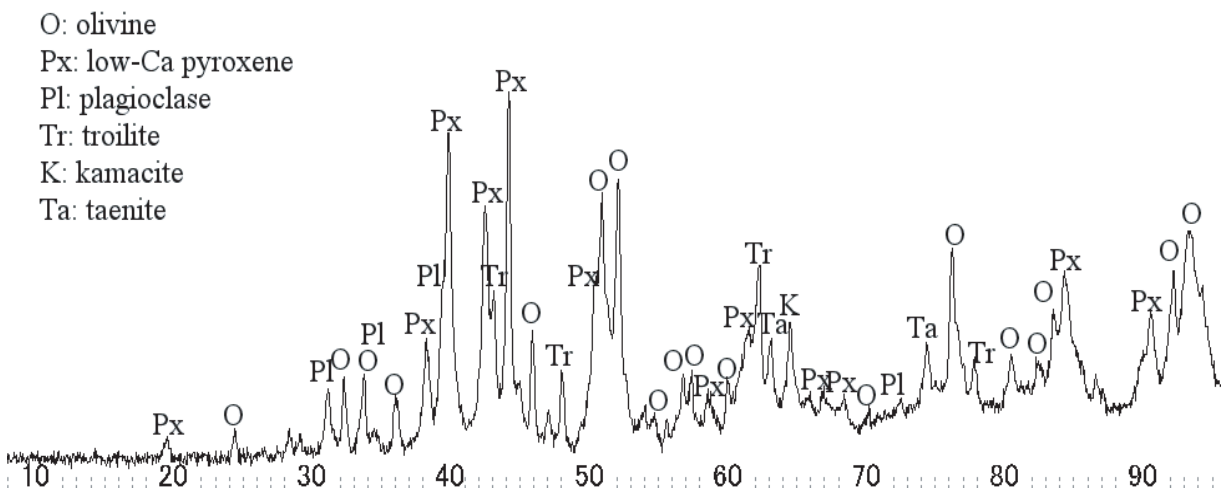

2BC8

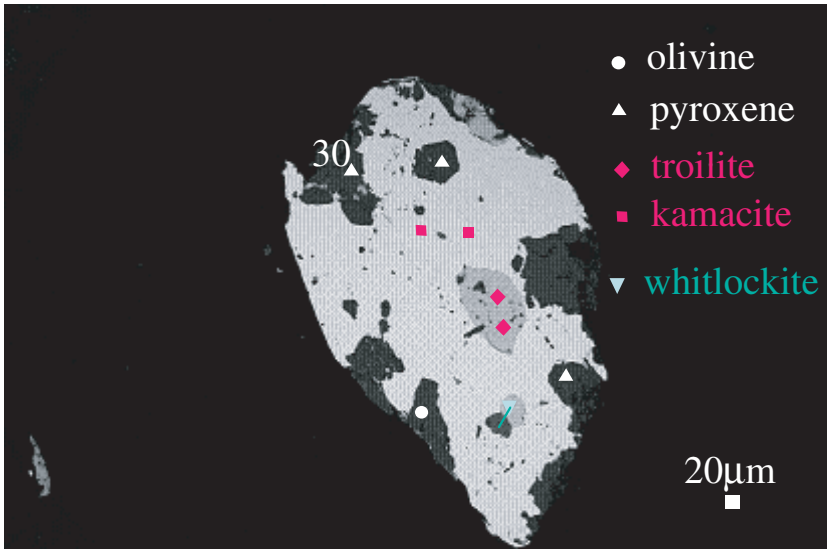

wt %	tr	kam
Ni	0.0	6.4
Fe	64.4	94.5
Mn	0.0	0.0
Co	0.0	0.4
Cr	0.0	0.0
S	36.3	0.0
P	0.0	0.0
Total	100.8	101.3

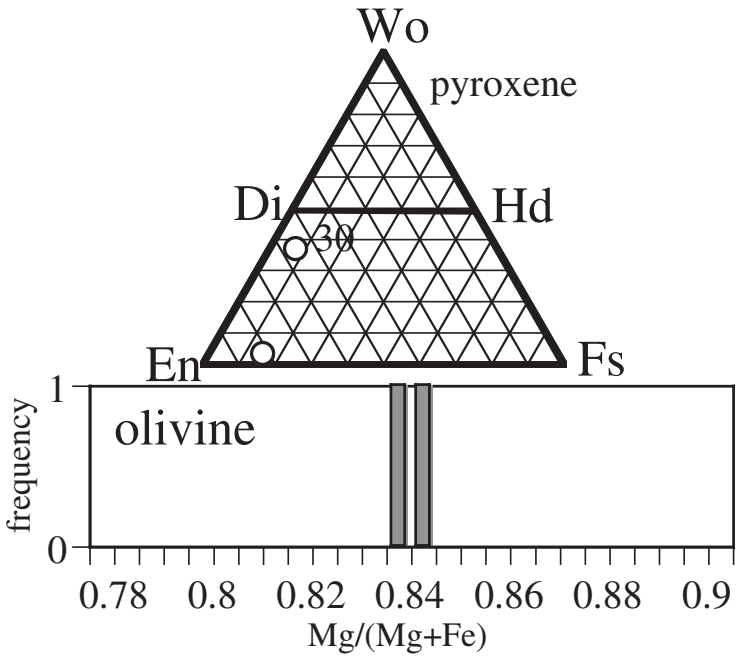

wt%	ol	low-Ca px	high-Ca px
SiO_2	39.1	54.5	51.7
TiO2	0.1	0.1	0.9
Al_2O_3	0.0	1.7	3.0
FeO	15.5	10.2	4.0
MnO	0.5	0.6	0.3
MgO	44.9	30.0	19.1
CaO	0.0	1.5	17.4
Na_2O	0.0	0.0	0.4
K_2O	0.0	0.0	0.0
Cr_2O_3	0.1	0.8	0.7
NiO	0.0	0.0	0.0
P_2O_5	0.0	0.0	0.0
SO_3	0.0	0.0	0.0
total	100.3	99.6	98.6

No X-ray diffraction analysis was performed on this sample.

2BC9

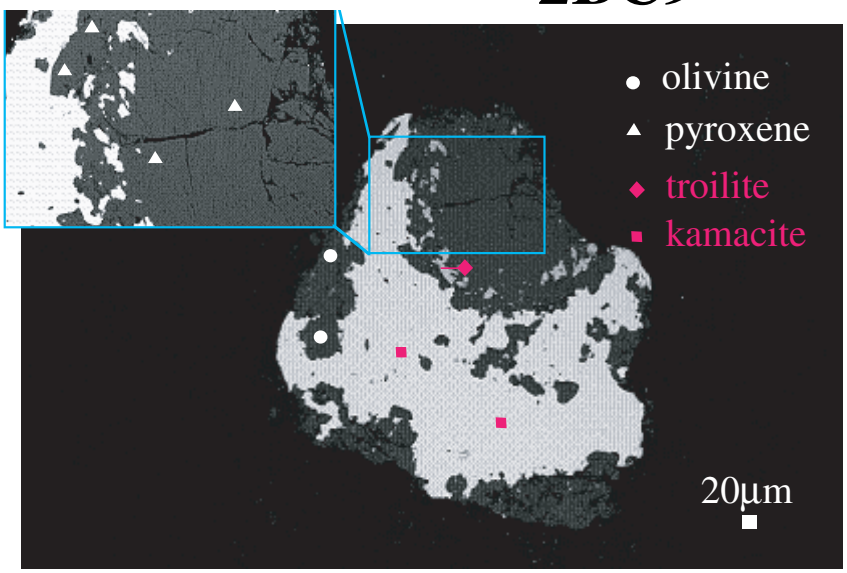

wt %	tr	kam
Ni	0.1	6.2
Fe	59.6	94.4
Mn	0.0	0.0
Co	0.0	0.4
Cr	0.0	0.0
S	33.5	0.0
P	0.0	0.0
Total	93.3	101.0

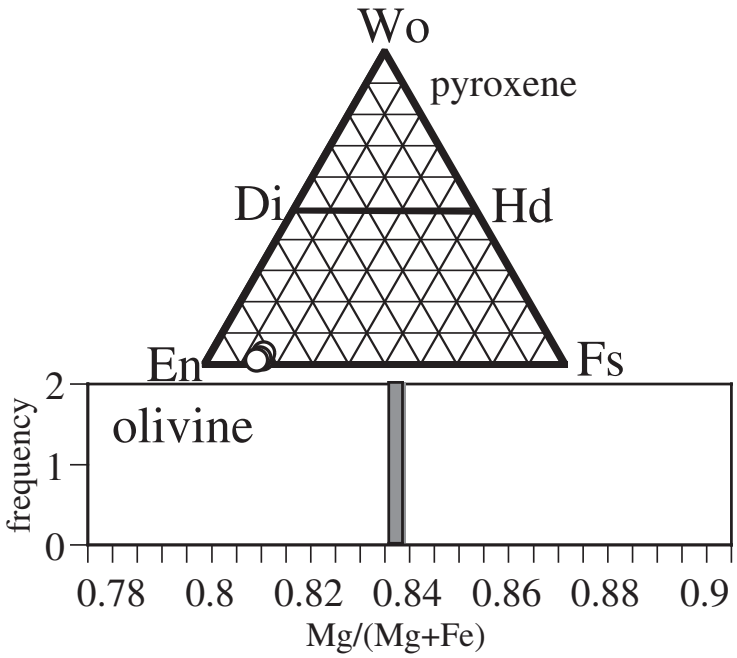

wt%	ol	low-Ca px	high-Ca px
SiO_2	39.4	56.7	
TiO2	0.0	0.1	
Al_2O_3	0.0	0.3	
FeO	15.7	10.2	
MnO	0.5	0.6	
MgO	45.2	31.5	
CaO	0.0	0.8	
Na_2O	0.0	0.1	
K_2O	0.0	0.0	
Cr_2O_3	0.0	0.1	
NiO	0.0	0.0	
P_2O_5	0.0	0.0	
SO_3	0.0	0.0	
total	100.9	100.4	

No X-ray diffraction analysis was performed on this sample.

Mössbauer Spectroscopic Characterization of Iron Species in the Test Samples of 4A and 4B for the Second HASPET Competition

By

Yoichi SAKAI[1] and Yoshitaka MINAI[2]

Abstract: It was revealed in the preset Mössbauer investigation that four iron-bearing minerals were contained in both the unknown samples named “4A” and “4B” for the second HASPET competition; they are olivine, pyroxene, kamacite and troilite. For purpose of the identification, Mössbauer spectra were measured for mineral samples being ensured to be what it is. It was concluded that the samples of 4A and 4B should be meteorite materials; the former be a stony meteorite while the latter be an iron meteorite from our ^{57}Fe-Mössbauer measurement and analysis.

1. INTRODUCTION

Iron is one of the most important elements from geochemical and cosmochemical viewpoints. It is well known that iron has various valence (oxidation) states from +1 to +6, leading to plenty of iron species in terrestrial or extraterrestrial materials (Greenwood and Earnshaw, 1984; Cox,1995). What is the chemical states of iron in the materials? How about the proportion of each fraction of the iron species contained in the material? These two questions are expected to be key-factors to identify a geo- and/or cosmochemical sample because they should be related closely to the formation origin and weathering history of the sample. The mineralogical and geochemical applications of the ^{57}Fe-Mössbauer spectroscopy have developed for iron-bearing materials, possibly giving us information on the physical and chemical states of iron (Tominaga and Minai,1984; McCammon, 1995; Constantinescu et al., 1997). A recent remarkable topic of the application was ^{57}Fe-Mössbauer exploration of the Mars with MINOS II by a collaboration of NASA and a German group (Klingelhofer, 2004). The Mössbauer hyperfine parameters provide information on the valence states, the symmetry of coordination, and the magnetic environments, which are obtained from three hyperfine parameters of isomer shift (IS), quadrupole splitting (QS), and internal magnetic field (H_f), respectively (Dickson and Berry, 1986; Murad and Cashion, 2004). In the case that there are existed several components of iron species, we can observe a spectrum as the superimposition of each component and obtain the relative abundances of the iron species by deconvolution. It should be emphasized that a ^{57}Fe-Mössbauer spectrum can be measured non-destructively under in-situ condition for a small amount of samples, approximately a few-tens milligram. If necessary, the samples used for Mössbauer measurements can be returned or reused for the other kinds of analysis after the investigation. From such advantages the spectroscopy could be greatly suitable to the analysis of rare and precious materials, for example, the samples to be returned from Itokawa by the Hayabusa mission in 2007. The test samples of 4A and 4B reached us on December 6, 2004. In the present article, the results of Mössbauer spectroscopic examinations for the two unknown samples distributed for the competition are reported. Some minerals and a standard reference material sample were also analyzed for comparison.

1 Department of Chemistry, Daido Institute of Technology, Nagoya 457-8530, JAPAN

2 Center for Arts and Sciences, Musashi University and Nedzu Chemistry Laboratory,Tokyo 176-8534, JAPAN

2. EXPERIMENTAL

2.1. Sample materials

Each sample (about 100 mg) mailed to us on December of 2004 was inspected by eyes at first. Both the samples are dark-grey (nearly black). The sample 4A was seen as powder while the 4B was composed of small grains with the size of 0.2 to 1.0 mm. The powder of 4A was submitted to Mössbauer measurements without further treatment. Although the grains for the 4B sample were tried to be crashed and milled into fine powders using an agate mortar with a pestle, the milling was not effectively carried out due to the hardness of the grains, which allowed us to speculate that it contained metals, alloys, or metallic compounds as a major component. The sample weights and thicknesses for the measurements are summarized in Table 1. It had been suggested from the first series of the preliminary ^{57}Fe-Mössbauer measurements that the test samples contained some kinds of iron-bearing minerals, leading us to the measurements for some minerals and a chemical reagent as reference samples. Those minerals were obtained from Hori Mineralogy Co. as listed in Table 1. Commercially available iron(II) sulfide FeS was purchased from Kishida Chemical Co. A standard soil sample was also measured for semi-quantitative estimation of iron content of the test samples, which was issued as "JSAC 0411" by the Japan Society of Analytical Chemistry.

2.2. Mössbauer measurements and analysis

Mössbauer spectra were measured with Mössbauer spectrometers of Model MD-222B and Model MDF-500F fabricated by Topologic Systems, Inc. against a Mössbauer source of 370-MBq or 925-MBq ^{57}Co in Rh foil. Measurement temperatures were ranged from 80.0 to 293.0 K regulated by using an Oxford cryostat DN-1726 with a temperature controller ITC-601. Each spectrum was measured for the duration time of a few days. The curve fitting of spectra were performed by means of a non-linear least-square method, a commercially available Mössbauer analysis program named MossWinn 3.0i developed by Klencsar of University of Kaposvar, Hungary (Klencsar, 2005), with a personal computer, assuming that all the spectra were composed of Lorentzian-shaped absorption peaks. A Lorentzian peak, characteristic to absorption or emission of nuclear transition energy, has the following three quantities; the peak position, and intensity, and line-width. In the present fitting procedure, the isomer shift (IS), quadrupole splitting (QS), and internal magnetic field (H_f) could be calculated from the peak positions while the relative peak area was calculated using the peak intensity and the line-width. The IS values and Doppler velocity scale were calibrated with respect to the centroid of sextet of metallic iron (α -Fe) at room temperature.

Table 1. Samples submitted to ^{57}Fe-Mössbauer measurement.

Name	Sampling site	Weight mg	Thickness mg/cm^2
4A	unknown	27.9	63.1
4B	unknown	38.2	53.1
olivine/forsterite	Pakistan	10.9	23.6
pyroxene/augite	Checz	29.5	29.5
pyroxene/enstatite	Sli Lanca	7.1	15.1
pyroxene/enstatite	Tanzania	49.1	49.1
FeS(troilite)	chemical regent*1	44.5	44.5
standard soil sample	JSAC 0411*2	52.9	52.9

*1. Chemical reagent of iron(II) sulfide (FeS) was commercially available from Kishida Chem. Co. which contained troilite of about 40 wt%, estimated by our Mössbauer measurement.

*2. This standard sample was purchased from the Japan Society for Analytical Chemistry(JSAC), which had been preppared using volcanic ash soil sampled in Naruko-cho,Miyagi Prefecture. The content of iron reported by JSAC was 3.300 wt%.

3. RESULTS

^{57}Fe-Mössbauer spectra measured at the temperatures of 80.0, 150.0, 170.0, 220.0 and 293.0 K for the test samples of 4A and 4B were shown in Figs. 1 and 2, respectively. The spectra of 4A and 4B were successfully fitted by assuming that there were four and three components, respectively, as seen in the figures, the characterizations of which are described in the following discussion section (4-1). The obtained Mössbauer hyperfine parameters and the relative areas are summarized in Tables 2 and 3. The Mössbauer spectra and hyperfine parameters for the minerals are shown in Fig. 3 and Table 4. The temperature dependences of the Mössbauer parameters and the area of each component are illustrated for the samples of 4A and 4B in Figs. 4 to 7.

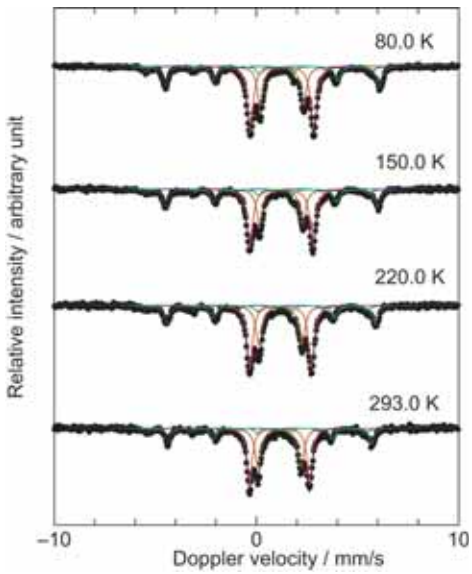

Figure 1. ^{57}Fe-Mössbauer spectra at 80.0, 150.0, 220.0, and 293.0 K for the test sample of 4A. Red curves set for a DB(O) (olivine) component, brown for a DB(I) (pyroxene), blue for a SX(H) (kamacite), and green for a SX(L) (troilite).

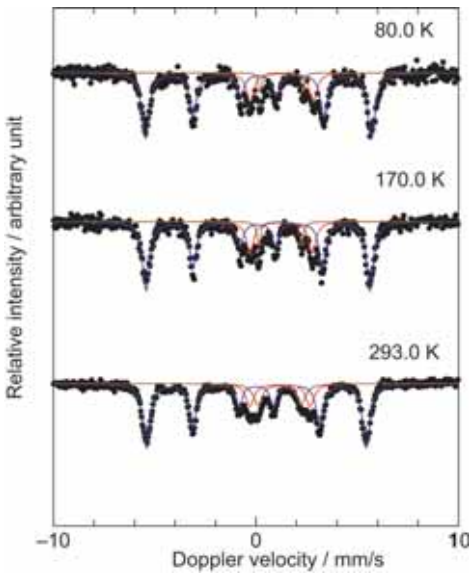

Figure 2. ^{57}Fe-Mössbauer spectra at 80.0, 170.0, and 293.0 K for the test sample of 4B. Red curves set for a DB(O) (olivine) component, brown for a DB(I) (pyroxene), and blue for a SX(H) (kamacite).

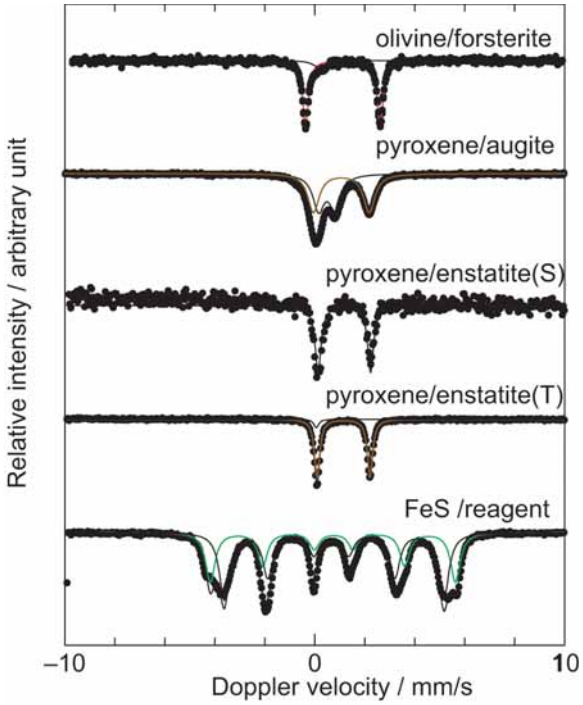

Figure 3. ^{57}Fe-Mössbauer spectra at 293.0 K for mineral samples and FeS reagent:Red curves set for a DB(O) (olivine) component, brown for a DB(I) (pyroxene), and green for a SX(L) (troilite)

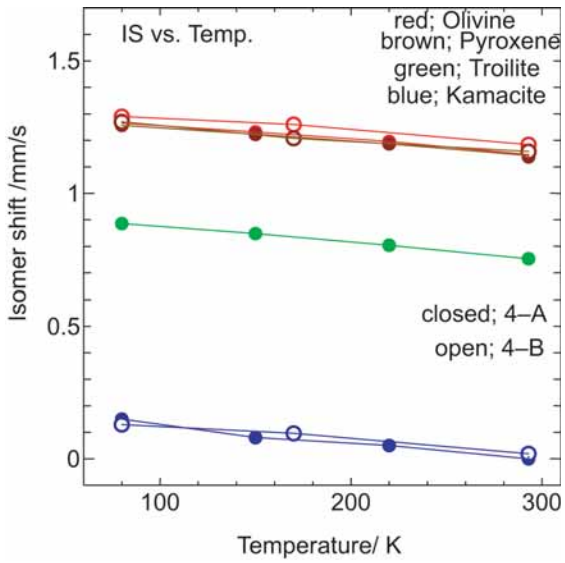

Figure 4. Temperature-dependence of isomer shifts of olivine, pyroxene, kamacite, and troilite in the test samples 4A and 4B.

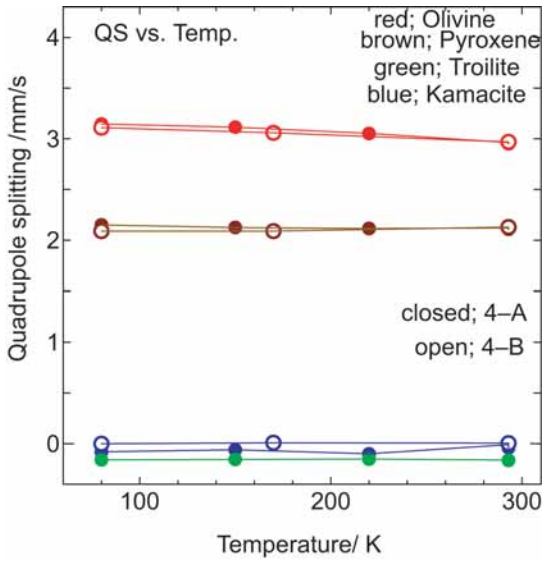

Figure 5. Temperature-dependence of quadrupole splittings of olivine, pyroxene, kamacite, and troilite in the test samples 4A and 4B.

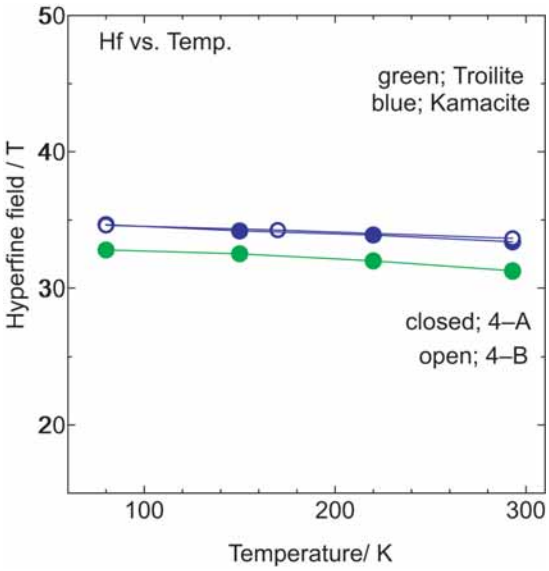

Figure 6. Temperature-dependence of hyperfine fields of kamacite and troilite in the test samples 4A and 4B.

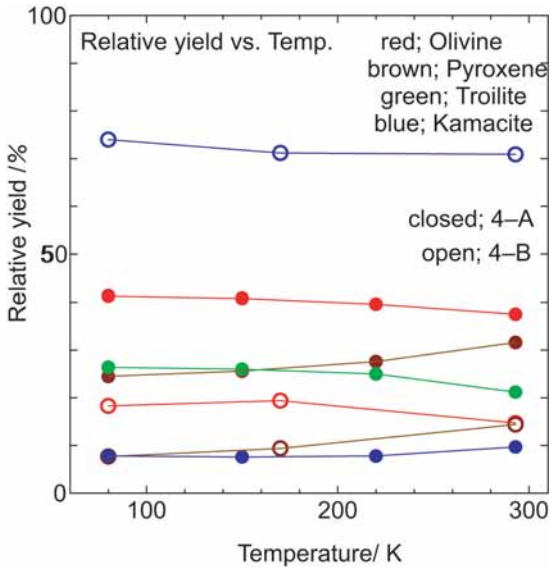

Figure7. Temperature-dependence of relative yields of olivine, pyroxene, kamacite, and troilite in the test samples 4A and 4B.

4. DISCUSSION

4.1. Assignments of the iron-bearing components for the test samples of 4A and 4B

As shown in Figs. 2 and 3, our Mössbauer analysis revealed the following points:

1. The 4A sample should contain four iron species, corresponding to two doublets and two sextets in the Mösbauer spectra, which are denoted as DB(O), DB(I), SX(H), and SX(L) in the present report.

2. The 4B sample should contain three iron species. The three species are correspondent to two doublets and one sextet in the spectra. The parameters of the two doublets are found to be fairly agreed with those of DB(O) and DB(I) in the sample 4A. The sextet parameter of the 4B sample is greatly close to that of SX(H) in the 4A.

3. Therefore, it is just 4 iron species that we have to reveal what it is in both the samples of 4A and 4B; i.e., DB(O), DB(I), SX(H), and SX(L).

4. The abbreviations of DB(O), DB(I), SX(H), and SX(L) made tentatively here mean “outer doublet”, “inner doublet”, “sextet with a higher H_f”, and “sextet with a lower H_f”, respectively.

The Mössbauer parameters of IS and QS for DB(O) and DB(I) are close to those for olivine and pyroxene, respectively, reported previously (Akasaka and Shinno, 1992; McCammon, 1995; Calogero et al., 1999). The results of our measurements of several minerals gave confirmative assignments. Both the IS and QS values obtained for DB(O) of the test samples of 4A and 4B are found to agree to those of forsterite, a kind of olivine, as shown in Table 4. As to DB(I), comparison of the parameters of IS and QS for the test samples (Tables 1 and 2) and the minerals (Table 3) leads us to an important finding of much more excellent assignment with those for orthopyroxene than clinopyroxene.

The IS and QS parameters, being nearly zero, of SX(H) observed here could ascribe it to metallic iron or iron-bearing alloy such as Fe-Ni, kamacite according to the literatures (McCammon, 1995; Calogero et al., 1999). We know that there can be taenite as another Fe-Ni alloy mineral. However, the hyperfine magnetic field H_f of 33-34 T at 293.0 K in our measurement was agreement with one for kamacite (33.8 T) but not with one for taenite (28.9 T) (McCammon, 1995). The iron species corresponding to SX(L) might be resumed to be troilite in a similar way. The IS and H_f values obtained here were found to be very close to those ot troilite in literatures. These values were also agreed with those for FeS in this study. The QS parameter was also observed to be in a relative wide range (-0.8 to 0.15 mm/s) of troilite reported previously. Our assignments are summarized inTable 5.

Table 2. Mössbauer parameters obtained for the test sample 4A.

	IS*	QS	H_f	Γ	A
mm/s	mm/s	mm/s	T	mm/s	%
80.0 K					
DB(O/)olivine	1.265 (1)	3.147 (2)		0.346 (3)	41.3
DB(I)/pyroxene	1.257 (2)	2.151 (3)		0.346 (5)	24.5
SX(H)/kamacite	0.15 (1)	-0.08 (2)	34.66 (7)	0.41 (3)	7.8
SX(L)/troilite	0.886 (2)	-0.160 (5)	32.80 (2)	0.337 (7)	26.4
150.0 K					
DB(O)/olivine	1.232 (1)	3.115 (3)		0.344 (5)	40.8
DB(I)/pyroxene	1.223 (2)	2.126 (5)		0.365 (8)	25.6
SX(H)/kamacite	0.08 (2)	-0.06(3)	34.2 (1)	0.45 (6)	7.6
SX(L)/troilite	0.848 (4)	-0.156 (7)	32.52 (2)	0.34 (1)	26.0
220.0 K					
DB(O)/olivine	1.196 (1)	3.053 (3)		0.342 (5)	39.6
DB(I)/pyroxene	1.187 (2)	2.116 (6)		0.380 (9)	27.6
SX(H)/kamacite	0.05 (2)	-0.10 (3)	33.9 (1)	0.42 (6)	7.8
SX(L)/troilite	0.804 (4)	-0.152 (8)	32.00 (3)	0.36 (1)	25.0
293.0 K					
DB(O)/olivine	1.146 (1)	2.963 (4)		0.307 (6)	37.5
DB(I)/pyroxene	1.143 (2)	2.121 (6)		0.37 (1)	31.6
SX(H)/kamacite	0.000 (1)	-0.01 (2)	33.4 (1)	0.47 (6)	9.7
SX(L)/troilite	0.753 (5)	-0.162 (9)	31.27 (3)	0.30 (1)	21.2

*Relative to α -iron.

Table 3. Mössbauer parameters obtained for the test sample 4B.

	IS*	QS	H_f	Γ	A
mm/s	mm/s	mm/s	T	mm/s	%
80.0 K					
DB(O)/olivine	1.29 (1)	3.11 (3)		0.48 (5)	18.3
DB(I)/pyroxene	1.27 (1)	2.09 (2)		0.25 (4)	7.7
SX(H)/kamacite	0.129 (4)	0.00 (1)	34.61 (3)	0.44 (1)	74.0
170.0 K					
DB(O)/olivine	1.26 (1)	3.06 (2)		0.49 (5)	19.4
DB(I)/pyroxene	1.208 (9)	2.09 (2)		0.28 (4)	9.4
SX(H)/kamacite	0.096 (3)	0.009 (7)	34.26 (3)	0.41 (1)	71.2
293.0 K					
DB(O)/olivine	1.184 (8)	2.97 (3)		0.51 (4)	14.7
DB(I)/pyroxene	1.158 (8)	2.13 (3)		0.53 (4)	14.4
SX(H)/kamacite	0.019 (2)	0.005 (5)	33.65 (1)	0.433 (6)	70.9

*Relative to α -iron.

Table 4. Mössbauer parameters obtained at 293 K for minerals.

	IS*	QS	Γ	A
mm/s	mm/s	mm/s	mm/s	%
olivine from Pakistan				
doublet	1.125 (1)	2.989 (2)	0.273 (3)	89.0
singlet	0.20 (2)		0.60(5)	11.0
pyroxene from Czech				
outer doublet	1.064 (2)	2.231 (4)	0.551 (5)	52.7
inner doublet	0.484 (2)	0.663 (4)	0.547 (7)	47.3
pyroxene from Sri Lanca				
doublet	1.185 (4)	2.103 (8)	0.29 (1)	100
pyroxene from Tanzania				
doublet	1.151 (2)	2.115 (4)	0.253 (2)	93.6
singlet	0.06 (2)		0.24 (3)	6.4

*Relative to α -iron.

Table 5. Assignments of iron species observed in the Mössbauer spectra at 293 K for the 4A and 4B test samples.

	IS*	QS	H_f	Mineral	Chemical formulae
mm/s*	mm/s	T			
DB(O)	1.146(1)	2.963(9)		olivine	$(Mg,Fe)_2Si_4$
	1.184(8)	2.97(3)			
DB(I)	1.143(2)	2.121(6)		pyroxene	$(Mg,Fe)_2Si_2O_6$
	1.158(8)	2.13(3)			
SX(H)	0.000(1)	-0.01(2)	33.4(1)	kamacite	FeNi
	0.019(2)	0.005(5)	33.65(1)		
SX(L)	0.753(5)	-0.162(9)	31.27(3)	troilite	FeS

*Relative to α -iron.
The first line sets for the test sample of 4A, and the second one for the 4B. The component of SX(L) was observed for the 4A, not in the 4B. According to the literatures (McCammon, 1995; Calogero et al., 1999), the Mössbauer parameters were reported as follows;
For olivine, IS are in the range from 1.14 to 1.16 mm/s, QS; 2.94 to 2.99 mm/s.
For pyroxene, IS; 1.13 to 1.16 mm/s, QS; 2.09 to 2.10 mm/s.
For kamacite, IS; about 0 mm/s, QS; about 0 mm/s; Hf; 33.4 to 34.0 T.
For troilite, IS; 0.75 to 0.81 mm/s, QS; -0.8 to 0.15 mm/s (wide range !); Hf; 31.3 to 31.6 T.
The parameters for olivine and pyroxene were obtained in the present work, showing a good agreement with those cited above (see Table 4).

4.2. Identification of the test samples 4A and 4B

Four minerals of olivine, pyroxene, kamacite, and troilite found in the test samples are popular as iron-bearing components of meteorite samples (Calogero et al., 1999). When measuring a Mössbauer spectrum of the sample of 4A at the first stage of this work, we noticed that the overall absorption profile is closely resemble to those reported for meteorites (Endo et al., 1994; Bland et al., 1998). After our further measurements and comparison with reported data, it was revealed that the 4A sample showed the similar spectral feature not only in the line shapes but also in the peak positions. Tables 1 and 2 and Fig. 7 show that the major components for the sample 4A are iron-bearing silicate minerals of olivine and pyroxene, and that the main component for the sample 4B is Fe-Ni alloy of kamacite. It was concluded at the final stage of the present HASPET work that the test samples of 4A and 4B can be ascribed to some kinds of meteorite. Perhaps, the 4A sample would be a stony meteorite containing iron-bearing silicates as major components while the 4B sample would be an iron meteorite made mainly from metallic iron and/or alloy such as Fe-Ni. The Mössbauer spectra of the 4A sample was resemble to those for the Antarctica meteorites reported by Endo et al. (1994) as described above. However, there has been recognized to be a different feature in the spectra between the previous results and ours. It was proved that the meteorites contained Fe3+ species with a substantial yield of a few-tens paecentage while no or negligible amounts of ferric component was found in our Mössbauer spectrum of the 4A sample. This implies that the 4A, if it is a meteorite sample, might relatively be fresh and/or not be oxidized (or weathered) before and after the falling.

4.3. Temperature dependence of Mössbauer spectra fro the test samples of 4A and 4B

The spectral line-shape was not dependent on temperature as seen in Figs. 1 and 2. Temperature dependences of the Mössbauer parameters are summarized in Tables 1 and 2, and also illustrated in Figs. 4 to 7. Slight decrease of IS on temperature, observed for each component in Fig. 4, are due to the second-order Doppler shift effect. There was found a little decrease of H_f with increasing temperature in kamacite and troilite in Fig. 6. This might be caused by magnetic-moment fluctuation due to thermal agitation. No or little change in the Mössbauer line-shape with temperature suggested the particles of kamacite or troilite should be not enough fine so that they could show super-paramagnetic character. The mean of the particle sizes would be approximately more than several-tens nanometer.

4.4. Semi-quantitative estimation of iron content in the sample of 4A from the Mössbauer measurements

It is sometimes difficult to determine quantitatively the iron content in a material by Mössbauer spectroscopy. The peak

area, of course, reflects the amount of an iron species existing in the sample, but not proportional exactly to the amount because of the difference in the recoilless fractions, that is, the absorption intensities per iron atom, of various iron species. We dared to determine the iron content of the 4A sample by comparing the total absorption area with that of the standard sample (JSAC-0411, issued by the Japan Society of Analytical Chemistry) containing a known amount of iron (3.300 wt%), giving an iron content of ca. 15 wt%.

REFERENCES

Akasaka, M., Shinno, I., 1992, Mössbauer Spectroscopy and Its Recent Application to Silicate Minerals, *Ganseki-Kobutsu Zasshi*, **21**, 3-20 (in Japanese).

Bland, P. A., Berry, F. J., Pillinger, C. T., 1998, *Meteoritic and Planetary Sci*., **33**, 127-129.

Calogero, S., Stievano, L., Benoit, P. H., 1999, Mössbauer and TL Studies of Meteorites from Frontier Mountain, Antarctica, *J. Geophys. Res*., **104**, 30817-30823.

Constantinescu, S., Ududbasa, Gh., Calogero, S., 1997, Mössbauer Spectroscopy in Mineralogy and Geochemistry, *The 4th Symposium on Mineralogy*, Lecture Note. Cox, P. A., 1995, *The Element on Earth*, Oxford Univ. Press.

Dickson, D. P., Berry, F. J., 1986, Mössbauer Spectroscopy, Cambridge Univ. Press.

Endo, K., Hirunuma, R., Shinonaga, T., Ebihara, M., Nakahara, H., 1994, Mössbauer Spectro- scopic Study of Meteorites Recovered on Antarctica, *Hyp. Int*., **91**, 557-561.

Greenwood, N. N. and Earnshaw, A., 1984, *Chemistry of the Elements*, Butterworth Heinemann Ltd.

Klencsar, Z., 2005, http://www.mosswinn.com/english/index.html.

Klingelhofer, G., Mössbauer Exploration of the Surface of Mars with MINOS II and the Mars- Exploration-Rovers, *J. Nucl. Radiochem. Sci*., **5** (Suppl.) 15-18.

McCammon, C., 1995, Mössbauer Spectroscopy of Minerals, Mineral Physics and Crystallogra- phy, *A Handbook of Physical Constants*, The American Geophysical Union, pp.332-347.

Murad, E., Cashion, J., 2004, *Mössbauer Spectroscopy of Environmental Materials and their Industrial Utilization*, Kluber Academic Pub.

Tominaga, T., Minai, Y., 1984, Applications of Mössbauer Spectroscopy to Environmental and Geochemical Studies, *Nucl. Sci. Appl*., **1**, 749.

Test Samples for the Hayabusa Sample-Return Mission: Mineralogy and Petrology

By

Kazushige TOMEOKA[1], Ichiro OHNISHI[1], Naotaka TOMIOKA[1], Mitsuhiro SUGITA[1] and Kouji ADACHI[2]

Abstract: We have studied the mineralogy and petrology of the Hayabusa test samples, 3A and 3B, using an optical microscope, a scanning electron microscope (SEM) and an electron probe micro-analyzer. We also used an analytical field emission SEM and an analytical transmission electron microscope to obtain information especially at high magnification. The 3A sample is powder composed of particles (<150 μm in diameter) that consist mainly of fine grains of Fe-rich olivine, low-Ca pyroxene and lesser amounts of high-Ca pyroxene and plagioclase. The 3B sample is composed of rounded to subrounded particles (0.2-2.3 mm in diameter) that consist mainly of Fe-Ni metal and lesser amounts of Fe-rich olivine and low-Ca pyroxene. Both 3A and 3B particles contain materials that are analogous in texture to chondrules in chondrites. Fe-rich olivine and low-Ca pyroxene in both 3A and 3B are highly homogeneous in composition. Although the general appearance and the relative abundances of constituent minerals are different between 3A and 3B, most constituent minerals occur in common and have very similar compositions that closely resemble those of the counterparts in equilibrated H ordinary chondrites. The results suggest that 3A is made of a silicate-rich fraction of an equilibrated H chondrite and 3B is made of a metal-rich fraction of an equilibrated H chondrite. 3B particles may correspond to individual silicate-bearing metal grains in an H chondrite. Although precise determination of petrologic type is difficult because of very small particle size, we suggest that the petrologic type of both 3A and 3B is relatively low.

1. INTRODUCTION

Hayabusa is the first sample-return mission to an asteroid in the human history, and thus the outcome of this mission is awaited with great expectation. The target asteroid 25143 Itokawa made its close approach to Earth in 2001, and during that time, extensive ground-based telescopic observations were made to characterize its physical and chemical properties in preparation for the mission. Visible and near-infrared spectroscopic measurements (Binzel et al., 2001) reveal that the surface material of Itokawa has a red-slope S-type spectrum analogous to those measured for LL ordinary chondrites. Photometric measurements (Lederer et al., 2005) indicate that Itokawa appears to be a space-weathered, atypical S-class asteroid. Although much still remains to be known, these results suggest that Itokawa may be related to the primitive chondrite meteorites.

Our group in Kobe University has long been involved in research on chondrite meteorites and interplanetary dust particles (IDPs). These materials consist largely of extremely small mineral grains, most of which are submicrometer in size. Thus, to study them we have used a combination of various techniques capable of viewing and analyzing ultra-microscopic particles.The sample that will be collected from Itokawa is regarded to be very small in amount and consist of very small particles. We believe that our expertise and experience that we have gained through the studies of the fine-grained meteorites and IDPs would contribute to the study of the sample returned from Itokawa.

1 Department of Earth and Planetary Sciences, Faculty of Science, Kobe University, 1-1 Rokkoudai-cho, Nada, Kobe 657-8501, JAPAN

2 Graduate School of Science and Technology, Kobe University, 3-11 Tsurukabuto, Nada, Kobe 657-8501, JAPAN

We have received two test samples, termed 3A and 3B (each weighs～100 mg), from ISAS/JAXA on December 7, 2004. Both samples are composed of very small particles that themselves consist of fine grains of various minerals. In this paper, we present the results of petrographic and electron microscopic studies of these two test samples. The objective of our study is to provide mineralogical and petrological details of the test samples, and thereby to demonstrate our capability of characterizing small particles. We assumed that the test samples were probably prepared from meteorites. Thus, we also intend to determine their meteoritic classification as precisely as possible.

2. MATERIALS AND METHODS

2.1. Samples

The 3A sample (～100 mg) is dark grayish powder that consists of angular to irregularly shaped particles ranging in diameter from 10 to 150 μm (Fig. 1a). Four powder samples, each weighs 0.5-1.5 mg (～5 mg in total), were scooped up from the 3A sample and used for the following investigation. Initially one sample was observed by a field emission scanning electron microscope (FESEM) to study morphology and surface mineralogy of particles. Other two samples were embedded in an epoxy resin on glass slides, and polished sections of powder particles were made of them. The last sample was ground by an agate mortar to make finer-grained powder for transmission electron microscope (TEM) investigation. A small droplet of ethanol, in which the powder was suspended, was dried on a TEM grid that is reinforced with a thin carbon film.

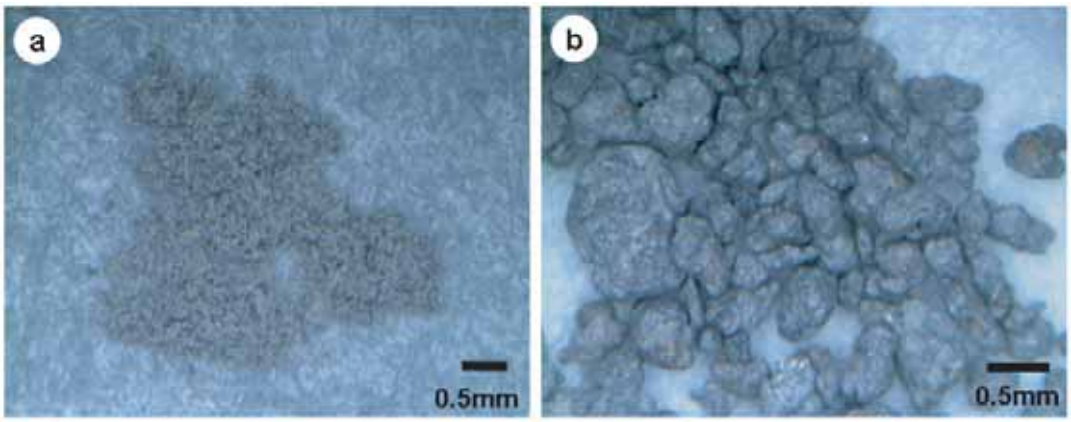

Figure 1. Optical micrographs of the 3A sample (a) and the 3B sample (b).

Table 1. Diameters and areas of 3B particles and modal abundances of Fe-Ni metal measured on the sections.

Particle name	Particle diameter* (mm)	Particle area (mm^2)	Metal area (%)
3B-1	2.3	3.41	42
3B-2	1.6	1.77	46
3B-3	0.8	0.37	48
3B-4	1.3	1.12	44
3B-5	1.0	0.60	55
3B-6	1.3	1.00	61
3B-7	0.8	0.33	55
3B-8	0.5	0.12	72

*Average of two dimensions.

The 3B sample (～100 mg) consists of dark grayish, rounded to sub-rounded particles that range in diameter from 0.2 to 2.3 mm (Fig. 1b). They are commonly elongated and uneven on the surfaces, exhibiting a peculiar, potato-like external shape. Most particles partly have metallic luster. Two largest particles (～2.3 and ～1.6 mm in diameter) and six relatively large particles (0.5-1.3 mm), termed 3B-1 to 3B-8, were hand-picked under an optical stereo-microscope for the following investigation (Table 1); the total amount of the particles is ～39 mg. Polished thin and thick sections were made from those eight particles. 3B was not studied by the TEM, because grain sizes of most minerals in 3B are much larger than those in 3A, and thus, most of mineralogical data could be obtained by the SEM and EPMA.

2.2. Analytical Methods

Polished thin and thick sections were studied using an optical microscope, a scanning electron microscope (SEM) (JEOL JSM-6480) and a field emission scanning electron microscope (FESEM) (JEOL JSM-6330F), both equipped with energy dispersive X-ray spectrometers (EDS), and an electron probe micro-analyzer (EPMA) (JEOL JXA-8900) equipped with wavelength-dispersive X-ray spectrometers (WDS). EDS analyses with the SEM were obtained at 15 kV and 0.4 nA, those with the FESEM at 15 kV and 0.3 nA, and WDS analyses at 15 kV and 12 nA. Data corrections were made by the Phi-Rho-Z method for EDS analyses. For WDS analyses of silicates and oxides, data corrections were made by the Bence-Albee method. For WDS analyses of metals and sulfides, data corrections were made by the ZAF method. For WDS analyses of metals, special care was taken to determine Co contents; Co background counts were taken at wavelengths of 0.177 nm and 0.183 nm to eliminate the contribution of the Fe K_β peak to the Co K_α peak (Rubin, 1990; Shibata, 1996). Well-characterized natural and synthetic minerals and glasses were used as standards. For most SEM and FESEM observations, we used backscattered electron (BSE) imaging. For the analysis of each mineral grain, we used a focused electron beam of ～2 μm in diameter.

Imaging and electron diffraction were performed with a transmission electron microscope (TEM) (JEOL JEM-2010) equipped with EDS, operated at 200 kV. Identification of crystal structure was based on selected-area electron diffraction (SEAD) and high-resolution imaging.

The modal analysis of metal was performed by using an image processing method. Digitized backscattered electron images were converted, using the Adobe Photoshop software package, to a histogram showing a brightness distribution of individual pixels in the images. Metal shows the highest brightness among the constituent minerals in the samples. After determining a proper threshold level in the histogram, a 255 level black and white image was converted to a straight black and white (0/255) image, and modal% of metal was calculated as an area percentage of white spaces (which correspond to metal) to a whole image.

3. RESULTS ON 3A SAMPLE

3.1. Petrography and Mineralogy

SEM observations of the polished sections of the particles reveal that they consist mainly of fine grains (5-150 μm in size) of olivine, low-Ca pyroxene, and lesser amounts of high-Ca pyroxene and plagioclase (Figs. 2a, b). Minor minerals include Fe-Ni metal, troilite, Ca-phosphate and chromite. In most particles, olivine and pyroxene occur as porous aggregates of very fine grains (5-20 μm) that are angular to irregular in shape and commonly have fine fractures and voids at high density (Fig. 2b). Fe-Ni metal, mostly kamacite with minor taenite, and troilite comprise <10 vol%; they occur as grains 5-50 μm in size. Particles that consist entirely of a single mineral of Fe-Ni metal or troilite occur in minor proportions. Neither hydrous minerals such as phyllosilicates nor Ca-Al-rich inclusion-like materials have been observed.

Some particles have textures similar to the interior of chondrules in chondrites (Figs. 3a-d), although no whole chondrules have been observed. The textural types include porphyritic olivine (PO), porphyritic pyroxene (PP) and barred olivine (BO). Plagioclase fills interstices between olivine and pyroxene grains and commonly has fine, acicular to lath-shaped crystallites (0.2-2 μm in width, 1-30 μm in length) of high-Ca pyroxene, mostly diopside (Fig. 3d), exhibiting an appearance similar to chondrule mesostasis. Because of small grain size and large sample thickness, we could not optically confirm the presence of isotropic glass in the

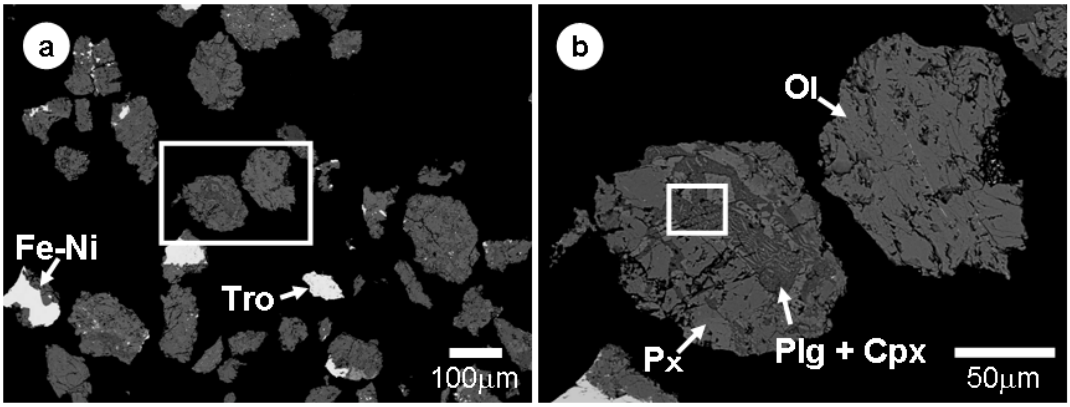

Figure 2. (a) Backscattered electron image of a polished section of 3A particles. (b) Image of boxed area in (a). Fe-Ni = Fe-Ni metal, Tro = troilite, Ol = olivine, Px = low-Ca pyroxene, Cpx = high-Ca pyroxene, Plg = plagioclase.

mesostasis. FESEM observations reveal that plagioclase in some particles has numerous submicron-size vesicles and spherical inclusions (<1-5 μm in diameter) of troilite and Fe-Ni metal as well as minor amounts of chromite and ilmenite (Figs. 4a, b).

Transmission electron microscope (TEM) observations of a powdered sample confirm the presence of most minerals described above. Olivine grains have very low densities of dislocations. Selected-area electron diffraction (SAED) patterns of low-Ca pyroxene grains show that they are mostly monoclinic clino-pyroxene with minor stacking faults on (100) plane (Figs. 5a, b). SEAD patterns of Na-Al-Si-O-rich grains show that they are mostly crystalline plagioclase but some are glassy; because of limited number of grains observed, relative abundance of crystalline and glassy phase is not clear.

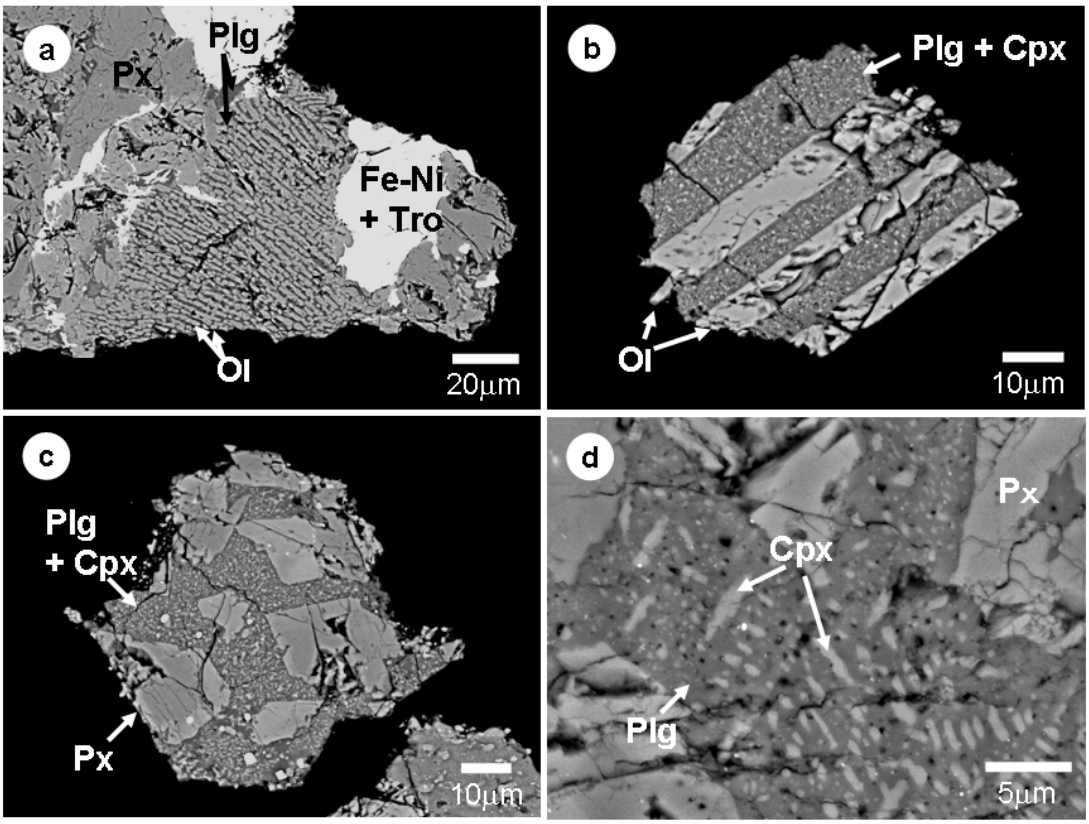

Figure 3. Backscattered electron images of 3A particles showing textures similar to the interior of chondrules in chondrites. (a, b) Barred olivine type. (c) Porphyritic pyroxene type.(d) High-magnification image of boxed area in Fig. 2b, obtained using the field emission SEM, showing quenched crystallites of high-Ca pyroxene (Cpx) in plagioclase (Plg) mesostasis. Fe-Ni = Fe-Ni metal, Tro = troilite, Ol = olivine, Px = low-Ca pyroxene.

3.2. Mineral Compositions

Olivine is very homogeneous, averaging $Fa_{15.8}$ (standard deviation in Fa content = 0.6) (Table 2; Fig. 6). It contains significant amounts of Mn (～0.5 wt% MnO) and extremely low amounts of Ca (<0.05 wt% CaO), Ti (<0.05 w% TiO_2) and Cr (<0.05wt% Cr_2O_3).

Low-Ca pyroxene is also very homogeneous, averaging $Fs_{14.2}$ (standard deviation in Fs content=1.0) (Fig. 7) and $Wo_{0.9}$ (Table 2; Fig. 8). It contains significant amounts of Al (～0.2 wt% Al_2O_3), Cr (～0.2 wt% Cr_2O_3) and Mn (～0.5 wt% MnO). High-Ca pyroxene is also homogeneous in Fs content, averaging $Fs_{6.4}$ (standard deviation in Fs content = 0.9) and $Wo_{40.2}$ (Table 2), but shows slight variations in Ca content (standard deviation in Wo content = 4.1) (Fig. 8). High-Ca pyroxene contains significant amounts of Na (～0.7 wt% Na_2O), Al (～1.5 wt% Al_2O_3), Ti (～0.5 wt% TiO_2), Cr (～1.5 wt% Cr_2O_3) and Mn (～0.3 wt% MnO).

Plagioclase is albitic (Na-rich). In contrast to olivine and pyroxene, it is variable in composition from grain to grain, ranging from An_{12} to An_{33} (Table 2; Fig. 9).

Kamacite contains ～5.5 wt% Ni and ～0.45 wt% Co (Table 3). Taenite contains ～33.0 wt% Ni and trace amounts of Co (～0.07 wt%). Ni contents in taenite show considerable variation (28-40 wt% Ni) from grain to grain.

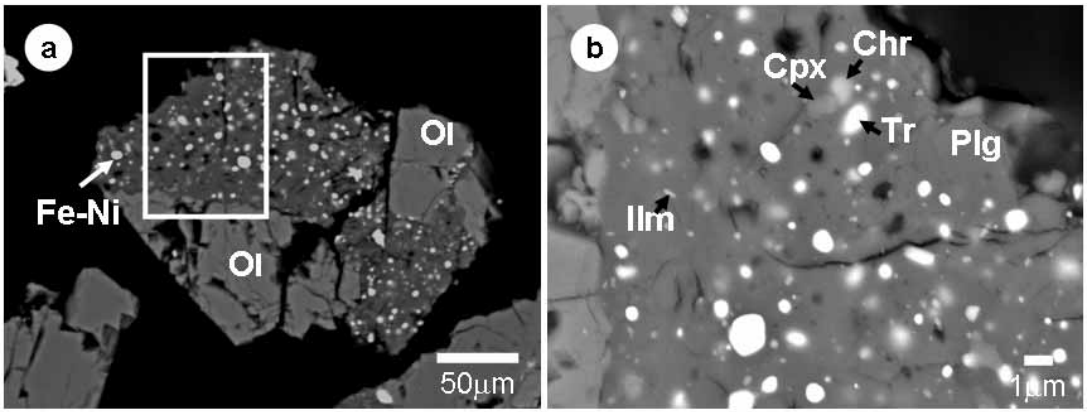

Figure 4. (a) Backscattered electron image of a 3A particle that contains numerous submicron-size spherical inclusions and vesicles in plagioclase (Plg). (b) High-magnification image of boxed area in (a), obtained using the field emission SEM, showing inclusions of high-Ca pyroxene (Cpx), ilmenite (Ilm), chromite (Chr), and troilite (Tro) grains and vesicles (dark in contrast) in plagioclase. Fe-Ni = Fe-Ni metal, Ol = olivine, Px = low-Ca pyroxene.

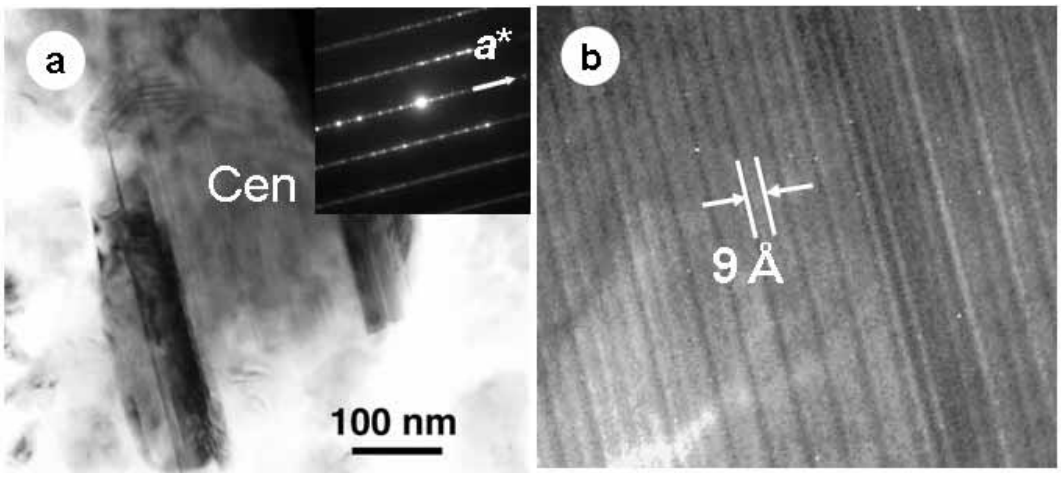

Figure 5. (a) TEM image of a low-Ca pyroxene (clino-enstatite: Cen) grain in the 3A sample. The selected-area electron diffraction (SAED) pattern from this grain (inset) shows diffuse streaks along a^* with intensity maxima corresponding to clino-enstatite. (b) High-resolution TEM image of the grain in (a) showing irregularities produced by stacking faults between ortho- and clino-enstatite.

Table 2. Electron microprobe analyses of olivine, low-Ca pyroxene, high-Ca pyroxene and plagioclase in the 3A sample (wt%).

	Olivine		Low-Ca pyroxene		High-Ca pyroxene		Plagioclase	
No. of Analyses	33	s.d.	45	s.d.	5	(s.d.)	9	(s.d.)
Na_2O	0.01	(0.01)	0.02	(0.02)	0.73	(0.09)	8.61	(0.68)
MgO	45.1	(0.4)	32.5	(0.7)	18.6	(1.3)	0.33	(0.21)
Al_2O_3	0.01	(0.01)	0.19	(0.12)	1.48	(0.95)	22.9	(1.3)
SiO2	39.0	(0.4)	56.2	(0.5)	53.8	(0.6)	62.1	(2.1)
K_2O	0.00	(0.01)	0.01	(0.01)	0.01	(0.01)	0.26	(0.08
CaO	0.02	(0.02)	0.6	(0.28)	19.5	(1.9)	4.77	(1.37)
TiO_2	0.03	(0.04)	0.10	(0.08)	0.49	(0.31)	0.17	(0.13)
Cr_2O_3	0.02	(0.03)	0.18	(0.13)	1.53	(0.19)	0.29	(0.44)
MnO	0.45	(0.04)	0.48	(0.07)	0.34	0.03)	0.02	(0.02)
FeO	15.1	(0.6)	9.69	(0.65)	3.95	(0.53)	0.59	(0.28)
NiO	0.01	(0.02)	0.01	(0.02)	0.02	(0.03)	0.01	(0.01)
Total	99.8		99.9		100.4		100.0	
Mol%								
Fa	15.8	(0.6)	-	(-)	-	(-)	-	(-)
Fs	-	(-)	14.2	(1.0)	6.4	(0.9)	-	(-)
Wo	-	(-)	0.9	(0.5)	40.2	(4.1)	-	(-)
Ab	-	(-)	-	(-)	-	(-)	75.5	(6.1)
An	-	(-)	-	(-)	-	(-)	23.1	(6.5)
Or	-	(-)	-	(-)	-	(-)	1.5	(0.5)

s.d.: standard deviation.

Table 3. Electron microprobe analyses of kamacite, taenite and troilite in the 3A sample (wt%).

	Kamacite}		Taenite		Troilite	
No. of Analyses	27	(s.d.)	13	(s.d.)	11	(s.d.)
P	0.00	(0.00)	0.00	(0.00)	0.00	(0.00)
Si	0.01	(0.01)	0.01	(0.01)	0.01	(0.01)
S	0.00	(0.00)	0.02	(0.04)	36.9	(0.1)
Cr	0.01	(0.01)	0.01	(0.02)	0.01	(0.01)
Fe	93.8	(0.6)	66.2	(4.7)	62.8	(0.4)
Ni	5.46	(0.40)	33.0	(4.4)	0.04	(0.10)
Co	0.45	(0.01)	0.17	(0.08)	0.00	(0.00)
Total	99.8		99.4		99.8	

s.d.: standard deviation.

Because Ca-phosphate and chromite occur as very fine grains (<2 μm), it was difficult to obtain good quantitative analyses from them. Ca-phosphate contains Cl but no F, and thus is probably chlorapatite. Chromite contains considerable Al, Mg, appreciable Mn and Ti.

4. RESULTS ON 3B SAMPLE

4.1. Petrography and Mineralogy

4.1.1. General Petrography

Optical microscope and SEM observations of the thin sections indicate that they consist mainly of Fe-Ni metal and silicates (Figs. 10a, b). X-ray chemical mapping also enables us to visualize the distribution of metal and silicates in the particles (Figs.

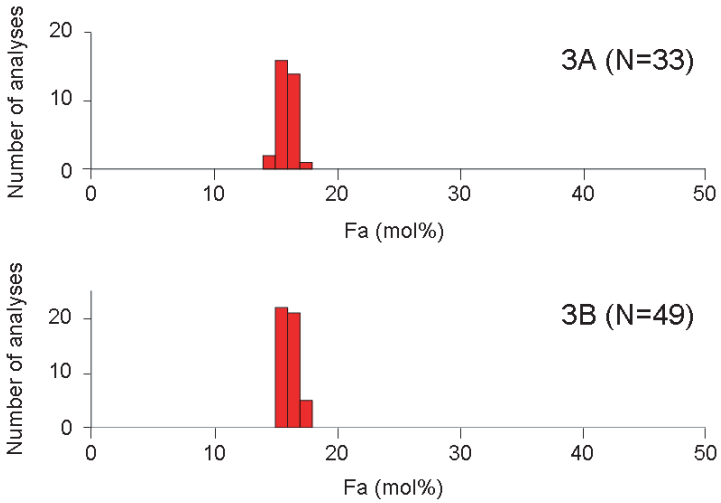

Figure 6. Fayalite concentrations in olivine in the 3A and 3B samples. Shown in the parentheses are number of analyses.

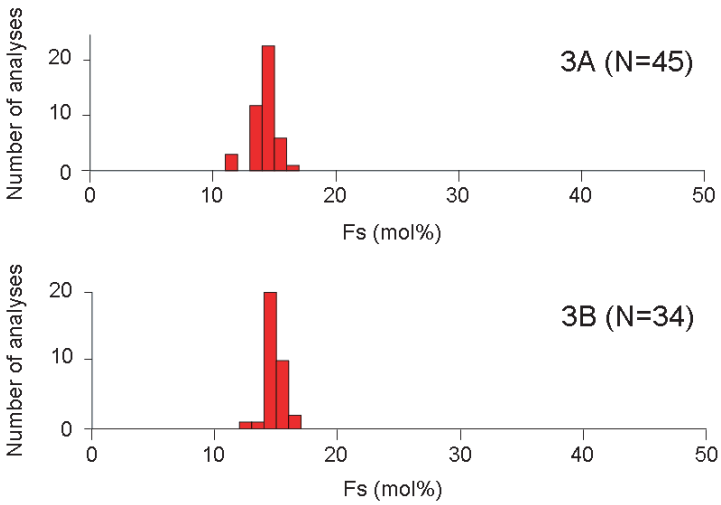

Figure 7. Ferrosilite concentrations in low-Ca pyroxene in the 3A and 3B samples. Shown in the parentheses are number of analyses.

11a-d). Fe-Ni metal fills interstices between silicate grains and is volumetrically the most abundant phase. The modal analysis indicates that metal comprises 42-72 vol% of each sample; the rest are mostly silicates (Table 1). Silicates are mainly olivine, low-Ca pyroxene and lesser amounts of high-Ca pyroxene and plagioclase. The silicates occur as rounded to subrounded aggregates (100 to 400 μm in diameter) and also as irregularly shaped aggregates (500-1000 μm) (Figs. 10a, b); the latter occur along the edge of individual particles and appear to be part of larger aggregates. Their external shape and internal texture suggest that they are chondrules and chondrule fragments. Olivine and low-Ca pyroxene also occur as single mineral fragments that are commonly rounded to subrounded in shape and range in diameter from 10 to 100 μm. Minor minerals are troilite, chromite and Ca-phosphate. Neither hydrous minerals nor Ca-Al-rich inclusion-like materials have been observed.

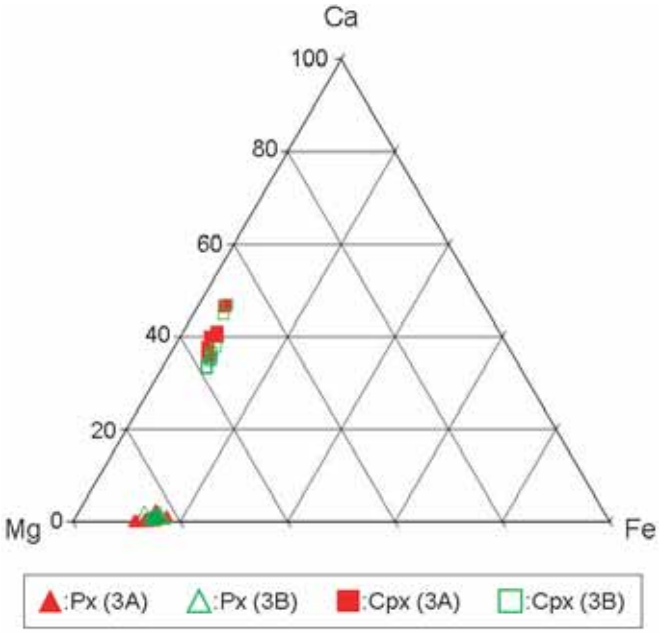

Figure 8. Analyses of low-Ca and high-Ca pyroxene in the 3A and 3B samples in terms of atomic percents of Ca, Mg, and Fe.Px = low-Ca pyroxene, Cpx = high-Ca pyroxene.

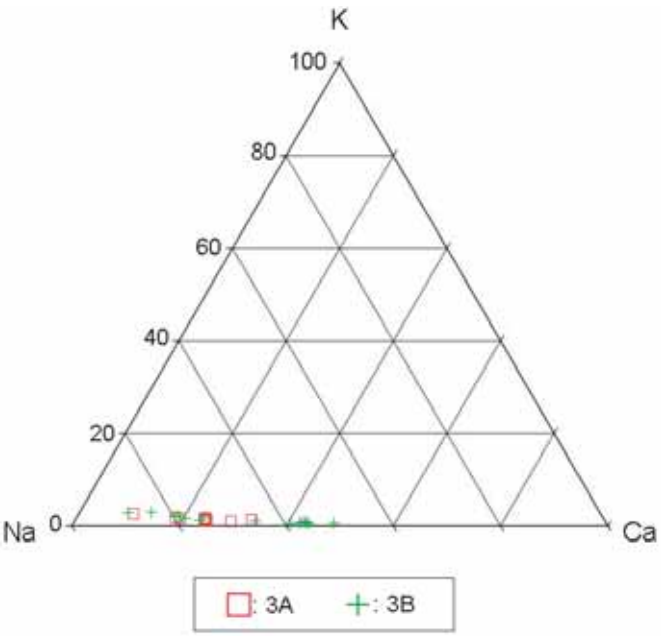

Figure 9. Analyses of plagioclase in the 3A and 3B samples in terms of atomic percents of K, Na, and Ca.

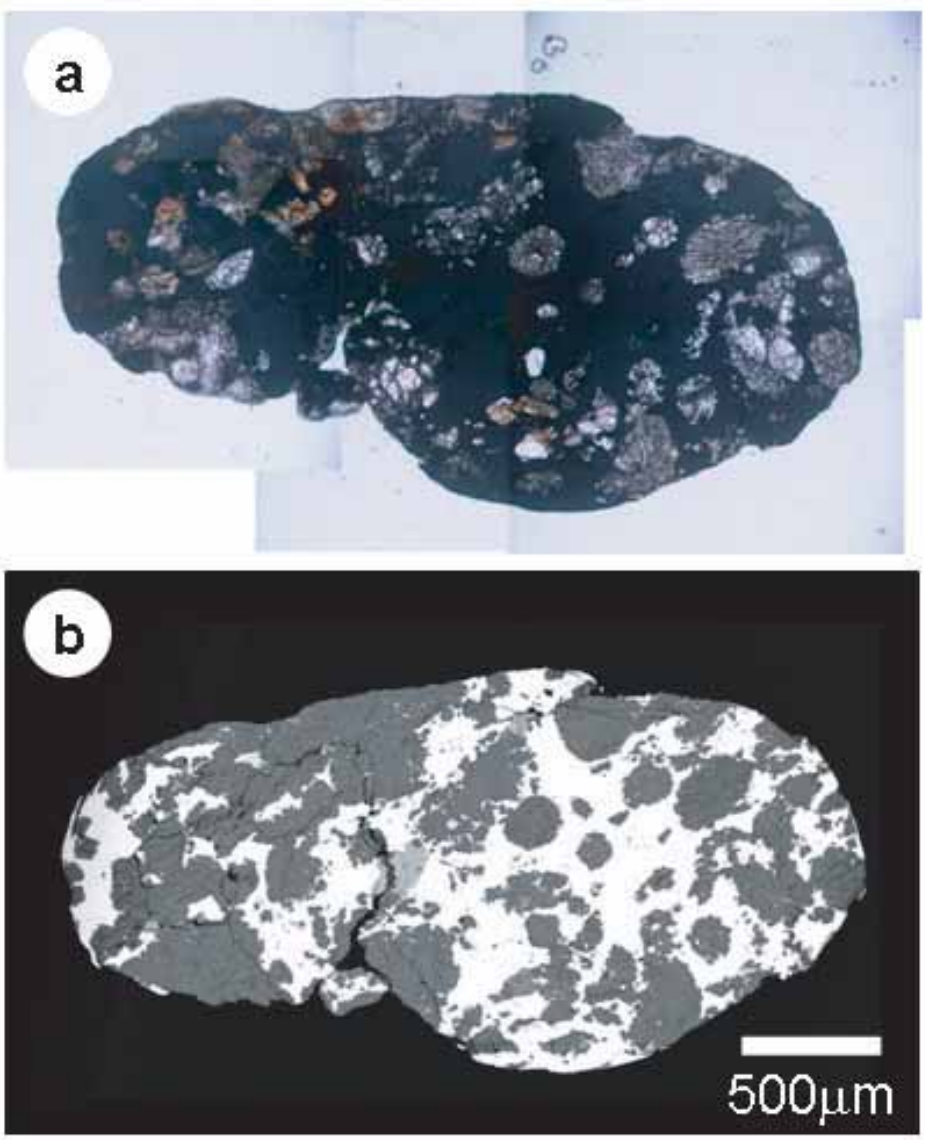

Figure 10. (a) Transmitted, plane-polarized light image of a thin section of the largest particle in the 3B sample. (b) Backscattered electron image of the same particle. The grayish areas consist of silicates, whereas the whitish areas consist of Fe-Ni metals.Note that the particle contains many chondrule-like silicate aggregates.

4.1.2. Silicate Aggregates

Silicate aggregates have porphyritic olivine (PO), porphyritic olivine-pyroxene (POP), and barred olivine (BO) type textures (Figs. 12a-d); other minor textural types include granular olivine (GO) and porphyritic pyroxene (PP). Olivine and low-Ca pyroxene occur as phenocrysts that range in size from 5 to 50 μm. Mesostases are filled with a material that is compositionally consistent with plagioclase; because of small grain size, it was difficult to optically confirm the presence of glass in the mesostasis; thus we call the mesostasis phase plagioclase. The plagioclase commonly contains fine, acicular to lath-shaped quenched crystallites (1-2 μm in width and 5-30 μm in length) of high-Ca pyroxene, mostly diopside (Fig. 12d). In places, it contains numerous vesicles (<2 μm in diameter) and micro-inclusions (<2 μm in diameter) of chromite and ilmenite. Troilite occurs as grains 1-20 μm in diameter; its abundance is much less than in 3A. Ca-phosphate occurs as irregularly shaped grains 20-100 μm in size. Although the silicate aggregates have a close resemblance to chondrules, no fine-grained matrix-like material has been found.

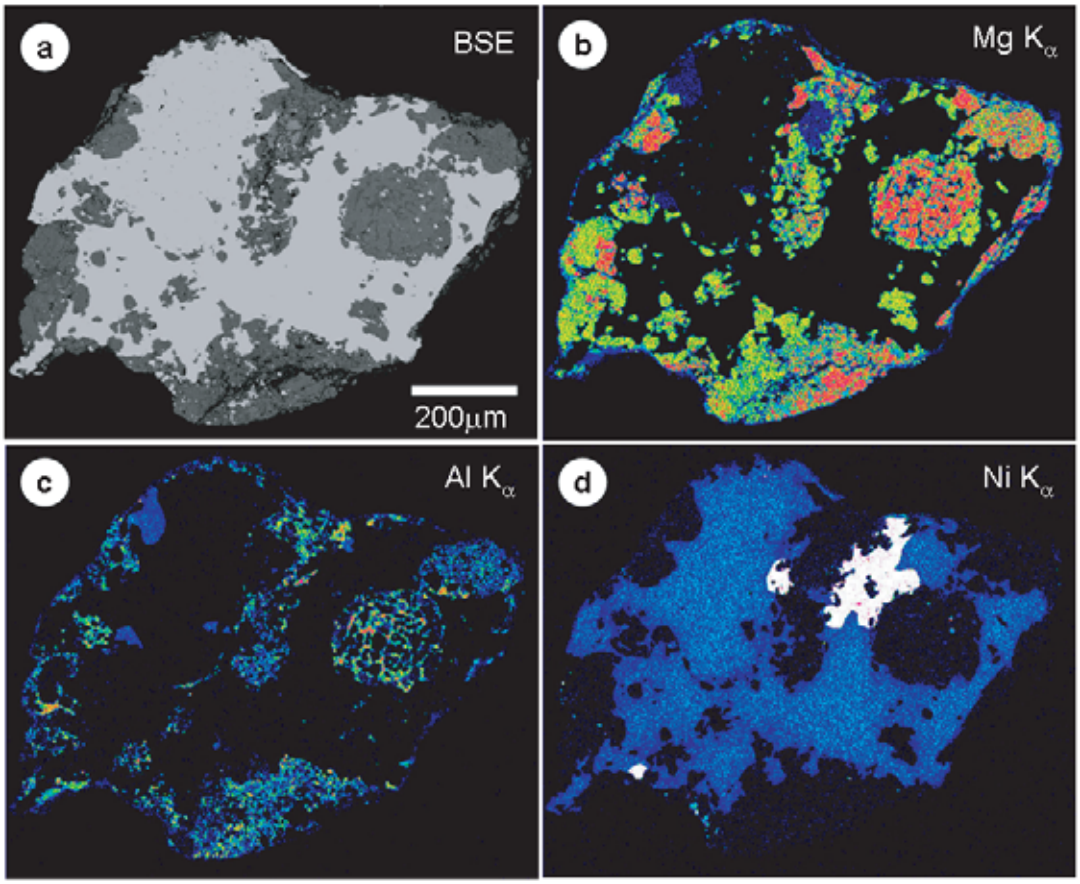

Figure 11. Backscattered electron image (a) and X-ray chemical maps of Mg K_α (b), Al K_α (c) and Ni K_α (d) of a 3B particle. In the X-ray chemical maps, the brighter an area is, the higher the concentration of an element is.Mg concentrations in (b) correspond to olivine and low-Ca and high-Ca pyroxene, Al concentrations in (c) to plagioclase, high-Ca pyroxene and chromite, and Ni concentrations in (d) to kamacite and taenite (bright grains). The map of Ni K_α (d) shows that kamacite grains exhibit compositional zoning, with a core of Ni-rich kamacite surrounded by a rim of more Ni-poor kamacite.

4.1.3. Metals

The predominant metal is kamacite. Minor amounts of taenite coexist with kamacite as grains ranging in size from 50 to 200 μm. Low-contrast BSE imaging reveals that kamacite shows a lamellae texture that consists of parallel oriented bands (1-10 μm in width) of Ni-poor kamacite in Ni-rich kamacite. X-ray chemical mapping shows that kamacite grains exhibit compositional zoning, with higher Ni contents in their cores than at their edges (Fig. 11d). Taenite grains also exhibit compositional zoning, with a core of Ni-poor taenite surrounded by a rim of more Ni-rich taenite.

4.1.4. Minor Minerals

Troilite and chromite occur as massive grains (5-50 μm in diameter) commonly near grain boundaries between metal and silicates. Two exceptionally large chromite grains (～200 μm and ～100 μm in diameter) are found in two different 3B particles.

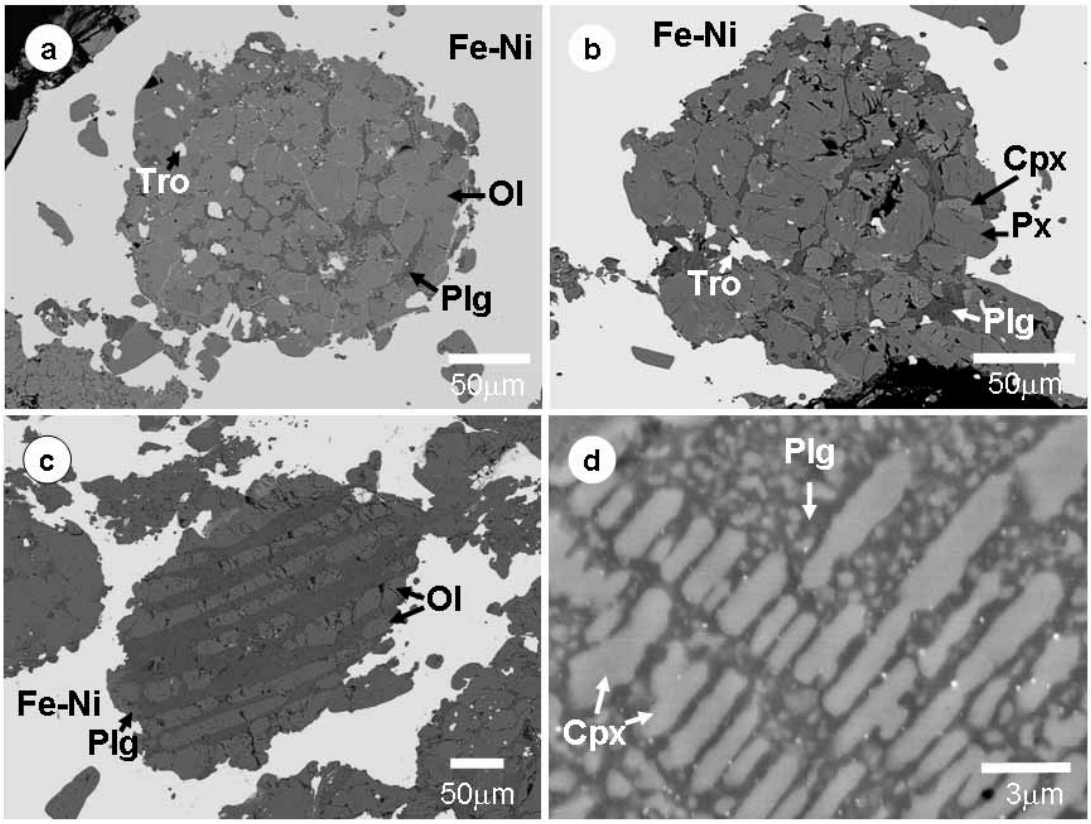

Figure 12. Backscattered electron images of chondrule-like silicate aggregates in 3B particles. (a) Porphyritic olivine type. (b) Porphyritic pyroxene type. (c) Barred olivine type. (d) High-magnification image of a portion of chondrule-like silicate aggregate, obtained using the field emission SEM, showing quenched crystallites of high-Ca pyroxene (Cpx) in plagioclase (Plg) mesostasis..Fe-Ni = Fe-Ni metal, Tro = troilite, Ol = olivine, Px = low-Ca pyroxene.

4.1.5. Shock Stage

In order to determine shock stage, we examined 14 olivine grains that are >50 μm in diameter in the 3B-1 and 3B-2 particles by the optical microscope. All the olivine grains exhibit sharp extinction, thus indicating that 3B is shock stage S1 (Stöffler et al., 1991), which means that it has no significant shock effects.

4.2. Mineral Compositions

Olivine is very homogeneous, averaging $Fa_{16.2}$ (standard deviation in Fa content = 0.6) (Table 4; Fig. 6). Olivine contains significant amounts of Mn (～0.5 wt% MnO) and trace amounts of Ca (<0.05 wt% CaO), Ti (<0.05 wt% TiO_2) and Cr (<0.1 wt% Cr_2O_3). It should be noted that these compositional characteristics are almost identical to those of the olivine in 3A.

Low-Ca pyroxene is also very homogeneous, averaging $Fs_{14.8}$ (standard deviation in Fs content = 0.8) (Fig. 7) and $Wo_{1.0}$ (Table 4; Fig. 8). It contains significant amounts of Al (～0.2 wt% Al_2O_3), Cr (～0.2 wt% Cr_2O_3), Mn (～0.5 wt% MnO). High-Ca pyroxene is also homogeneous, averaging $Fs_{7.5}$ (standard deviation in Fs content = 1.1) and $Wo_{37.3}$ (standard deviation in Wo content = 4.3), but less homogeneous than low-Ca pyroxene (Fig. 8). High-Ca pyroxene contains significant amounts of Na (～0.6 wt% Na_2O), Al (～4.0 wt% Al_2O_3), Ti (～0.7 wt% TiO_2), Cr (～1.7 wt% Cr_2O_3) and Mn (～0.4 wt% MnO). We note that, like olivine, the compositions of both low-Ca and high-Ca pyroxenes are closely similar to those in 3A.

Plagioclase is albitic (Na-rich) and variable in composition from grain to grain, ranging from An_{15} to An_{37} (Table 4; Fig. 9). The compositional characteristics are very similar to those of plagioclase in 3A.

Kamacite contains ～6.0 wt% Ni and ～0.45 wt% Co (Table 5). Taenite contains 50.1 wt% Ni and extremely low amounts of

Table 4. Electron microprobe analyses of olivine, low-Ca pyroxene, high-Ca pyroxene, plagioclase and chromite in the 3B sample (wt%).

	Olivine		Low-Ca		High-Ca		Plagioclase		Chromite	
No. of Analyses	49	(s.d.)	34	(s.d.)	10	(s.d.)	15	(s.d.)	6	(s.d.)
Na_2O	0.01	(0.01)	0.02	(0.02)	0.61	(0.14)	7.40	(1.35)	0.04	(0.02)
MgO	45.0	(0.6)	32.5	(0.4)	18.3	(1.5)	0.07	(0.13)	3.99	(1.39)
Al_2O_3	0.01	(0.02)	0.21	(0.19)	3.99	(0.60)	25.3	(2.2)	5.88	(0.24)
SiO_2	39.2	(0.4)	56.2	(0.5)	51.5	(0.5)	59.8	(4.0)	0.02	(0.02)
K_2O	0.00	(0.01)	0.00	(0.01)	0.00	(0.01)	0.22	(0.14)	0.00	(0.00)
CaO	0.03	(0.10)	0.55	(0.23)	17.2	(1.8)	6.19	(2.70)	0.00	(0.00)
TiO_2	0.04	(0.05)	0.08	(0.05)	0.67	(0.22)	0.04	(0.02)	1.42	(0.14)
Cr_2O_3	0.05	(0.07)	0.20	(0.26)	1.67	(0.13)	0.03	(0.06)	58.6	(0.6)
MnO	0.45	(0.04)	0.49	(0.06)	0.35	(0.06)	0.01	(0.01)	1.46	(0.16)
FeO	15.5	(0.6)	10.2	(0.6)	4.47	(0.71)	0.61	(0.30)	27.4	(1.6)
NiO	0.02	(0.03)	0.03	(0.06)	0.01	(0.01)	0.01	(0.02)	0.02	(0.03)
Total	100.3		100.5		98.8		99.7		98.8	
Mol%										
Fa	16.2	(0.6)	-	(-)	-	(-)	-	(-)	-	(-)
Fs	-	(-)	14.8	(0.8)	7.5	(1.1)	-	(-)	-	(-)
Wo	-	(-)	1.0	(0.4)	37.3	(4.7)	-	(-)	-	(-)
Ab	-	(-)	-	(-)	-	(-)	68.4	(10.7)	-	(-)
An	-	(-)	-	(-)	-	(-)	25.8	(11.2)	-	(-)
Or	-	(-)	-	(-)	-	(-)	1.5	(0.7)	-	(-)

s.d.: standard deviation.

Table 5. Electron microprobe analyses of kamacite, taenite and troilite in the 3B sample (wt%).

	Kamacite		Taenite		Troilite	
No. of Analyses	87	(s.d.)	18	(s.d.)	11	(s.d.)
P	0.00	(0.00)	0.00	(0.00)	0.00	(0.00)
Si	0.01	(0.02)	0.01	(0.01)	0.05	(0.02)
S	0.00	(0.00)	0.00	(0.00)	36.9	(0.2)
Cr	0.02	(0.05)	0.01	(0.01)	0.02	(0.02)
Fe	93.8	(0.7)	49.3	(1.4)	62.8	(0.6)
Ni	5.95	(0.42)	50.1	(1.5)	0.01	(0.01)
Co	0.45	(0.02)	0.07	(0.01)	0.00	(0.00)
Total	99.8		99.4		99.8	

s.d.: standard deviation.

Co (～0.07 wt%). The slight compositional variation in taenite (standard deviation in Ni content = 4.4 wt%) may be ascribed to the core-to-rim Ni zoning. Kamacite closely resembles in composition that in 3A, whereas taenite is considerably richer in Ni content than that in 3A.

Chromite contains considerable Mg (～4.0 wt% MgO), Al (～5.9 wt% Al_2O_3), appreciable Ti (～1.4 wt% TiO_2) and Mn (～1.5 wt% MgO) (Table 4). Ca-phosphate contains neither Cl nor F.

5. DISCUSSION

5.1. 3A sample

We initially assumed that this test sample is powder prepared by crushing and grinding a meteorite sample, and we tried to

determine its classification based on petrographic and mineralogical characteristics.

At the early stage of our study, we found that particles in 3A contain materials that are obviously part of chondrules. They are similar to the most common textural types of chondrules in chondrites such as PO, PP and BO. Therefore, we thought that 3A is probably powder of a chondrite. The major constituent minerals are Fe-rich olivine and pyroxene that are highly homogeneous in composition. These characteristics led us to further assume that this sample is an equilibrated ordinary chondrite that belongs to one of H, L and LL groups. Most major and minor minerals in 3A occur in equilibrated ordinary chondrites (OC). Equilibrated OC are classified as petrologic types 4-6 that have undergone significant equilibration as a result of thermal metamorphism on meteorite parent bodies. Major constituent minerals of type 4-6 OC are olivine, low-Ca pyroxene and Fe-Ni metal, and their compositions can be used as fundamental diagnostic properties to determine the classification of OC into H, L and LL.

5.1.1. Chemical Group

It is well established that olivine and low-Ca pyroxene compositions in type 4-6 OC from H, L and LL groups fall in well-defined fields in a plot of the fayalite (Fa) content versus the ferrosilite (Fs) content (e.g., Mason, 1963; Keil and Fredriksson, 1964; Sears and Axon, 1976; Afiattalab and Wasson, 1980; Rubin, 1990) (Fig. 13). Molar Fe/(Fe+Mg) ratios in both olivine and low-Ca pyroxene increase linearly with overall oxidation state of the chondrite. Our study revealed that the compositions of olivine and low-Ca pyroxene in 3A are plotted near the Fe-poor end within the H chondrite field (Fig. 13).

Minor element contents of olivines in type 4-6 OC are known to be very uniform, regardless of chemical group (e.g., Brearley and Jones, 1998). MnO contents are between 0.4 and 0.5, but TiO_2, Al_2O_3, Cr_2O_3 and CaO contents are all extremely low, <0.1 wt%. All the minor element contents of olivine in 3A are consistent with those in type 4-6 OC (Table 2).

Low-Ca pyroxenes in type 4-6 OC have <2 mol% Wo ($CaSiO_3$) contents and contain various minor elements that show significant ranges, but MnO and Cr_2O_3 contents are relatively uniform, 0.4-0.5 wt% and 0.1-0.2 wt%, respectively (e.g., Brearley and Jones, 1998). The Wo contents and the minor element contents of low-Ca pyroxene in 3A also fall in the ranges for those in type 4-6 OC.

High-Ca pyroxenes in type 4-6 OC have relatively narrow ranges of Fs content. However, like low-Ca pyroxene, mean Fs contents for each chondrite group have a tendency to increase from Fs_7 (H) to $Fs_{8.5}$ (L) to Fs_{10} (LL) (Brearley and Jones, 1998). The mean Fs content of high-Ca pyroxene in 3A ($Fs_{6.4}$) most closely fits the H group.

Metals in type 4-6 OC have been extensively studied in the past, and the relationship between their compositions and chondrite groups has been well established. Previous workers (Sears and Axon, 1975, 1976; Afiattalab and Wasson, 1980; Rubin, 1990) showed that Co contents in kamacite progressively increase, whereas Ni contents decrease from H to L to LL chondrites, and that Co and Ni contents fall in distinct ranges within each of the different groups (Fig. 14). On the other hand, Co and Ni contents in taenite also fall in different ranges, although the resolution of the ranges is not as distinct as kamacite. Both Co and Ni contents in kamacite and taenite in 3A fall in the ranges for H chondrites (Fig. 14).

Because fayalite (Fa) contents in olivine and Co contents in kamacite are excellent parameters for OC classification as shown above, Kallemeyn et al. (1989) and Rubin (1990) constructed a plot of Co content versus Fa content (Fig. 15). The plot shows the beautiful exponential relationship. H chondrites form a tight cluster at the lower left that is well separated from L and LL chondrites that form clusters at the center and the right, respectively. The 3A sample falls near the Fa-poor and Co-poor end within the H chondrites cluster (Fig. 15).

In summary, the compositional characteristics of olivine, low-Ca and high-Ca pyroxene and Fe-Ni metals in 3A are the most similar to those in equilibrated ordinary chondrites of H type among the known chondrite groups. The compositional characteristics of other minerals, including plagioclase, chromite and phosphate, are also similar to those in equilibrated H chondrites.

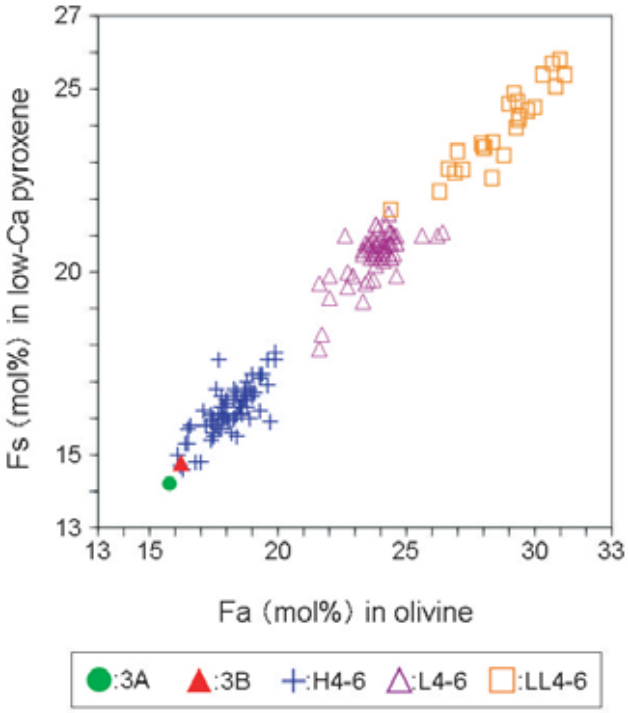

Figure 13. Fs vs Fa contents (mol%) of low-Ca pyroxene and olivine in the 3A and 3B samples and the type 4-6 ordinary chondrites.Data source of ordinary chondrites: Brearley and Jones (1998).

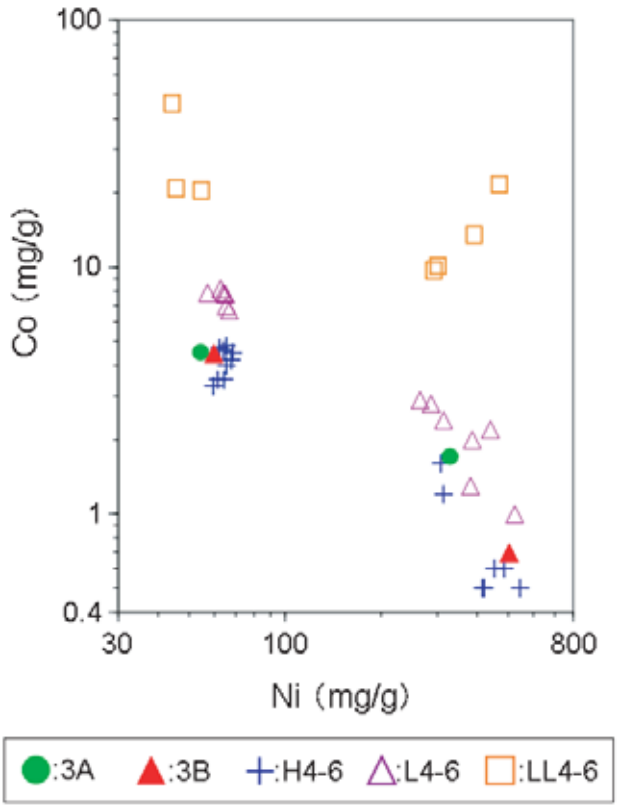

Figure 14. Co vs Ni (mg/g) diagram for kamacite and taenite in the 3A and 3B samples and the type 4-6 ordinary chondrites.Data source of ordinary chondrites: Brearley and Jones (1998).

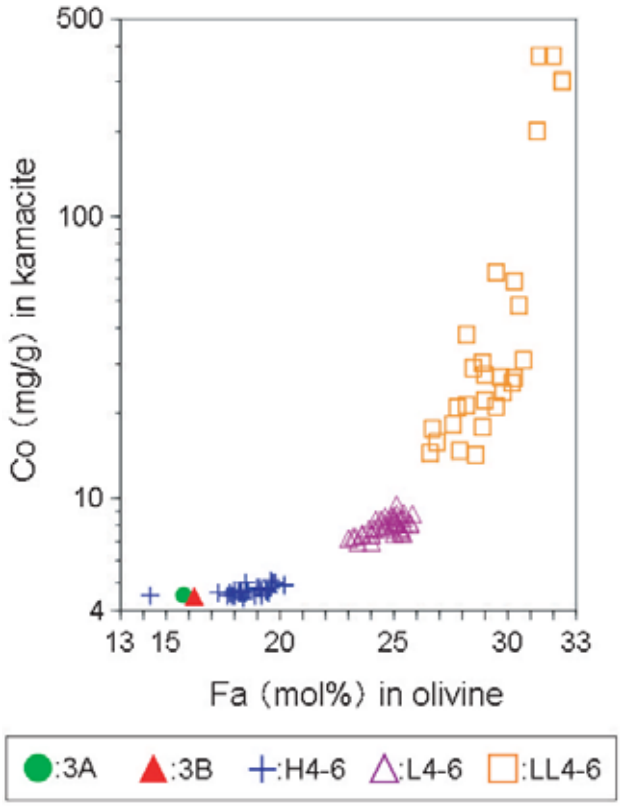

Figure 15. Co (mg/g) vs Fa (mol%) contents of kamacite and olivine in the 3A and 3B samples and the type 4-6 ordinary chondrites.Data source of ordinary chondrites: Brearley and Jones (1998).

5.1.2. Petrologic Type

Because 3A is powder consisting of small particles (<150 μm in diameter), it was difficult to determine petrologic type of its parent chondrite from petrographic characteristics. However, fine-grained olivine and pyroxene that appear to have constituted chondrite matrix are abundant in the particles, and chondrule mesostasis with fine-grained quenched crystallites are well preserved. TEM observations showed that most low-Ca pyroxene grains are clino-pyroxene and glassy grains with plagioclase composition are present. All these characteristics suggest that the parent chondrite is relatively low petrologic type, perhaps type 4.

It is known that Fa contents of olivine and Fs contents of low-Ca pyroxene within each of H, L and LL chondrite groups show slight increases as a function of petrologic type, although the changes are not so remarkable (Scott et al., 1986; Rubin, 1990; McSween and Labotka, 1993; Brearley and Jones, 1998). The increases may be due to progressive oxidation that occurred during metamorphism in the OC parent bodies (McSween and Labotke, 1993). Both olivine and low-Ca pyroxene compositions in 3A fall near the Fe-poor end within the H chondrite range (Fig. 15), which also supports our view that 3A can be classified into a relatively low petrologic type.

5.1.3. Shock Metamorphic Effects

Because we did not make regular thin sections, we could not precisely determine shock stage of 3A. Our limited observations, using a transmitted light optical microscope, show that some olivine grains exhibit weak undulatory extinction, but they are minor in abundance, which suggests that shock metamorphic effects are very minor. The dislocation-poor nature of olivine and the low degree of stacking disorder in clino-pyroxene are also consistent with the minor effects of shock metamorphism. However, we found some evidence suggesting shock effects. Plagioclase in some particles contains numerous

vesicles and micro-inclusions of Fe-Ni metal and troilite (Figs. 4a, b). The texture is similar to the vesicular, inclusion-rich plagioclase in CK chondrites (Tomeoka et al., 2001, 2005), which has been regarded as a product of recrystallization from shock-induced melts. However, because of very limited data available, it is difficult to further confirm the relationship between plagioclase in 3A and CK chondrites.

5.2. 3B sample

As in the case of 3A, we assumed that 3B has been prepared by crushing and grinding a meteorite sample and tried to determine its classification. At the beginning, however, we were puzzled with the peculiar rounded, potato-like morphology of the particles and the predominant occurrence of Fe-Ni metal (42-72 vol%) in the particles. We thought that it is difficult to produce such uniformly rounded particles simply by crushing and grinding a meteorite sample and it is also difficult to crush such a metal-rich rock to produce such small particles.

Silicate-rich portions in the 3B particles occur as aggregates that are analogous in texture to chondrules in chondrites. Some are fragments, most of which appear to have been derived from larger complete chondrules. Most of the major textural types of chondrules including PO, POP, BO, GO and PP are present. Few large fragments preserve arcuate edges with large radii of curvature. From these observations, we thought that 3B has been prepared from a chondrite, like 3A. Because of high abundance of Fe-Ni metal, we initially assumed that 3B belongs to one of the metal-rich chondrite groups such as CB, CH and CR. However, as we studied the details of mineralogy and petrology, we became to be suspicious of this assumption, since many mineralogical and petrological characteristics of 3B do not exactly fit any of the known metal-rich chondrites.

The major constituent minerals of the silicate aggregates, which we identified as chondrules, in 3B are Fe-rich olivine and pyroxene that are highly homogenous in composition. To our surprise, the compositions of both olivine and low-Ca pyroxene are almost identical to those in 3A (Tables 2 and 4). In addition, the compositions of kamacite are also indistinguishable from those in 3A (Tables 3 and 5). All these results indicate that 3B is related to equilibrated H chondrites. After knowing these results, we recognized the possibility that 3B does not necessarily represent a bulk meteorite but a fraction of a meteorite. We envisaged that the rounded 3B particles may correspond to individual metal grains contained in an H chondrite.

It is known that equilibrated H chondrites contain ～8.4 vol% Fe-Ni metal (e.g., Krot et al., 2004), which occurs as grains typically 0.1-3 mm in size, evenly distributed throughout the meteorites, in addition to globules which occur inside chondrules. Those metal grains commonly contain chondrules and chondrule fragments, bearing a close resemblance to the 3B particles. We presume that, if such chondrule-bearing metal grains are separated from the parent meteorite and ground by a mortar, such rounded (potato-like) mineral assemblages as seen in the 3B particles would be produced.

In addition to the major minerals in 3B, most of less abundant minerals, including high-Ca pyroxene, plagioclase, chromite, phosphate and taenite, also have compositions being similar to those of the counterparts in equilibrated H chondrites (e.g., Brearley and Jones, 1998). Other mineralogical and petrological characteristics in 3B such as (1) chondrule textures, (2) lamellae texture in kamacite, (3) compositional zoning in kamacite and taenite are also known to be common in equilibrated OC (Gooding and Keil, 1981; Brearley and Jones, 1998; Willis and Goldstein, 1983; Wood, 1967; Nagahara, 1979). Therefore, we conclude that 3B is probably related to equilibrated H chondrites. As discussed above (section 5.1), Fa contents of olivine and Fs contents of low-Ca pyroxene in 3B suggest that its petrologic type is relatively low.

6. SUMMARY

The general appearance and mineral abundances of the 3A and 3B sample are very different. 3A is composed of angular to irregularly shaped particles (<150 μm in diameter) that consist mainly of Fe-rich olivine, low-Ca pyroxene and lesser amounts of high-Ca pyroxene and plagioclase, whereas 3B is composed of rounded to subrounded particles (0.2-2.3 mm in diameter) that consist mainly of Fe-Ni metal and lesser amounts of Fe-rich olivine and low-Ca pyroxene. However, the results of our study revealed that most of the constituent minerals in 3A and 3B occur in common, and almost all of them have very similar

compositions that are most similar to those of the counterparts in equilibrated H ordinary chondrites. Therefore, we suggest that 3A is powder made of a silicate-rich fraction of an H chondrite sample and 3B is made of a metal-rich fraction of an H chondrite sample. 3B particles may be silicate-bearing metal grains that were separated from a disaggregated H chondrite sample. Because the compositions of olivine, low-Ca pyroxene and kamacite in 3A and 3B are very close to each other, we think it is possible that 3A and 3B have been prepared from the same meteorite. Although precise determination of petrologic type could not be made because of very small particle size, the mineralogical characteristics of 3A and 3B suggest that the petrologic type of both samples is relatively low.

Acknowledgments: We thank Mr. Y. Shibata for discussion about EPMA analyses of metals and Prof. Y. Tainosho for the use of FESEM. Electron microprobe analysis was performed at the Venture Business Laboratory, Kobe University. This work was supported by Grant-in-Aid (No. 16204042) and "The 21st Century COE Program of Origin and Evolution of Planetary Systems" of the Japan Ministry of Education, Culture, Sports, Science and Technology.

REFERENCES

Afiattalab, F. and Wasson, J.T., 1980, Composition of the metal phases in ordinary chondrites: Implications regarding classification and metamorphism, *Geochimica et Cosmochimica Acta*, **44**, 431-446.

Binzel, R.P., Rivkin, A.S., Bus, S.J., Sunshine, J.M. and Burbine, T.H., 2001, MUSES-C target asteroid (25143) 1998 SF36: A reddened ordinary chondrite, *Meteoritics and Planetary Science*, **36**, 1167-1172.

Brearley, A.J. and Jones, R.H., 1998, Chondritic meteorites, in Planetary Materials, Reviews in Mineralogy (ed. J. J. Papike) *Mineralogical Society of America*, **36**, 398.

Gooding, J.L. and Keil, K., 1981, Relative abundances of chondrule primary textural types in ordinary chondrites and their bearing on conditions of chondrule formation, *Meteoritics*, **16**, 17-43.

Kallemeyn, G.W., Rubin, A.E., Wang, D. and Wasson, J.T., 1989, Ordinary chondrites: Bulk compositions, classification, lithophile-element fractionations, and composition-petrographic type relationships, *Geochimica et Cosmochimica Acta*, **53**, 2747-2767.

Keil, K. and Fredriksson, K., 1964, The iron, magnesium, and calcium distribution in coexisting olivines and rhombic pyroxenes of chondrites, *J. Geophys. Res*., **64**, 3487-3515.

Krot, A.N., Keil, K., Goodrich, C.A. and Scott, E.R.D., 2004, Classification of Meteorites, 83-128., in Meteorites, Comets, and Planets (ed. A.M. Davis) Vol. 1 Treatise on Geochemistry (eds. H.D. Holland and K.K. Turekian), Elsevier-Pergamon, Oxford.

Lederer, S.M., Domingue, D.L., Vilas, F., Abe, M., Farnham, T.L., Jarvis, K.S., Lowry, S.C., Ohba, Y., Weissman, P.R., French, L.M., Fukai, H., Hasegawa, S., Ishiguro, M., Larson, S.M. and Takagi, Y., 2005, Physical characteristics of Hayabusa target Asteroid 25143 Itokawa, *Icarus*, **173**, 153-165.

Mason, B., 1963, Olivine composition in chondrites, *Geochimica et Cosmochimica Acta*, **27**, 1011-1023.

McSween, H.Y. Jr. and Labotka, T.C., 1993, Oxidation during metamorphism of the ordinary chondrites, *Geochimica et Cosmochimica Acta*, **57**, 1105-1114.

Nagahara, H., 1979, Petrological Study of Ni-Fe Metal in Some Ordinary Chondrites, *Mem. NIPR. Spec. Issue*., **15**, 111-122.

Rubin, A.E., 1990, Kamacite and olivine in ordinary chondrites: Intergroup and intragroup relationships, *Geochimica et Cosmochimica Acta*, **54**, 1217-1232.

Scott, E.R.D., Taylor, G.J., Keil, K., McKinely, S.G. and Wilson, I.E., 1986, Accretion, metamorphism and brecciation of ordinary chondrites: Evidence from petrologic studies of meteorites from Roosevelt Country, *Meteoritics*, **21**, 509.

Sears, D.W. and Axon, H.J., 1975, Metal of high Co content in LL chondrites, *Meteoritics*, **11**, 97-100.

Sears, D.W. and Axon, H.J., 1976, Ni and Co content of chondritic metal, *Nature*, **260**, 34-35.

Shibata, Y., 1996, Opaque minerals in Antarctic CO3 carbonaceous chondrites, Yamato-74135, -790992, -791717, -81020, -81025, -82050 and Allan Hills-77307, *Proc. NIPR symp. Antarct. Meteorites*, **9**, 79-96.

Stöffler, D., Keil, K. and Scott, E.R.D., 1991, Shock metamorphism of ordinary chondrites, *Geochimica et Cosmochimica Acta*, **55**, 3845-3867.

Tomeoka, K., Ohnishi, I. and Nakamura, N., 2001, Silicate darkening in the Kobe CK chondrite: Evidence for shock metamorphism at high temperature, *Meteoritics and Planetary Science*, **36**, 1535-1545.

Tomeoka, K., Kojima, T., Ohnishi, I., Ishii, Y. and Nakamura, N., 2005, The Kobe CK carbonaceous chondrite: Petrography, mineralogy and metamorphism, *Journal of Mineralogical and Petrological Sciences*, **100**, 116-125.

Willis, J. and Goldstein, J.I., 1983,A three-dimensional study of metal grains in equilibrated, ordinary chondrites, *Proc. Lunar Planet. Sci*., **14B**, 287-292.

Wood, J. A., 1967, Chondrites: Their metallic minerals, thermal histories, and parent planets, *Icarus*, **6**, 1-49.

Hayabusa Analogue Sample Analysis Using Synchrotron Imaging

By

Akira TSUCHIYAMA [1] , Kentaro UESUGI [2] and Tsukasa NAKANO [3]

Abstract: Densities of Hayabusa analog samples were measured without contamination using synchrotron X-ray microtomography at BL20XU of SPring-8 and an ultra-microbalance. The density of sample II-1A is 6.37 ± 0.02 g/cm^3. The density of sample II-1B were scattered (5.05-7.18 g/cm^3). This may caused by volume estimation problem in the microtomography due to the presence of a large amount of highly absorbed materials (probably Fe-Ni metal) and less absorbed materials (probably silicates). Increment of the number of projection in the tomographic imaging will solve the problem. Three-dimensional grain size distribution of sample II-1A was obtained by identification of individual grains in the 3-D CT images. This will give the basic physical poperties of regolith, which may be present on Itokawa¹s surface. Several phases were recognized in the 3-D CT images using CT value histograms of the images, and their 3-D distribution maps were obtained with the spatial resolution of down to about 0.5 ¾m. This will helpful for planning later destructive analyses. The density, phase estimation (probably plagioclase, Fe-Mg silicates, troilte, kamacite and taenite in sample II-1A and Fe-Mg silicates, kamacite and taenite in sample II-1B if meteorites are assumed) and their modes and textures suggest possibility of an ordinary chondrite (LL is favarable) with high petrologic type for sample II-1A and a stony iron for sample II-1B although the conclusion cannot be made definitely from the CT images alone. Subtraction microradiography was also applied to sample II-1A to search Zr-bearing minerals effectively for the Pb-Pb dating. Any Zr-bearing minerals were not observed within the spatial resolution of about a few ¾m, but zircon grains added in sample II-1A were easily recognized by this method.

1. INTRODUCTION

X-ray computed tomography (CT) is a non-destructive method that provides cross-sectional images (CT images) of objects using X-ray attenuation. Three-dimensional (3-D) internal structures can be obtained by stacking successive CT images. A synchrotron radiation (SR) source provides tunable, monochromatized, and naturally collimated (parallel) X-ray beams that have many advantages for CT (Flannery et al. 1987; Bonse and Busch 1996). Monochromatized beams eliminate beam hardening, which causes CT image artifacts, and thus permit CT values, which correspond to the X-ray linear attenuation coefficient (LAC) of a material obtained by tomographic reconstruction, to relate quantitatively to LACs (Tsuchiyama et al. 2005). Furthermore, collimated beams readily yield 3-D images with high spatial resolution. Uesugi et al. (1999, 2001) have developed a projection X-ray microtomographic system, named SP-μCT, using SR at SPring-8, a third generation SR facility at Nishi-harima, Hyogo Prefecture, Japan. SP-μCT has been applied to earth and planetary materials (e.g., Tsuchiyama et al. 2001, 2003ab; Nakashima et al. 2005). 3-D element images were also obtained by imaging objects just above and below the X-ray absorption edge energy of an element (the so-called “subtraction” method: e.g., Thompson et al. 1984) for Fe in a micrometeorite (Tsuchiyama et al. 2001) and Cs in a Cs-doped partially molten granite (Ikeda et al. 2004). In addition to the micotomography, we can also apply microradiography technique using SP-μCT to larger samples than those for the microtomography.

In this report, we applied the microtopmography and micoradiography at SPring-8 to Hayabusa analogue samples (HASPET

1 Department of Earth and Space Science, Graduate School of Science, Osaka University, Toyonaka, 560-0043, Japan

2 SPring-8/Japan Synchrotron Radiation Research Institute, Mikazuki, Hyogo Prefecture, 679-5198 Japan

3 Geological Survey of Japan/National Institute of Advanced Industrial Science and Technology, Tsukuba, 305-8567 Japan

samples), which were prepared by ISAS/JAXA for the second HASPET selection. 3-D structures of the samples are obtained non-destructively by the microtomography. The main purpose is to obtain the bulk densities of the samples non-destructively without contamination. In this menasurement, the densities are obtained from the volumes based on the 3-D structures and the masses, which are measured by an ultra-microbalance (>0.1 μg). This will be compared with the average density of Itokawa, which will be measured during ran-de-vous of the spacecraft with Itokawa, to estimate the internal structure of the asteroid in connection with the rubble pile model (Britt et al. 2003). It should be noted that we cannot use the Archimedian method, a conventional method for measuring the densities of meteorites (Britt and Consolmagno 2003), because Archimedian fluids, such as water and helium, act as contaminants for the precious Hayabusa sample. Thre is also a possibility that the sample amount will be so small that the accuracy for the Archimedian method will be insufficient. The second purpose of the microtomographic analysis is to discriminate individual sample grains and obtain the size distribution and other statistical 3-D shape features, such as aspect ratios, of the grains. This will give basic physical properties of regolith, which may be present on the Itakawa's surface. The third purpose is to describe the 3-D structures of some individual grains for planning later destructive analysis by sectioning the samples, such as SEM and TEM observations and many chemical analyses. As a CT image is expressed as a spatial distribution of CT values and the constituent minerals can be estimated based on the CT values, we can roughly estimate 3-D distributions of minerals.

Specific phases, where some important elements are concentrated, can be searched by the subtraction method. Although subtraction microtomography will give 3-D distribution of the specific minerals (Tsuchiyama et al., in preparation), the sample volume is restricted if high spatial resolution is required. In contrast, larger amounts of samples can be used with high resolution by microradiography. Another purpose of this study is to search Zr-bearing minerals, such as zircon and badeleite, effectively for age determination using the Pb-Pb mehod and some highly-refractory minerals with platinum element group, Mo, W etc. In the present study, only Zr-bearing minerals were searched due to the limited beam time at SPring-8.

2. EXPERIMENTS

Imaging experiments using SP-μCT are available at three different beamlines, BL20B2, BL20XU and BL47XU, mainly depending on the sample size. The effective spatial resolutions are about 13 μm at BL20B2 for samples smaller than 5 mm in diameter (Uesugi et al. 1999) and about 1 μm at BL20XU and BL47XU for samples smaller than 0.45 mm in diameter (Uesugi et al. 2001). The present HASPET samples were imaged at BL20XU and BL20B2. However, as the sample sizes are so small that the samples were not suitable for imaging at BL20B2, only the results at BL20XU are reported here.

Two kinds of samples were sent from ISAS/JAXA: II-1A is a fine powder sample (<~100 μm in size) in gray color (Figure 1) and II-1B is composed of rounded dark gray grains (a few tens to a few hundreds μm in size) (Figure 38). Single or multiple grains attached on glass fibers or powders in Al capsules were imaged. Glycole phthalate was used as a glue to stick sample grains on the top of a glass fiber of 5 or 200 μm in diameter. Glycole phthalate can be easily removed by acetone without any serious contamination even for noble gas measurements (Tomoki Nakamura, a personal communication). A list of samples and their imaging conditions are summarized in Table 1. Some of the sample mass were measured by an ultra-microbalance (Sartorius SC-2: >0.1 μg). Each mass was measured six times and the average and standard deviation were calculated. The ample preparation and the mass measurement was carried out in a clean room at Osaka University.

2.1. Micotomography

SP-μCT is composed of an X-ray source, a sample stage, and an X-ray beam monitor (Fig. A1). Details of the system is essentially the same as that described in Tsuchiyama et al. (2005). Images of transmitted X-ray intensities through a sample were taken at X-ray energies of 10 to 30 keV depending on the size of the samples. The samples were rotated by 180 degrees with a rotational step angle of 0.12 degrees (1500 projections). Images of direct X-ray beams with no sample (I_0 images) and dark current of the detector system were measured by thirty times respectively, before and after the CT measurement for correction of the images. All images were obtained by an X-ray detector, where the X-ray was transformed into visible light by a fluorescent screen,

(a)

II-1A_x40.JPG

(b)

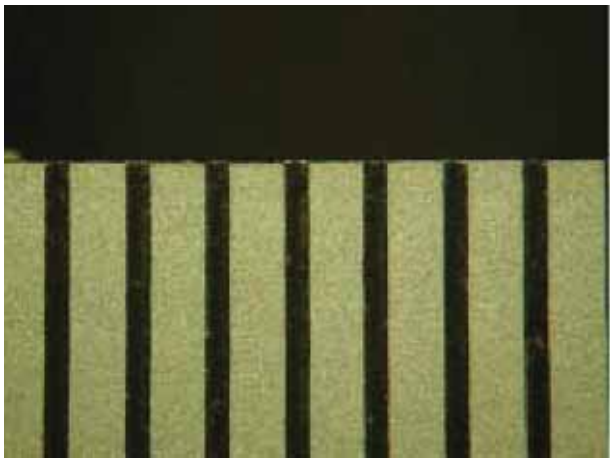

scale_x40.JPG (0.5 mm)

(c)

II-1A_x90.JPG

(d)

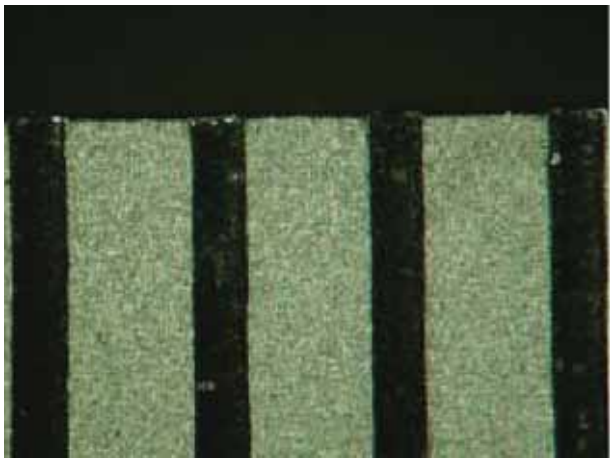

scale_x90.JPG (0.5 mm)

Figure 1. Photomicrographs of HASPET sample II-1A. (a) Low magnification. (b) A scale for (a). The separation between each scale bar is 0.5 mm. (c) High magnification. (d) A scale for (c). The separation between each scale bar is 0.5 mm.

expanded by a relay lens and subsequently detected by a cooled CCD camera (2000 × 1312 format with a full well of 13000 electrons). The sample and fluorescent screen were positioned as close together as possible (~1 mm) to avoid X-rays refracted by the sample. Imaging required 1 to 5 hrd depending on the X-ray energy and sample size. After the standard pre-processing of raw X-ray intensities and their logarithm conversions, CT images (2000 × 2000 pixels in full images) were reconstructed by a convolution back-projection algorithm (Nakano et al. 1997, 2000) with a Chesler's type convolution filter. 3-D structures were reconstructed by stacking 200-1312 slice images. Two long samples were imaged three times after moving the samples vertically in each time (041009d, e and f for II-1A-P1 and 041009g, h and I for II-1A-P2). The size of each cubic voxel (pixel in 3-D) in the 3-D images was 0.195, 0.47 or 0.948 μm, and the effective spatial resolution was about 0.5 to a few μm depending on the pixel size.

Sample portions in 3-D images were extracted by using threshold of CT values. The threshold values 4 were determined from CT value histograms (frequency diagram of CT values) of the 3-D images. The threshold values were adopted as mean values of the representative CT values for phases, which are determined by peaks or bumps of the histograms (e.g., see Figure 4). Validity of taking the mean value as the threshold was checked by some materials with known densities (mineral grains and powder of glass beads). The densities were well reproduced by this threshold within the errors of about 3% (Hurukawa, 2005). The volumes of the solid samples, each phase and internal voids were calculated from the numbers of voxels those belong to the phases or voids and the voxel size (0.195^3, 0.470^3 or 0.948^3 μm: Table 1). The modes of the phases were estimated from the volumes. Image analysis was carried out using 3-D image analysis tool, SLICE (Tsuchiyama et al., 2005). We can also estimate phases from the CT values because LAC is a physical property as a function of the bulk density and the chemical composition of a material and X-ray energy. If the monochromatic beam is used CT values should be ideally equal to LACs. However, they are not identical due to non-linearity of the system (Tsuchiyama et al., 2005). Qualitative CT value - LAC relation was determined at BL20B2 by imaging standard materials (Tsuchiyama et al., 2005). Prior to the HASPET sample imaging, CT value - LAC relation was determined at BL20XU to estimate real LAC values from CT values. The results are shown in Appendix (LAC = 0.8850(0.0110) × CT value: Figure. A2). Phases in the HASPET samples were estimated from the CT values (and thus LAC values) with the relation. The compositions of solid solutions (e.g., Fo content of oliviene) were also roughly estimated from the CT values.

2.2. Microradiography

Powder samples (II-1A) were sandwiched between Al foils of about 1 x 1 cm for searching Zr-bearing minerals by subtraction microradiography (Figure 51). Projection images were measured at X-ray energies just above and below the Zr K-edge (18.04 and 17.98 keV). Each image has 2000 × 800 format with the pixel size of 0.948 μm (about 1.9 × 0.76 mm^2). Mosaic images of the samples were formed by tiling multiple projection images (55 and 60 images). X-ray transmittance ($q = (I-I_d)/(I_0-I_d)$, where I, I_0, and I_d are the X-ray intensities of transmitted, inciodent and dark beams, respectively). Images expressed by q were obtained for the two set of images, and subtraction images from the q images were obtained. The subtraction of the transmittance, Δq, is expressed as $\exp(-\mu_1 S)-\exp(-\mu_2 S)$, where μ_1 and μ_2 are LACs at below and above the edge energy and S is the sample thickness. $\mu = \rho\sum_i w_i\tau_i$ (E), where w_i is the weight fraction of element-i and τ_i is the mass attenuation coefficient (MAC) as a function of X-ray energy, E. If the X-ray energy interval at above and below the Zr K-edge is small, only τ_{Zr}'s are different, and thus, Zr-bearing materials should have $\Delta q>0$ and other materials have $\Delta q=0$. If a mineral grain is at a Bragg angle, the contrast of this grain is affected by the Bragg reflection. In order to check this possibility, another set of projection images were measured by rotating the samples by 1 degree. Stereographs were also made from the two sets of images with different angles.

3. RESULTS AND DISCUSSION

The results are briefly summarized in Table 2.

Table 1. A list of samples and conditions for the present imaging experiments.

beam line	imaging no.	sample	sample form and its containor	energy (keV)	exposure (sec)	number of projection	number of I_0 image	number of dark image	pixel size (μm)	remarks
BL20XU	041007e	II-1A-009ag-B10	aggregate on glass fiber	25	0.25	1500	30	30	0.47	
BL20XU	041009d	II-1A-P1-1*	powder in Al capsule(1.0/1.5ø)	25	0.2	1500	30	30	0.948	
BL20XU	041009e	II-1A-P1-2*	powder in Al capsule(1.0/1.5ø)	25	0.2	1500	30	30	0.948	upper region of 041009d by 600μm
BL20XU	041009f	II-1A-P1-3*	powder in Al capsule(1.0/1.5ø)	25	0.2	1500	30	30	0.948	upper region of 041009e by 600μm
BL20XU	041009g	II-1A-P2-1*	powder in Al capsule(1.0/1.5ø)	25	0.2	1500	30	30	0.948	
BL20XU	041009h	II-1A-P2-2*	powder in Al capsule(1.0/1.5ø)	25	0.2	1500	30	30	0.948	upper region of 041009g by 500μm
BL20XU	041009i	II-1A-P2-3*	powder in Al capsule(1.0/1.5ø)	25	0.2	1500	30	30	0.948	upper region of 041009h by 500μm
BL20XU	041008b	II-1A-005-A5	single grain on glass fider	10	0.25	1500	30	30	0.195	
BL20XU	041008c	II-1A-004-A4	single grain on glass fider	10	0.25	1500	30	30	0.195	
BL20XU	041008d	II-1A-003-A3	single grain on glass fider	10	0.25	1500	30	30	0.195	
BL20XU	041008e	II-1A-002-A2	single grain on glass fider	10	0.25	1500	30	30	0.195	
BL20XU	041008f	II-1A-001-A1	single grain on glass fider	10	0.25	1500	30	30	0.195	
BL20XU	041008h	II-1A-006-A6	single grain on glass fider	10	0.25	1500	30	30	0.195	
BL20XU	041008i	II-1A-010-A14	single grain on glass fider	10	0.25	1500	30	30	0.195	
BL20XU	041007a	II-1B-004-A10*	single grain on glass fider	30	0.25	1500	30	30	0.47	
BL20XU	041007b	II-1B-008-A15*	single grain on glass fider	30	0.25	1500	30	30	0.47	
BL20XU	041007c	II-1B-002-A8*	single grain on glass fider	30	0.25	1500	30	30	0.47	
BL20XU	041008a	II-1B-001-A7*	single grain on glass fider	25	0.25	1500	30	30	0.47	
BL20XU	041010a	II-1A-P3, II-1A-P4z	powder wrapped in Al foil	18.04, 17.98	0.2	55-60	30	30	0.948	radiography for seraching Zr-bearing minerals using subtraction method
		* mass measured								

Table 2. Brief summary of the present report.

sample No.	**009ag-B10**	**P1, P2**	**001-006,010**			
imaging No.	**041007e**	**041009def, ghi**	**041009b,c,d,e,f,h,i**			
sample	**grain aggregate**	**powder**	**grain**			
grain density (g/cm^3)	**n.d.**	**3.67(0.02)**	**n.d.**	**3.64(0.12)**	**3.51(0.11)**	**3.48(0.08)**
bulk density (g/cm^3)				**3.40(0.18)**	**3.35(0.16)**	**3.21(0.22)**
mode (%)						
plagioclase			**12.0(5.2)**			
Mg-Fe silicates	**91.2**	**95.5(0.1)**	**85.5(7.7)**			
troilite	**4.9**	**3.2(0.2)**	**1.5(3.0)**			
Fe-Ni metal	**3.8**	**1.3(0.3)**	**0.4(1.3)**			
kamacite	**3.7**	**1.1(0.2)**	**0.4(1.3)**			
taenite	**0.1**	**0.2(0.0)**				
void	**n.d.**	**n.d.**	**0.6(0.4)**	**6.0(4.5)**	**5.8(4.7)**	**9.3(8.5)**
composition						
plagioclase (An)			**63-100**			
olivine (Fo)	**91**	**87**	**84-93**			
orhtopyroxenen (En)	**88**	**82**	**77-90**			
kamacite (Fe/Fe+Ni)	**69**	**86**				
taenite (Fe/Fe+Ni)	**50**	**57, 36?**				
HASPET sample	**II-1B**	**II-1B**		**pallasites***	**mesosiderites***	
sample No.	**002,004,008**	**001**				
imaging No.	**041007a,b,c**	**041008a**				
sample	**grain**	**grain**				
grain density (g/cm^3)	**6.89(0.29)**	**5.05(0.32)**		**4.76(0.10)**	**4.40(0.36)**	
bulk density (g/cm^3)				**4.49(0.53)**	**4.25(0.02)**	
mode (%)						
plagioclase						
Mg-Fe silicates	**37.7(2.7)**	**67.3**				
troilite		**32.7**				
Fe-Ni metal	**62.3(2.7)**					
kamacite	**61.4(3.1)**					
taenite	**0.9(0.7)**					
void	**n.d.**	**n.d.**		**0.0(0.52)**	**3.0(8.1)**	
composition						
plagioclase (An)						
olivine (Fo)	**83**	**89**				
orhtopyroxenen (En)	**76**	**85**				
kamacite (Fe/Fe+Ni)	**88**	**97**				
taenite (Fe/Fe+Ni)	**43**					
				*** Britt and Consolmagno (2003)**		

3.1. Tomographic study of sample II-1A

(a) Sample II-1A-009ag-B10

Sample II-1A-009ag-B10 is an aggregate of grains attached on a glass fiber (Figure. 2). A browse image, where CT images at some slices are shown, is given in Figure 3. The left bar in the browse image shows the size scale in cm, and the right bar shows the gray scale of CT value in cm^{-1}. Brighter objects have larger CT values or larger X-ray absorption and vise versa. A glass fiber of about 200 μm in diameter is also seen in the slices 0462, 0617, 0722 and 0927. Absorption by glycole phthalate (glue) is so small that it is expressed as very dark object although the surface can be recognized as a slightly bright curve as refraction contrast (e.g., slice 0927 in Figure 3). Four phases were recognized form the CT images and its CT value histogram (Figure 4: in this histogram pixel value, PV, of 16 bit CT images is used in stead of CT values for convenience for image analysis because the image analysis was made using the 16 bit CT images). Clear peaks were recognized at 6.10 and 107.6 cm^{-1}, which are attributed to phases-A and C, respectively. Two bumps were also recognized at about 32.95 and 115.3 cm^{-1}, which are attributed to phases-B and D, respectively. If representative minerals in meteorites are assumed, the phases-A, B, C and D should be Fe-Mg silicates (olivine and/or orthopyroxene), troilite, kamacite and taenite (Table 3). The Fo and En contents of olivine and orthopyroxene , respectively, and Fe/(Fe+Ni) ratios of kamacite-taenite were roughly estimated in Table 3 too. It should be noted that the errors of the compositions are large (Fo91 probably means Fo80-100 or relatively Mg-rich olivine), and the accurate compositions should be determined by EPMA. It is also noted that we cannot discriminate olivine and orthopyroxene (and clinopyroxene also) in CT images due to overlapping of their LACs.

3-D distribution of the phases (Figure 5) was obtained from CT value threshold, which is taken as the mean value of the two peaks (Figure 4). The mode of each phase was estimated from this 3-D distribution (Table 4). If phases-A and B are in contact, thin regions with the intermediate CT values, which are recognized wrongly as phase-C, appear artificially between them in CT images (e.g., see concentric distribution of phases-A, B and C in Figure 5b). Therefore, the mode of phase-C might be overestimated. However, the roughly estimated modes can be used as tentative values. 3-D information about the rough distribution will contribute to later destructive analysis by sectioning the samples. The accuracy of the mode will be increased by increasing the number of projection in the tomographic imaging. The volume of the bulk solid should not have such large error. However, the density was not obtained for this sample because the mass was not measured. If the density obtained for other powders of the same sample (3.67 g/cm^3) is adopted, the mass should be 0.075 mg.

Each grain was also identified in this sample by image analysis procedure. The results are shown in Fig.5c, where the glass fiber was removed from the CT images manually. In this image, grains with different color sjow different grains. However, only seven colors are used to recognize individual grains, different grains may have the same color. In fact, three red and three yellow grains in Figure 5c are different grains. Bird's eye view of the sample is shown in Figure 6. A plaster model, enlarged accurately from the 3-D CT images, can be made using rapid prototyping method (Tsuchiyama et al., 2003b). Statistics of the grain size and shape was obtained from the information about the individual grains. Grain size was calculated as the diameter of a sphere with the same volume of a grain. The size distribution is shown as a histogram of the grain size (in ϕ scale) in Figure 7 and a cumulative frequency diagram in Figure 8. The distribution shows that similar to log-normal distribution although the size range and number of grains are small. Some parameters for the size distribution were also calculated (Table 5). If a grain is approximated as a three-axis ellipsoid, the major, intermediate and minor axis length (A>B>C) can be calculated. Figure 9 shows the plot of the axial ratios, C/B vs. B/A for different sizes. The grains are equally distributed in the prolate (C/B>B/A) and oblate regions (C/B<B/A), and the aspect ratio (C/A) ranges from about 0.4 to 0.9.

(b) Sample II-1A-P1 and P2

These samples are filled in Al capsules (Fig. 10). Browse images are shown in Figures 11 and 17. Combined successive CT images were made from the CT images by three imaging experiments. Bird's eye views and vertical sliced CT images are shown in Figures 14 and 15 for II-1A-P1 and Figures 19 and 20 for II-1A-P2, respectively. In the bird's eye views, the Al capsules were removed manually. However, the inner surface portions were slightly remains as thin films (Figure 14 and 19). CT value histogram for the sample regions (Figure 12) shows that the phases and their modes are consistent with those estimated from the sample II-

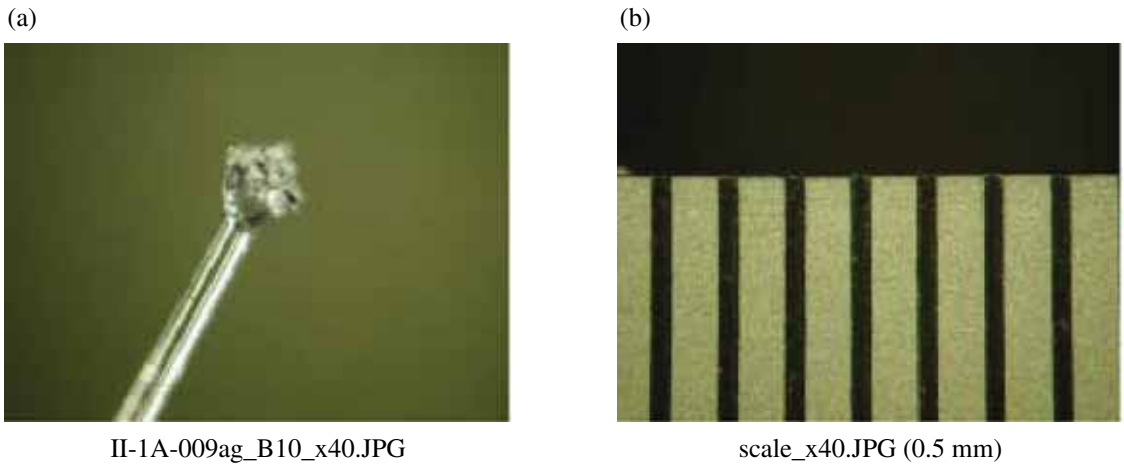

Figure 2. A photomicrograph of HASPET sample II-1A-009ag-B10 (041007e). (a) A powder sample is attached on a glass fiber with glycole phthalate. (b) A scale for (a). The separation between each scale bar is 0.5 mm.

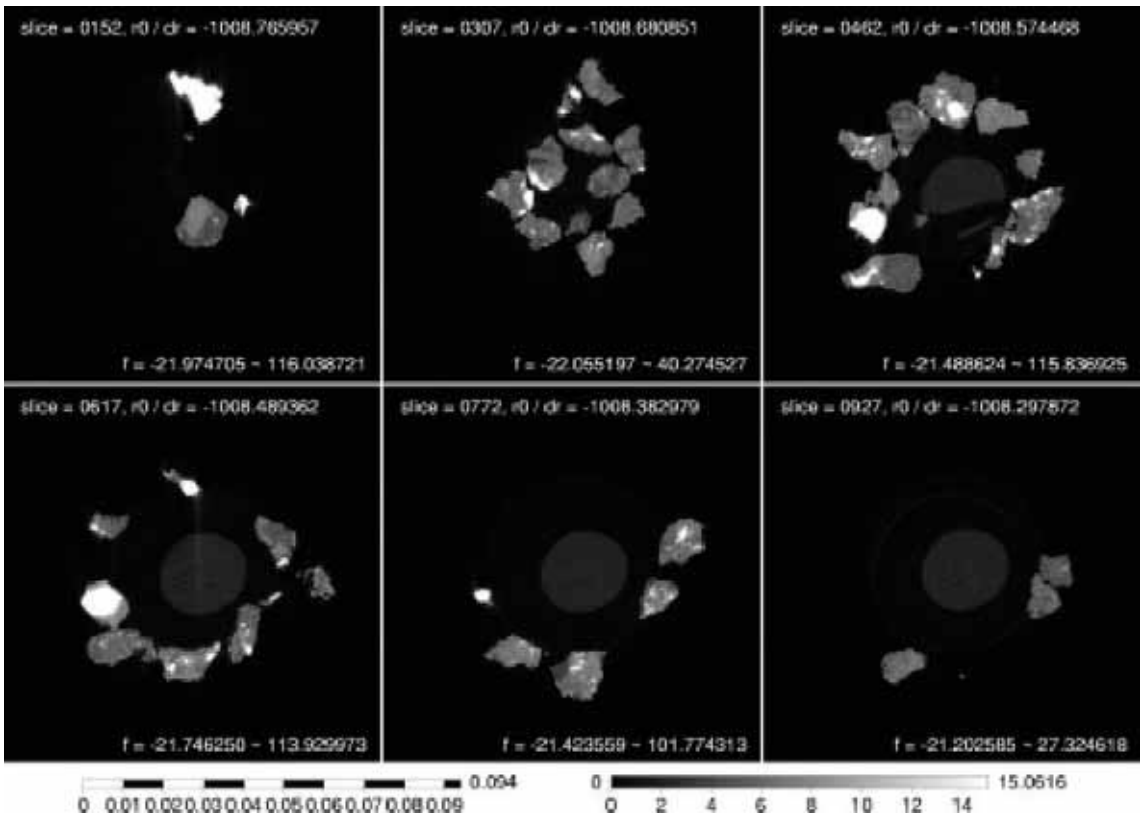

Figure 3. A browse image of CT slices of HASPET sample II-1A_009ag-B10. The left and right bars are a scale bar in cm and a gray scale bar for CT values in cm^{-1}, respectively.

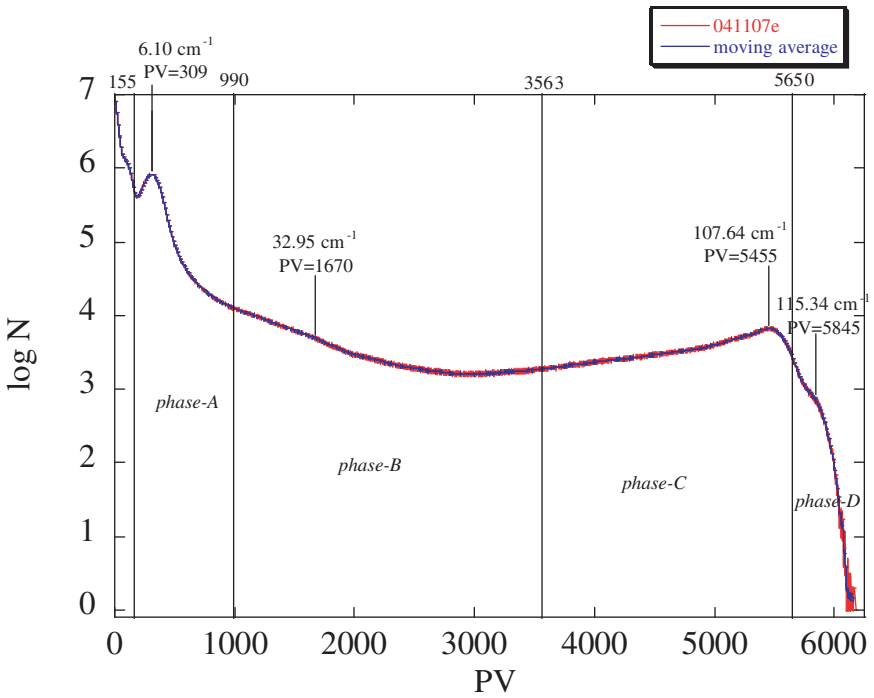

Figure 4. A CT value histogram of HASPET sample II-1A-009ag-B10. The CT values, *f*, are replaced by the pixel values, PV, in 16 bit images (f = 0.019733 cm^{-1} x PV). Peak PVs and CT values for phases-A, B, C and D, and threshold PVs between the phases are shown.

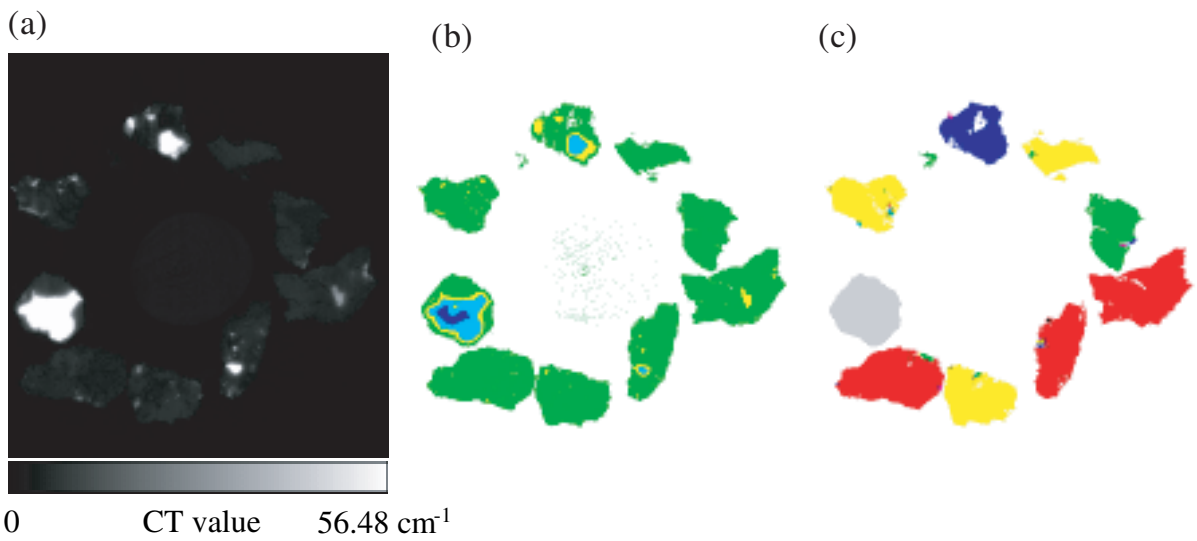

Figure 5. A typical CT slice of HASPET sample II-1A-009ag-B10. (a) A CT image (56.48 cm^{-1} corresponds to PV=2862 in Figure 4. The width of the image is 663.64 μm. (b) An image showing phases. Green: phase-A (probably Mg-Fe silicates), yellow: phase-B (probably troilite), cyan: phase-C (probably kamacite, and blue: phase-D (probably taenite). (c) An image showing individual grains. A glass fiber, which holds sample grains, was removed manually.

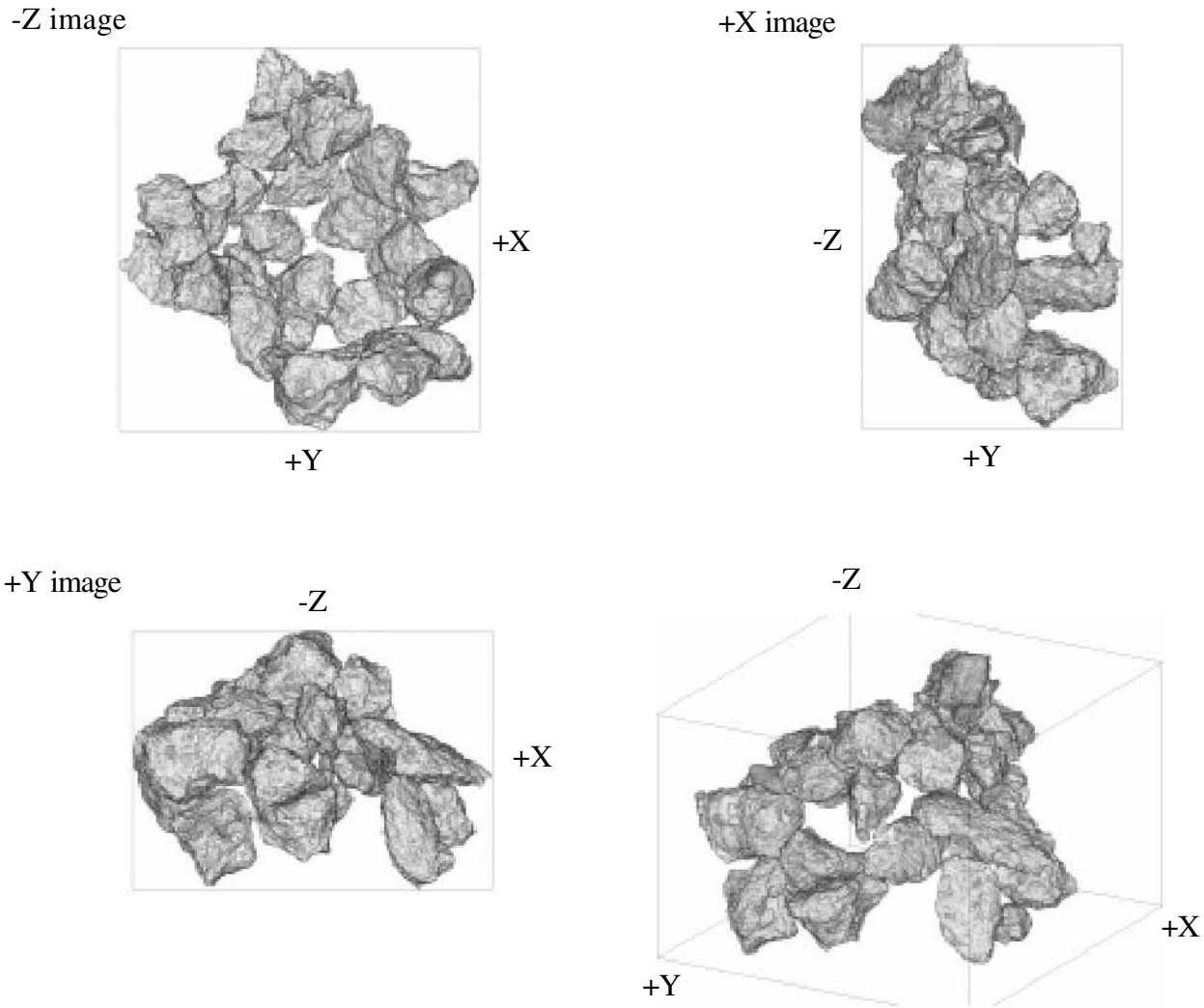

Figure 6. Bird's eye view of HASPET sample II-1A-009ag-B10. The sample size of the sample is about 660x700x470 μm. A glass fiber, which holds sample grains, was removed manually.

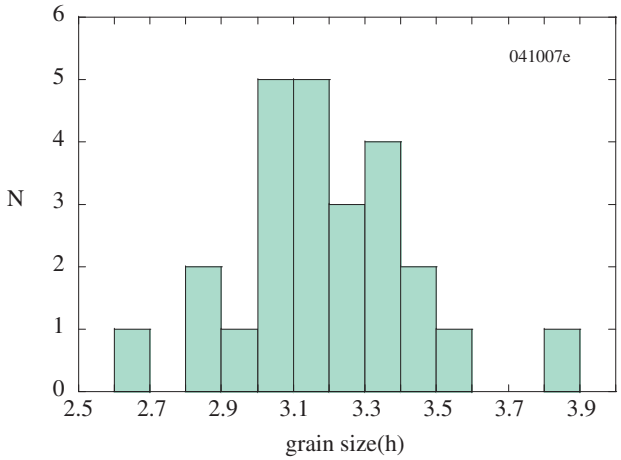

Figure 7. A histogram of grain size (in ϕ scale) of HASPET sample II-1A-009ag-B10.

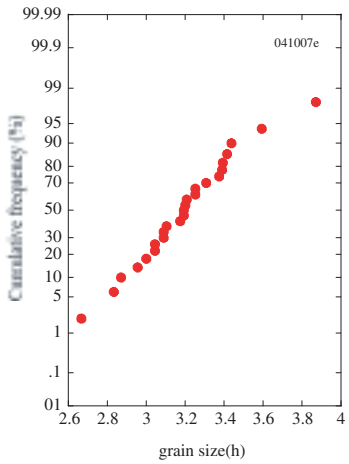

Figure 8. A cumulative frequency of grain size (in ϕ scale) of HASPET sample II-1A-009ag-B10.

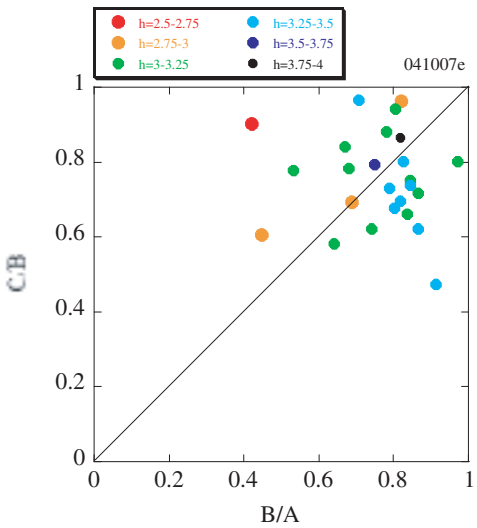

Figure 9. Grain shape distribution of HASPET sample II-1A-009ag-B10. Grains are regarded as three-axial ellipsoids (A>B>C) and the axial ratios, C/B and B/A are plotted.

Table 3. The LACs of phases-A, B, C and D in HASPET sample II-1A-009ag-B10, calculated form their CT values and estimation of their mineral candidates and compositions.

	CT value (cm^{-1})	LAC (cm^{-1})	candidates		LAC (cm^{-1})		LAC (cm^{-1})
phase-A	6.10	6.89	silicate	Fo91	6.89	En88	6.89
phase-B	32.95	37.24	trolite	troilite	48.25		
phase-C	107.64	121.63	kamacite	Fe69	121.61		
phase-D	115.34	130.33	taenite	Fe50	130.32		

Table 4. The volume of HASPET sample II-1A-009ag-B10 and the modes of the phases.

	041007e	
sample(mg)	n.d.	
stdev	n.d.	
volume (voxel)	24737545	
volume (cm^3)	2.055E-05	
density (g/cm^3)	n.d.	
stdev	n.d.	
mode (%)		candidates
phase-A	91. 2	silic ates
phase-B	4. 9	troilite
phases-C and D	3.8	Fe-Ni metal
phase-C	3.7	kamacite
phase-D	0.1	taenite

Table 5. Statistics of grain size distribution in HASPET sample II-1A-009ag-B10.

number of grains	25	
median diameter	54.70	μm
arithmatic mean	55.27	μm
geometric mean	54.48	μm
maximum grain size	78.74	μm
minimum grain size	34.18	μm
skewness	0.407	
kurtosis	1.206	

1A-009gr-B10 (Tables 6 and 7, see also Table 2). Distribution of the phases is shown in Figures 13 and 18. The densities of the samples were calculated from the masses and volumes. This density corresponds to grain density and was 3.67 (0.02) g/cm^3 (Table 7).

In this sample, a large amount of fine particles are present in the large irregular grains as seen in Figures 13b and 18b. We have tried to identify individual grains in the samples, but some grains were not separated clearly due to the fine grains and close contact of irregular grains. In contrast, we have succeeded in separating rounded particles, such as beach sands. Separation of closely packed irregular shaped grains remains as feature issue.

(c) Sample II-1A-001-A1, 002-A2, 003-A3, 004-A4, 005-A5, 006-A6 and 010-A14

A single grain was picked up and attached to a glass fiber of 5 μm in diameter (Figures 21 and 22). The masses were not measured for the small grains. From the volumes, we can estimate the masses using the average density of 3.67 g/cm^3 (Table 9). Some can be measured by the ultra-microbalance. On the other hand, we can image these small samples with the highest spatial resolution (0.195 μm voxel size: Table 1). Based on the CT images and CT value histogram (Figure 23), one additional phase, which has smaller CT values than the "Fe-Mg silicates", was recognized. The CT values can be explained by plagioclase. Plagioclase and Fe-Mg silicates were not discriminated well in the previous samples imaged with relatively lower spatial resolution. Because the LAC range of the plagioclase solid solution is narrow (77.6 and 49.9 cm^{-1} for anorthite and albite, respectively), a large error should be included in the An contents in Table 8. Browse images, phase distribution maps and bird's eye views of individual grains are shown in Figures 24-33. There are some variations of the modes of the phases, the averaged modes are consistent with the previous ones (Table 9, see also Table 2). The mode of "plagioclase" is about 10 vol.%. Some blur is present in the periphery of large metal grains (e.g., Figure 35a). This might cause overestimation of plagioclase mode (Figure 35b). Plagioclase is present as interstitially between Fe-Mg silicate crystals (e.g., Figures 32 and 33). The size of the plagioclase grains are the order of 100 μm or smaller. Detailed 3-D structures of the grains with this high spatial resolution will help further destructive analyses.

(d) What is sample II-1A?

It is impossible to conclude definitely the material of the sample based on CT images alone. However, we can give some speculation on this sample if the sample is assumed to be a meteorite. The density, texture and estimated phase are not inconsistent with an ordinary chondrite with high petrologic type, such as 6. The measured density (3.67 g/cm^3) is mostly similar to the average density of H condrite (3.64 g/cm^3: Britt and Consolmagno, 2003), but we cannot exclude the possibility of L and LL chondrites if we consider the range of the density of individual chondrites (Table 2). If the modes of troilite and metal are taken into considered, LL chondrite is favorable. Strictly speaking, possibility of a primitive achondrite, such as winonaites, can not be excluded.

3.2. Tomographic study of sample II-1B

All the samples imaged are a single grain attached on 200 μm glass fibers (Figures 39 and 40). Sample II-1B-002-A8, 004-A10 and 008-A15 were imaged at 30 keV and II-1B-001-A7 at 25 keV. As the samples consists of large amounts of materials with very high LACs (phases-B and C) and relatively low LACs (phase-A) (Figures 41 and 48), there are no best X-ray energies, which gives clear CT images. Especially, there are noise in phase-A and blur near the surface of pahses-B and C (Figures 43b, 46b, 47b and 50b). The images at 25 keV, where the peak of phase-A can be recognized in the CT value histogram (Figure 48), is better than those at 30 keV, where only bumps are recognized (Figure 39). At any rate, the volumes obtained from the 3-D CT images are not so accurate compared with sample II-1A. The density is about 6.9 g/cm^3 for the 30 keV samples and 5.1 g/cm^3 for the 25 keV sample (Tables 11 and 13, respectively, and see also Table 2). The modes of phase-A are different and this causes the density difference. We do not know the discrepancy is due to the energy difference or merely variation of individual grains.

The CT values suggest that phases-A, B and C should be Mg-rich silicate(s), kamacite and taenite , respectively (Tables 10 and 12). Troilite may be present as shown in Figure 50a, where materials with intermediate brightness between phases-A and B are present although there is not any peak or bump in the CT value histogram (Figure 48). The metal grains are rounded and the size is the order of 100 μm. Any Widmanstatten structures were not observed.

The above features suggest that the sample is a stony iron meteorite. The grain size of the sample is smaller than most of

(a)

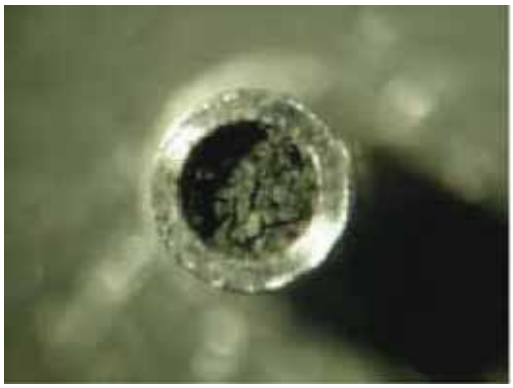

II-1A-P1_x40.JPG

(b)

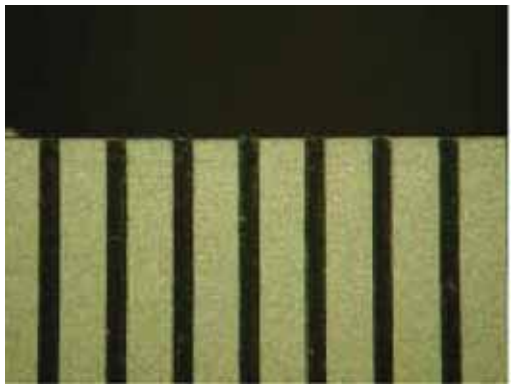

scale_x40.JPG (0.05 mm)

Figure 10. Photomicrograph of HASPET sample II-1A-P1 (041009d, e and f). (a) A powder sample is put into an Al capsule of 1.0 and 1.5 mm in inner and outer diameters, respectively and about 1.7 mm in depth. (b) A scale for (a). The separation between each scale bar is 0.5 mm.

(a)

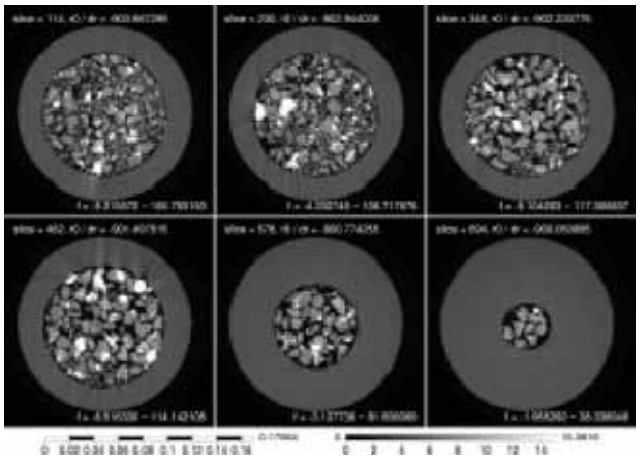

(b)

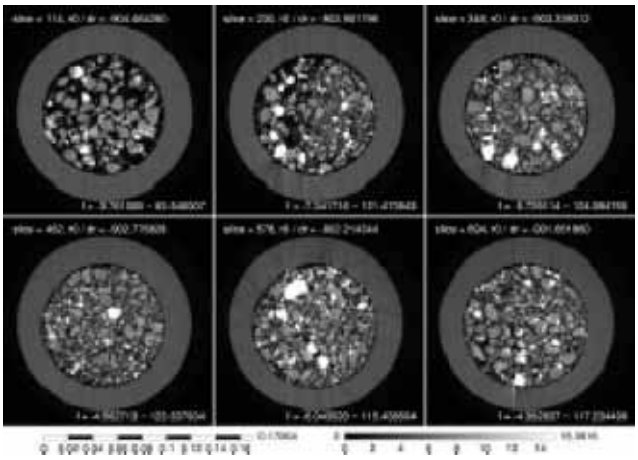

(c)

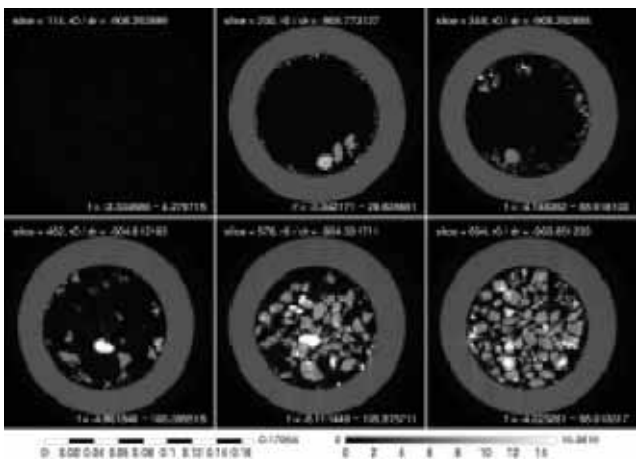

Figure 11. A browse image of CT slices of HASPET sample II-1A-P1. The left and right bars are a scale bar in cm and a gray scale bar for CT values in cm^{-1}, respectively. (a) 041009d. The bottom portion of the capsule. (b) 041009e. The middle portion of the capsule. (c) 041009f. The top portion of the capsule.

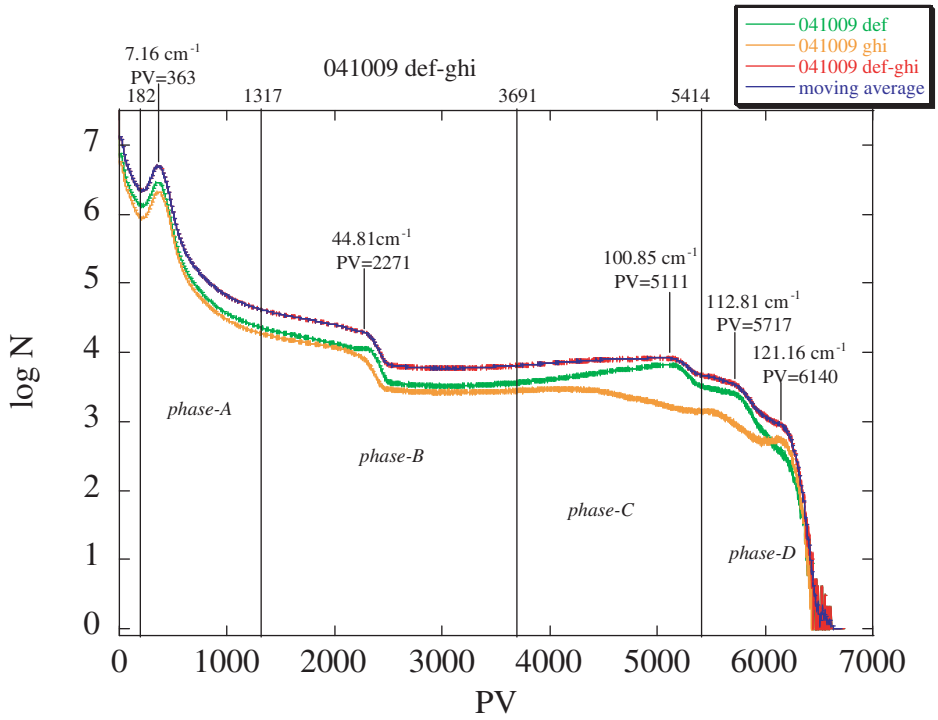

Figure 12. A CT value histogram of HASPET samples II-1A-P1 and II-1A-P2. Al capsules were removed manually. The CT values, *f*, are replaced by the pixel values, PV, in 16 bit images (f = 0.019733 cm^{-1} x PV). Peak PVs and CT values for phases-A, B, C and D, and threshold PVs between the phases are shown.

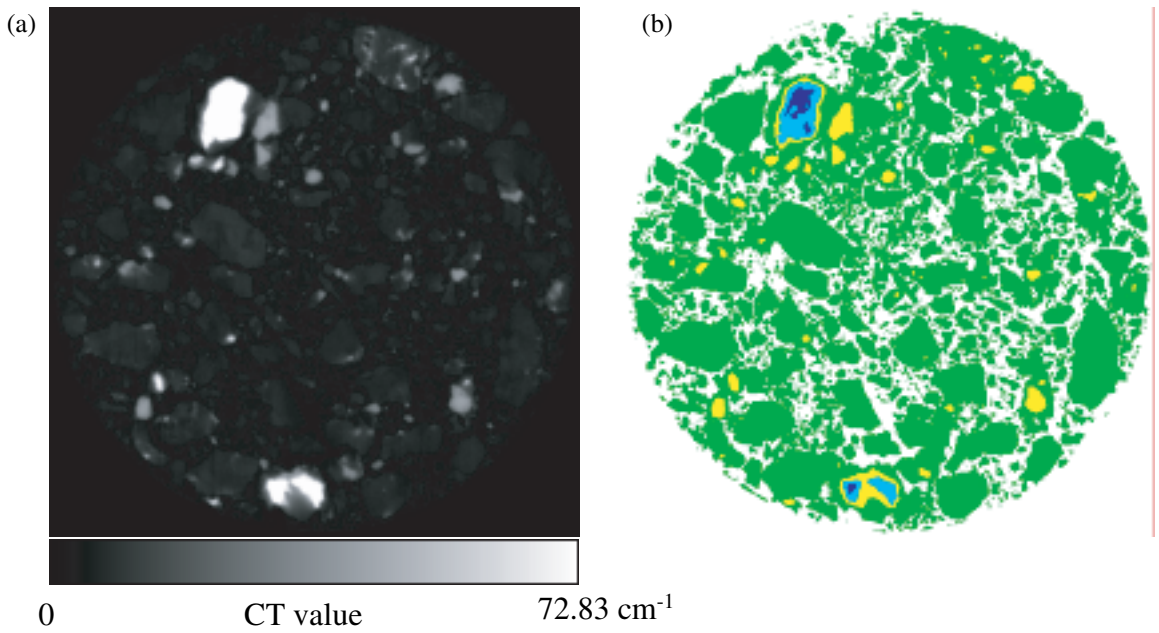

Figure 13. A typical CT slice of HASPET sample II-1A-P1. (a) A CT image (72.83 cm^{-1} corresponds to PV=3691 in Figure 12. The width of the image is 1019.5 μm. (b) An image showing phases. Green: phase-A (probably Mg-Fe silicates), yellow: phase-B (probably troilite), cyan: phase-C (probably kamacite, and blue: phase-D (probably taenite). An Al capsule was removed manually in this image.

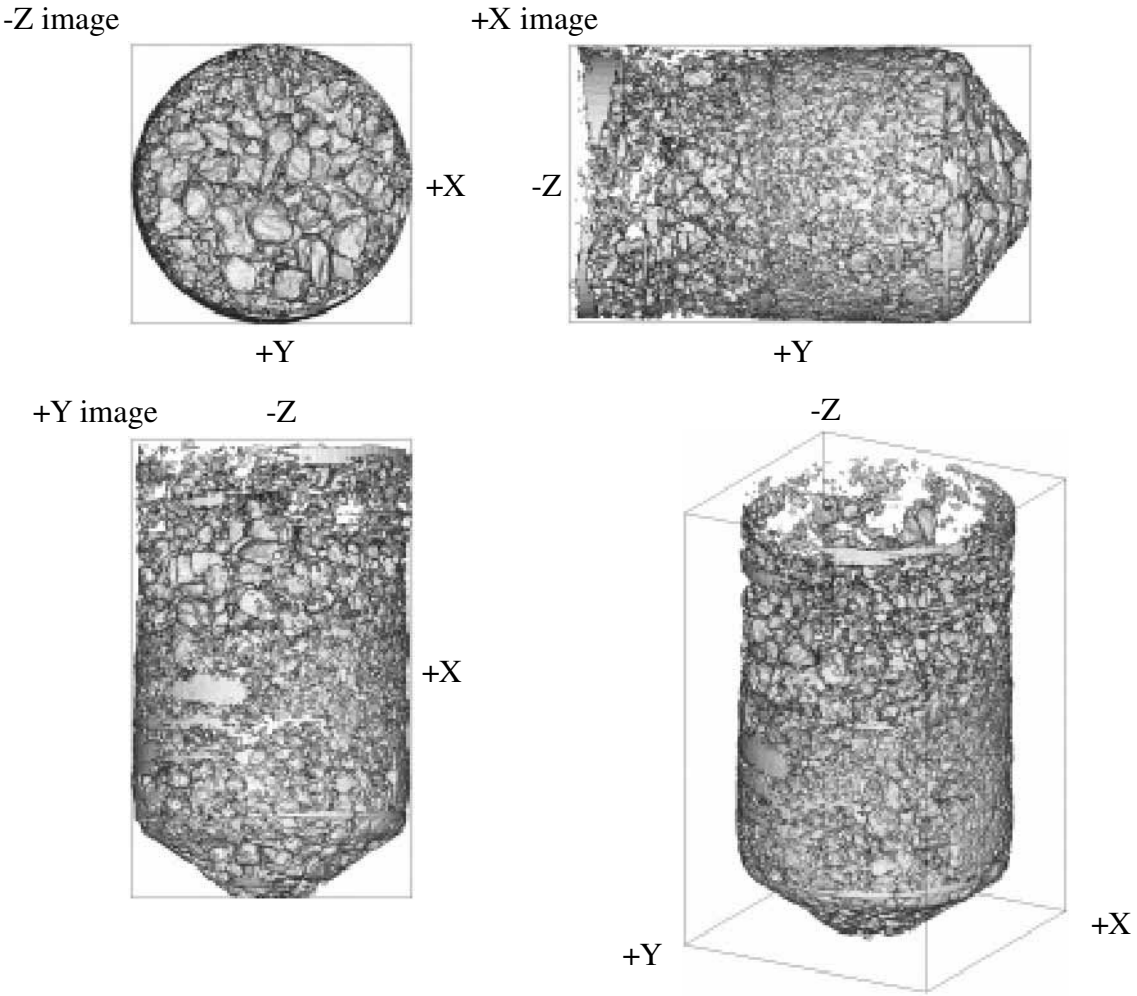

Figure 14. Bird's eye view of HASPET sample II-1A-P1. The sample size of the sample is about 1000x1000x1700 μm. An Al capsule was removed manually.

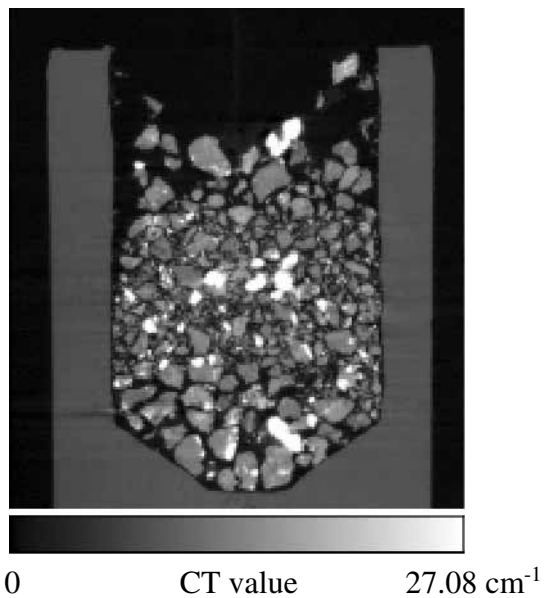

Figure 15. A CT image along a Y-Z slice of HASPET sample II-1A-P1. The image width is 1703 μm.

(a)

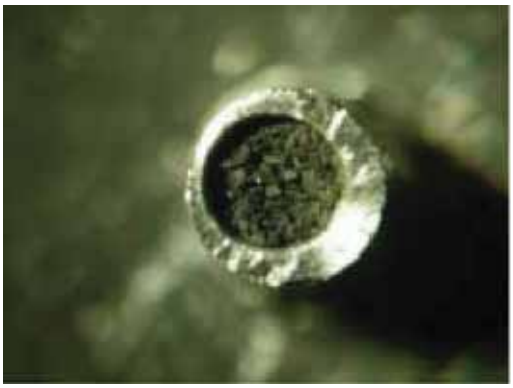

II-1A-P2_x40.JPG

(b)

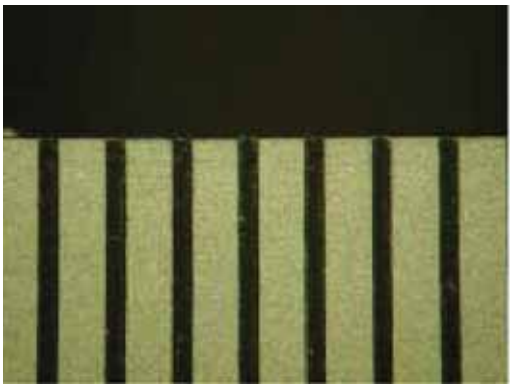

scale_x40.JPG (0.05 mm)

Figure 16. Photomicrograph of HASPET sample II-1A-P2 (041009g, h and i). (a) A powder sample is put into an Al capsule of 1.0 and 1.5 mm in inner and outer diameters, respectively and about 1.4 mm in depth. (b) A scale for (a). The separation between each scale bar is 0.5 mm.

(a)

(b)

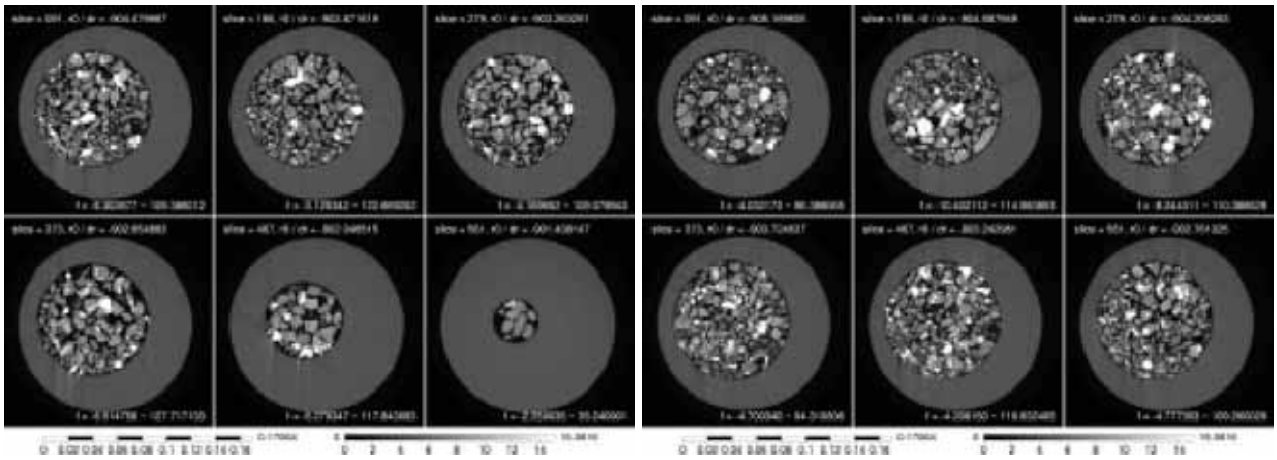

(c)

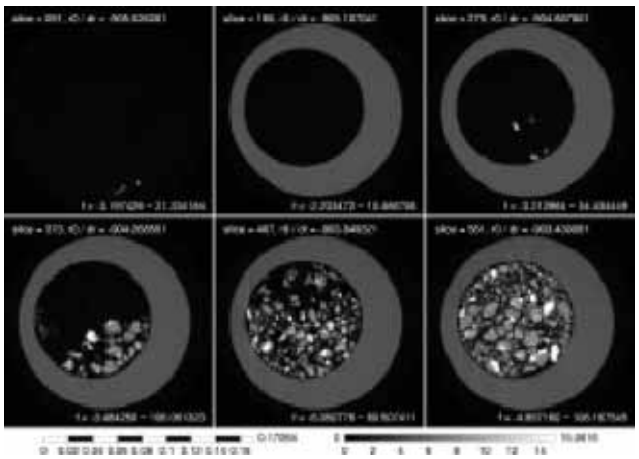

Figure 17. A browse image of CT slices of HASPET sample II-1A-P2. The left and right bars are a scale bar in cm and a gray scale bar for CT values in cm^{-1}, respectively. (a) 041009g. The bottom portion of the capsule. (b) 041009h. The middle portion of the capsule. (c) 041009i. The top portion of the capsule.

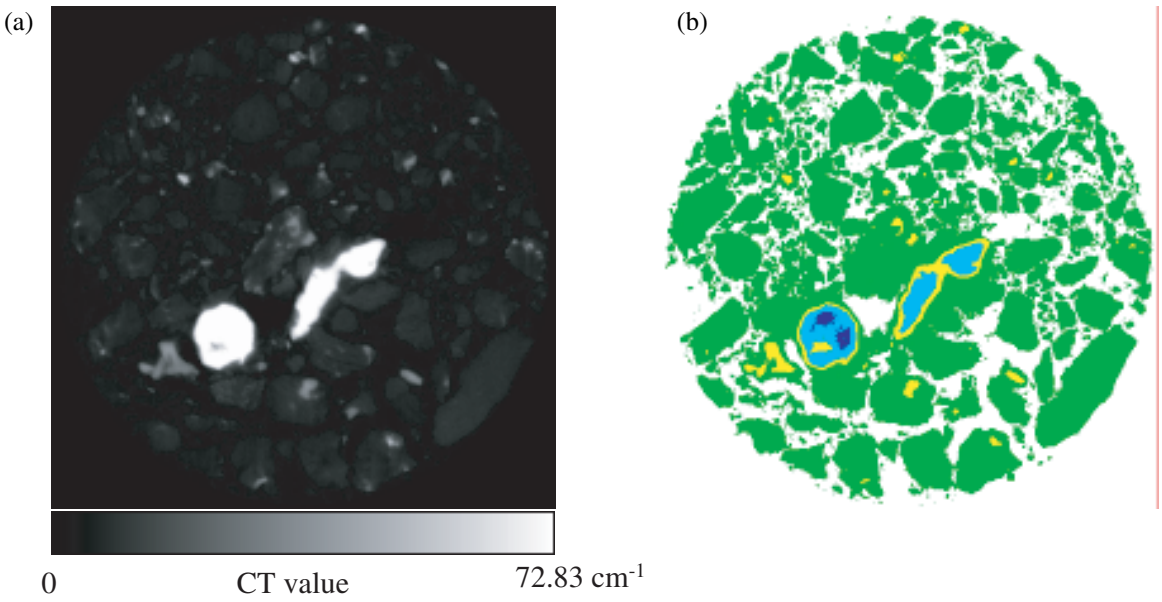

Figure 18. A typical CT slice of HASPET sample II-1A-P2. (a) A CT image (72.83 cm^{-1} corresponds to PV=3691 in Figure 12. The width of the image is 972.6 μm. (b) An image showing phases. Green: phase-A (probably Mg-Fe silicates), yellow: phase-B (probably troilite), cyan: phase-C (probably kamacite, and blue: phase-D (probably taenite). An Al capsule was removed manually in this image.

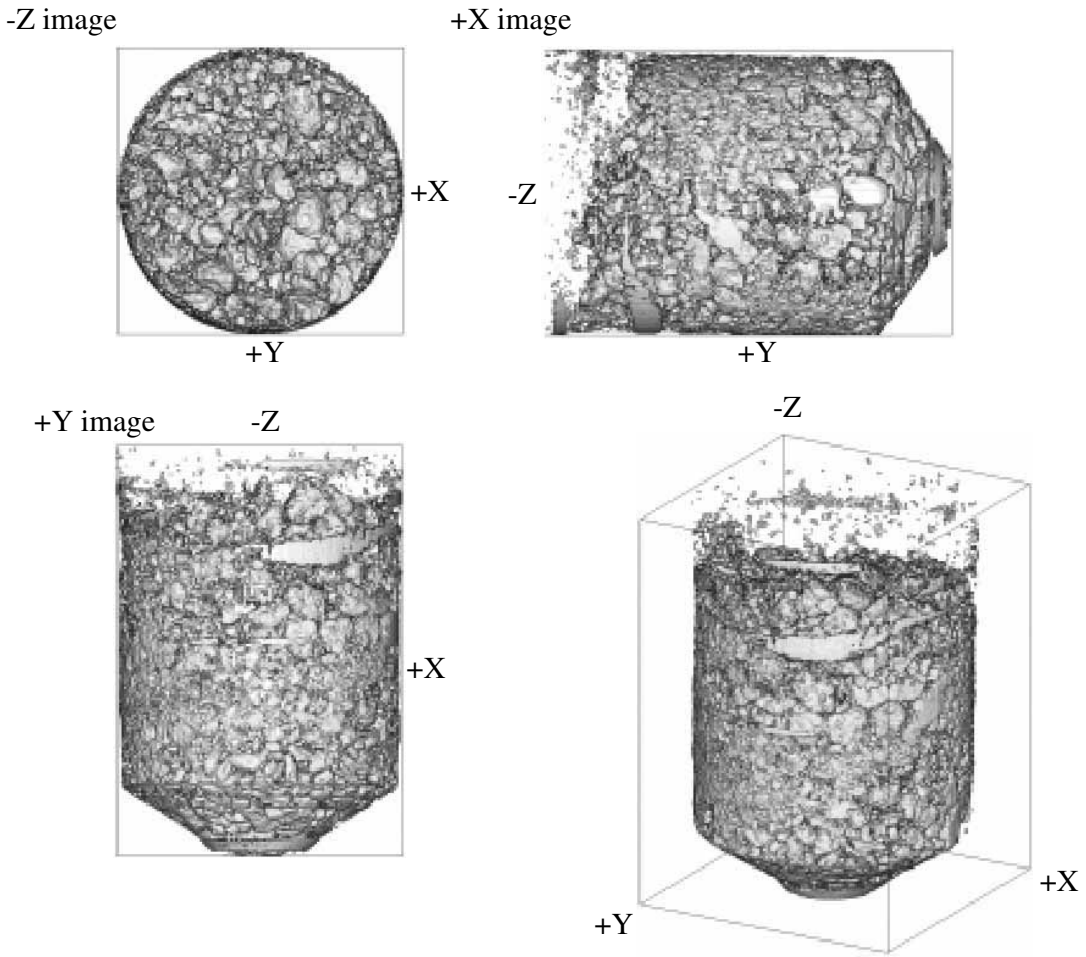

Figure 19. Bird's eye view of HASPET sample II-1A-P2. The sample size of the sample is about 1000x1000x1350 μm. An Al capsule was removed manually.

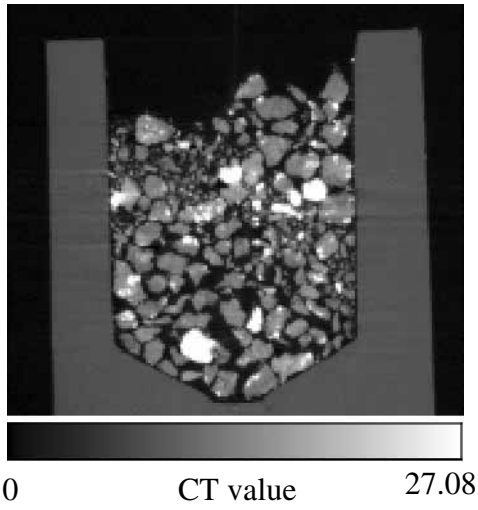

Figure 20. A CT image along a Y-Z slice of HASPET sample II-1A-P2. The image width is 1706 μm.

Table 6. The LACs of phases-A, B, C and D in HASPET samples II-1A-P1 and －P2, calculated form their CT values and estimation of their mineral candidates and compositions.

	CT value (cm^{-1})	LAC (cm^{-1})	candidates		LAC (cm^{-1})		LAC (cm^{-1})
phase-A	7.16	8.09	silicate	Fo87	8.09	En82	8.09
phase-B	44.81	50.64	troilite	troilite	48.25		
phase-C	100.85	113.95	kamacite	Fe86	113.96		
phase-D	112.81	127.47	taenite	Fe57	127.46		
phase-D?	121.16	136.90	taenite?	Fe36	136.89		

Table 7. The volume of HASPET samples II-1A-P1 and －P2 and the modes of the phases.

	041009def	041009ghi	wt.mean	stdev	
sample(mg)	2.1181	1.5585			
stdev	0.0003	0.0003			
volume (voxel)	680716896	497204960			
volume (cm^3)	5.800E-04	4.236E-04			
density (g/cm^3)	3.65	3.68	3.67	0.02	
stdev	0.00	0.00			
mode (%)					candidates
phase-A	95.4	95.6	95.5	0.1	silicates
phase-B	3.1	3.4	3.2	0.2	troilite
phases-C and D	1.5	1.0	1.3	0.3	metal
phase-C	1.3	0.8	1.1	0.2	kamacite
phase-D	0.2	0.1	0.2	0.0	taenite

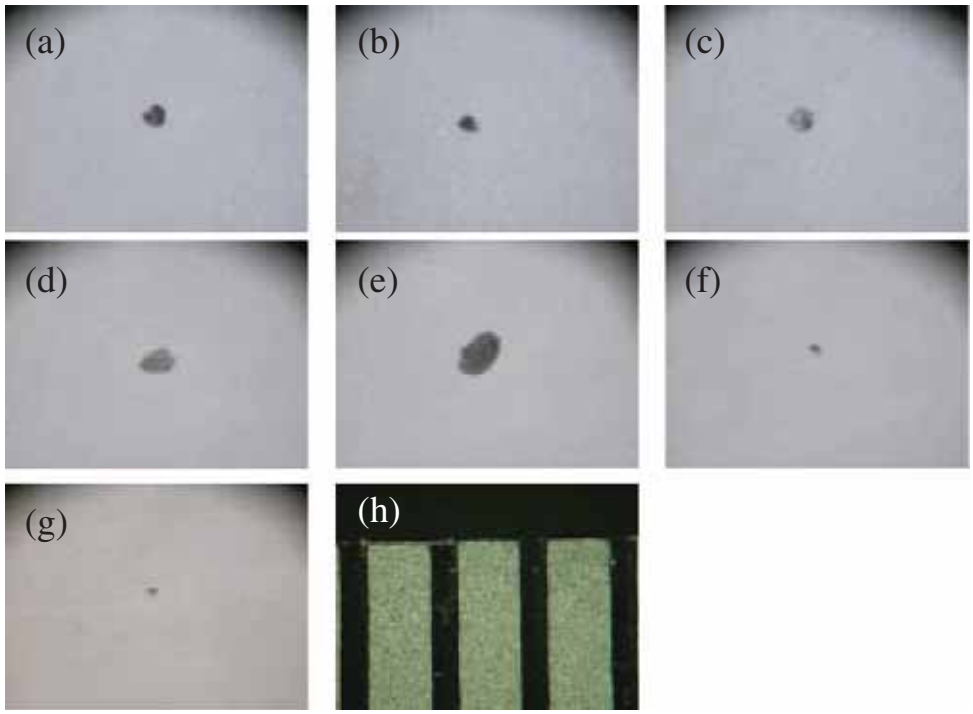

Figure 21. Photomicrograph of single grains (HASPET sample II-1A) . (a) 001-A1 (041008f). (b) 002-A2 (041008e). (c) 003-A3 (041008d). (d) 004-A4 (041008c). (e) 005-A5 (04108b). (f) 006-A6 (041008h). (g) 010-A14 (041008i). (h) A scale. The separation between each scale bar is 0.5 mm.

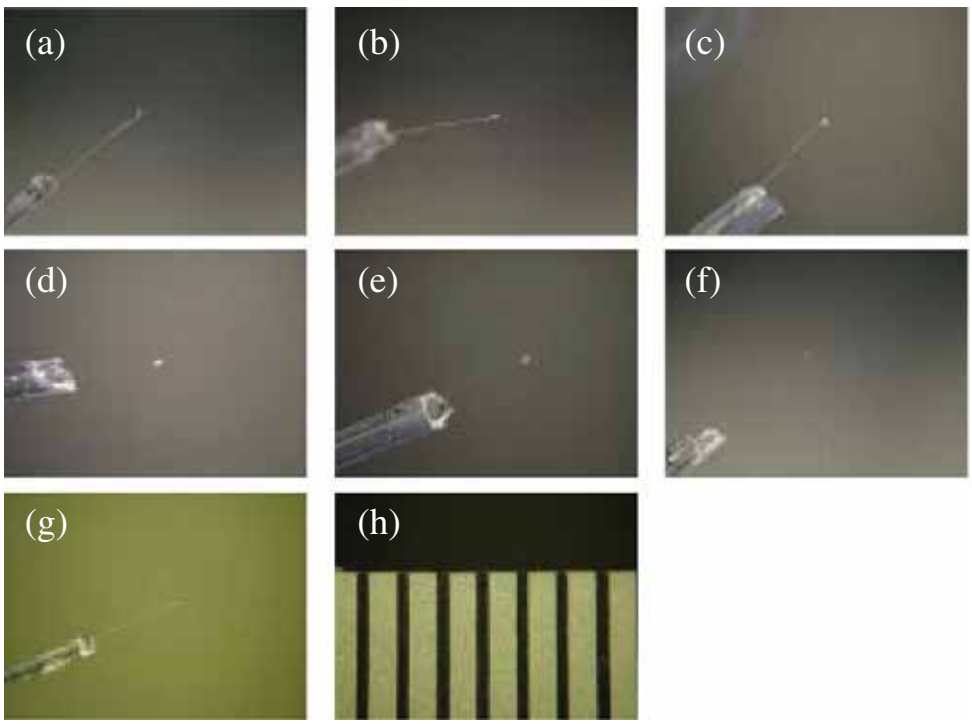

Figure 22. Photomicrograph of single grains (HASPET sample II-1A) on a glass fiber. (a) 001- A1 (041008f). (b) 002-A2 (041008e). (c) 003-A3 (041008d). (d) 004-A4 (041008c). (e) 005-A5 (04108b). (f) 006-A6 (041008h). (g) 010-A14 (041008i). (h) A scale. The separation between each scale bar is 0.5 mm.

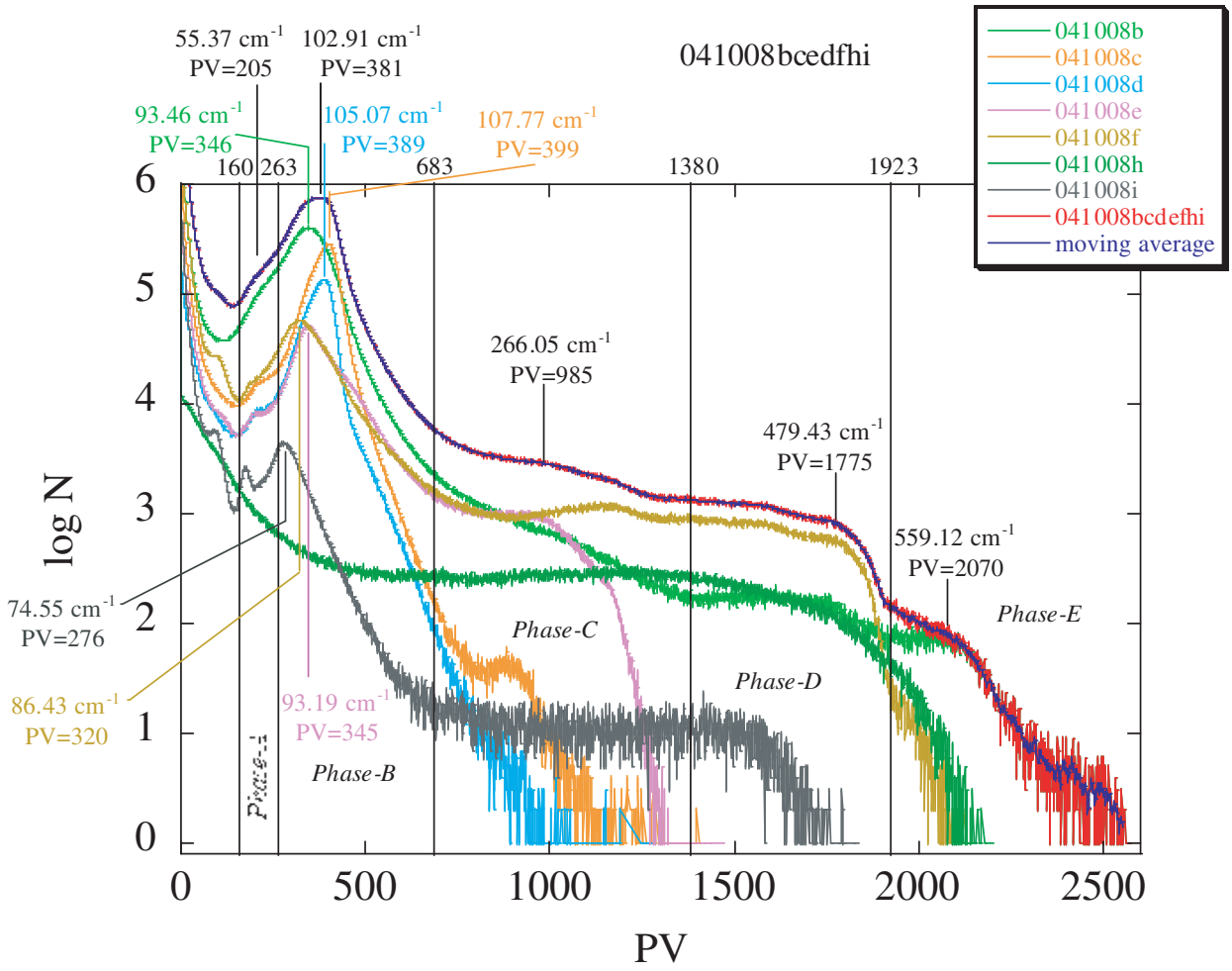

Figure 23. A CT value histogram of HASPET samples II-1A-001-A1(041008f), 002-A2 (041008e), 003-AA3 (041008d), 004-A4 (041008c), 005-A5 (041008b), 006-A6 (041008h) and 010-A14 (041008i). The CT values, *f*, are replaced by the pixel values, PV, in 16 bit images (f = 0.27010 cm^{-1} x PV). Peak PVs and CT values for phases-A, B, C, D and E, and threshold PVs between the pahses are shown.

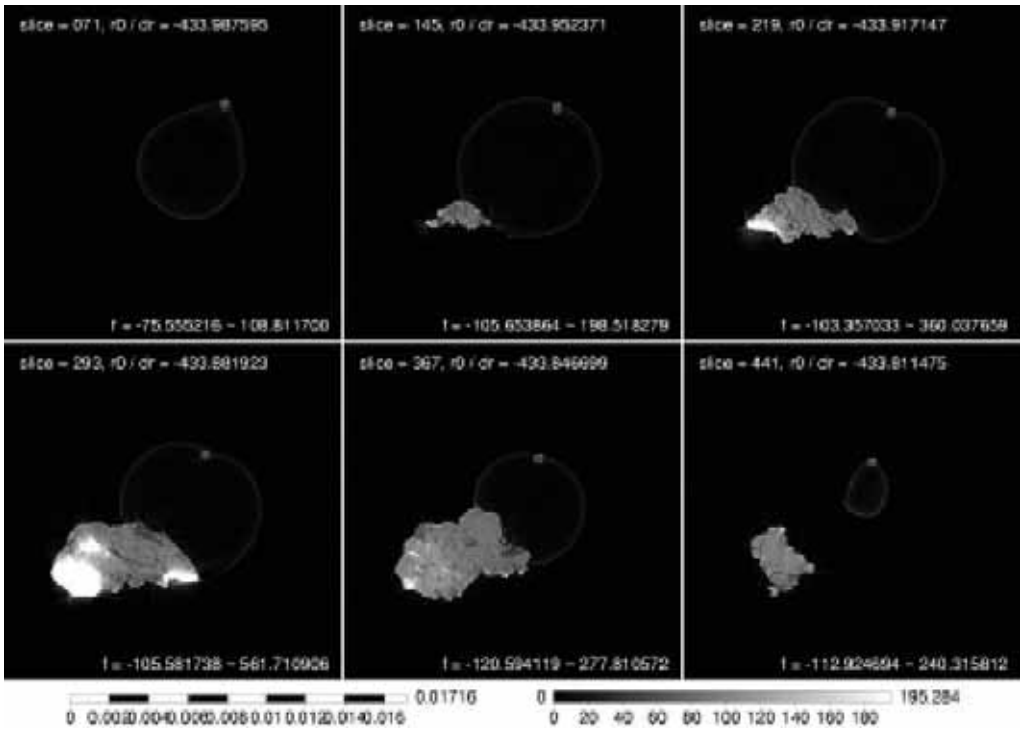

Figure 24. A browse image of CT slices of HASPET sample II-1A-001-A1 (041008f). The left and right bars are a scale bar in cm and a gray scale bar for CT values in cm^{-1}, respectively.

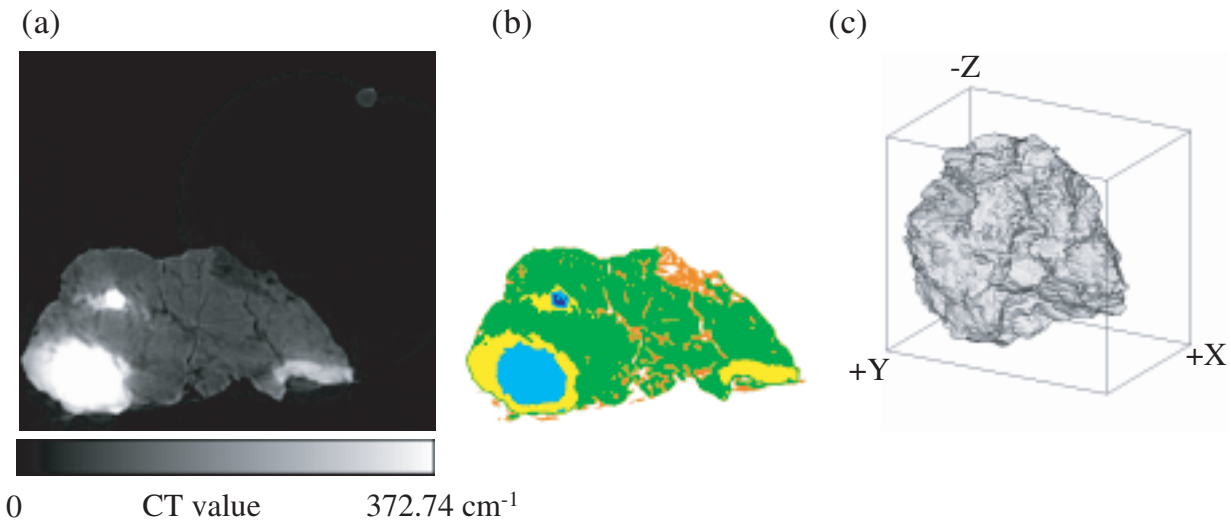

Figure 25. A typical CT slice and a bird's eye view of HASPET sample II-1A-001-A1 (041008f). (a) A CT image (372.74 cm^{-1} corresponds to PV=1380 in Figure 23. The width of the image is 95.16 μm. (b) An image showing phases. Orange: phase-A (probably plagioclase), Green: phase-B (probably Mg-Fe silicates), yellow: phase-C (probably troilite), cyan: phase-D (probably kamacite, and blue: phase-E (probably taenite). (c) A bird's eye view image (sample size: 80 x 53 x 72 μm).

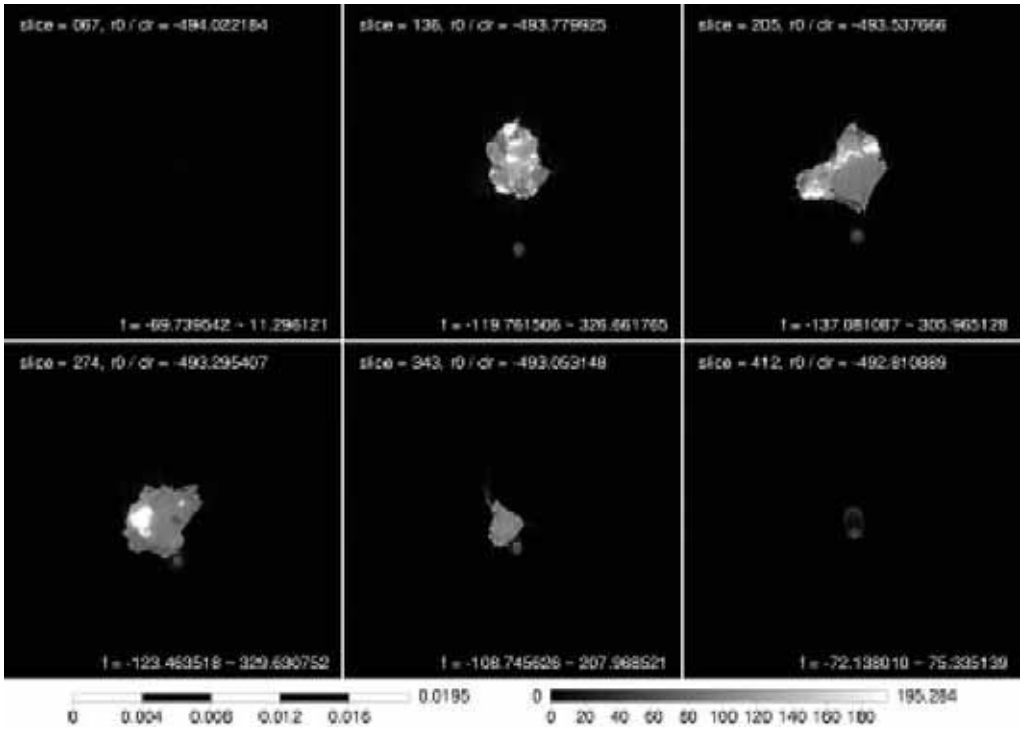

Figure 26. A browse image of CT slices of HASPET sample II-1A-002-A2 (041008e). The left and right bars are a scale bar in cm and a gray scale bar for CT values in cm^{-1}, respectively.

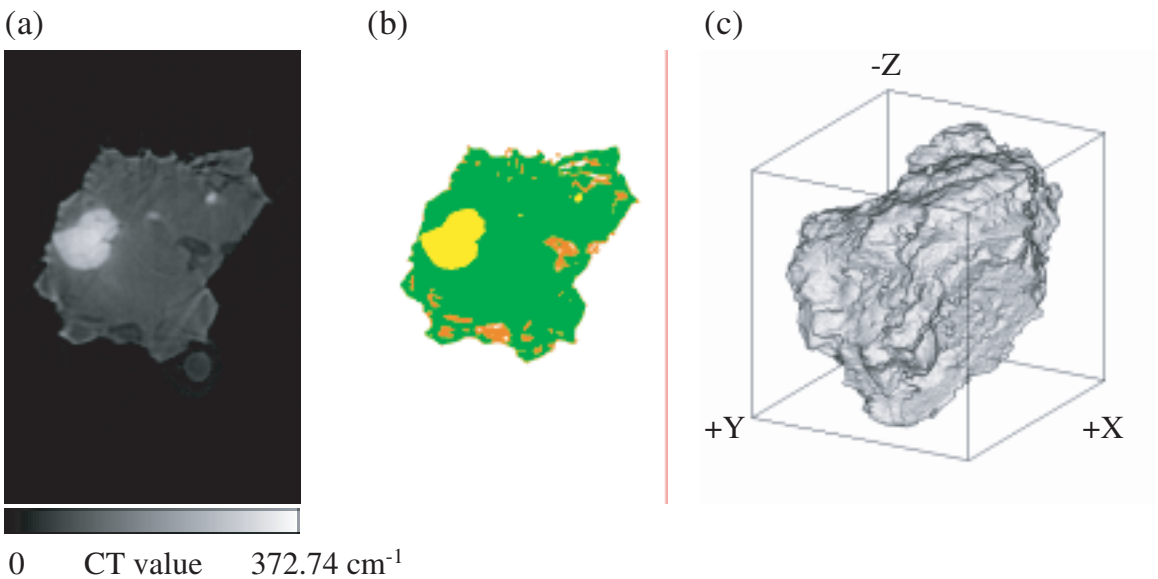

Figure 27. A typical CT slice and a bird's eye view of HASPET sample II-1A-002-A2 (041008e). (a) A CT image (372.74 cm^{-1} corresponds to PV=1380 in Figure 23. The width of the image is 56.745 μm. (b) An image showing phases. Orange: phase-A (probably plagioclase), Green: phase-B (probably Mg-Fe silicates) and yellow: phase-C (probably troilite). (c) A bird's eye view image (sample size: 56 x 60 x 59 μm).

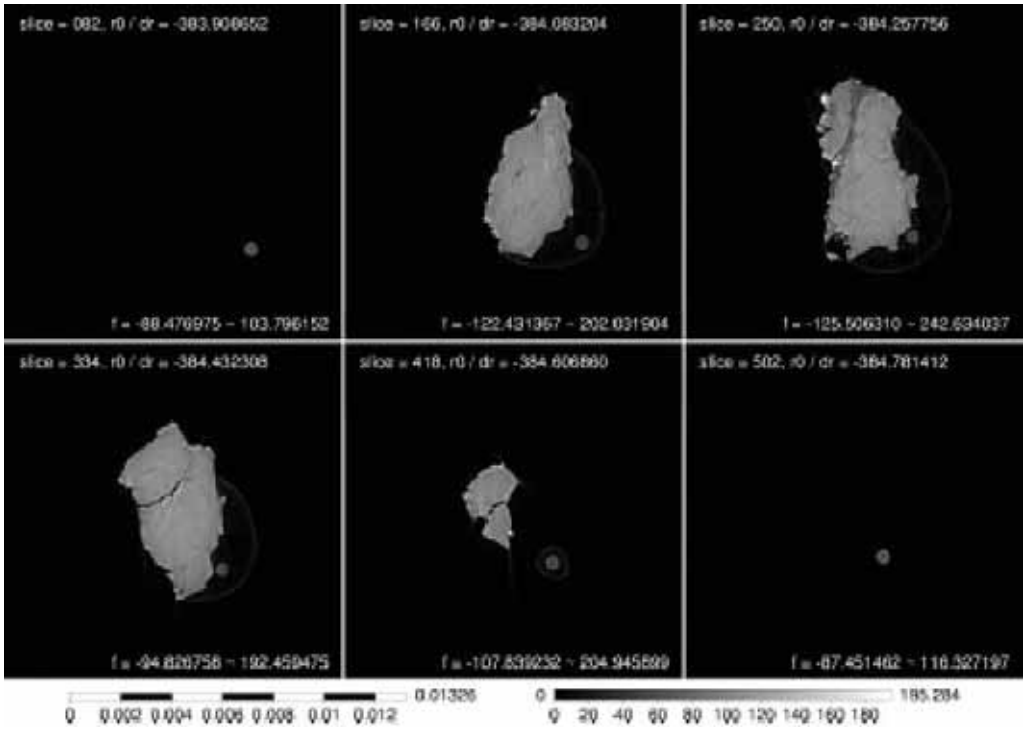

Figure 28. A browse image of CT slices of HASPET sample II-1A-003-A3 (041008d). The left and right bars are a scale bar in cm and a gray scale bar for CT values in cm^{-1}, respectively.

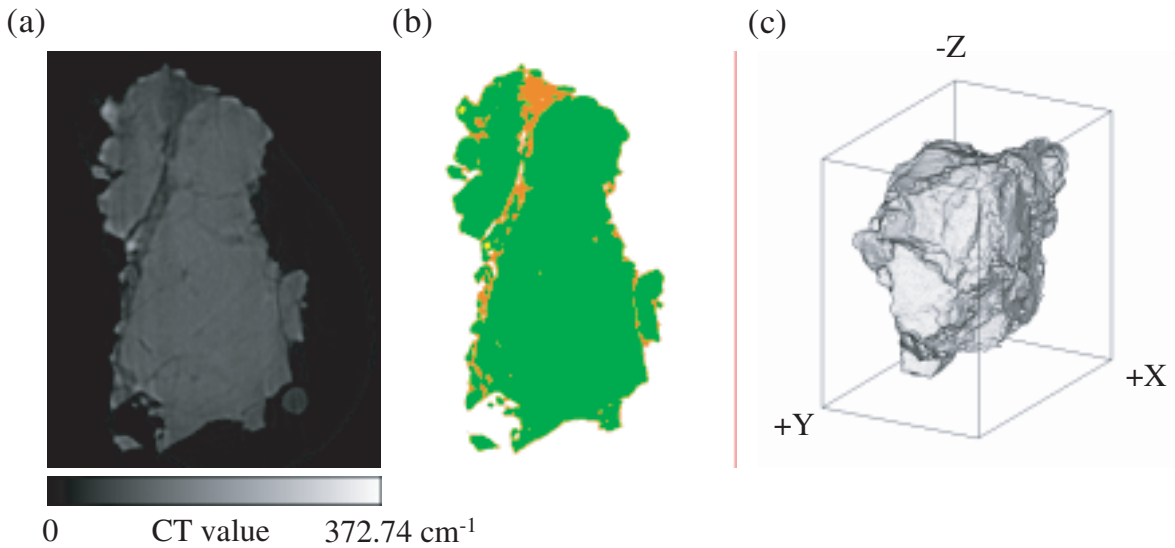

Figure 29. A typical CT slice and a bird's eye view of HASPET sample II-1A-003-A3 (041008d). (a) A CT image (372.74 cm^{-1} corresponds to PV=1380 in Figure 23. The width of the image is 62.205 μm. (b) An image showing phases. Orange: phase-A (probably plagioclase), Green: phase-B (probably Mg-Fe silicates) and yellow: phase-C (probably troilite). (c) A bird's eye view image (sample size: 52 x 76 x 76 μm).

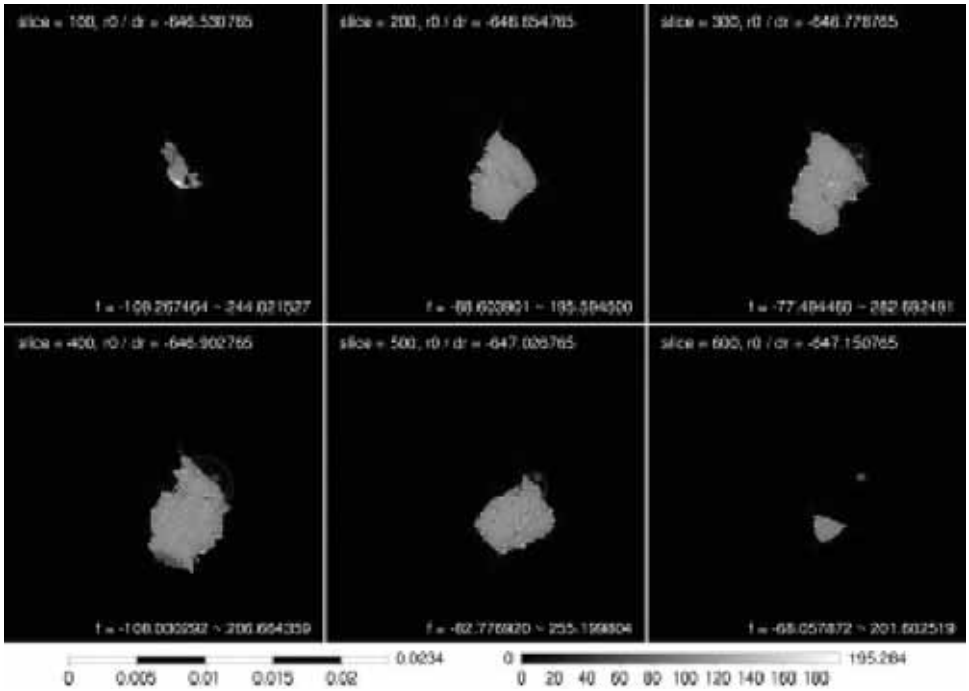

Figure 30. A browse image of CT slices of HASPET sample II-1A-004-A4 (041008c). The left and right bars are a scale bar in cm and a gray scale bar for CT values in cm^{-1}, respectively.

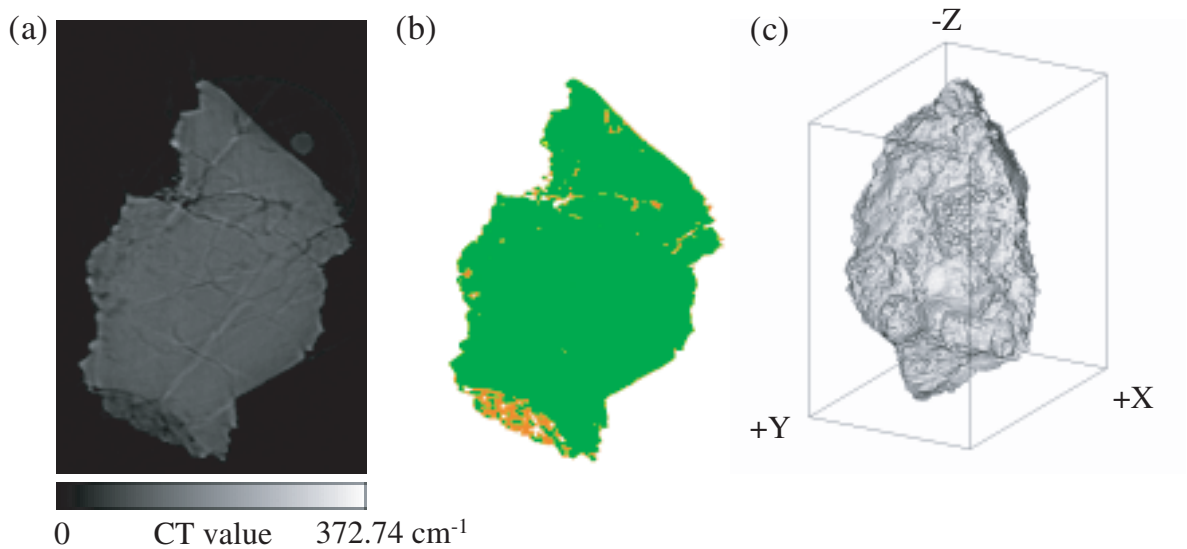

Figure 31. A typical CT slice and a bird's eye view of HASPET sample II-1A-004-A4 (041008c). (a) A CT image (372.74 cm^{-1} corresponds to PV=1380 in Figure 23. The width of the image is 69.615 μm. (b) An image showing phases. Orange: phase-A (probably plagioclase), Green: phase-B (probably Mg-Fe silicates) and yellow: phase-C (probably troilite). (c) A bird's eye view image (sample size: 69 x 101 x 117 μm).

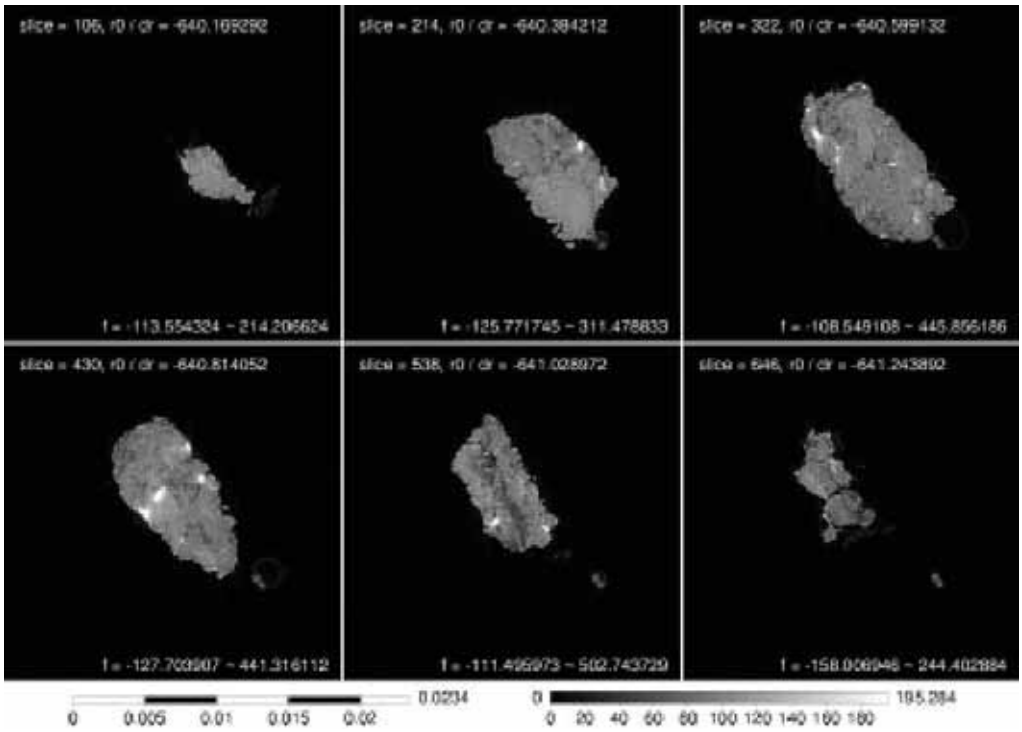

Figure 32. A browse image of CT slices of HASPET sample II-1A-005-A5 (041008b). The left and right bars are a scale bar in cm and a gray scale bar for CT values in cm^{-1}, respectively.

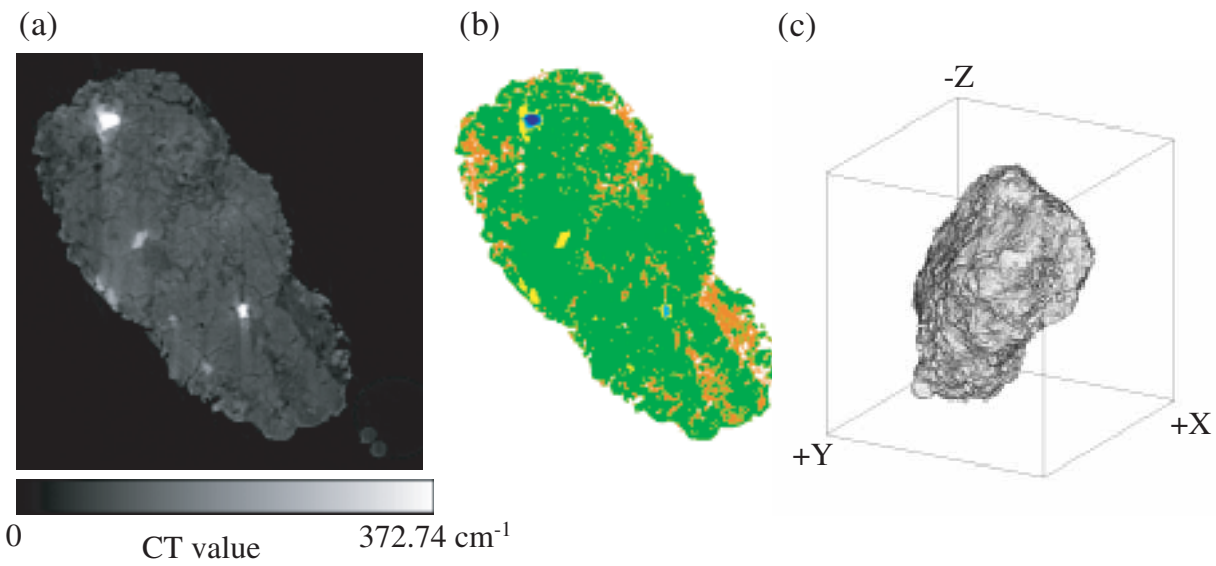

Figure 33. A typical CT slice and a bird's eye view of HASPET sample II-1A-005-A5 (041008b). (a) A CT image (372.74 cm^{-1} corresponds to PV=1380 in Figure 23. The width of the image is 122.46 μm. (b) An image showing phases. Orange: phase-A (probably plagioclase), Green: phase-B (probably Mg-Fe silicates), yellow: phase-C (probably troilite), cyan: phase-D (probably kamacite, and blue: phase-E (probably taenite). (c) A bird's eye view image (sample size: 121 x 125 x 134 μm).

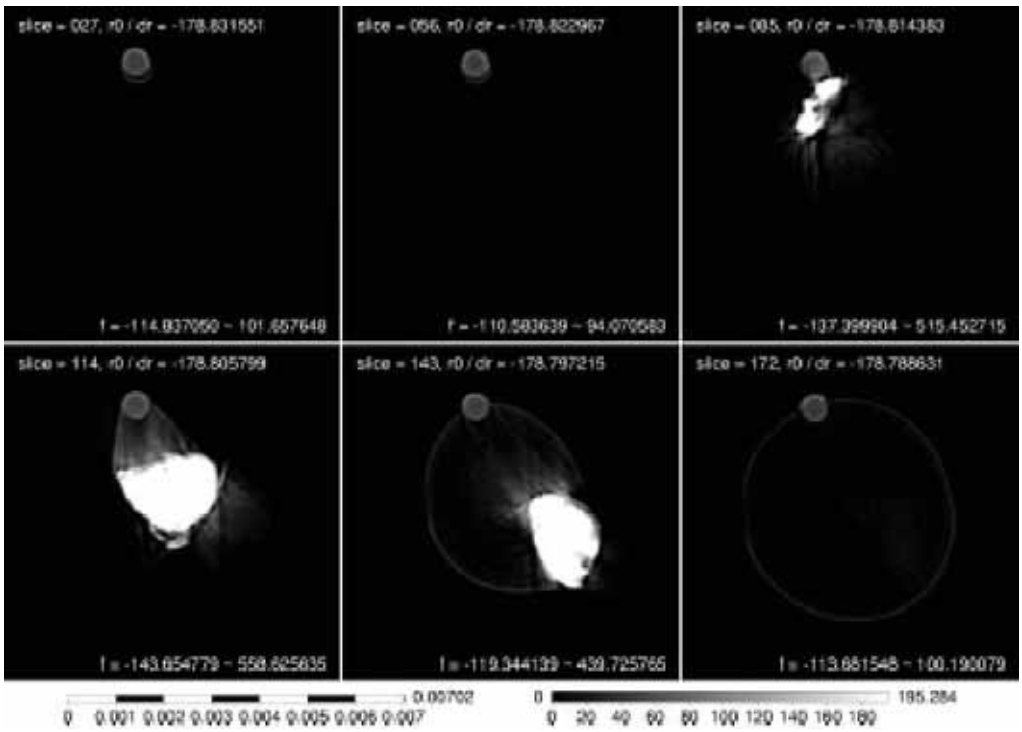

Figure 34. A browse image of CT slices of HASPET sample II-1A-006-A6 (041008h). The left and right bars are a scale bar in cm and a gray scale bar for CT values in cm^{-1}, respectively.

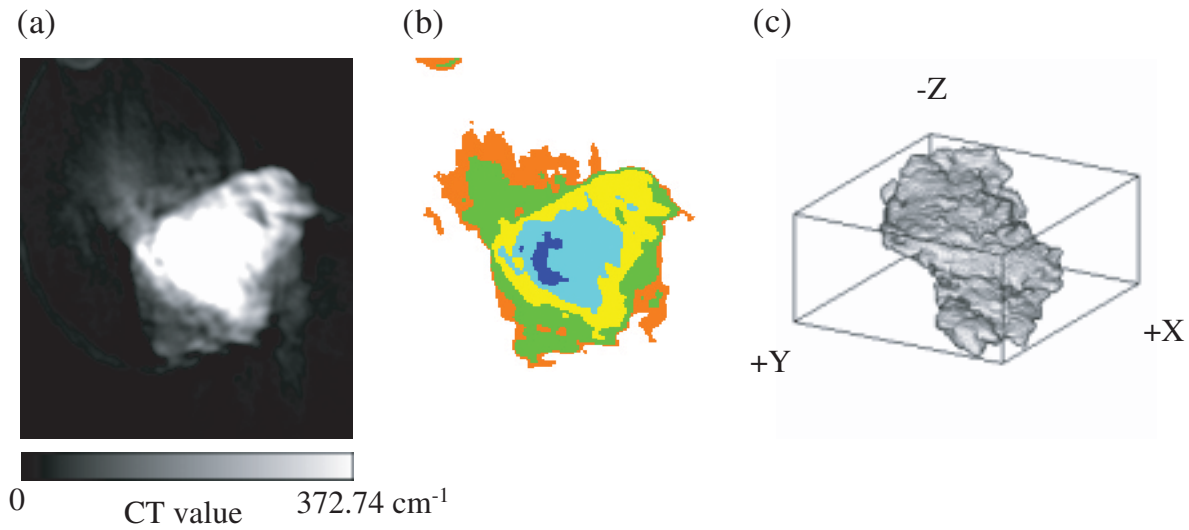

Figure 35. A typical CT slice and a bird's eye view of HASPET sample II-1A-006-A6 (041008h). (a) A CT image (372.74 cm^{-1} corresponds to PV=1380 in Figure 23. The width of the image is 32.37 μm. (b) An image showing phases. Orange: phase-A (probably plagioclase), Green: phase-B (probably Mg-Fe silicates), yellow: phase-C (probably troilite), cyan: phase-D (probably kamacite, and blue: phase-E (probably taenite). (c) A bird's eye view image (sample size: 32 x 36 x 15 μm).

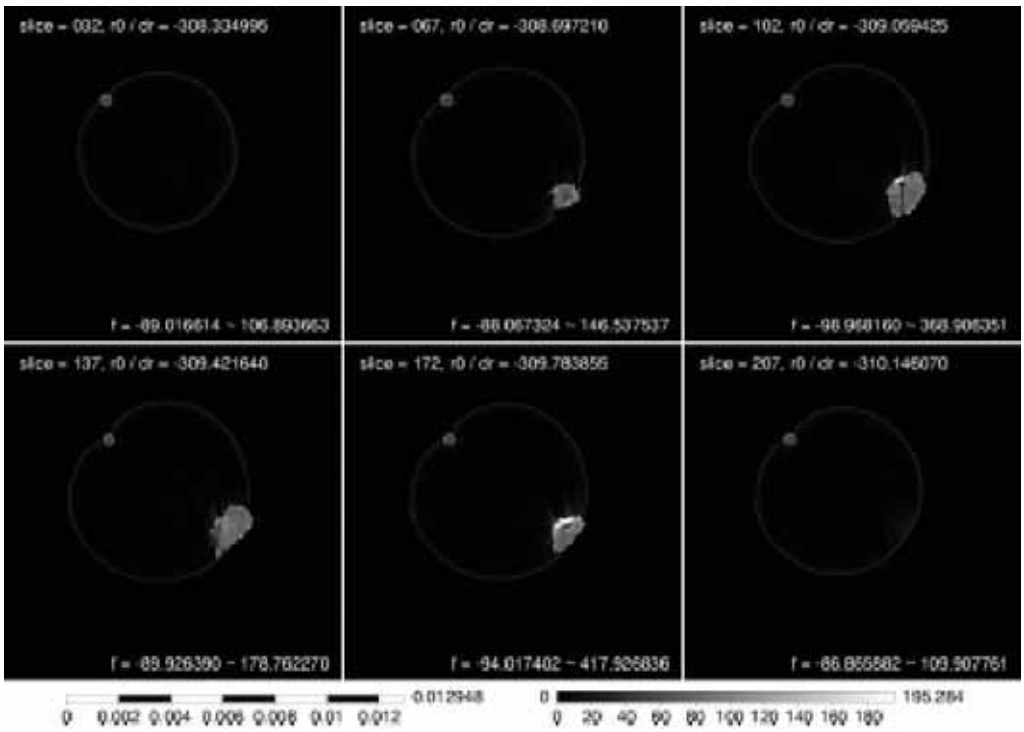

Figure 36. A browse image of CT slices of HASPET sample II-1A-0014-A14 (041008i). The left and right bars are a scale bar in cm and a gray scale bar for CT values in cm^{-1}, respectively.

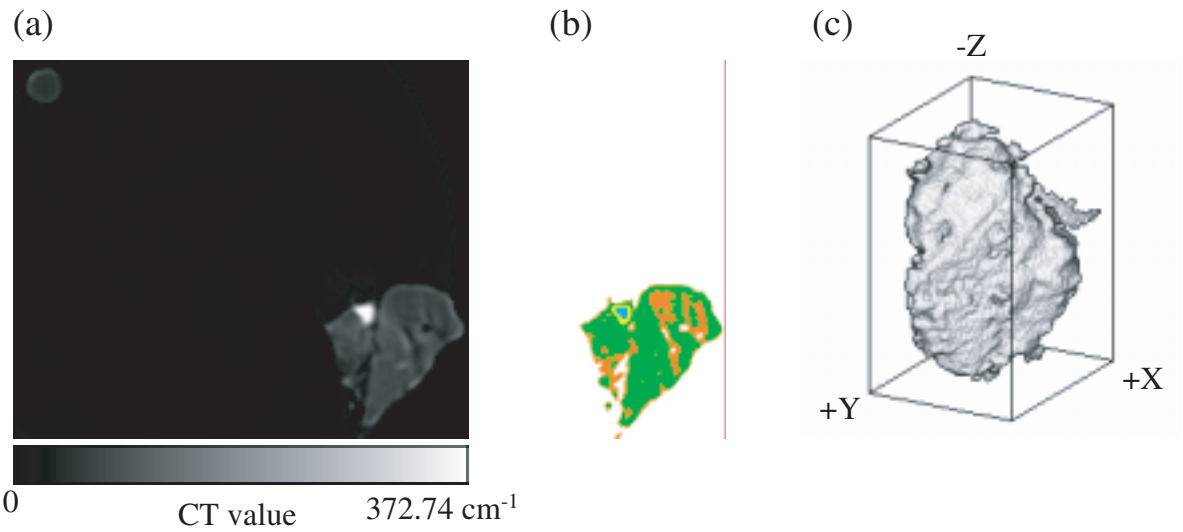

Figure 37. A typical CT slice and a bird's eye view of HASPET sample II-1A-014-A14 (041008i). (a) A CT image (372.74 cm^{-1} corresponds to PV=1380 in Figure 23. The width of the image is 60.645 μm. (b) An image showing phases. Orange: phase-A (probably plagioclase), Green: phase-B (probably Mg-Fe silicates), yellow: phase-C (probably troilite) and cyan: phase-D (probably kamacite. (c) A bird's eye view image (sample size: 19 x 24 x 33 μm).

Table 8. The LACs of phases-A, B, C, D and E in HASPET samples II-1A-001-A1(041008f), 002-A2 (041008e), 003-AA3 (041008d), 004-A4 (041008c), 005-A5 (041008b), 006-A6 (041008h) and 010-A14 (041008i), calculated form their CT values and estimation of their mineral candidates and compositions. LAC values of phases-C, D and E calculated form the CT values should be smaller than the real values due to their large LAC values.

	CT value (cm^{-1})	LAC (cm^{-1})	candidates		LAC (cm^{-1})		LAC (cm^{-1})		LAC (cm^{-1})
phase-A	55.4	62.6	plagioclase	An51	62.6				
phase-B (041008b)	93.5	105.6	Mg-Fe silicate	Fo87	105.8	En82	105.6		
phase-B (041008c)	100.8	113.9	Mg-Fe silicate	Fo85	113.9	En79	113.8		
phase-B (041008d)	105.1	118.7	Mg-Fe silicate	Fo84	118.7	En77	118.7		
phase-B (041008e)	93.2	105.3	Mg-Fe silicate	Fo87	105.4	En82	105.3		
phase-B (041008f)	86.4	97.7	Mg-Fe silicate	Fo89	97.7	En85	97.6		
phase-B abd C?(041008i)	74.6	84.2	silicate	An100	77.6	Fo93	84.3	En89.9	84.3
phase-B (041008bcdef)	102.9	116.3	Mg-Fe silicate	Fo84	116.3	En78	116.3		
phase-C	266.1	300.6	troilite	troilite	612.9				
phase-D	479.4	541.7	kamacite	Fe	1346.6				
phase-E	559.1	631.8	taenite	Ni	1862.2				

Table 9. The volume of HASPET samples II-1A-001-A1(041008f), 002-A2 (041008e), 003- AA3 (041008d), 004-A4 (041008c), 005-A5 (041008b), 006-A6 (041008h) and 010-A14 (041008i) and the modes of the phases.

	041008b	**041008c**	**041008d**	**041008e**	**041008f**	**041008h**	**041008i**	**wt.mean**	**stdev**	
volume (voxel)	**64796591**	**27345006**	**12766017**	**7945645**	**11071598**	**530389**	**501100**			
volume (µm 3)	**4.805E+05**	**2.028E+05**	**9.466E+04**	**5.892E+04**	**8.209E+04**	**3.933E+03**	**3.716E+03**			
mode /%										
phase-A	**16.0**	**5.0**	**5.6**	**7.8**	**15.3**	**19.5**	**28.9**	**12.0**	**5.2**	**plagioclase**
phase-B	**82.1**	**94.8**	**94.3**	**86.7**	**74.3**	**27.6**	**68.4**	**85.5**	**7.7**	**Mg-Fe silicates**
phase-C	**0.8**	**0.1**	**0.0**	**5.3**	**6.6**	**36.0**	**1.7**	**1.5**	**3.0**	**troilite**
phase-D	**0.1**	**0.0**	**0.0**	**0.0**	**3.1**	**16.3**	**0.5**	**0.4**	**1.3**	**kamacite**
phase-E	**0.0**	**0.0**	**0.0**	**0.0**	**0.0**	**0.6**	**0.0**	**0.0**	**0.0**	**taenite**
voids	**1.0**	**0.1**	**0.1**	**0.2**	**0.7**	**0.1**	**0.5**	**0.6**	**0.4**	
mass estimaged (µg)		**17.6**	**7.4**	**3.5**	**2.2**	**3.0**	**0.1**	**0.1**		

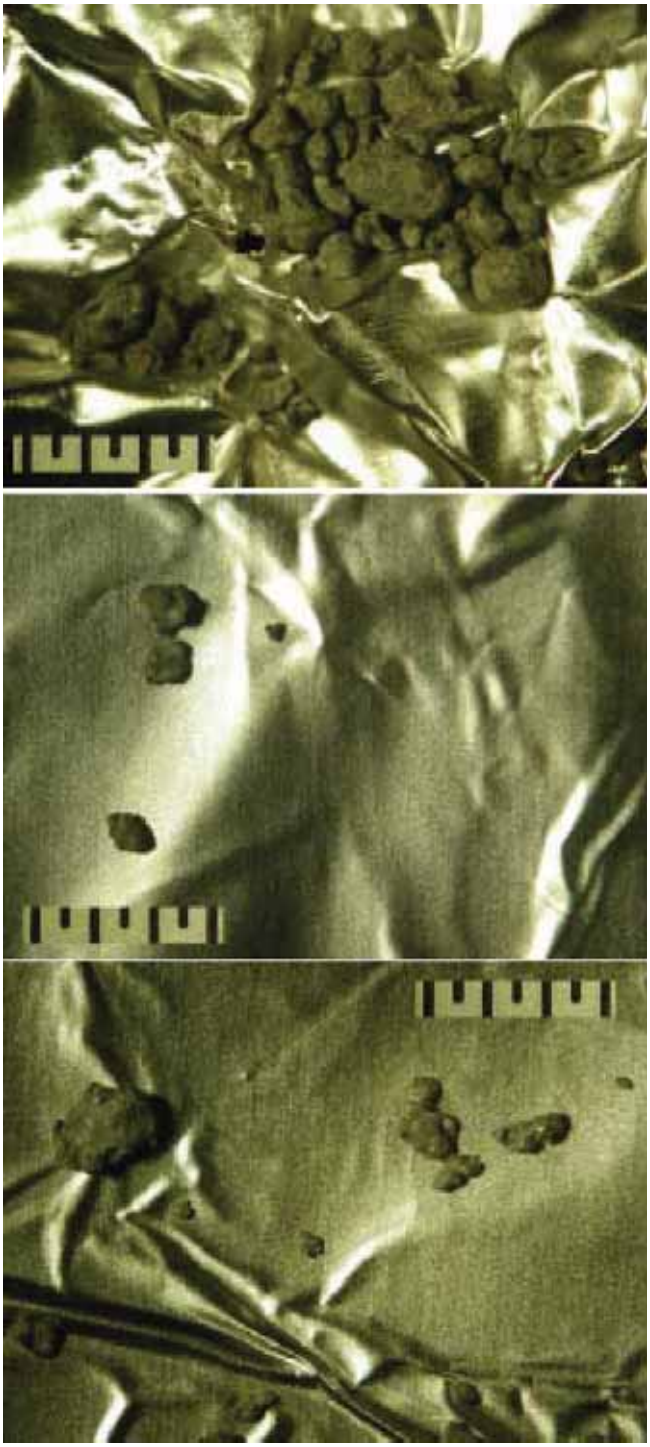

Figure 38. Photomicrographs of HASPET sample II-1B. Sample grains are on an Al foil. The separation between each scale bar is 0.5 mm.

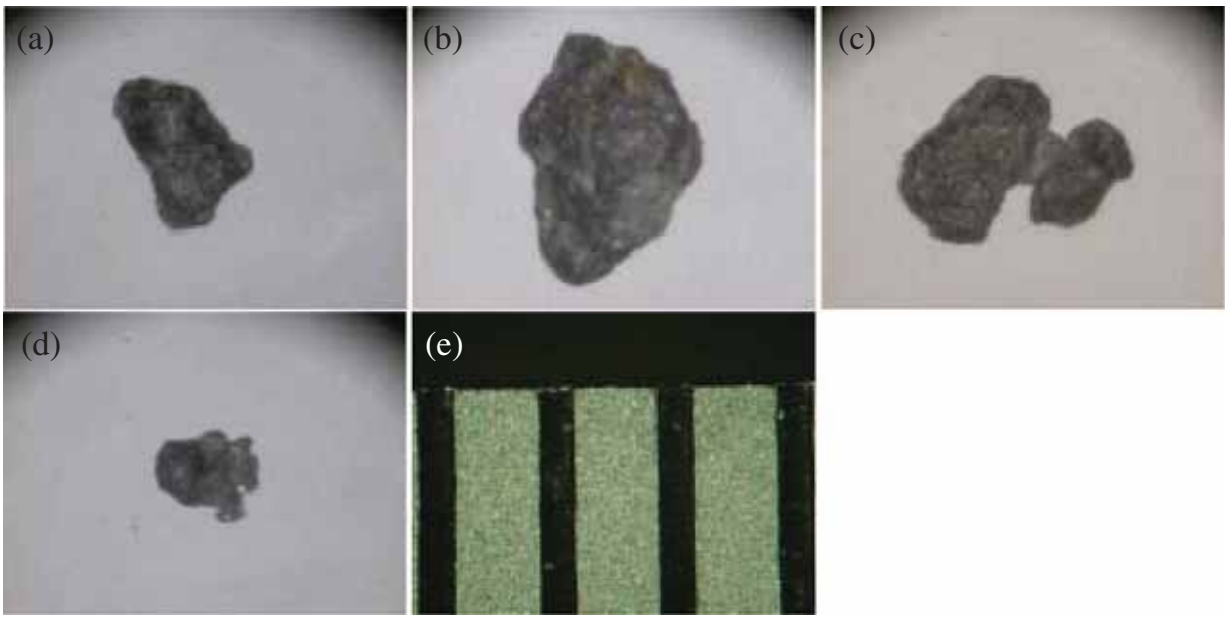

Figure 39. Photomicrograph of single grains (HASPET sample II-1B) . (a) 002-A8 (041007c). (b) 004-A10 (041007a). (c) 008-A15 (041007b). (d) 001-A7 (04108a). (e) A scale. The separation between each scale bar is 0.5 mm.

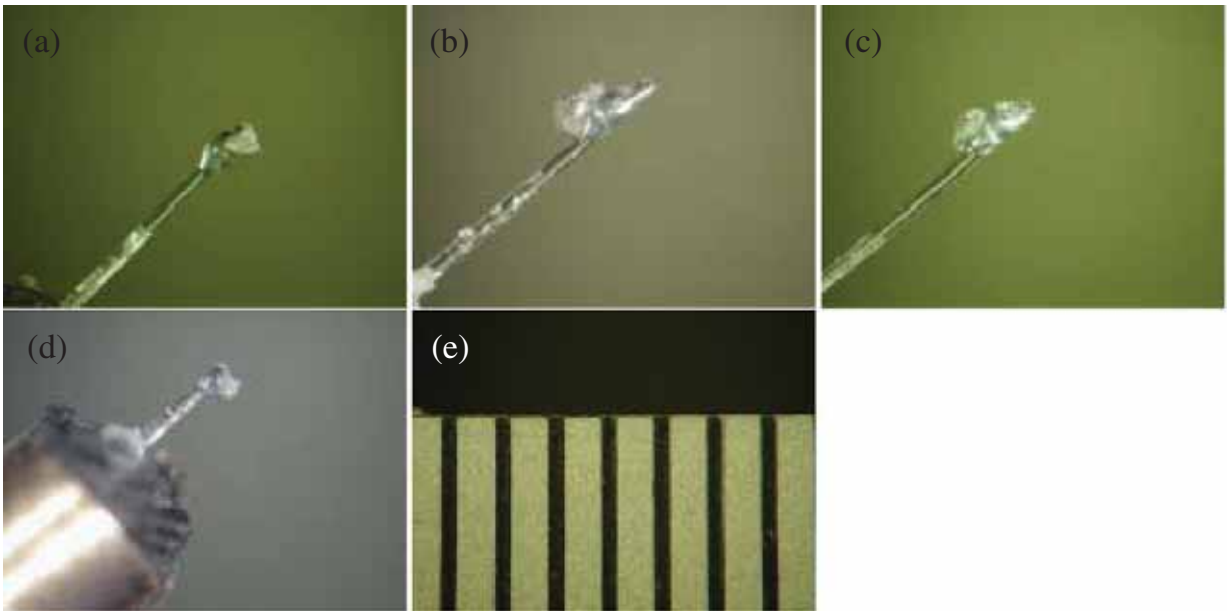

Figure 40. Photomicrograph of single grains (HASPET sample II-1B) on a glass fiber. (a) 002- A8 (041007c). (b) 004-A10 (041007a). (c) 008-A15 (041007b). (d) 001-A7 (04108a). (e) A scale. The separation between each scale bar is 0.5 mm.

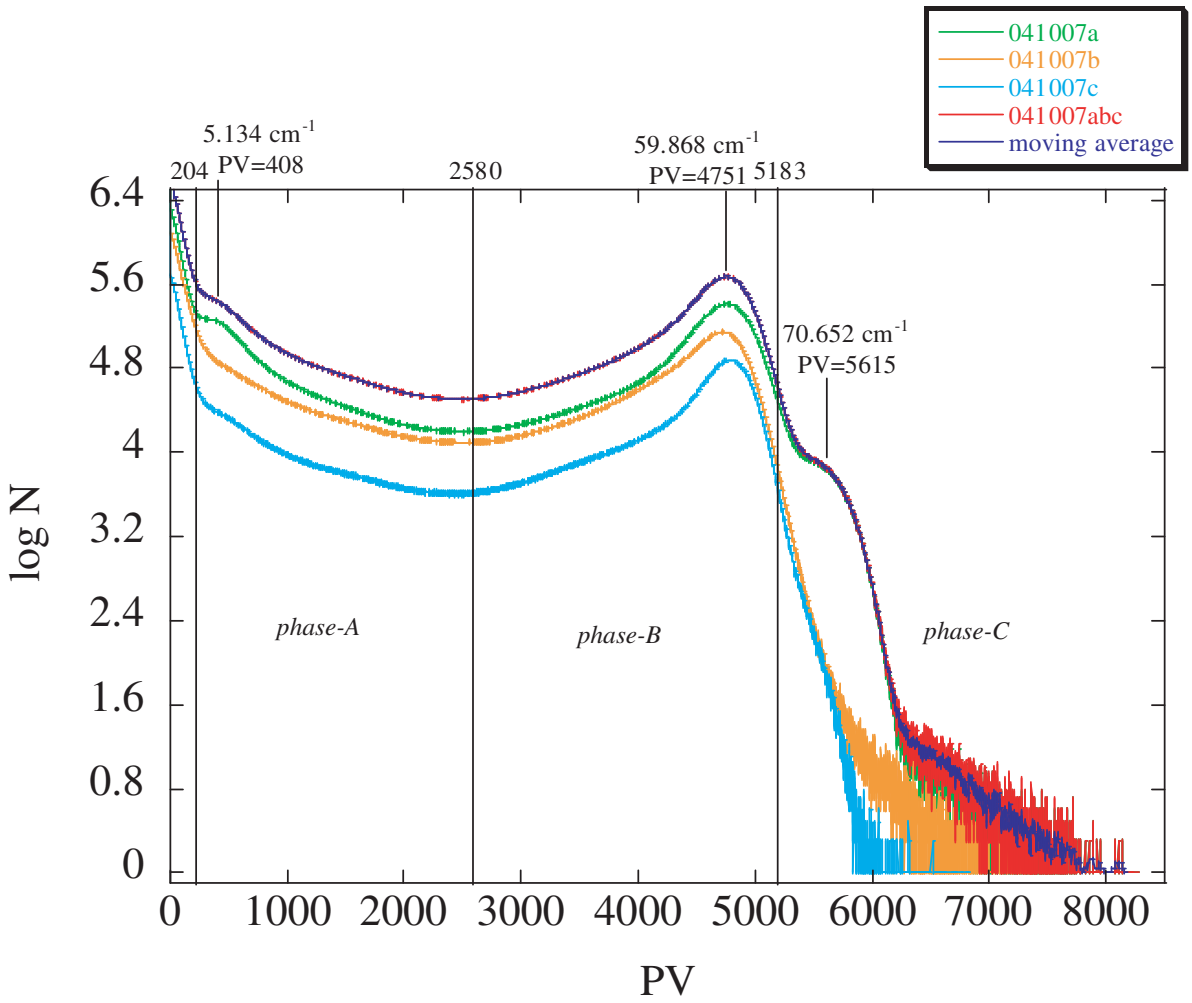

Figure 41. A CT value histogram of HASPET samples II-1B-002-A8 (041007c), 004-A10 (041007a) and 008-A15 (041007b). The CT values, *f*, are replaced by the pixel values, PV, in 16 bit images ($f = 0.012583$ cm^{-1} x PV). Peak PVs and CT values for phases-A, B and C, and threshold PVs between the phases are shown.

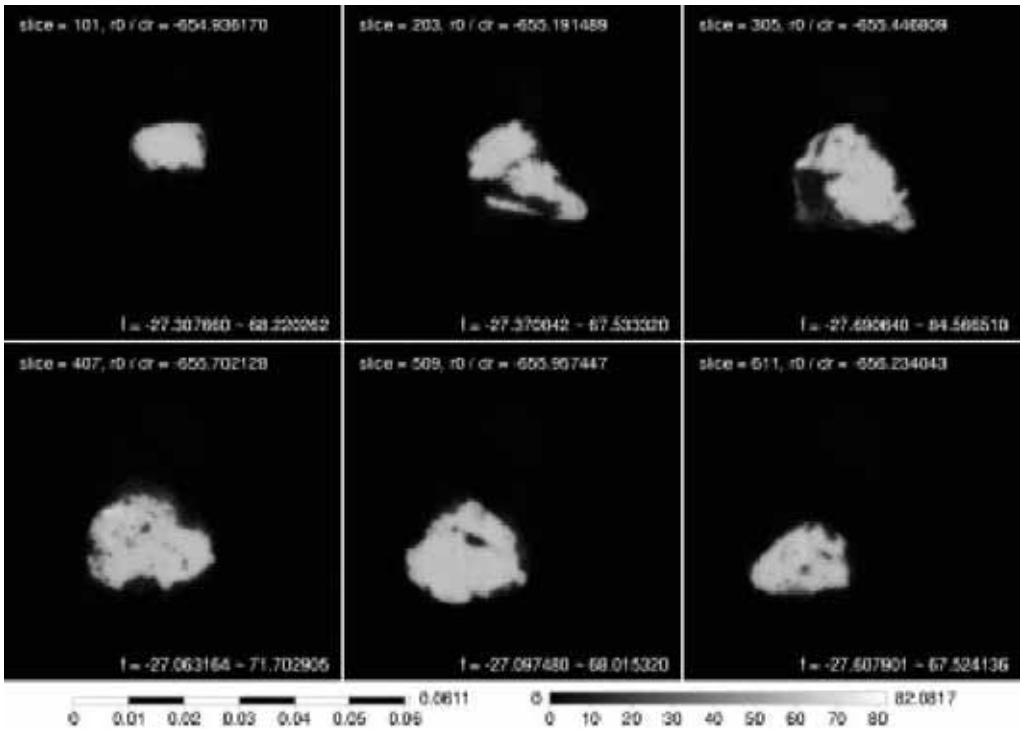

Figure 42. A browse image of CT slices of HASPET sample II-1B-002-A8 (041007c). The left and right bars are a scale bar in cm and a gray scale bar for CT values in cm^{-1}, respectively.

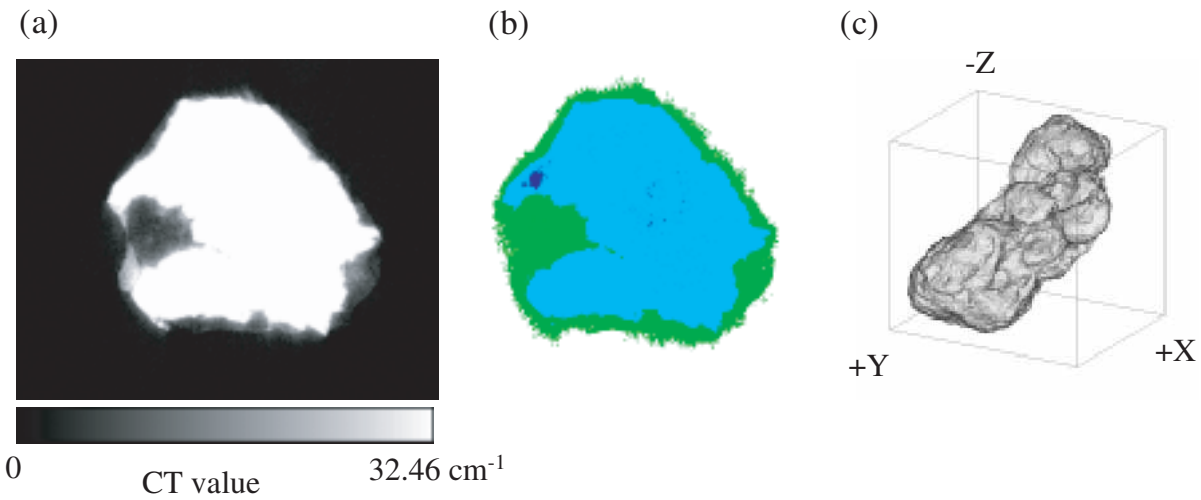

Figure 43. A typical CT slice and a bird's eye view of HASPET sample II-1B-002-A8 (041007c). (a) A CT image (32.46 cm^{-1} corresponds to PV=2580 in Figure 41). The width of the image is 344.98 μm. (b) An image showing phases. Green: phase-A (probably Mg-Fe silicates), cyan: phase-B (probably kamacite, and blue: phase-C (probably taenite). (c) A bird's eye view image (sample size: 332 x 226 x 308 μm).

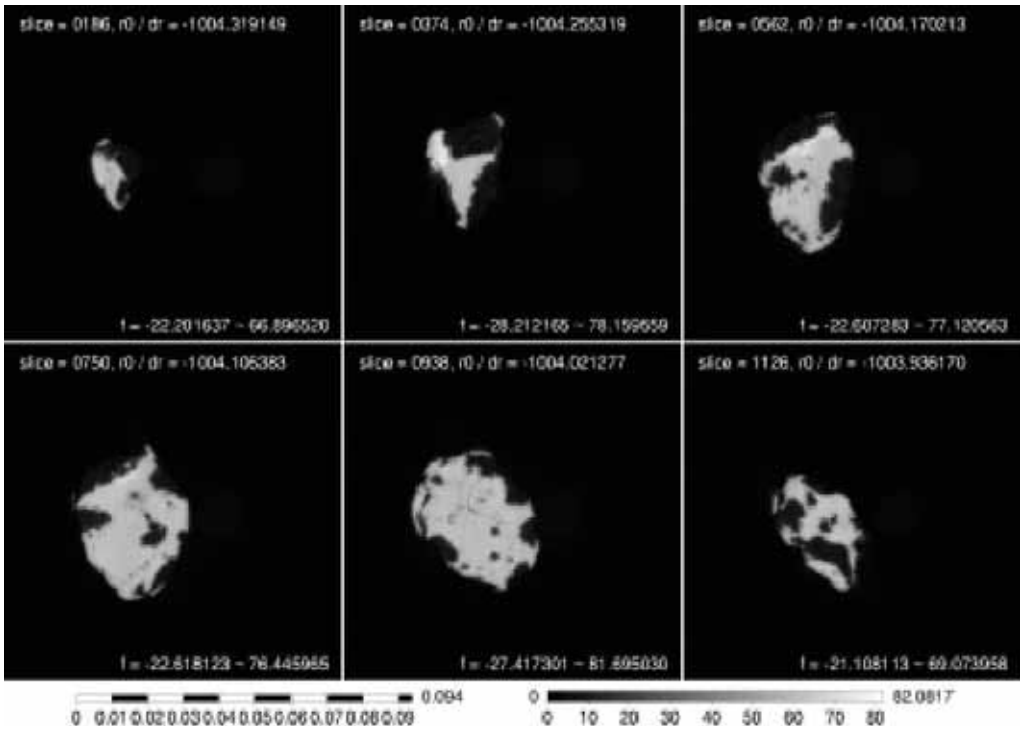

Figure 44. A browse image of CT slices of HASPET sample II-1B-004-A10 (041007a). The left and right bars are a scale bar in cm and a gray scale bar for CT values in cm^{-1}, respectively.

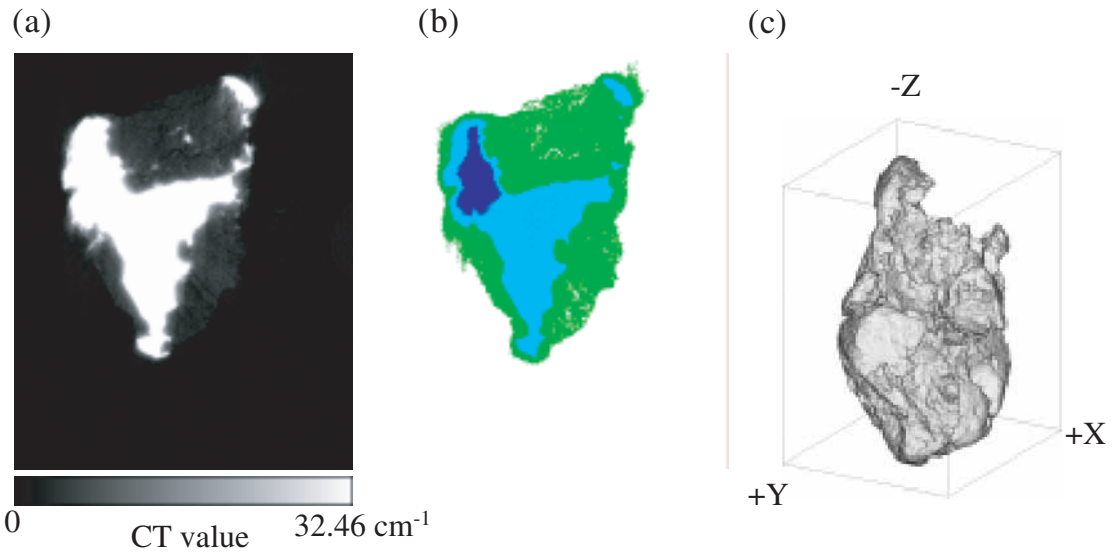

Figure 45. A typical CT slice and a bird's eye view of HASPET sample II-1B-004-A10 (041007a). (a) (32.46 cm^{-1} corresponds to PV=2580 in Figure 41). The width of the image is 383.99 μm. (b) An image showing phases. Green: phase-A (probably Mg-Fe silicates), cyan: phase-B (probably kamacite, and blue: phase-C (probably taenite). (c) A bird's eye view image (sample size: 368 x 436 x 570 μm).

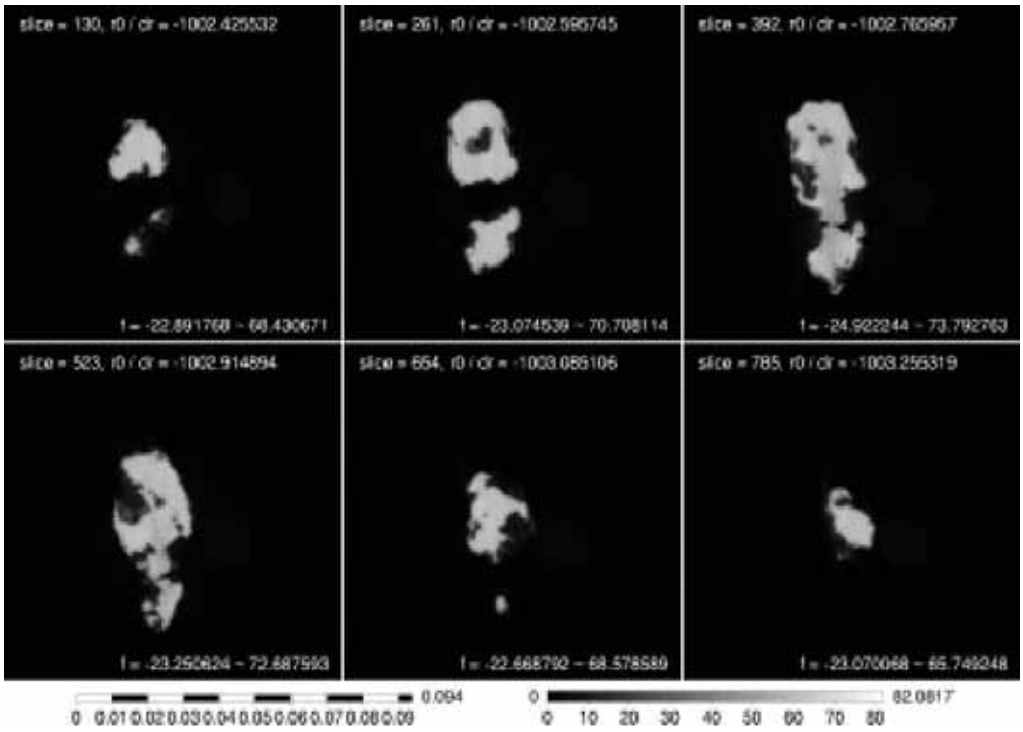

Figure 46. A browse image of CT slices of HASPET sample II-1B-008-A15 (041007b). The left and right bars are a scale bar in cm and a gray scale bar for CT values in cm^{-1}, respectively.

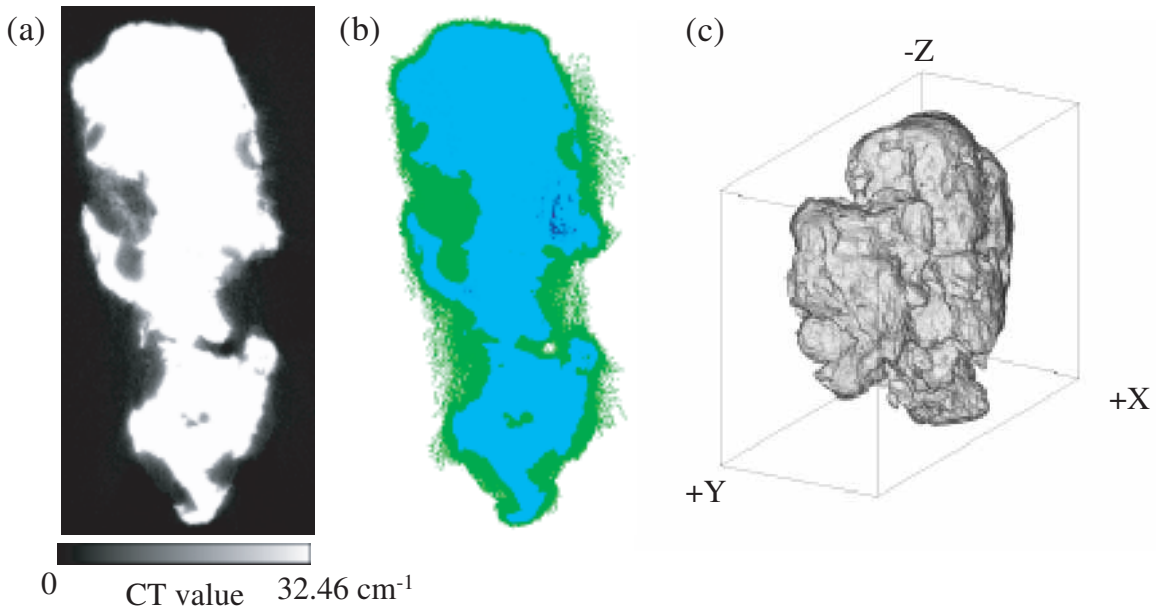

Figure 47. A typical CT slice and a bird's eye view of HASPET sample II-1B-008-A15 (041007b). (a) A CT image (32.46 cm^{-1} corresponds to PV=2580 in Figure 41). The width of the image is 272.6 μm. (b) An image showing phases. Green: phase-A (probably Mg-Fe silicates), cyan: phase-B (probably kamacite, and blue: phase-C (probably taenite). (c) A bird's eye view image (sample size: 252 x 599 x 405 μm).

Table 10. The LACs of phases-A, B and C in HASPET samples II-1B-002-A8 (041007c), 004-A10 (041007a) and 008-A15 (041007b)., calculated form their CT values and estimation of their mineral candidates and compositions.

	CT value (cm^{-1})	LAC (cm^{-1})	candidates		LAC (cm^{-1})		LAC (cm^{-1})
phase-A	5.13	5.80	silicate	Fo83	5.80	En76.1	5.81
phase-B	59.87	67.65	kamacite	Fe88	67.64		
phase-C	70.65	79.83	taenite	Fe43	79.83		

Table 11. The volume of HASPET samples II-1B-002-A8 (041007c), 004-A10 (041007a) and 008-A15 (041007b) and the modes of the phases.

	041007a	041007b	041007c	wt.mean		
sample(mg)	0.2400	0.1344	0.0576			
stdev	0.0004	0.0007	0.0011			
volume (voxel)	336716996	195684963	77218257			
volume (cm^3)	3.496E-05	2.032E-05	8.017E-06			
density (g/cm^3)	6.87	6.62	7.18	6.89		
stdev	0.01	0.03	0.14	0.29		
mode (%)						candidates
phase-A	38.9	38.3	30.6	37.7	2.7	silicates
phase-B	61.1	61.7	69.4	62.3	2.7	metal
phase-C	59.6	61.6	69.1	61.4	3.1	kamacite
phase-D	1.5	0.2	0.2	0.9	0.7	taenite

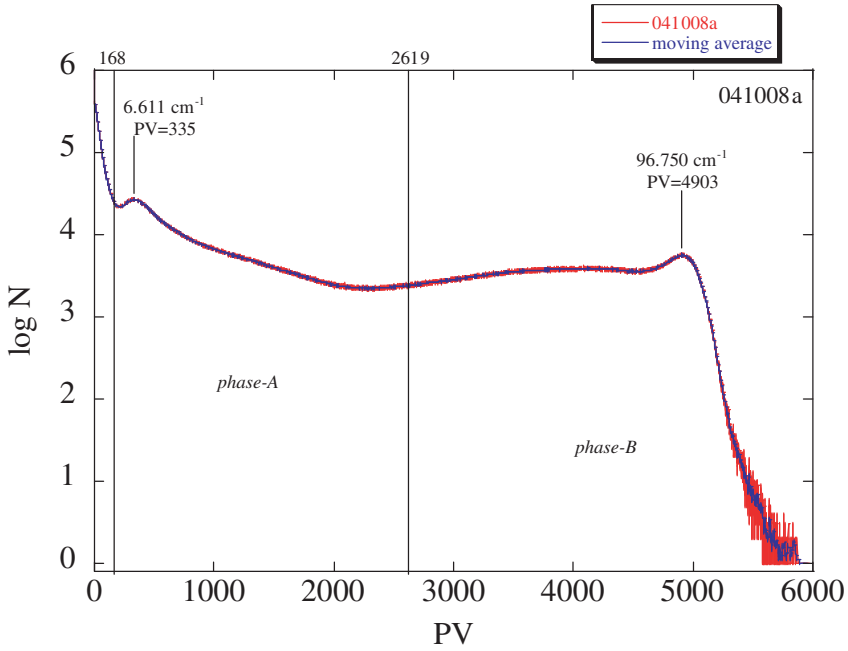

Figure 48. A CT value histogram of HASPET sample II-1B-001-A7 (041008a). The CT values, *f*, are replaced by the pixel values, PV, in 16 bit images ($f = 0.019733$ cm^{-1} x PV). Peak PVs and CT values for phases-A, B and C, and threshold PVs between the phases are shown.

Table 12. The LACs of phases-A and B in HASPET sample II-1B-001-A7 (041008a) calculated form their CT values and estimation of their mineral candidates and compositions.

	CT value (cm^{-1})	LAC (cm^{-1})	candidates			LAC (cm^{-1})		LAC (cm^{-1})
phase-A	6.61	7.47	Mg-Fe silicates	Fo89	7.47	En85	7.47	
phase-B	96.75	109.32	kamacite	Fe97	109.34			

Table 13. The volume of HASPET sample II-1B-001-A7 (041008a) and the modes of the phases.

	041009def	
sample(mg)	0.0144	
stdev	0.0009	
volume (cm^3)	2.847E-06	
density (g/cm^3)	5.05	
stdev	0.32	
mode (%)		candidate
phase-A	67.3	Mg-Fesilicates
phase-B	32.7	metal

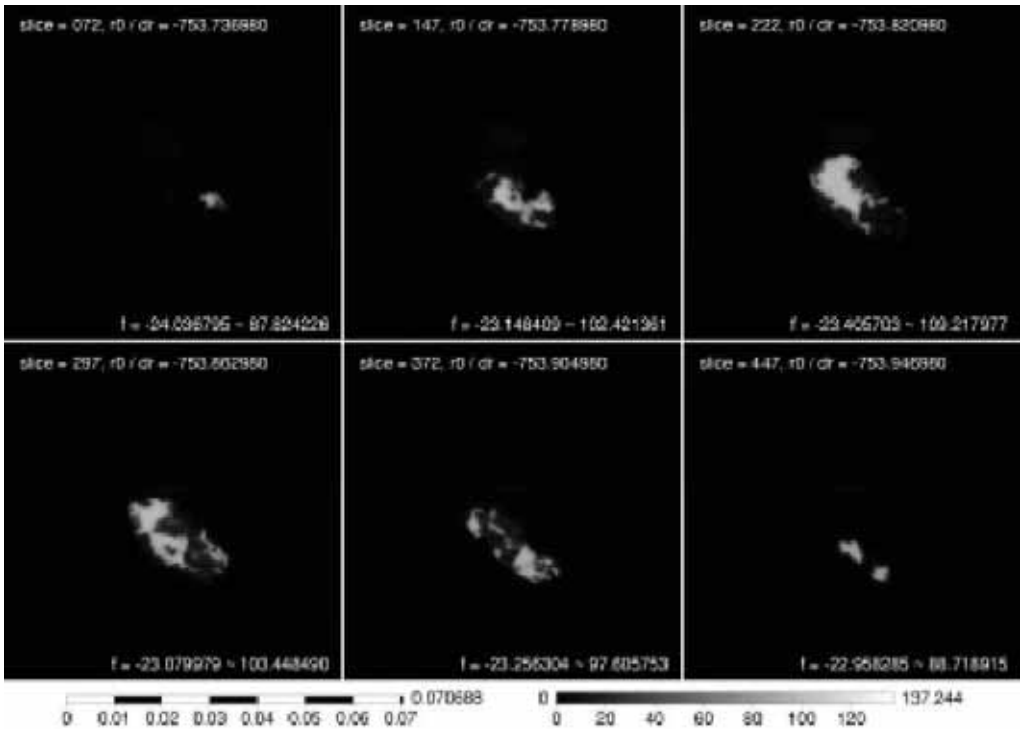

Figure 49. A browse image of CT slices of HASPET sample II-1B-001-A7 (041008a). The left and right bars are a scale bar in cm and a gray scale bar for CT values in cm^{-1} , respectively.

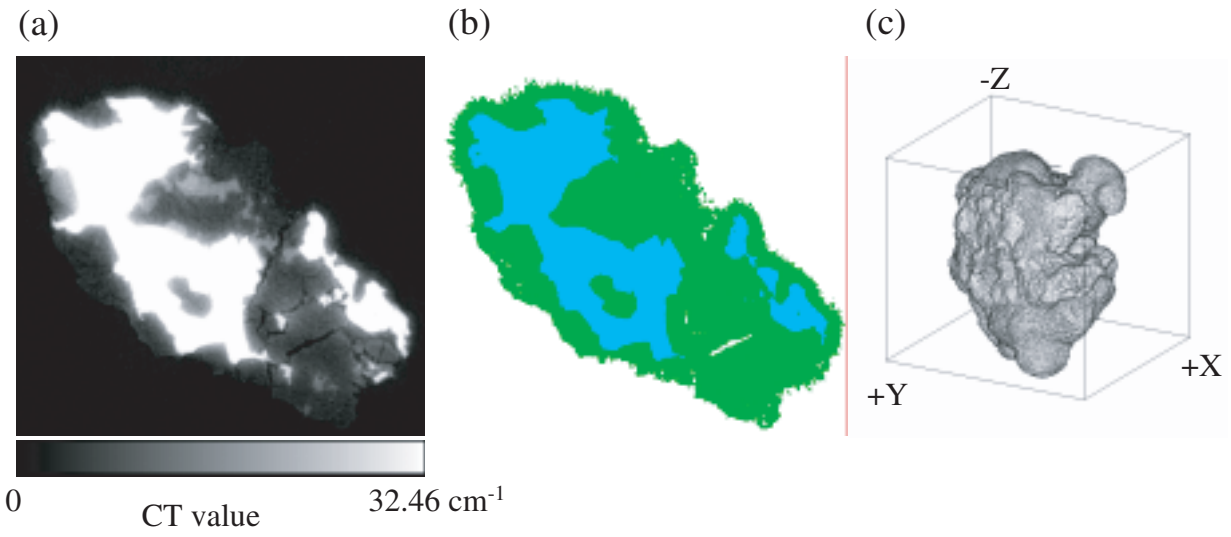

Figure 50. A typical CT slice and a bird's eye view of HASPET sample II-1B-001-A7 (041008a). (a) A CT image (32.46 cm^{-1} corresponds to PV=2580 in Figure 41). The width of the image is 227.95 μm. (b) An image showing phases. Green: phase-A (probably Mg-Fe silicates), cyan: phase-B (probably kamacite, and blue: phase-C (probably taenite). (c) A bird's eye view image (sample size: 227 x 210 x 215 μm).

pallasites. The density (5.1-6.9 g/cm^3) is larger than that of pallasirte (4.76 g/cm^3: Britt and Consolmagno, 2003). An Eagle station pallasite might be possible for the grain size. Some silicate inclusions in iron meteorites might be another possibility.

3.3. Radiographic study of sample II-1A

Figure 52 shows mosaic images of sample II-1A-P3. We can observe many grains as well as Al foils in the projection images at above and blow the Zr K-edge energy. Any bright spots were not seen in the subtraction image, suggesting Zr-bearing phase within the spatial resolution of the image (about a few μm) is absent in this sample. In contrast, many zircon grains are easily recognized in the subtraction image of sample II-1A-P4z, where zircon grains were added to II-1A powder. Figure 54 shows stereographs of close up of sample II-1A-P4z. The same bright spots are present in the two subtract images with different beam angles by 1 degree. This shows that all the bright spots are not due to Bragg reflection contrast but due to Zr contrast.

We have already applied this subtraction method to an eucrite (Millbillillie) for searching zircon crystals in meteorites using tomography (Tsuchiyama et al., in preparation). We observed large zircon grains of up to 60 μm. in a 3.2 mm^3 sample. Therefore, this technique will be also useful to the samples returned from Itokawa.

(a)

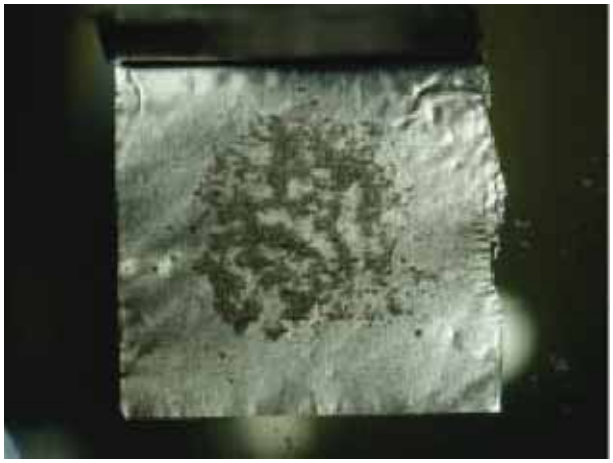

II-1A-P3_x10.JPG

(b)

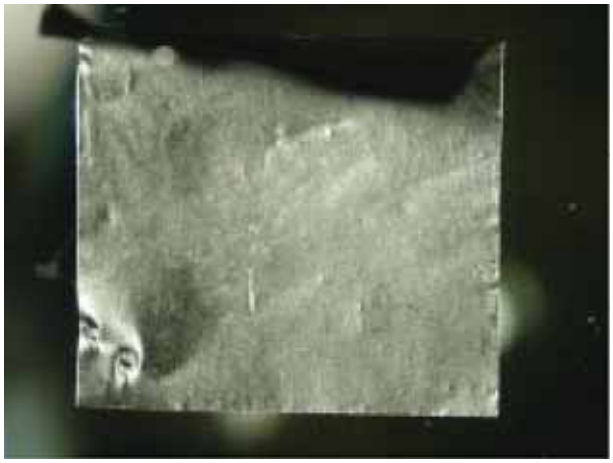

II-1A-P4z_zr_x10.JPG

(c)

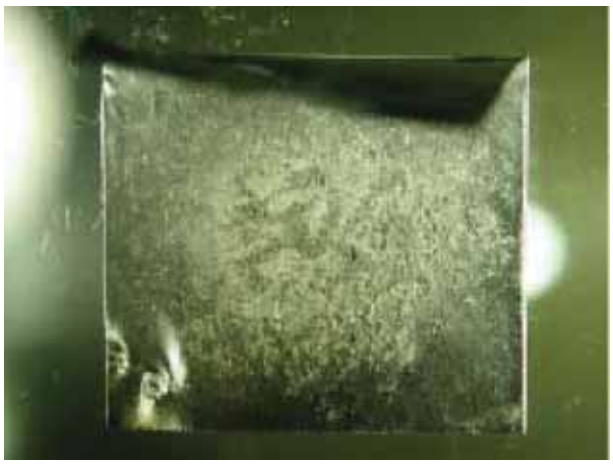

II-1A-P4z_x10.JPG

(d)

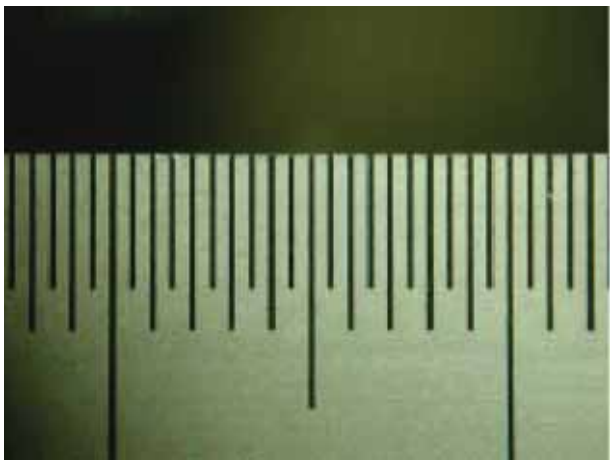

scale_x10-2.JPG (0.5 mm)

Figure 51. Photomicrographs of HASPET sample II-1A-P3 and P4z (041010a) for zircon serach. (a) A powder sample of II-1A-P3, where zircon crystals are not added, on an Al foil. (b) A powder sample of II-1A-P4z, where zircon crystals are added, on an Al foil. (c) II-1A-P4z sandwiched between Al foils. (d) A scale for (a), (b) and (c). The separation between each scale bar is 0.5 mm.

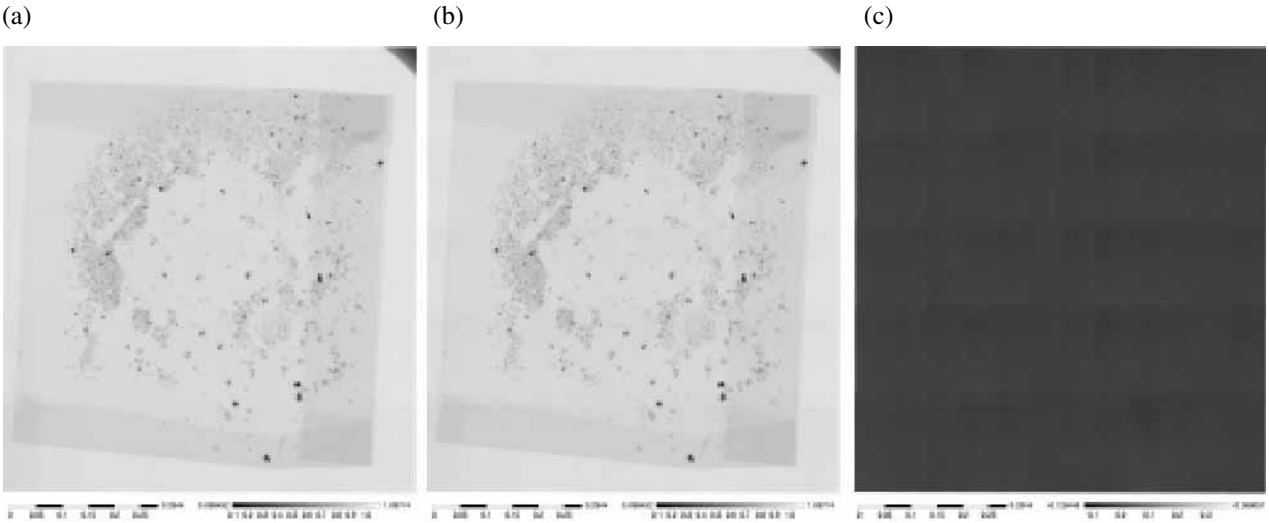

Figure 52. Mosaic projection images of HASPET sample II-1A-P3 (without zircon). The left and right bars are a scale bar in cm and a gray scale bar for transmittance, respectively. (a) Above the Zr K-edge energy. (b) Below the Zr K-edge energy. © Subtraction image. Zr-bearing minerals are not seen in this sample.

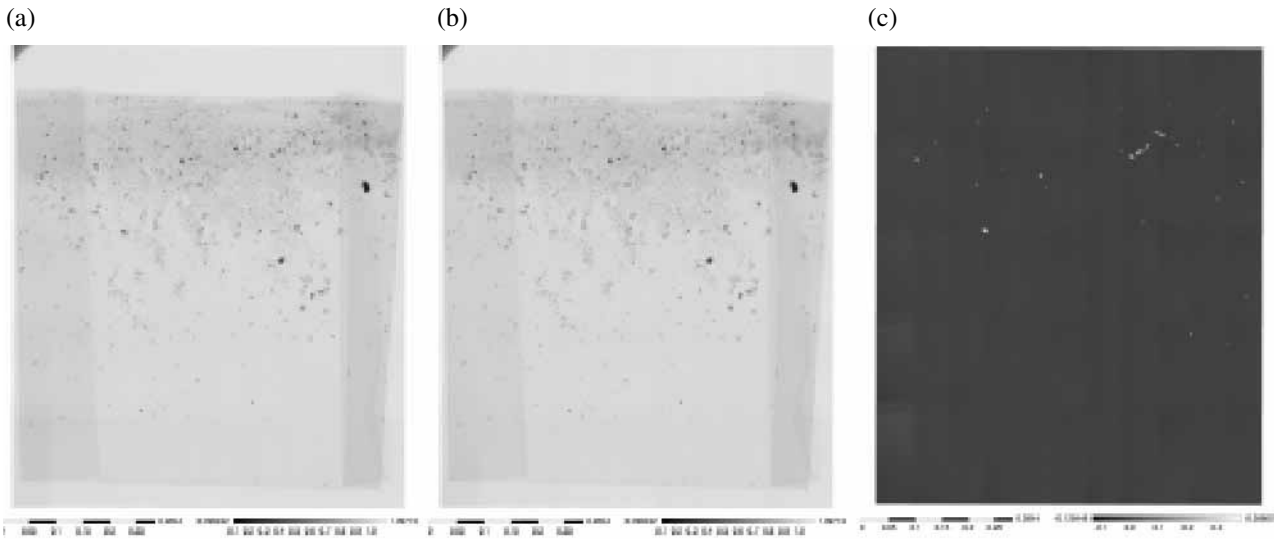

Figure 53. Mosaic projection images of HASPET sample II-1A-P4z (with zircon). The left and right bars are a scale bar in cm and a gray scale bar for transmittance, respectively. (a) Above the Zr K-edge energy. (b) Below the Zr K-edge energy. (c) Subtraction image. Zircon grains are recognized as bright spots.

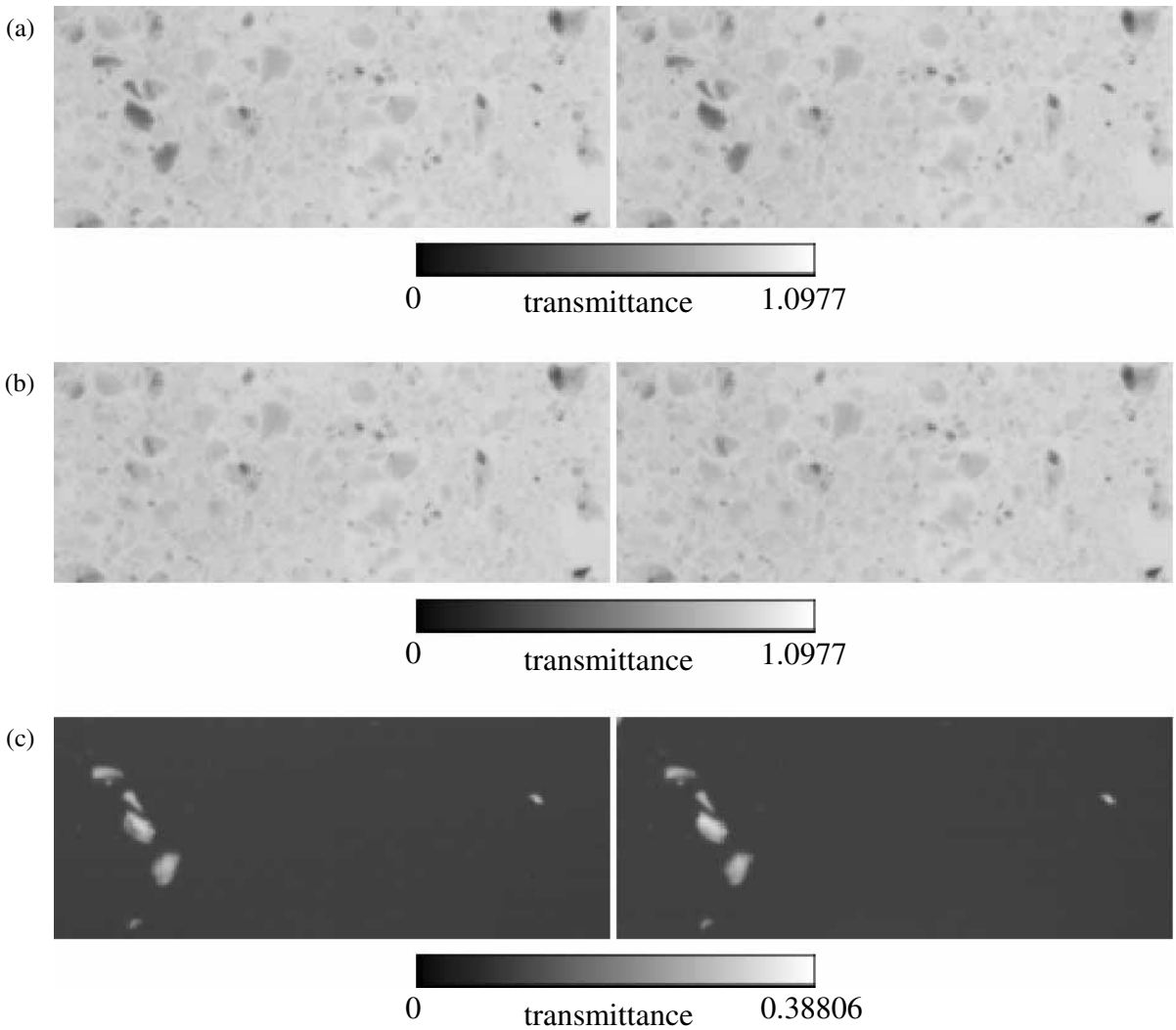

Figure 54. Stereographs for a projection images of HASPET sample II-1A-P4z (with zircon) imaged above the Zr K-edge energy. (a) Above the Zr K-edge energy. (b) Below the Zr K-edge energy. (c) Subtraction image. Gray scales are for transmission rates. The width of each projection image is 1.896 μm.

Acknowledgements: This study is possible only at SPring-8 in Japan. The authors are grateful to Dr. Yoshio Suzuki of JASRI/SPring-8. We also thank to Mrs. Kentaro Nakamura and Hirokazu Furukawa of Osaka University for their helps. Especially, Mr. Nakamura obtained the CT value − LAC relation at BL20B.

REFERENCES

Bonse, U. and Busch, F., 1996, X-ray computed microtomography (μCT) using synchrotron radiation (SR), *Progress in Biophysics and Molecular Biology*, **65**, 133-169.

Britt, D.T. and Consolmagno, G., 2003, Stony meteorite porosities and densities: a review of the data through 2001, *Meteoritics and Planetary Science*, **38**, 1161-1180.

Britt, D.T., Yeomans, D., Housen, D., and Consolmagno, G., 2003, Asteroid density, porosity, and structure. in Asteroids III, 485-500.

Flannery, B.P., Deckman, H.W., Roberge, W.G., and D'Amico, K.L., 1987, Three-dimensional X-ray microtomography, *Science*, **237**, 1439-1444.

Hurukawa H., 2005, Density measurement and estimation of minerals in Hayabusa analog samples, Bachelor Thesis at Osaka University. (text in japanese).

Ikeda, S., Nakano, T., Tsuchiyama, A., Uesugi, K., Suzuki, Y., Nakamura, K., Nakashima, Y. and Yoshida, H., 2004, Nondestructive three-dimensional element-concentration mapping of a Cs-doped partially molten granite by X-ray computed tomography using synchrotron radiation, *American Mineralogist*, **89**, 1304-1312.

Nakano, T., Nakamura, K., Someya, T. and Ohtsuka, H., 1997, Observation of 3-dimensional internal structures of rock using X-ray CT: (1) density calibration of CT value (in Japanese with English abstract), *Geoinformatics*, **8**, 239-255.

Nakano, T., Nakashima Y., Nakamura, K. and Ikeda, S., 2000, Observation and analysis of internal structure of rock using X-ray CT (in Japanese with English abstract), *Journal of Geolical Society of Japan*, **106**, 363-378.

Nakashima, Y., Nakano, T., Nakamura, K., Uesugi, K., Tsuchiyama, A., and Ikeda, S., 2004, Three-dimensional diffusion of non-sorbing species in porous sandstone: computer simulation based on X-ray microtomography using synchrotron radiation, *Jour*. Contaminant Hydrology, **74**, 253-264.

Thompson, A.C., Llacer, J., Campbell Finman, L., Hughes, E.B., Otis, J.N., Wilson, S. and Zeman, H.D., 1984, Computed tomography using synchrotron radiation, *Nuclear Instruments and Methods in Physics Research*, **222**, 319-323.

Tsuchiyama, A., Uesugi, K., Noguchi, T., Yano, H., Nakano, T. and Suzuki, Y., 2001, Three-dimensional microstructures of Antarctic micrometeorites by X-ray computed tomography using synchrotron radiation at SPring-8, *Meteoritics and Planetary Science*, **36**, Suppl. A210.

Tsuchiyama, A., Shigeyoshi, R., Kawabata, T., Nakano, T., Uesugi, K. and Shirono, S., 2003a, Three-dimensional structures of chondrules and their high-speed rotation, *Abst. Lunar and Planetary Science Conference*, **XXXIV**, Abstract #1271, Lunar and Planetary Institute, Houston (CD-ROM).

Tsuchiyama, A., Osada, Y., Nakano, T. and Uesugi, K., 2003b, Experimental reproduction of classic barred olivine chondrules: open system behavior and thermal history of chondrule formation, *Geochimica et Cosmochimica Acta*., **68**, 653-672.

Tsuchiyama, A., Uesugi, K., Nakano, T., and Ikeda, S., 2005, Quantitative evaluation of attenuation contrast of X-ray computed tomography images using monochromatized beams, *American Mineralogist*, **90**, 132-142.

Uesugi, K., Tsuchiyama, A., Nakano, T., Suzuki, Y., Yagi, N., Umetani, K. and Kohmura, Y., 1999, Development of micro-tomography imaging system for rock and mineral samples, *Proceedings of Society of Photo-Optical Instrumentation Engineers*, **3772**, 214-221.

Uesugi, K., Suzuki, Y., Yagi, N., Tsuchiyama, A. and Nakano, T., 2001, Development of high spatial resolution X-ray CT system at BL47XU in SPring-8, *Nuclear Instruments and Methods in Physics Research A*, **467-468**, 853-856.

Appendix: CT value − LAC relation

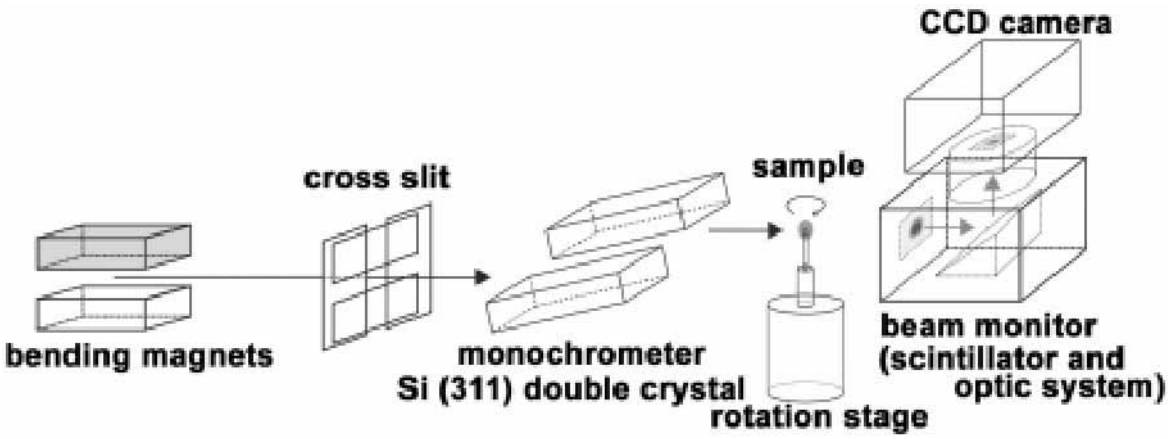

Figure A1. The schematic illustration of a projection microtomographic system at SPring-8 (Tsuchiyama et al., 2005).

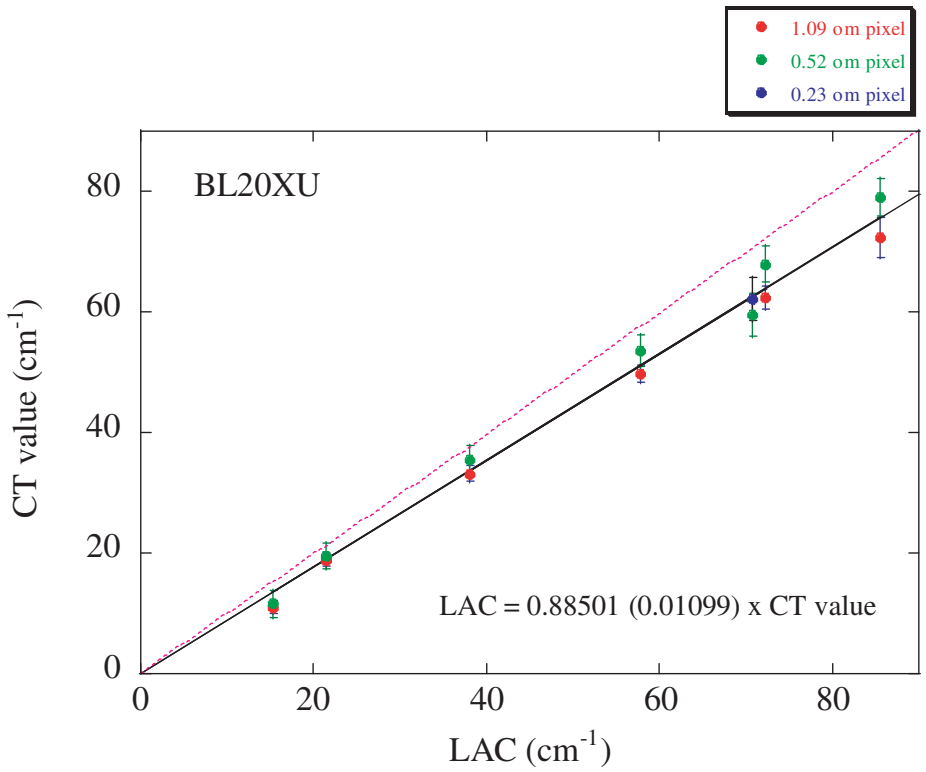

Figure A2. The relation between CT values and LAC determined by imaging standard materials at BL20XU (Nakamura et al., 2005)

LIST OF AUTHORS AND CO-AUTHORS

ADACHI, K.	Kobe University
FUJIWARA, A.	ISAS/JAXA
KUSHIRO, I.	University of Tokyo
MINAI, Y.	Musashi University
NAKAMURA, T.	Kyushu University
NAKANO, T.	AIST
NOGUCHI, T.	Ibaraki University
OHNISHI, I.	Kobe University
SAKAI, Y.	Daido Institute of Technology
SUGITA, M.	Kobe University
TANAKA, M.	KEK
TOMEOKA, T.	Kobe University
TOMIOKA, N.	Kobe University
TSUCHIYAMA, A.	Osaka University
UESUGI, K.	SPring-8
YAMAMOTO, T.	Hokkaido University
YANO, H.	ISAS/JAXA

JAXA Special Publication JAXA-SP-05-021E

Date of Issue : March 31, 2006
Edited and Published by : Japan Aerospace Exploration Agency
7-44-1 Jindaiji-higashimachi, Chofu-shi, Tokyo 182-8522, Japan
URL: http://www.jaxa.jp/

Inquires about copyright and reproduction should be addressed to the Aerospace Information Archive Center, Information Systems Department JAXA.
2-1-1 Sengen, Tsukuba-shi, Ibaraki 305-8505, Japan
phone: +81-29-868-5000 fax: +81-29-868-2956